Quantum non-linearities of a qubit ultra-strongly coupled to a waveguide

Nicolas Gheeraert

Communauté
UNIVERSITÉ Grenoble Alpes

THÈSE

Pour obtenir le grade de

DOCTEUR DE LA COMMUNAUTÉ UNIVERSITÉ GRENOBLE ALPES

Spécialité : Physique Théorique

Arrêté ministériel : 25 mai 2016

Présentée par

Nicolas GHEERAERT

Thèse dirigée par **Serge FLORENS**
et codirigée par **Nicolas ROCH**
préparée au sein du **Laboratoire Institut Néel**
dans **l'École Doctorale Physique**

Non-linéarités quantiques d'un qubit en couplage ultra-fort avec un guide d'ondes

Quantum non-linearities of a qubit ultra-strongly coupled to a waveguide

Thèse soutenue publiquement le **11 octobre 2018**,
devant le jury composé de :

Monsieur MANUEL HOUZET
INGENIEUR CHERCHEUR, CEA GRENOBLE, Examinateur
Monsieur VOLKER MEDEN
PROFESSEUR, UNIVERSITE RWTH AACHEN - ALLEMAGNE, Rapporteur
Monsieur JERÔME ESTEVE
CHARGE DE RECHERCHE, CNRS DELEGATION ILE-DE-FRANCE SUD, Examinateur
Monsieur BENOIT BOULANGER
PROFESSEUR, UNIVERSITE GRENOBLE ALPES, Président
Monsieur JERÔME CAYSSOL
PROFESSEUR, UNIVERSITE DE BORDEAUX, Rapporteur

Aknowledgements

First, I would like to thank Serge for guiding my PhD during these past four years. His readiness to devote a lot of time to his students was very beneficial to me, especially in the early stages of my PhD. I am also grateful to him for reading my manuscript in great detail, and for his thorough feedback that helped me bring it to completion.

I am obliged to Nicolas for introducing me to the experimental side of microwave optics, and for providing me with the opportunity to get actively involved in his lab. Moreover, it is with his support that I was able to apply for the Raman-Charpak fellowship that allowed me to spend a year in the lab of Vijay at the Tata Institute of Fundamental Research (TIFR) in India.

I am very thankful as well to Vijay for welcoming me to his lab, and for spending the time to help me settle down in Mumbai. During my time at TIFR, I greatly appreciated his readiness and enthusiasm to clarify any doubts that I would have. His idea to pair me up on the project with Suman, a senior PhD student in the lab, was a very natural one. Suman already had a great deal of experience in running microwave experiments, and I benefited a lot from working with him.

Thank you to Jérôme Cayssol and Volker Meden for their thorough review my manuscript, and to Manuel Houzet, Jérôme Estève and Benoît Boulanger for taking part in the jury.

Finally, the work presented in this thesis would not have been possible without the support of the Nanoscience Foundation which funded my PhD, and without the Raman-Charpak fellowship, granted to me by CEFIPRA, which funded six months of my stay in India. Here, I would especially like to thank Alain Fontaine, director of the Nanoscience Foundation, for his support of my initiative to spend part of my PhD abroad.

Abstract

In the recent years, the field of light-matter interaction has made a further stride forward with the advent of superconducting qubits ultra-strongly coupled to open waveguides. In this setting, the qubit becomes simultaneously coupled to many different modes of the waveguide, thus turning into a highly intricate light-matter object. Investigating the wealth of new dynamical phenomena that emerge from the high complexity of these engineered quantum many-body systems is the main objective of this thesis.

As a first crucial step, we tackle the time-evolution of such a non-trivial system using a novel numerical technique based on an expansion of the full state vector in terms of multi-mode coherent states. Inspired by earlier semi-classical approaches, this numerically exact method provides an important advance compared to the state-of-the-art techniques that have been used so far to study the many-mode ultra-strong coupling regime. Most importantly, it keeps track of every detail of the dynamics of the complete qubit-waveguide system, allowing both to perform the tomography and to extract multi-particle scattering of the waveguide degrees of freedom.

An exploration of the many-mode ultra-strong coupling regime using this new technique led to the two core theoretical predictions of this thesis. The first demonstrates that the radiation spontaneously emitted by an excited qubit takes the form of a Schrödinger cat state of light, a result strikingly different from the usual single-photon emission known from standard quantum optics. The second prediction concerns the scattering of low-power coherent signals on a qubit, a very common experimental protocol performed routinely in laboratories. Most remarkably, it is shown that the qubit non-linearity, transferred to the waveguide through the ultra-strong light-matter interaction, is able to split photons from the incoming beam into several lower-energy photons, leading to the emergence of a low-frequency continuum in the scattered power spectrum that dominates the inelastic signal. By studying the second-order correlation function of the radiated field, it is also shown that emission at ultra-strong coupling displays characteristic signatures of particle production.

In the final part of the thesis, the second-order correlation function is investigated again, but this time experimentally, and in the regime of moderate coupling. Although the results are still preliminary, this part of the thesis will also provide an instructive account of quantum signal measurement theory and of the experimental procedure involved in measuring microwave signal correlations. Moreover, the experimental developments and microwave simulations tools described in this section could be applied in the future to signals emitted by ultra-strongly coupled qubits, in order to observe the signatures of particle production revealed by the second-order correlation function.

Résumé

Au cours des dernières années, le domaine de l'interaction lumière-matière a fait un pas de plus en avant avec l'avènement des qubits supraconducteurs couplés ultra-fortement à des guides d'ondes ouverts. Dans ce contexte, un qubit devient simultanément couplé à de nombreux modes du guide d'onde, se transformant ainsi en un objet hybride lumière-matière hautement intriqué. L'étude de nouveaux phénomènes dynamiques qui émergent de la grande complexité de ces systèmes quantiques à N-corps est l'objectif principal de cette thèse.

Dans une première étape cruciale, nous abordons l'évolution dans le temps d'un tel système en utilisant une nouvelle technique numérique basée sur un développement complet du vecteur d'état en termes d'états cohérents multimodes. Inspirée par des approches semi-classiques antérieures, cette technique numériquement exacte fournit un progrès important par rapport aux méthodes de pointe qui ont été utilisées jusqu'à présent pour étudier le régime de couplage ultra-fort à N-corps. Fondamentalement, cette approche préserve également le détail de la dynamique du système complet réunissant le guide d'onde et le qubit, permettant à la fois d'effectuer la tomographie et d'extraire la diffusion multi-particule des degrés de liberté du guide d'onde.

Une exploration du régime de couplage ultra-fort multi-mode utilisant cette nouvelle technique a conduit aux deux prédictions théoriques fondamentales de cette thèse. La première démontre que le rayonnement émis spontanément par un qubit excité prend la forme d'un chat de Schrödinger de lumière, un résultat étonnamment différent de l'émission de photon unique habituelle en optique quantique. La seconde prédiction concerne la diffusion de signaux cohérents de faible puissance sur un qubit, un protocole expérimental très courant en laboratoire. De façon remarquable, il est montré que la non-linéarité du qubit, transférée au guide d'onde par l'interaction ultra-forte avec la lumière, est capable de diviser les photons du faisceau entrant en plusieurs photons de plus basse énergie, conduisant à l'émergence d'un continuum basse fréquence dans le spectre de puissance, qui domine le signal hors-résonant. En étudiant la fonction de corrélation de second ordre dans le champ rayonné, il est également démontré que l'émission en couplage ultra-fort présente des signatures caractéristiques de la production de particules.

Dans la dernière partie de la thèse, la fonction de corrélation de second ordre est à nouveau étudiée, mais cette fois expérimentalement, et dans le régime du couplage modéré. Bien que les mesures soient encore préliminaires, cette partie de la thèse présente un compte-rendu instructif de la théorie de la mesure du signal et permet de comprendre en détail la procédure expérimentale impliquée dans la mesure de correlations dans les signaux micro-ondes. De plus, à l'avenir, les développements expérimentaux et les outils de simulation décrits pourraient être appliqués aux signaux émis par des qubits ultra-fortement couplés, afin d'observer les signatures de production de particules révélées par la fonction de corrélation du second ordre.

Contents

Chapter 1

Motivation

1.1 Waveguide quantum optics

It was first remarked in the early 1980s [1] that, in theory, one could construct a two-level quantum system out of a nearly macroscopic electrical circuit by engineering a superconducting ring interrupted by a tunnel junction. The idea was that if one could achieve a stable half quantum of flux $\Phi_0/2 = (h/2e)/2$ threading the ring, one could in principle use the two opposite values of the induced persistent currents, $|\circlearrowleft\rangle$ and $|\circlearrowright\rangle$, as the two quantum levels of the device, in direct analogy with the $|\uparrow\rangle$ and $|\downarrow\rangle$ states of a spin qubit.

About 15 years later, the first observation of coherent oscillations however happened in a different Josephson superconducting device, known as the Cooper pair box [2], a quantum two-level system that is the dual of the superconducting quantum ring: instead of persistent currents, one isolates two charge states of a small superconducting island to create a qubit. It took more time, until 2003, to observe coherent oscillations in a flux qubit [3], mainly because of the high sensitivity of a single flux quantum to external flux variations [4]. In fact, to address this stability issue, the flux qubit was only achieved using a more complex configuration than the one initially thought of, that involved a ring interrupted by three junctions of different sizes. Today, the most commonly used superconducting qubit is the transmon qubit, which is a variant of the Cooper-pair box made less sensitive to charge noise by reducing the charging energy of the superconducting island.

The advent of superconducting qubits is an important turning point, as these artificial atoms opened the way for expanding the field of quantum optics and light-matter interaction, to the field of microwave optics in quantum circuits, also known as circuit QED (circuit Quantum Electro-Dynamics). With the support of modern nano-fabrication techniques that allowed to engineer circuit architectures of many types, the control over the interaction between electromagnetic waves and qubits took a great leap forward, making possible for instance, to strongly couple qubits to microwaves confined in one dimensional waveguides. This allowed Astafiev *et al.* in 2010 to achieve 94% extinction in the transmission of a coherent signal scattering on a flux qubit [5], as shown in Fig. 1.1c, at a time when standard optical experiments had barely managed an extinction of 12%, using a GaAs quantum dot [6], or a single dye molecule [7].

Further observation of the structure of the microwave radiation in quantum circuits however has proven very challenging, essentially because the efficient detection of single photons is a very difficult task in the field of microwave quantum circuits where microwave quanta have frequencies four to five orders of magnitude smaller than their optical counterpart. The measurement of microwaves is in fact restricted to the digitization of the signal voltage using linear detectors [9], which is a very indirect way of measuring quantum signals, such as itinerant

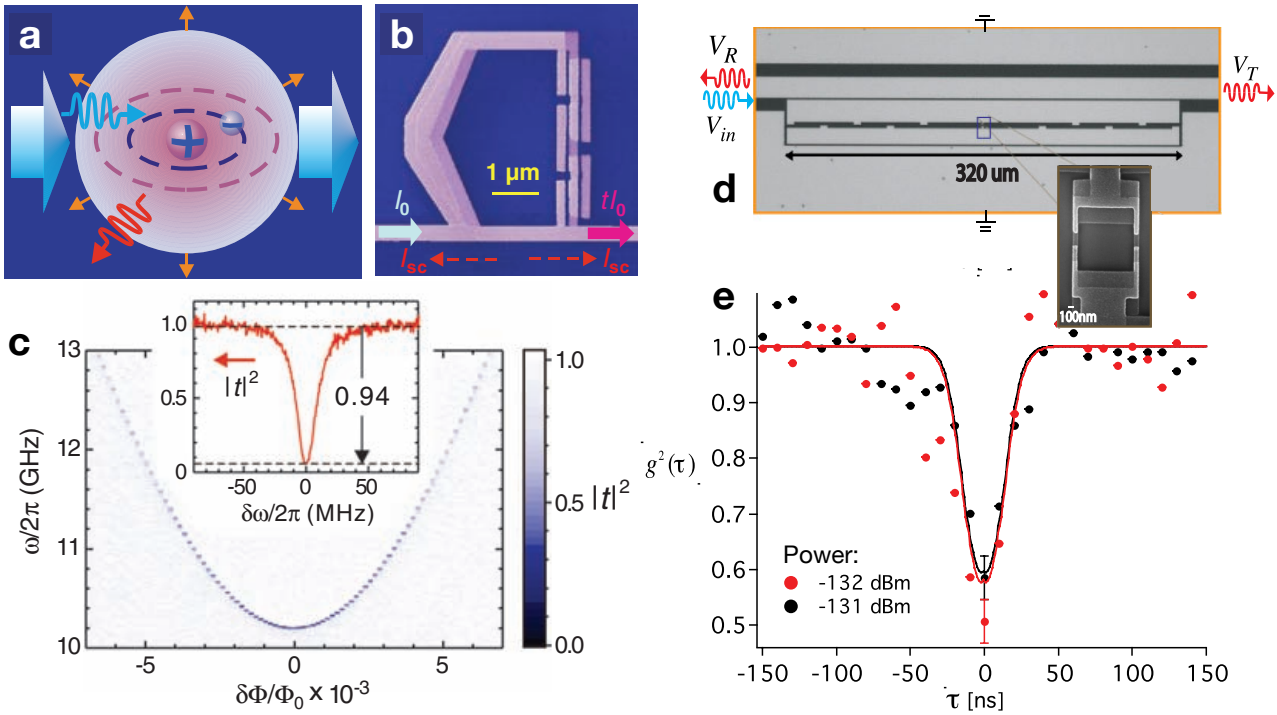

Figure 1.1: **Waveguide quantum optics. Left panels:** Resonant wave scattering on a single artificial atom by Astafiev *et al.* [5]. **(a)** Sketch of a natural atom in open space. The atom resonantly absorbs and reemits photons in a solid angle of 4π. **(b)** False-colored SEM image of the artificial atom coupled to a 1D transmission line: a loop with four Josephson junctions (flux qubit) is inductively coupled to the line. Here, the incident wave (blue arrow) is scattered only backward and forward (red arrows). The transmitted wave is indicated by a magenta arrow. **(c)** Spectroscopy of the artificial atom. Shown is the power transmission coefficient $|t|^2$ versus the flux bias $\delta\Phi$ and incident microwave frequency $\omega/2\pi$. When the incident radiation is in resonance with the atom, a dip in $|t|^2$ appears in the 3D plot. (Inset) Power transmission coefficient $|t|^2$ at $\delta\Phi = 0$ as a function of incident wave detuning $\delta\omega/2\pi$ from the resonance frequency, showing a maximal power extinction of 94%. **Right panels:** measurement of photon anti-bunching in a waveguide by Hoi *et al.* [8]. **(d)** Transmon qubit coupled to a CPW waveguide (superconducting aluminum elements are in light-grey). **(e)** $g_2(\tau)$ correlation function in the reflected signal: $g_2(0) < 1$ indicates anti-bunching.

photons [10]. Moreover, before performing any measurement of a device in quantum circuits, the quantum signal has to be amplified, which brings the additional challenge of minimizing the noise added by the amplification chain. In spite of these difficulties, the measurement of anti-bunching (the temporal anti-correlation of photons) in an open transmission line (see Fig. 1.1d-e) was achieved in 2013 by Hoi *et al.* [8] using linear amplifiers and by performing a very large number of averages to filter out the noise. Later on, the use of Josephson parametric amplifiers (JPA) [11, 12], pioneered at Bell labs 30 years back, brought a dramatic improvement to the measurement accuracy by allowing to pre-amplify quantum signals more than 100 times while only adding half a photon of noise. Most notably, those amplifiers were pivotal in achieving the first measurement of quantum jumps in superconducting qubits [13]. A more recent example among many experiments demonstrating the key role of JPAs, is the measurement of second-order correlations between two photons emitted in cascade by a superconducting qubit initially prepared in its third energy state [14] .

On the theoretical side, these experiments are very well modeled by the rotating wave approximation (RWA), which essentially truncates the system dynamics to resonant transitions.

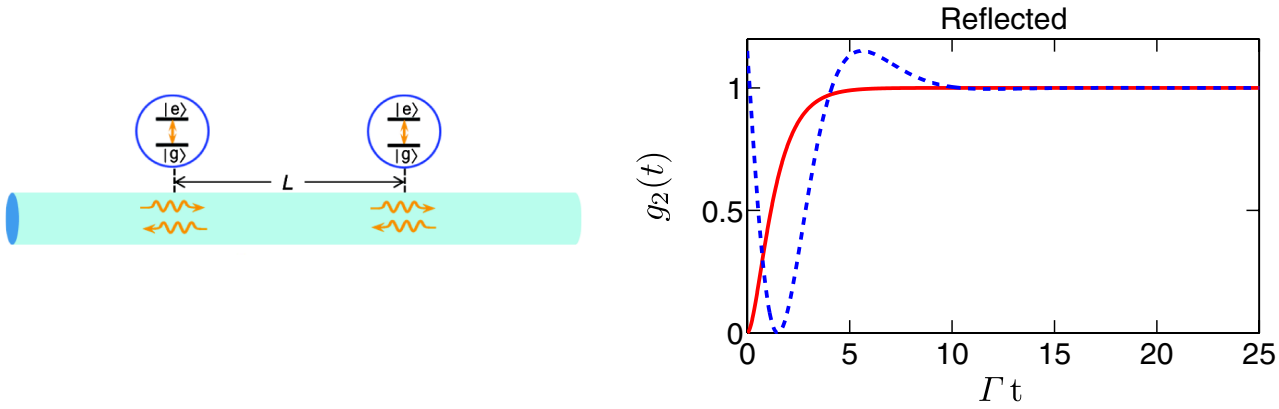

Figure 1.2: RWA calculation of the $g_2(t)$ correlation function in the signal reflected by two qubits separated by a distance L in a waveguide, by Zheng *et al.* [15]. When $k_0 L = 0$, where k_0 is the frequency of the incoming signal on resonance with the qubit (red curve), the reflected signal shows perfect anti-bunching at $\Gamma t = 0$, as if there were a single scatterer (Γ being the resonance linewidth). When $L = k_0\pi/2$, however, the g_2 function reveals a more complex structure in the waveguide including bunching at $\Gamma t = 0$ ($g_2 > 1$), and pure anti-bunching at finite time.

In other words, it allows the excitation of the atom upon absorption of a photon or the relaxation of the atom upon emission of a photon, but forbids any higher order process, such as the simultaneous excitation of the atom *and* the emission of a photon. As an example of such predictions, very recently Zheng *et al.* [15] used the RWA technique to calculate the second-order correlations of the field reflected by two qubits in series. As shown on Fig. 1.2, when the two qubits are next to one another, they behave as a single scatterer, with in particular $g_2(0) = 0$, signature that the signal is completely anti-bunched. When the qubits are located away from each other however, the reflected signal presents a highly non-trivial pattern, including pure anti-bunching at finite times, and bunching ($g_2 > 1$) at $t = 0$. These theoretical predictions nicely illustrate the versatility of waveguide quantum electro-dynamics (wQED) to explore quantum optical phenomena.

1.2 The ultra-strong coupling regime of circuit QED

One of the great strengths of doing quantum optics in circuits is the large number of ways one can engineer qubits and electromagnetic environments, such as 1D waveguides. This also means that the fine structure constant α dictating the fundamental value of the coupling can itself be tuned by choosing the right circuit design. When α becomes large enough, the system enters the regime of ultra-strong coupling, in which the relaxation rate of the atom Γ becomes a sizeable fraction of the energy splitting Δ of the atom. It is worth noting that this regime of coupling is far more intense than what we referred to as "strong coupling" in the previous paragraph. Indeed, "strong" in the present context means nothing more than having a qubit that relaxes to the waveguide at a rate Γ much greater than the qubit intrinsic losses Γ_ϕ (as in Fig. 1.1c), but which remains small compared to the qubit energy Δ.

The regime of *ultra*-strong coupling between a qubit and a many-mode waveguide was demonstrated experimentally very recently both by using a flux qubit [17] and a transmon qubit [16]. In the later realization, Puertas-Martinez *et al.*, engineered a waveguide consisting of an array of 4700 SQUIDs coupled to a transmon, as shown on the optical microscope image of Fig. 1.3b. In this system, it is the huge impedance of this array (in blue), as well as the large

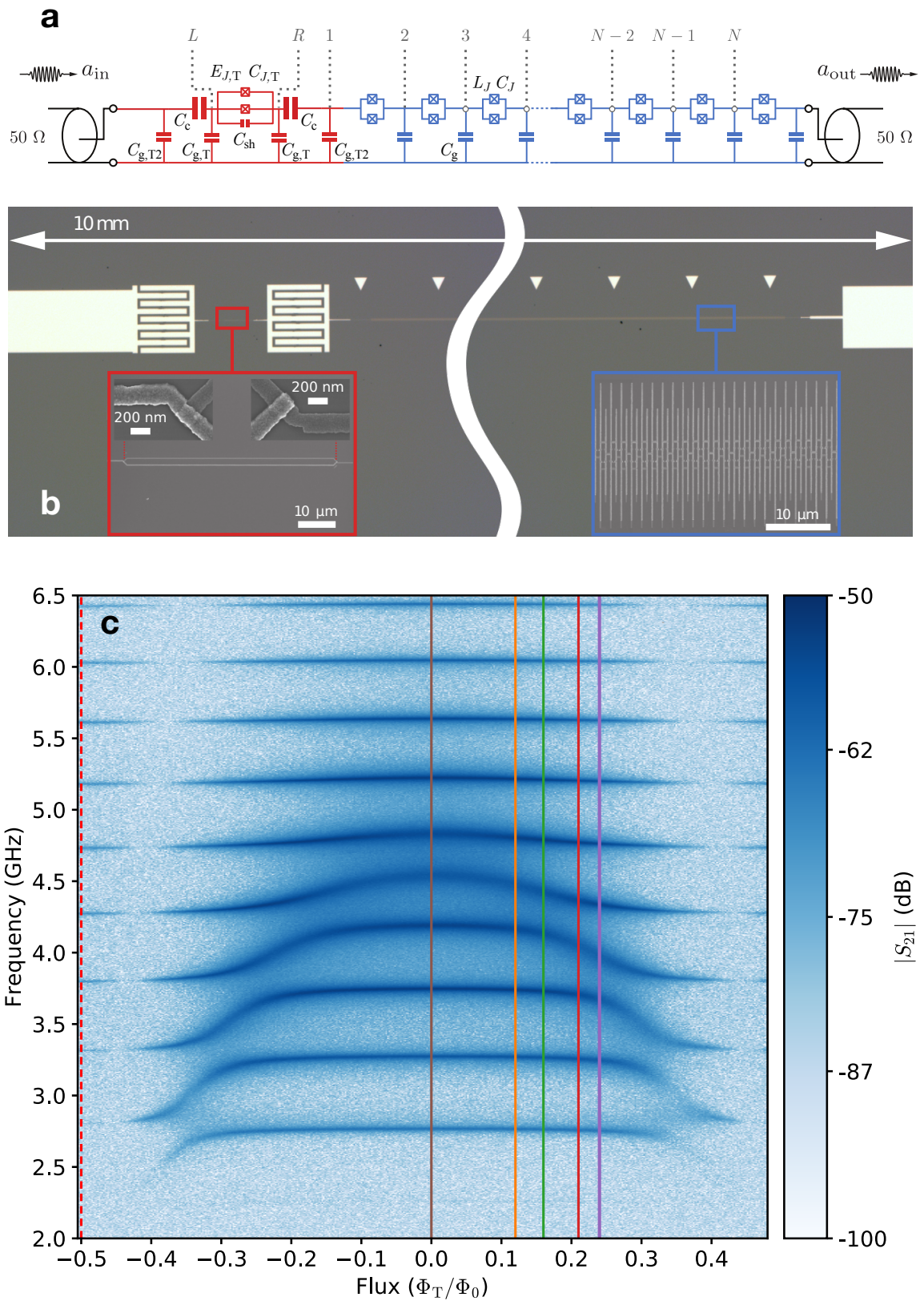

Figure 1.3: **A Josephson platform for waveguide quantum electrodynamics (Puertas-Martinez *et al.* [16]). (a)** Lumped element model of the circuit. **(b)** Optical microscope image of the sample. The two zoom-in are SEM images of the SQUID of the qubit (red square) and the SQUIDs in the chain (blue square). The qubit is capacitively coupled to the chain and to a 50Ω measurement line, via large interdigital contacts. Only a small portion of the Josephson chain, which comprises 4700 SQUIDs in total, is shown. **(c)** Microwave transmission measurement $|S_{12}|$ of the complete device (transmon and chain) shown above, as a function of flux threading the qubit.

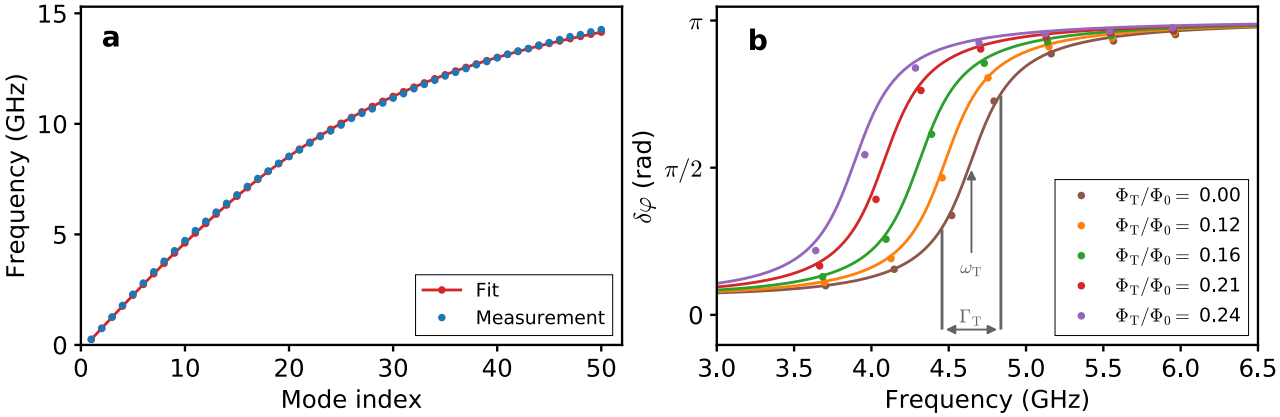

Figure 1.4: Modes of the Josephson array (Fig. 1.3a-c) [16]. **(a)** Dispersion relation of the chain alone obtained from the fit of the resonances obtained at a value of the flux threading the transmon of $\Phi_T = -\Phi_0/2$ (red-dashed line in Fig. 1.3c), so that the chain modes are not hybridized with the transmon. **(b)** Normalized frequency shift $\delta\phi_n$ of the discrete chain modes as a function of mode frequency ω_n for the transmon fluxes Φ_T indicated by the solid vertical lines in Fig. 1.3c (with the same color code). The values of the relaxation rate Γ_T of the qubit is extracted from the hybridization of the chain modes as indicated by the frequency shifts.

interdigitated capacitances of the qubit (in red) that generate the ultra-strong qubit-microwave interaction. Owing to the tunable flux Φ_T threading the SQUID loop of the qubit, the qubit energy can itself be varied.

The measurement of the transmission $|S_{21}|$ of this system is shown in Fig. 1.3c, where the transmon energy was varied over a full period by sweeping the flux Φ_T. For $\Phi_T/\Phi_0 = -0.5$, as shown by the red dashed line, the qubit is detuned in frequency, allowing to probe the modes of the unhybridised array. As shown by the frequency of the first 50 unhybridised modes that have been plotted on Fig. 1.4a, the collective charge density modes along the array present a sound-like dispersion relation.

As the threading flux is moved away from $\Phi_T/\Phi_0 = -0.5$ in Fig. 1.3c, one can estimate the frequency of the transmon by locating the most prominent avoided crossings, signatures of the hybridization of the chain modes with the qubit. As explained in detail in the paper [16], one can infer the coupling strength of a certain mode to the qubit from the difference between its hybridized frequency and the unhybridised mode frequencies (the latter being obtained when $\Phi_T/\Phi_0 = -0.5$). This hybridization frequency shift $\delta\Phi_n$, where n labels the mode number, is shown in Fig. 1.4b for 5 values of the qubit flux indicated by the vertical solid lines on the Fig. 1.3c, from which one can clearly see that up to 7 modes are interacting simultaneously with the qubit over a large range of frequencies. From the range of frequencies the qubit interacts with (Fig. 1.4b), one can then deduce that the relaxation rate of qubit is 10% of the resonance frequency of the qubit, $\Gamma_T/\omega_T \sim 0.1$. This corresponds to a coupling constant of $\alpha \sim 10\%$, evidence of the ultra-strong coupling regime.

These very recent developments in the field of quantum circuits, that allowed to reach this regime of extreme coupling by tweaking the fine-structure constant α, do not have any counter-part in standard quantum optics where the fine structure constant in vacuum is fixed by the value $\alpha = 1/137$. There are nonetheless alternatives to enhance light-matter interaction in vacuum. The most common way is to confine the electromagnetic field in a cavity, which leads to higher couplings between the atom and the cavity field [18, 19, 20]. Another strategy, demonstrated recently, consists in inducing strong photon-photon interaction by making use of the cooperativity of an ensemble of Rydberg atoms [21, 22]. Although these strategies do allow

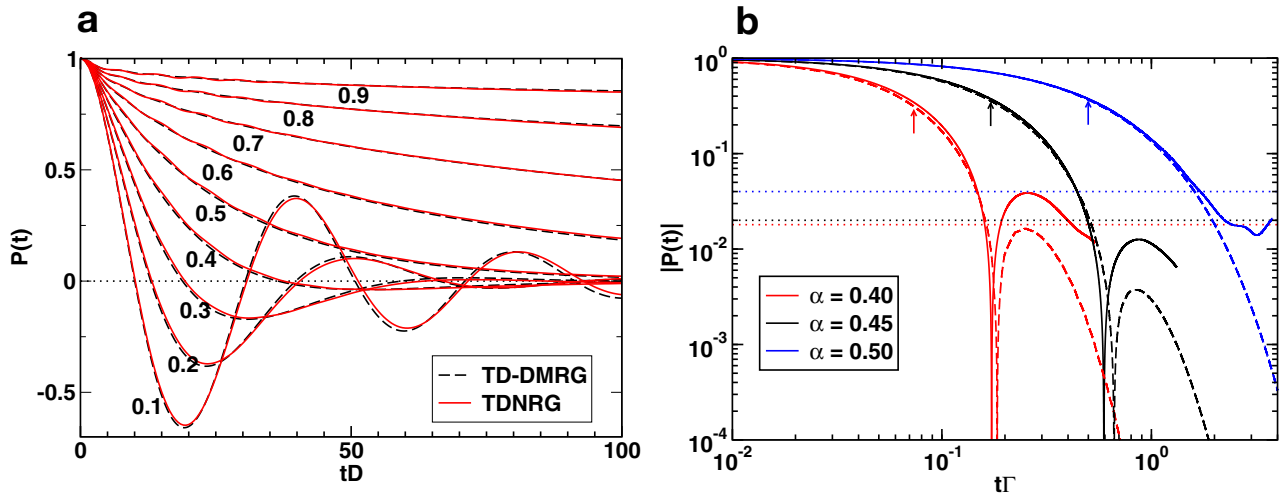

Figure 1.5: **(a)** TD-NRG and TD-DMRG dynamics in the ultra-strong coupling regime of the decay of the $\langle\sigma_z(t)\rangle = P(t)$ component of the spin, upon preparation of the spin in the $|\uparrow\rangle$ state, for various values of the coupling constant α (from [28]). In these simulations, the bare qubit energy is $\Delta/\omega_c = 0.1$ and the time is in units of half the cutoff frequency $D = \omega_c/2$. **(b)** TD-NRG decay of $\langle\sigma_z(t)\rangle$ (solid lines) at long time in log-log scale for a small qubit rate $\Delta/\omega_c = 0.001$. The time axis is units of the inverse of the relaxation rate $\Gamma = \Delta^2/\omega_c = 2 \times 10^{-6}$. The dotted lines are the incorrect finite values of the z component of the spin at infinite time $|\langle\sigma_z(t=\infty)\rangle|(= |P(\infty)|)$ obtained within the TD-NRG. Dashed lines are the analytical estimates from a ressumed perturbation theory around the Toulouse limit $\alpha = 0.5$.

to obtain strong light-matter couplings that can enhance non-linear effects, the intensities of coupling are still much below the ultra-strong coupling regime achieved in the experiment by Puertas-Martinez *et al.*. Moreover, in their current state, these optical systems are limited to the interaction with a single cavity mode, which means that many-body effects involving the strong coupling of a qubit to a large number of modes at once are currently impossible in the optical domain.

The significance of the ultra-strong coupling regime is in fact more far reaching than it appears, in particular with its close connection to Kondo physics [23, 24, 25]. Indeed, it was shown that in certain conditions, the physics of a bath of bosons interacting ultra-strongly with a spin 1/2, *is identical* to the physics of a magnetic impurity interacting with a Fermi sea [26]. The ultra-strong coupling platform engineered by Puertas-Martinez *et al.* is therefore a very promising development to observe, in an all-electrical setup, aspects of Kondo physics that have proven extremely difficult to measure in its fermionic form. One exciting prospect is regarding the Kondo screening cloud, which has never been observed due to the daunting task of measuring long-range magnetic correlations, but which could soon be accessible by measuring the spatial correlations in the microwave signal scattered on a Josephson impurity [27].

1.3 Quantum dynamics at ultra-strong coupling in waveguides

The simplest model to represent a qubit coupled to a many-mode waveguide is the spin-boson model [26], which describes the dissipation of a quantum two-level system into a many-mode bosonic bath. In systems involving a large number of degrees of freedom however, solving the

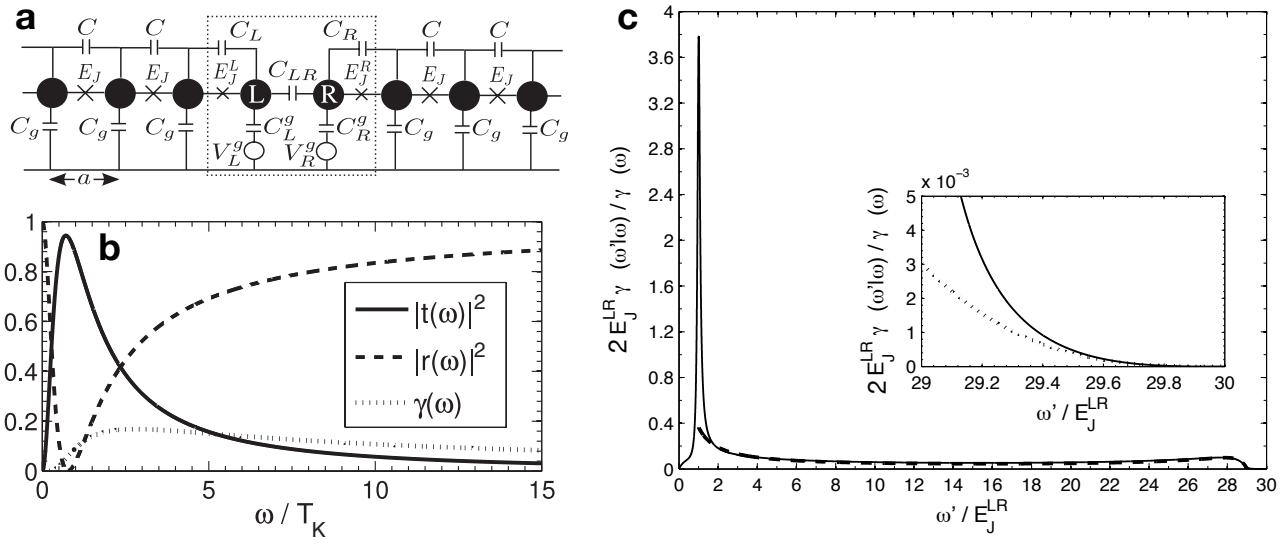

Figure 1.6: Inelastic scattering of a single photon on an impurity embedded in the centre of a symmetric Josephson waveguide. These results were obtained by Goldstein *et al.* using a perturbative approach [29]. **(a)** Circuit diagram. **(b)** Elastic transmission $|t(\omega)|$, elastic reflection $|r(\omega)|$, and total inelastic scattering $|\gamma(\omega)|$ probabilities at the Toulouse point $\alpha = 0.5$ for a single incoming photon at frequency ω/T_K, with T_K the Kondo temperature. **(c)** Frequency-resolved inelastic conversion spectrum $\gamma(\omega'|\omega)$, for an incident photon with frequency $\omega'/E_J^{LR} = 30$, where E_J^{LR} is the qubit energy, referred to as Δ in the rest of this thesis.

spin-boson model can prove a very challenging task. This is clearly the case in the experiment by Martinez *et al.* described above, in which the SQUID chain includes 4700 modes. The complete microscopic model with all 4700 modes leads to a Hilbert space of size 4700^N, where N is the maximum number of occupied quanta in a mode. This is clearly out of hand for any brute force numerical technique. Despite the gigantic size of the Hilbert space, in practice only a small number of modes hybridized with the qubit (up to 10 in the experiment by Puertas-Martinez *et al.*), which seems to imply that the problem could be simplified by truncating the problem to this smaller set of hybridized modes. It turns out however that this does not work, as the dispersion relation of the modes depends on the microscopic details of the whole array. A theoretical approach that can incorporate the realistic dispersion relation of multi-mode arrays is therefore unavoidable.

A few methods exist for solving the time-dynamics of the spin-boson model in the ultra-strong coupling regime. Recent results by Nghiem et al. [28] use the time-dependent density matrix renormalisation group (TD-DMRG) and the time-dependent numerical renormalisation group (TD-NRG). The decay of $\langle\sigma_z(t)\rangle$ calculated with these two techniques for a preparation of the qubit in the up state $|\uparrow\rangle$ and of the waveguide in the vacuum state is compared in Fig. 1.5a for various values of coupling strengths α. Although the TD-DMRG is accurate to describe the dynamics all the way up to $\alpha = 0.9$, it is limited by numerical costs to the simulation of dynamics on the time scale of $t = 50\omega_c^{-1}$, where ω_c is the cutoff frequency of the spectrum of modes. TD-NRG on the other hand, can achieve longer time-scales by using a logarithmic discretization of the spectrum, as shown by the decay of $\langle\sigma_z(t)\rangle$ on Fig. 1.5b in log-log scale. However, within the TD-NRG, $\langle\sigma_z(t)\rangle$ does not decay to zero, as should be the case, and instead relaxes to a finite value $\langle\sigma_z(\infty)\rangle$ given by the horizontal dotted lines. TD-NRG is therefore not adequate either to predict long-time dynamics in the ultra-strong coupling regime, and in addition cannot be used as a full microscopic technique due to the logarithmic discretization of the modes. Apart from these methods, a stochastic approach

based on path-integrals also exists [30], which manages to describe spin dynamics to a good level of accuracy up to a coupling strength of $\alpha = 0.5$. For $\alpha > 0.5$, this method however breaks down, which highlights once again the highly non-trivial physics of the USC regime. Finally, many-body wave-functions inspired by quantum chemistry methods [31] have been developed, and these will be reviewed in more detail in chapter 3.

These approaches however either discard the dynamics of the modes of the bath from beginning to lighten the computational cost, or have not been used to attempt to investigate the physics taking place in the environment of the qubit. An example of an interesting phenomenon happening in the bath was demonstrated by Goldstein *et al.* [29]: by considering a double-island qubit coupled to a Josephson waveguide (Fig. 1.6a) they showed that a photon impinging on the qubit can be "split" into several lower energy photons. This process, that generalizes to the many-body case the spontaneous parametric down-conversion of non-linear optics, is predicted to lead to a low-energy continuum of down-converted photons, peaked at the qubit frequency, as shown by the frequency-resolved inelastic conversion spectrum in Fig. 1.6c. Based on perturbation theory, these results are however limited to $\alpha \ll 1$, except at the Toulouse point $\alpha = 0.5$ at which equations drastically simplify and allow to treat the problem exactly. In fact, a significant result obtained at this single value of $\alpha = 0.5$ is the total inelastic scattering probabilities $\gamma(\omega)$ of a single incoming photon (Fig. 1.6b). Finally, other recent work [32] used the variational matrix product states (VMPS) technique to study the bath dynamics and visualize the time-evolution of the complete spectrum.

Much of the physics of the spin-boson model in the ultra-strong coupling regime remains to be explored and it is the purpose of this thesis to address some longstanding questions on this topic. In chapter 3, we will characterize the form of the radiation spontaneously emitted into a waveguide by an ultra-strongly coupled qubit prepared in the excited state. In low-coupling standard quantum optics, it is well known that the emitted radiation takes the form of a photon, but at ultra-strong coupling, where non-linear effects are significantly enhanced, we will show that radiation is expected to take a much more complex form. In chapter 4, we will study the multi-particle scattering of a coherent state on a qubit, a very common experimental protocol, that we investigate theoretically for the first time in the ultra-strong coupling regime. We will analyze in particular the frequency conversion that occurs, and the peculiar correlations resulting from the production of particles. Finally, the last chapter of this thesis will describe an experimental attempt to measure anti-bunching in the signal reflected by a qubit strongly coupled to a waveguide. Although the anti-bunching resulting from the emission of a weakly-coupled qubit has been measured several times, a measurement of the anti-bunching generated by a strongly-coupled qubit has not been performed yet with high precision.

Chapter 2

Light-Matter Interaction in Circuit Quantum Electrodynamics

2.1 Phonons, photons and plasmons

In this section we review the mathematical formulation of quantized electromagnetic modes in a cavity, and the analogous quantization in quantum circuits. Since a field mode is ultimately a harmonic oscillator, we will first derive the formalism based on the paradigmatic mechanical harmonic resonator [18], and then extend it to the quantization of field modes in a cavity [33, 34], and to the quantization of an LC resonator in a superconducting circuit [35].

2.1.1 The quantum mechanical oscillator

A mechanical harmonic oscillator (MHO) consists of a mass m moving in one dimension in the quadratic potential $V(x) = m\omega^2 x^2/2$ (Fig. 2.1a). Classically, the force associated to this potential will define the trajectory $(x_{\text{classical}}(t), p_{\text{classical}}(t))$ of the particle, which describes in phase space a circle centered at the origin, rotating at an angular velocity of ω. In quantum mechanics, position and momentum are ascribed to the operators $\hat{X}$ and $\hat{P}$, while the eigenstates of the Hamiltonian indicate the discrete set of possible states of the system. For the mechanical harmonic oscillator, the Hamiltonian is given by

$$\hat{H}_{\text{MHO}} = \frac{m\omega^2 \hat{X}^2}{2} + \frac{\hat{P}^2}{2m}. \tag{2.1}$$

In order to keep the formalism generic, applicable to harmonic systems of a different nature, we will work with the dimensionless operators given by:

$$\hat{X}_0 = \frac{\hat{X}}{2x_0} \quad \text{and} \quad \hat{P}_0 = \frac{\hat{P}}{2p_0}, \tag{2.2}$$

where

$$x_0 = \sqrt{\frac{\hbar}{2m\omega}} \quad \text{and} \quad p_0 = \sqrt{\frac{m\omega\hbar}{2}} \tag{2.3}$$

are the natural units of position and momentum. Substituting these in Eq. (2.1) we obtain:

$$\hat{H}_{\text{MHO}} = \hbar\omega\big[\hat{P}_0^2 + \hat{X}_0^2\big]. \tag{2.4}$$

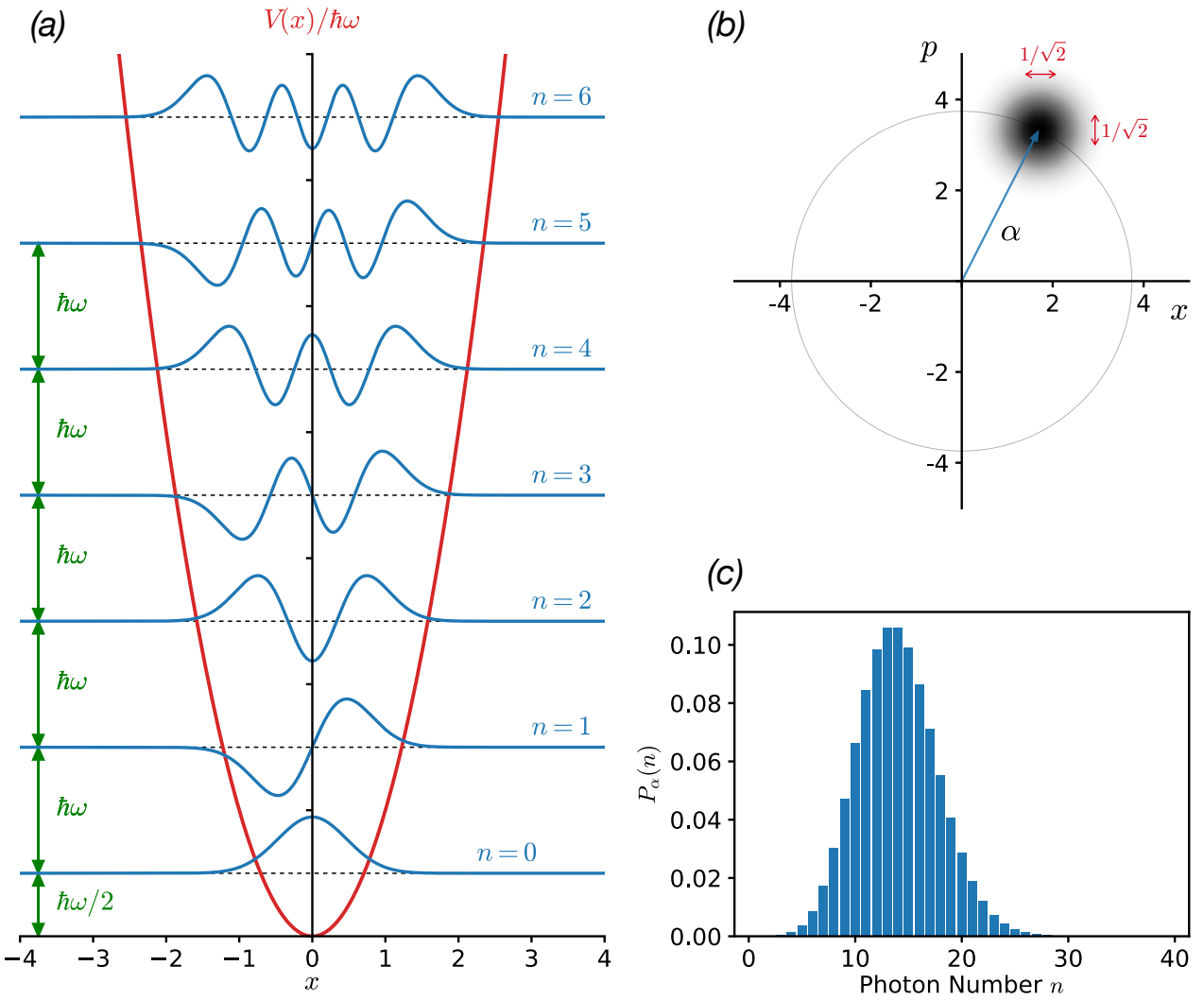

Figure 2.1: Quantum states of the harmonic oscillator. **(a)** The eigenstates, known as "Fock states" or "number states", expressed in the position basis: $\langle x|n\rangle$. **(b)** Illustration of the probability distribution in phase space of a coherent state displaced by $\alpha = \sqrt{14}e^{i0.35\pi}$. The x and p coordinates are smeared out just enough so as to satisfy the minimum Heisenberg uncertainty relations $(\Delta x)^2(\Delta p)^2 = 1/4$. **(c)** Fock state probability distribution $P_\alpha(n)$ corresponding to the coherent state with mean number of photons $\bar{n} = |\alpha|^2 = 14$ in (b).

Following the usual route [36, 18], we define the non-Hermitian bosonic operators

$$\hat{a} = \hat{X}_0 + i\hat{P}_0 \quad \text{and} \quad \hat{a}^\dagger = \hat{X}_0 - i\hat{P}_0, \tag{2.5}$$

that verify the following commutation relations:

$$\left[\hat{a}, \hat{a}^\dagger\right] = \mathbb{1} \quad \text{and} \quad \left[\hat{a}, \hat{a}\right] = 0. \tag{2.6}$$

Re-expressing $\hat{X}_0$ and $\hat{P}_0$ in term of these operators as

$$\hat{X}_0 = \frac{\hat{a} + \hat{a}^\dagger}{2} \quad \text{and} \quad \hat{P}_0 = -i\frac{\hat{a} - \hat{a}^\dagger}{2}, \tag{2.7}$$

we can cast Hamiltonian (2.4) into its canonical form:

$$\hat{H}_{\text{MHO}} = \hbar\omega\left[\hat{a}^\dagger\hat{a} + 1/2\right]. \tag{2.8}$$

The energy origin can then be redefined to remove the vacuum fluctuation term in H_{MHO}:

$$\hat{H}'_{\text{MHO}} = \hbar\omega \hat{a}^\dagger \hat{a}. \tag{2.9}$$

The eigenstates of this Hamiltonian and their properties derive from a simple manipulation of the commutation relations (2.6) [36]. Here we will only state the result: the eigenstates are the Fock states $|n\rangle$ and verify:

$$|n\rangle = \frac{(\hat{a}^\dagger)^n}{\sqrt{n!}} |0\rangle \qquad \hat{H}\,|n\rangle = \hbar\omega(n + 1/2)\,|n\rangle\,, \tag{2.10}$$

where the action of a and $a^\dagger$ on a state $|n\rangle$ is defined by:

$$\hat{a}\,|n\rangle = \sqrt{n}\,|n-1\rangle \quad \text{and} \quad \hat{a}^\dagger\,|n\rangle = \sqrt{n+1}\,|n+1\rangle\,. \tag{2.11}$$

It follows that a and $a^\dagger$ have the effect of annihilating and creating quanta of energy equal to $\hbar\omega$, loosely identified as particles. In the specific case of the mechanical oscillator, these bosonic particles are know as phonons.

What about the spatial structure of these stationary states of the oscillator? For that we need to solve for $\langle x|n\rangle$, that is the eigenfunctions in position space. Note that we chose to work here with the dimensionless eigenvalues x and p, corresponding to the dimensionless operators $\hat{X}_0$ and $\hat{P}_0$ we have already defined. For the ground state $|0\rangle$, we can write [36]:

$$\langle x|\hat{a}|0\rangle = \langle x|\hat{X}_0 + i\hat{P}_0|0\rangle = 0. \tag{2.12}$$

Recalling that $\hat{P}_0 = -i\frac{d}{dx}$, we obtain a differential equation for $\langle x|0\rangle$:

$$\left(\hat{X}_0 + \frac{d}{dx}\right)\langle x|0\rangle = 0, \tag{2.13}$$

which yields the solution:

$$\langle x|0\rangle = (2/\pi)^{1/4} e^{-x^2}. \tag{2.14}$$

The rest of the eigenfunctions can be obtained by evaluating:

$$\langle x|n\rangle = \frac{1}{\sqrt{n!}}\langle x|(a^\dagger)^n|0\rangle = \frac{1}{\sqrt{n!}}\langle x|(\hat{X}_0 - i\hat{P}_0)^n|0\rangle = \frac{1}{\sqrt{n!}}\left(x - \frac{d}{dx}\right)^n \langle x|0\rangle\,. \tag{2.15}$$

More concisely, we can write the particle probability amplitude for the n-th state in the following way:

$$\langle x|n\rangle = (2/\pi)^{1/4}\frac{1}{\sqrt{2^n n!}} e^{-x^2} H_n(x\sqrt{2}), \tag{2.16}$$

where $H_n(u)$ are the Hermite polynomials given by:

$$H_n(u) = (-1)^n e^{u^2}\frac{d^n}{du^n} e^{-u^2}. \tag{2.17}$$

The first seven phonon states in position space are given in Fig. 2.1a.

2.1.2 States of minimum uncertainty product

As shown from the spatial probability distribution in Fig. 2.1a, the eigenstates $|n\rangle$ (for $n \neq 0$) of the harmonic oscillator describe a particle located nowhere in particular, and therefore very different from what one expects of the classical state of mechanical oscillator with well defined spatial coordinates. One could then wonder in what quantum state should the harmonic oscillator be in order to behave as nearly like a classical oscillator as possible? Clearly, a state of the particle with a well-defined position x and momentum p cannot be quantum, as it would violate the Heisenberg uncertainty relations. On the other hand, if we were to give the classical values x and p just enough quantum uncertainty so that the Heisenberg relations are verified, for example by smearing out the coordinates of the particle, as illustrated by the gray region of uncertainty in Fig. 2.1b, then that would make the quantum state of the oscillator as close to the state of a classical oscillator as it can possibly be.

These states, and more specifically those with equal minimal spread of their position and momentum, were first discovered in 1926 by Schrödinger, who referred to them as states of minimum uncertainty product [37, 38]. It is not until the 1960s however, that the importance of these states was recognized for the treatment of optical coherence, and that Glauber coined the term "coherent state" [39, 40]. Denoted $|\alpha\rangle$, coherent states are defined as the vacuum state $|0\rangle$ displaced by a complex number α in phase space [18, 38]:

$$|\alpha\rangle = D(\alpha)\,|0\rangle = e^{\alpha\hat{a}^\dagger - \alpha^*\hat{a}}\,|0\rangle\,, \tag{2.18}$$

where we have introduced $D(\alpha)$, the displacement operator. As an example, the oscillator state in Fig. 2.1b is a coherent state displaced by $\alpha = \sqrt{14}e^{i0.35\pi}$, and with mean number of photons $\langle\alpha|\hat{a}^\dagger\hat{a}|\alpha\rangle = 14$. A defining characteristic of coherent states is that they are the eigenstates of the annihilation operator $\hat{a}$:

$$\hat{a}\,|\alpha\rangle = \alpha\,|\alpha\rangle\,. \tag{2.19}$$

It can now be verified that for this category of states the canonical variables x and p indeed satisfy the *minimum* uncertainty product [38]:

$$\Delta x \Delta p = 1/2, \tag{2.20}$$

making coherent states as well-defined as quantum mechanics allows, and thus as close to classical states as quantum states can be. Note that coherent states are only a subclass of the oscillator states satisfying relation (2.20), with squeezed states being another notable example of states that satisfy this property.

A key point is that the set of all coherent states is a basis that can be used to represent any state of the harmonic oscillator, and which is uniquely defined in terms of the Fock state basis in the following way:

$$|\alpha\rangle = e^{-|\alpha|^2/2}\sum_n \frac{\alpha^n}{\sqrt{n!}}\,|n\rangle\,. \tag{2.21}$$

To illustrate this correspondence, the Fock state probability distribution associated to the coherent state in Fig. 2.1b is shown in Fig. 2.1c. Using this decomposition, and the harmonic oscillator Hamiltonian (2.9), one can then easily deduce the motion of a coherent state by

considering its time-evolution from an initial time $t_0 = 0$ to a time t:

$$\begin{aligned}
|\alpha(t)\rangle &= e^{-\frac{i}{\hbar}\hat{H}t} |\alpha(0)\rangle \\
&= e^{-i\omega\hat{a}^\dagger\hat{a}t} e^{-|\alpha(0)|^2/2} \sum_n \frac{\alpha(0)^n}{\sqrt{n!}} |n\rangle \\
&= e^{-|\alpha(0)|^2/2} \sum_n \frac{\alpha(0)^n}{\sqrt{n!}} e^{-in\omega t} |n\rangle \\
&= e^{-|\alpha(0)|^2/2} \sum_n \frac{(\alpha(0)e^{-i\omega t})^n}{\sqrt{n!}} |n\rangle \\
&= |\alpha(0)e^{-i\omega t}\rangle
\end{aligned} \tag{2.22}$$

The motion in phase space of a coherent state is therefore the same as that of classical amplitude: it describes a circle around the origin at an angular velocity ω, as represented by the grey circle in Fig. 2.1b.

Let us recall a few important properties of coherent states [38, 18]:

1. The set of all coherent states forms an over-complete basis of the Hilbert space of the oscillator, with the following closure relationship:

$$\mathbb{1} = \frac{1}{\pi} \int |\alpha\rangle \langle\alpha| \, d^2\alpha. \tag{2.23}$$

2. Because of the over-completeness of the basis, there is an infinite number of ways of expressing a coherent state in terms of other coherent states. For instance, the vacuum $|0\rangle$ can be rewritten as:

$$|0\rangle = \frac{1}{\pi} \int e^{-|\alpha|^2/2} |\alpha\rangle \, d^2\alpha. \tag{2.24}$$

3. The scalar product of two coherent states $|\alpha\rangle$ and $|\beta\rangle$ is given by:

$$\langle\alpha|\beta\rangle = e^{-\frac{1}{2}|\alpha|^2 - \frac{1}{2}|\beta|^2 + \alpha^*\beta}. \tag{2.25}$$

Moreover, the squared norm of the scalar product quantifies the overlap in phase space between two coherent state:

$$|\langle\alpha|\beta\rangle|^2 = e^{-|\alpha-\beta|^2}. \tag{2.26}$$

4. An major property of coherent states is that they can be used to represent any density matrix $\hat{\rho}$ describing the state of a harmonic oscillator entirely in terms of coherent state projectors $|\alpha\rangle\langle\alpha|$. This representation is known as the Glauber-Sudarshan P-representation [41, 42], and is expressed as:

$$\hat{\rho} = \int \phi(\alpha) |\alpha\rangle \langle\alpha| \, d^2\alpha, \tag{2.27}$$

where $\phi(\alpha)$ is a real function of α. This representation suggests that any state of the oscillator can be seen as a mixture of coherent states with weights $\phi(\alpha)$. One remarkable consequence of this decomposition is the optical equivalence theorem for normally ordered operators [42, 43, 38] that will be relevant to chapter 5.

2.1.3 Quantized field modes

A field mode in a cavity is precisely a one-dimensional harmonic oscillator [44], which can be described by the formalism we have just recalled for the mechanical harmonic oscillator. Instead of describing spatial displacements however, $\hat{X}_0$ and $\hat{P}_0$ in the Hamiltonian in Eq. (2.4) now describe *field* displacements. It follows, moreover, that $\hat{a}$ and $\hat{a}^\dagger$ become the *photon* creation and annihilation operators, with $\hat{N} = \hat{a}^\dagger\hat{a}$ the total number of photons exciting the field mode.

In the Schrödinger picture, the electric field in the cavity is given by

$$\hat{\mathbf{E}}(\mathbf{r}) = \mathcal{E}_0\big[\boldsymbol{\epsilon} f(\mathbf{r})\hat{a} + \boldsymbol{\epsilon}^* f^*(\mathbf{r})\hat{a}^\dagger\big], \tag{2.28}$$

where the dimensionless scalar $f(r)$, with upper bound 1, describes the spatial structure of the amplitude of the field while the vector $\boldsymbol{\epsilon}$ describes polarization. Note that we have indicated 3D vectors in bold, and that we have chosen the convention in which the electric field is associated with the $\hat{X}_0 = (\hat{a} + \hat{a}^\dagger)/2$ operator. For a Fock state, the expectation value of the electric field is zero,

$$\langle n|\hat{\mathbf{E}}(\mathbf{r})|n\rangle = 0, \tag{2.29}$$

whereas for a coherent state, it takes a finite value:

$$\langle \alpha|\hat{\mathbf{E}}(\mathbf{r})|\alpha\rangle = \mathcal{E}_0\big[\boldsymbol{\epsilon} f(\mathbf{r})\alpha + \boldsymbol{\epsilon}^* f^*(\mathbf{r})\alpha^*\big]. \tag{2.30}$$

It turns out that this expectation value coincides precisely with the value of a classical electric field with amplitude α in units of $\mathcal{E}_0$ [18]. For completeness, we also recall the corresponding expression for the vector potential:

$$\hat{\mathbf{A}}(\mathbf{r}) = -i\frac{\mathcal{E}_0}{\omega_c}\big[\boldsymbol{\epsilon} f(\mathbf{r})\hat{a} - \boldsymbol{\epsilon}^* f^*(\mathbf{r})\hat{a}^\dagger\big]. \tag{2.31}$$

The field normalization factor $\mathcal{E}_0$, can be derived by equating the integral over space of the energy of an n-photon state $\langle n|\int \epsilon_0|\hat{\mathbf{E}}_\mathbf{c}|^2 d^3\mathbf{r}|n\rangle$ to the energy of a harmonic oscillator with n quanta $\hbar\omega_c\big[\hat{a}^\dagger\hat{a} + 1/2\big]$ given in Eq. (2.8). The result is:

$$\mathcal{E}_0 = \sqrt{\frac{\hbar\omega_c}{2\epsilon_0\mathcal{V}}}, \tag{2.32}$$

with $\mathcal{V} = \int |f(r)|^2 d^3\mathbf{r}$ the effective mode volume.

2.1.4 Quantized circuits: the LC oscillator

In this thesis, we will be interested in studying the interaction between fields and matter in the context of electronic circuits. In this framework, the canonical harmonic oscillator is the LC oscillator (Fig. 2.2a), which is described by the following Hamiltonian:

$$\hat{H}_{LC} = \frac{\hat{Q}^2}{2C} + \frac{\hat{\Phi}^2}{2L}. \tag{2.33}$$

The operator $\hat{Q}$ for the charge on the capacitor C, and the generalized flux $\hat{\Phi}$, defined as the integral of the voltage across the inductor $\Phi = \int_{-\infty}^{t} \hat{V}(t)\, dt$, satisfy the commutation relation

$$\big[\hat{\Phi}, \hat{Q}\big] = i\hbar. \tag{2.34}$$

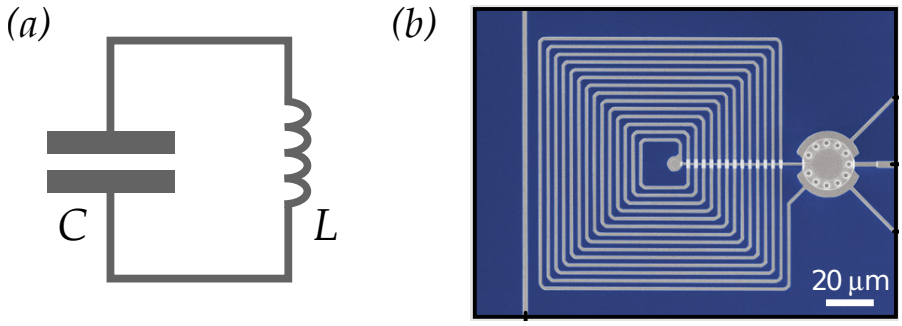

Figure 2.2: **(a)** Schematic of an LC oscillator. **(b)** Example of the implementation of a harmonic oscillator in circuit QED [45]: the inductor is the spiral-shaped conductor in the centre, while the capacitor is made of two superposed plates on the right (disc-shaped object). In this particular experiment, the plates of the capacitor are themselves free to oscillate, resulting in a coupling between the LC circuit and the mechanical motion of the capacitor.

Here again, the system can be described using the formalism of the harmonic oscillator given in paragraphs 2.1.1 and 2.1.2, by ascribing dimensionless charge and the dimensionless flux to the $\hat{X}_0$ and $\hat{P}_0$ operators:

$$\begin{aligned}\hat{Q} &= \sqrt{2\hbar}\left(\frac{C}{L}\right)^{1/4}\frac{\hat{a}+\hat{a}^\dagger}{2} = \sqrt{2\hbar}\left(\frac{C}{L}\right)^{1/4}\hat{X}_0 \\ \hat{\Phi} &= i\sqrt{2\hbar}\left(\frac{L}{C}\right)^{1/4}\frac{\hat{a}-\hat{a}^\dagger}{2} = -\sqrt{2\hbar}\left(\frac{L}{C}\right)^{1/4}\hat{P}_0\end{aligned} \tag{2.35}$$

For details on circuit quantization, the reader is referred to introductory notes by Vool and Devoret [35]. Note that we adopted the unusual (but legitimate) convention of ascribing the charge variable (and not the flux variable) to the sum of creation and annihilation operators. Since the qubits we will consider in the following are capacitively coupled to their environment through the charge degree of freedom, this choice will result in the standard form of the spin-boson Hamiltonian in section 2.4.

Substituting Eq. (2.35) in Hamiltonian (2.33), we find once again the diagonal form of the harmonic oscillator:

$$\hat{H}_{\mathrm{LC}} = \hbar\omega_{LC}\left[\hat{a}^\dagger\hat{a} + 1/2\right], \tag{2.36}$$

where this time $\omega_{\mathrm{LC}} = 1/\sqrt{LC}$ is the angular frequency of the collective charge oscillation in the circuit. The quanta with energy $\hbar\omega_{\mathrm{LC}}$ in this framework are sometimes referred to as "plasmons". A standard implementation of the inductance of an LC oscillator is by fabricating meanders or spiral-shaped inductors, an example of which is shown on Fig. 2.2b.

2.2 Superconducting qubits

In this section, after introducing the Josephson junction, that is the key element of superconducting qubits, we will present the single Cooper-pair box (SCPB) and the transmon qubit, two types of superconducting charge qubits central to the work in this thesis. For detailed treatment of Josephson junctions the reader is referred to the textbook by M. Tinkham [46], and for superconducting qubits to these Refs. [47, 35].

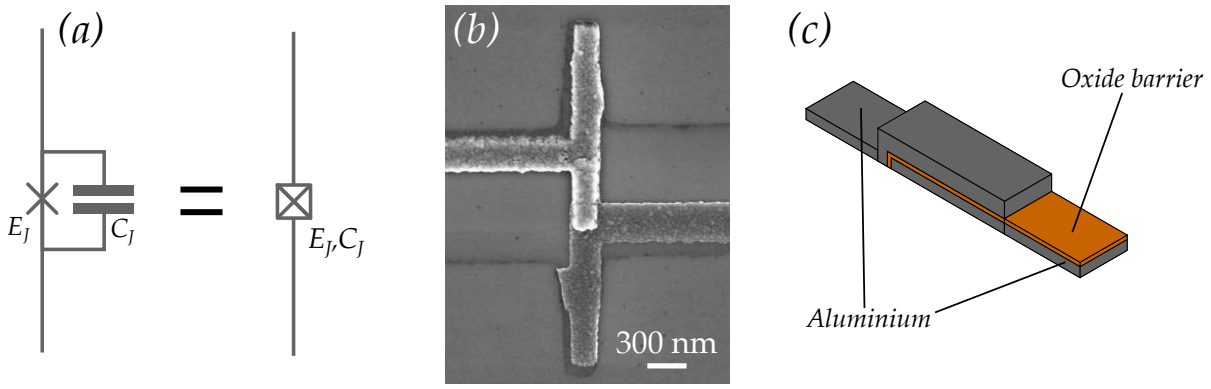

Figure 2.3: **(a)** Symbol of the Josephson element. **(b)** SEM image of a Josephson junction after e-beam lithography and aluminum deposition. **(c)** Schematic of the three layers of a Josephson junction: the two aluminum electrodes and the insulating oxide layer in-between.

2.2.1 The Josephson junction: constitutive relations

A Josephson junction consists of a pure superconducting tunnel junction in parallel with a capacitor (Fig. 2.3a). In practice, these junctions are fabricated in three steps. After depositing a first layer of aluminum, the metal is left to oxidize for some time in order to generate an insulating layer of oxidized aluminum. Another layer of metal is then deposited on top, which forms the second electrode. The symbol for a Josephson junction is given in Fig. 2.3a, and a scanning electron microscope (SEM) image of an actual junction is shown in Fig. 2.3b.

We start with the observation that the charge Q_J having passed the junction is an integer number N times the charge $-2e$ of a Cooper-pair:

$$Q_J(t) = -2eN(t). \tag{2.37}$$

Quantum-mechanically, we have to describe the number of Cooper-pairs by the operator $\hat{N}$ given by

$$\hat{N} = \sum_N N \left|N\right\rangle \left\langle N\right|. \tag{2.38}$$

It was shown that the states $|N\rangle$ are coupled together by the tunneling of Cooper-pairs through the junction [48], which leads to the following Hamiltonian:

$$\hat{H}_J = -\frac{E_J}{2} \sum_{N=-\infty}^{\infty} \left[\left|N\right\rangle \left\langle N+1\right| + \left|N+1\right\rangle \left\langle N\right| \right], \tag{2.39}$$

where the Josephson energy E_J is a macroscopic parameter depending on the conductance in the normal state G_N and on the superconducting gap Δ, that is given by [49]:

$$E_J = \frac{hG_N\Delta}{8e^2}. \tag{2.40}$$

Next, let us define a new basis:

$$\left|\varphi\right\rangle = \sum_{N=-\infty}^{\infty} e^{iN\varphi} \left|N\right\rangle. \tag{2.41}$$

It can easily be checked that the transformation back to the Cooper-pair number basis is given by:

$$|N\rangle = \frac{1}{2\pi}\int_0^{2\pi} d\varphi\ e^{-iN\varphi}\,|\varphi\rangle\,. \tag{2.42}$$

Substituting Eq. (2.42) into Eq. (2.39), we obtain an expression for the Josephson Hamiltonian in the $|\varphi\rangle$ basis:

$$\hat{H}_J = \frac{-E_J}{2\pi}\int_0^{2\pi} d\varphi\ \frac{e^{i\varphi}+e^{-i\varphi}}{2}\,|\varphi\rangle\langle\varphi|\,. \tag{2.43}$$

By defining the operator

$$e^{i\hat{\varphi}} = \frac{1}{2\pi}\int_0^{2\pi} d\varphi e^{i\varphi}\,|\varphi\rangle\langle\varphi|\,, \tag{2.44}$$

we can then rewrite the Hamiltonian in its most standard form:

$$\hat{H}_J = -E_J\cos\hat{\varphi}. \tag{2.45}$$

We further recall two important results which follow from the above equations [35]:

1. The super-current operator is:

$$\hat{I} = I_c\sin\hat{\varphi} \tag{2.46}$$

where I_c is the critical current of the junction given by

$$I_c = \frac{2e}{\hbar}E_J = E_J/\varphi_0. \tag{2.47}$$

In the last equality, we have also defined the reduced flux quantum $\varphi_0 = \hbar/(2e)$.

2. One can also derive the time-evolution of the phase in the Heisenberg picture:

$$\frac{d\hat{\varphi}}{dt} = \frac{2e}{\hbar}\hat{V} = \hat{V}/\varphi_0. \tag{2.48}$$

This equation allows us to identify $\hbar\hat{\varphi}/2e$ as the generalized flux operator $\hat{\Phi}_J = \int_{-\infty}^{t}\hat{V}dt$:

$$\hbar\hat{\varphi}/2e = \hat{\Phi}_J. \tag{2.49}$$

Eqs. (2.46) and (2.48) are the key relations of the Josephson element.

2.2.2 Inductance of the Josephson element

An important implication of Eqs. (2.46) and (2.48) is that the Josephson junction behaves as a non-linear inductance. More specifically, using these equations and the definition of inductance

$$V = L\frac{dI}{dt}, \tag{2.50}$$

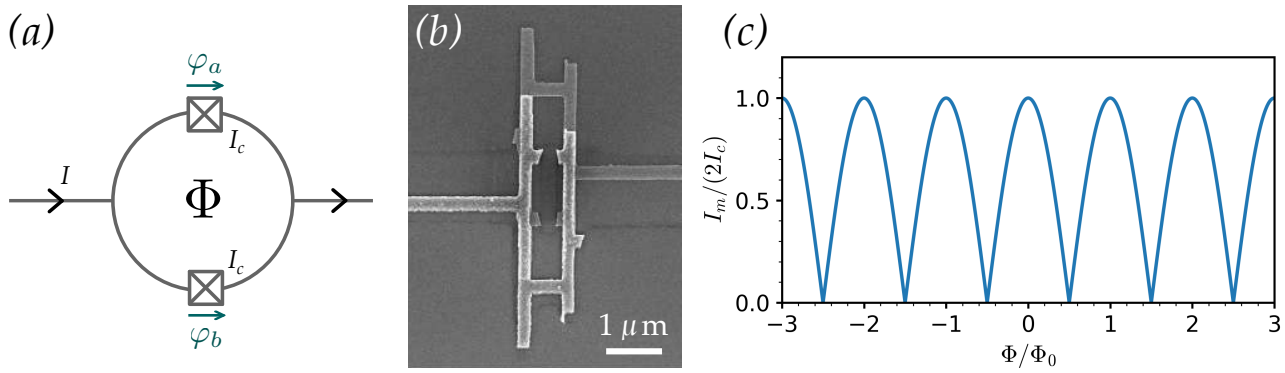

Figure 2.4: The SQUID: Superconducting Quantum Interference Device. **(a)** Circuit diagram of a SQUID made of two identical junctions with critical current I_c, threaded by a magnetic flux Φ. **(b)** SEM image of a SQUID. **(c)** Maximum current I_m which can flow in the SQUID. At integer values of the flux Φ/Φ_0, the SQUID behaves as a single junction with critical current $2I_c$.

we can straightforwardly derive the non-linear inductance

$$L(\varphi) = \frac{\varphi_0}{I_c \cos\varphi}, \tag{2.51}$$

which can be rewritten using Eq. (2.46) to obtain an expression in terms of the current:

$$L(I) = \frac{\varphi_0}{I_c\sqrt{1-\left(\frac{I}{I_c}\right)^2}}. \tag{2.52}$$

For $I \ll I_c$, we see that the $L(I)$ becomes constant:

$$L(I) \simeq \varphi_0/I_c = \varphi_0^2/E_J. \tag{2.53}$$

This implies that for large enough I_c compared to I, the Josephson junction becomes a linear oscillator with resonance frequency $1/\sqrt{LC}$. The main advantage of this LC circuit design, as compared for example to the superconducting spiral inductor design shown in Fig. 2.2b, is that it can provide a much higher inductance on a much smaller footprint. This property is useful when the aim is to engineer very high impedance transmission lines using a large number of junctions, such as in the experiment mentioned previously by Puertas-Martinez *et al.* [16], in which Josephson junction chain includes more than 4000 Josephson junctions.

2.2.3 The SQUID

An important device for superconducting qubits is the SQUID, or Superconducting QUantum Interference Device, which can be used to allow the flux-tuning of the qubit frequency. The device consists of two Josephson junctions in parallel enclosing a threading magnetic flux, as shown in Fig. 2.4a-b. The total current I flowing through the device is the sum of that flowing through the two individual junctions. Therefore, in the case of two identical junctions with phase differences φ_a and φ_b:

$$I = I_c \sin\varphi_a + I_c \sin\varphi_b, \tag{2.54}$$

which can be re-written as:

$$I = 2I_c \cos\left(\frac{\varphi_a - \varphi_b}{2}\right) \sin\left(\frac{\varphi_a + \varphi_b}{2}\right). \tag{2.55}$$

Quantization of flux within the ring [46] requires that

$$\varphi_b - \varphi_a = 2\pi \frac{\Phi}{\Phi_0} (\text{mod } 2\pi). \tag{2.56}$$

It then follows from Eqs. (2.55) and (2.56) that the SQUID behaves as a single junction with phase difference $(\varphi_a + \varphi_b)/2$ across the barrier, and with critical current given by

$$I_m = 2I_c \left| \cos\left(\pi \frac{\Phi}{\Phi_0} \right) \right|. \tag{2.57}$$

This critical current versus the threading flux is plotted on Fig. 2.4c. This shows that one can tune the critical current I_m (2.57) (by varying the flux Φ), and hence the induction of the SQUID.

Note that the description of the two types of superconducting qubit in the next paragraph include a single Josephson junction for simplicity, but an actual superconducting qubit would generally involve a SQUID, in order to make the frequency flux-tunable.

2.2.4 The single Cooper-pair box and the transmon qubit

Let us now introduce the single Cooper-pair box, the first superconducting two-level system on which quantum coherent oscillations were observed [2]. As shown on the circuit diagram in Fig. 2.5a, it consists of a superconducting island (in orange) connected via a Josephson junction to a superconducting reservoir. The idea is simple: one engineers a system with a very high charging energy

$$E_C = \frac{(2e)^2}{2(C_J + C_g)}, \tag{2.58}$$

so as to suppress the charge fluctuations on the island. One then tunes the gate voltage V_g to a voltage equivalent to a half-integer number of Cooper-pairs $N_g = C_g V_g / 2e$, thus forcing an integer number $N_g + \frac{1}{2}$ or $N_g - \frac{1}{2}$ of Cooper-pairs on the island. These two charge states, coupled together through the Josephson Hamiltonian (2.45), span the Hilbert space of the qubit.

Mathematically the Hamiltonian of the SCPB is given by:

$$\hat{H}_{\text{SCPB}} = E_C (\hat{N}_0 - N_g)^2 - E_J \cos(\hat{\varphi}). \tag{2.59}$$

Using Eqs. (2.38) and (2.39), and taking into account that the high charging energy $E_C \gg E_J$ constrains the system to the $\{|N_g + \frac{1}{2}\rangle, |N_g - \frac{1}{2}\rangle\}$ subspace, the Hamiltonian (2.59) to:

$$\begin{aligned} \hat{H}_{\text{SCPB}} &= \frac{E_C}{4} \left(|N_g - \tfrac{1}{2}\rangle \langle N_g - \tfrac{1}{2}| + |N_g + \tfrac{1}{2}\rangle \langle N_g + \tfrac{1}{2}| \right) \\ &\quad - \frac{E_J}{2} \left(|N_g + \tfrac{1}{2}\rangle \langle N_g - \tfrac{1}{2}| + |N_g - \tfrac{1}{2}\rangle \langle N_g + \tfrac{1}{2}| \right) \\ &= \frac{E_C}{4} \mathbb{1} - \frac{E_J}{2} \hat{\sigma}_x. \end{aligned} \tag{2.60}$$

Dropping the constant energy term, the single Cooper-pair box Hamiltonian takes the simple form:

$$\hat{H}_{\text{SCPB}} = -\frac{E_J}{2} \hat{\sigma}_x, \tag{2.61}$$

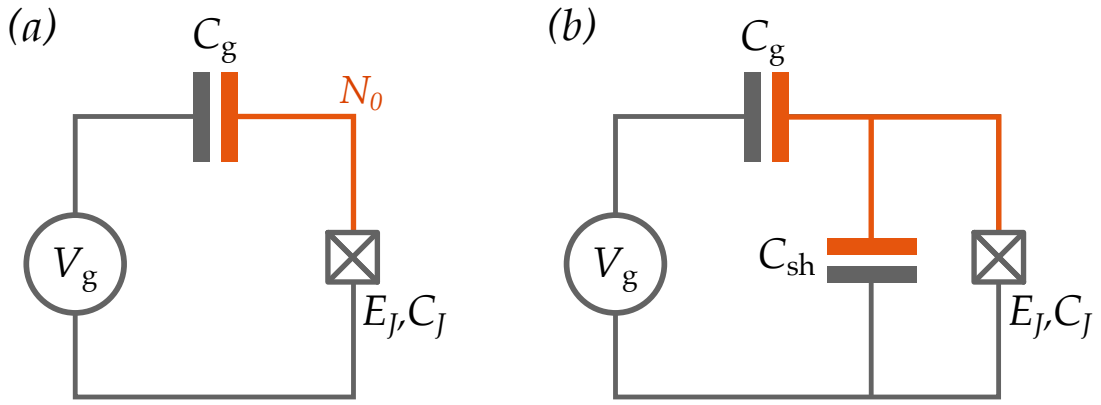

Figure 2.5: Circuit diagram of two types of superconducting qubit: **(a)** The Cooper-pair box: the bias V_g is used to tune the electric potential on the superconducting island (in orange) so that the two lowest energy charge states, $|C_g V_g/2e - \frac{1}{2}\rangle$ and $|C_g V_g/2e + \frac{1}{2}\rangle$, are degenerate. The Josephson junction hybridizes these two levels by coupling them together. **(b)** The transmon: with its additional shunting capacitance, it is much less non-linear than the Cooper-pair box, which makes it is also less sensitive to charge noise.

with its ground and excited eigenstates given by:

$$|g\rangle = \frac{1}{\sqrt{2}}\begin{pmatrix} 1 \\ 1 \end{pmatrix} \quad \text{and} \quad |e\rangle = \frac{1}{\sqrt{2}}\begin{pmatrix} 1 \\ -1 \end{pmatrix}. \tag{2.62}$$

Note also, that in this 2-state subspace, the pair number operator can be written in terms of the $\hat{\sigma}_z$ operator (this will be useful in the next section):

$$\begin{aligned} \hat{N}_0 &= (N_g - \tfrac{1}{2})\,|N_g - \tfrac{1}{2}\rangle\langle N_g - \tfrac{1}{2}| + (N_g + \tfrac{1}{2})\,|N_g + \tfrac{1}{2}\rangle\langle N_g + \tfrac{1}{2}| \\ &= N_g \mathbb{1} - \frac{1}{2}\hat{\sigma}_z \end{aligned} \tag{2.63}$$

The main drawback of the Cooper-pair box its high susceptibility to charge noise, and especially to quasi-particle poisoning [50, 51], which drastically limits the coherence time. For instance, a single quasi-particle relaxation on the capacitor plate C_g is enough to change the charge parity on the island, and thus destroy the quantum information stored in the qubit. To counter this effect, the idea was to create a modified version of SCPB, known as the transmon qubit [52, 53]. In this design, an additional shunting capacitance C_{sh} is added to the SCPB, as shown in Fig. 2.5b, which reduces the charging energy E_C of the qubit to $E_C \sim E_J/100$. With smaller E_C, a larger range of Cooper-pair occupation states $|N\rangle$ become energetically favorable, which makes the charge associated to a specific eigenstate less well-defined. In other words, the eigenstates become superpositions of a larger range of $|N\rangle$ states, and the consequence of this indeterminacy in the number of pairs, is that the qubit becomes less sensitive to charge noise, as it was demonstrated [53]. A disadvantage of having reduced the charging energy however is that now the qubit is a multi-level system, which can become an issue if the energy difference between the ground state and the 1$^{\text{st}}$ excited state (that is the two 'qubit' levels of the transmon) becomes too close to the energy difference between the 1$^{\text{st}}$ excited state and the 2$^{\text{nd}}$ excited state. A full solution of the transmon Hamiltonian is beyond the scope of this discussion, but we will simply mention that it can be solved exactly in terms of Mathieu functions [54] or by numerical diagonalization.

Regarding the theory work of this thesis (chapters 3 and 4), the Cooper-pair box is the only device of interest, since the spin-boson model that was studied assumes a purely two-level

system. The transmon will be relevant to chapter 5, where we present an experiment involving the scattering of coherent states on such a qubit.

2.3 Single-mode interaction: cavity QED

In this section, we begin by recalling the correspondence between an atom interacting with a cavity electromagnetic mode, and the Rabi model [18]. We will then re-derive the Rabi model, but this time starting from a superconducting qubit interacting with an LC resonator. Finally, we will give a basic overview of the physics related to the Rabi model.

2.3.1 The Rabi model in quantum optics

Let us consider a hydrogen-like atom with energy gap Δ between its two lowest eigenstates, and let us assume it is located near the center of an electromagnetic cavity with resonance frequency ω, as illustrated in Fig. 2.6. In quantum optics, the standard convention [18] consists in representing the Hamiltonian of the atom by the $\hat{\sigma}_z$ operator (this convention differs from the one used in most of this manuscript):

$$\hat{H}_{\text{atom}} = \frac{\Delta}{2}\hat{\sigma}_z, \tag{2.64}$$

and the eigenstates therefore by:

$$|0\rangle = \begin{pmatrix} 1 \\ 0 \end{pmatrix} \quad \text{and} \quad |1\rangle = \begin{pmatrix} 0 \\ 1 \end{pmatrix}. \tag{2.65}$$

We then denote by $\hat{\mathbf{R}}$ the position operator of the electron with respect to the nucleus, and by q the charge of that electron. It follows that the atomic dipole moment operator of the atom is given by:

$$\hat{\boldsymbol{\mu}} = q\hat{\mathbf{R}}. \tag{2.66}$$

By multiplying $\hat{\boldsymbol{\mu}}$ on the right and on the left by unity, we obtain the following expression:

$$\begin{aligned} \hat{\boldsymbol{\mu}} &= \big(\,|1\rangle\langle 1| + |0\rangle\langle 0|\,\big)\hat{\boldsymbol{\mu}}\big(\,|1\rangle\langle 1| + |0\rangle\langle 0|\,\big) \\ &= \boldsymbol{\mu_{11}}\,|1\rangle\langle 1| + \boldsymbol{\mu_{00}}\,|0\rangle\langle 0| + \boldsymbol{\mu_{10}}\,|1\rangle\langle 0| + \boldsymbol{\mu_{01}}\,|0\rangle\langle 1|\,, \end{aligned} \tag{2.67}$$

where $\boldsymbol{\mu_{ij}}$ are the matrix elements of $\langle i|\hat{\boldsymbol{\mu}}|j\rangle$. From symmetry considerations, $\boldsymbol{\mu_{00}}$ and $\boldsymbol{\mu_{11}}$ must vanish [38]. Defining the atomic raising and lowering operators $\hat{\sigma}^+ = |1\rangle\langle 0|$ and $\hat{\sigma}^- = |0\rangle\langle 1|$, we then obtain:

$$\hat{\boldsymbol{\mu}} = \boldsymbol{\mu_{10}}\,|1\rangle\langle 0| + \boldsymbol{\mu_{01}}\,|0\rangle\langle 1| = \boldsymbol{\mu_{10}}\hat{\sigma}^+ + \boldsymbol{\mu}^*_{\mathbf{10}}\hat{\sigma}^-. \tag{2.68}$$

Assuming the dipolar approximation ($|\mathbf{R}| \ll$ cavity size) [33], the electron-field interaction can be written in terms of the scalar product of the electric field at the nucleus with the dipole moment [18]:

$$\hat{H}_{\text{int}} = -\hat{\boldsymbol{\mu}} \cdot \hat{\mathbf{E}}(0). \tag{2.69}$$

Substituting Eqs. (2.68) and (2.28) into (2.69), we obtain:

$$\hat{H}_{\text{int}} = -(\boldsymbol{\mu_{10}}\sigma^+ + \boldsymbol{\mu}^*_{\mathbf{10}}\sigma^-) \cdot \mathcal{E}_0\big[\boldsymbol{\epsilon} f(\mathbf{r})\hat{a} + \boldsymbol{\epsilon}^* f^*(\mathbf{r})\hat{a}^\dagger\big]. \tag{2.70}$$

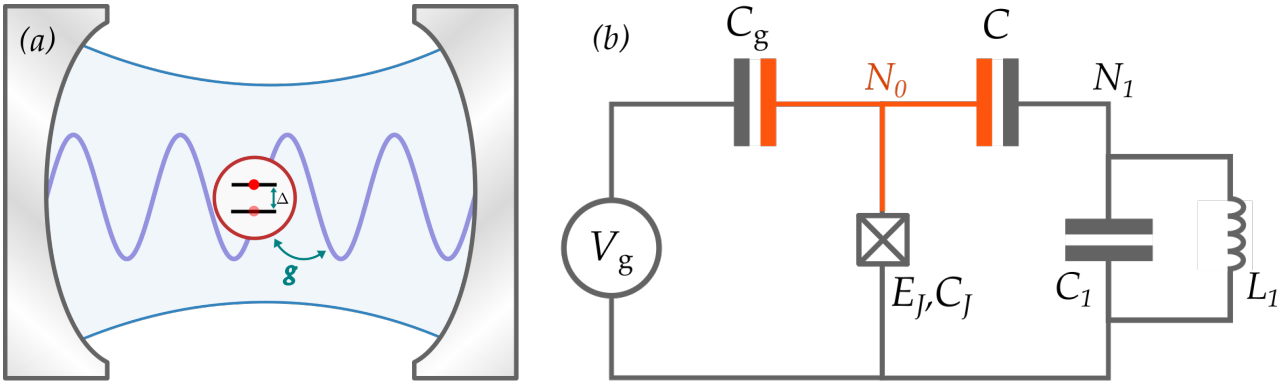

Figure 2.6: Two systems described by the Rabi model: **(a)** Atom in a cavity. The cavity resonance frequency limits the interaction with the electric dipole of the atom to a single mode of the electromagnetic field. **(b)** The two charge states of the Cooper box $|N_g - \frac{1}{2}\rangle$ and $|N_g + \frac{1}{2}\rangle$ couple via capacitance C to the LC resonator with inductance L_1 and capacitance C_1.

Since the spatial variations of the electric field are slow on the scale of the atom, we take the relative field amplitude $f(\boldsymbol{r}) = 1$. Let us now assume for simplicity that $\boldsymbol{\mu_{10}}$ and $\boldsymbol{\epsilon}$ are real, which brings the interaction Hamiltonian (2.70) into the following form:

$$H_{\text{int}} = -\frac{g}{2}(\hat{\sigma}^- + \hat{\sigma}^+)(\hat{a} + \hat{a}^\dagger), \tag{2.71}$$

where we have introduced the coupling constant g:

$$g = 2\mathcal{E}_0 \frac{\boldsymbol{\epsilon} \cdot \boldsymbol{\mu_{10}}}{\hbar}. \tag{2.72}$$

Combining Eqs. (2.72), (2.64) and (2.9), we obtain the Rabi model describing the interaction of an atom with a single mode of the field:

$$H_{\text{Rabi}} = \frac{\Delta}{2}\hat{\sigma}_z - \frac{g}{2}\hat{\sigma}_x(\hat{a}^\dagger + \hat{a}) + \omega \hat{a}^\dagger \hat{a}. \tag{2.73}$$

This model was explored extensively in atomic systems [18].

2.3.2 The Rabi model in circuit QED

More generally, the Rabi model describes any two-level quantum system interacting with a single-mode bosonic system. We will now re-derive the Rabi model, but this time starting from a quantum circuit by considering a superconducting qubit (here a Cooper-pair box) coupled to superconducting resonator (an LC circuit), an approach more relevant to this thesis. The circuit diagram is shown in Fig. 2.6b, from which we can write down the Hamiltonian in terms of capacitive and inductive terms:

$$H = \frac{1}{2}(M^{-1})_{00}(\hat{N}_0 - N_g)^2 + \frac{1}{2}(M^{-1})_{11}\hat{N}_1^2 + (M^{-1})_{01}\hat{N}_1\hat{N}_0 + \frac{\hat{\Phi}_1^2}{2L_1} - E_J \cos\hat{\varphi}, \tag{2.74}$$

where the matrix M is the capacitance matrix given by:

$$M = \frac{1}{(2e)^2}\begin{pmatrix} C_g + C_J + C & -C \\ -C & C_1 + C \end{pmatrix}. \tag{2.75}$$

The standard procedure to derive the Hamiltonian of such a circuit, shown for example in this thesis [55], is first to write down the Lagrangian in terms of the node fluxes $\hat{\Phi}_n$, and then to apply a Legendre transform to obtain an expression of the Hamiltonian in terms of the Cooper-pair numbers $\hat{N}_n$. It turns out however that one can directly write down the capacitance matrix (2.75), by applying the following simple prescription [56]:

$$\begin{cases} \text{For } i = j: & M_{ii} = \frac{1}{(2e)^2} \sum_k C_{ik} \\ \text{For } i \neq j: & M_{ij} = -\frac{1}{(2e)^2} C_{ij} \end{cases} \tag{2.76}$$

where C_{ij} denotes the capacitance between node i and node j. Note that since the bias V_g is constant, it can simply be added as a charge offset to the charge number $\hat{N}_0$, as we did for the Cooper-pair box.

Making the coefficients explicit in Hamiltonian (2.74), we obtain:

$$H = \frac{(2e)^2}{C_g(C + C_1 + C_J) + C(C_1 + C_J)} \left[\frac{1}{2}(\hat{N}_0 - N_g)^2(C_1 + C) + \frac{1}{2}\hat{N}_1^2(C_g + C_J + C) + C\hat{N}_1\hat{N}_0\right] + \frac{\hat{\Phi}_1^2}{2L_1} - E_J \cos\hat{\varphi}. \tag{2.77}$$

The first term in the brakets corresponds to the Cooper-pair box charging energy, which this time also involves the C and C_1 capacitances. Cleary, in order to make the charging energy high on the island and thus to constrain the Cooper-pair box to $|N_g + \frac{1}{2}\rangle$ and $|N_g - \frac{1}{2}\rangle$, it will also be necessary to keep $C \ll 1$. The second term, together with the $\hat{\Phi}_1^2$ term, we recognize as the Hamiltonian of a harmonic oscillator (Eq. 2.36) with effective resonance frequency

$$\omega_{\text{eff}} = \frac{1}{\sqrt{L_1 C_{\text{eff}}}}, \tag{2.78}$$

in which the effective capacitance C_{eff} is a combination of all capacitances of the circuit:

$$C_{\text{eff}} = \frac{C_g(C + C_1 + C_J) + C(C_1 + C_J)}{C_g + C_J + C}. \tag{2.79}$$

The third term in the brakets of Eq. (2.77) is the coupling term. Using Eq. (2.63) (in which we drop the energy offset) to rewrite $\hat{N}_0$, and Eq. (2.35) to rewrite $\hat{N}_1$, we get that:

$$(2e)\hat{N}_0\hat{N}_1 = -\frac{\sqrt{2\hbar}}{4}\left(\frac{C_{\text{eff}}}{L_1}\right)^{1/4} \hat{\sigma}_z(\hat{a}^\dagger + \hat{a}). \tag{2.80}$$

Bringing everything together, and recalling the form of the Josephson Hamiltonian in the subspace of the Cooper-pair box given in Eq. (2.61), we obtain:

$$H = -\frac{E_J}{2}\hat{\sigma}_x - \frac{g}{2}\hat{\sigma}_z(\hat{a}^\dagger + \hat{a}) + \omega_{\text{eff}}\hat{a}^\dagger\hat{a}, \tag{2.81}$$

where we have defined the coupling constant

$$g = \sqrt{\frac{\hbar}{2}}\left(\frac{C_{\text{eff}}}{L_1}\right)^{1/4} \frac{(2e)C}{C_g(C + C_1 + C_J) + C(C_1 + C_J)}. \tag{2.82}$$

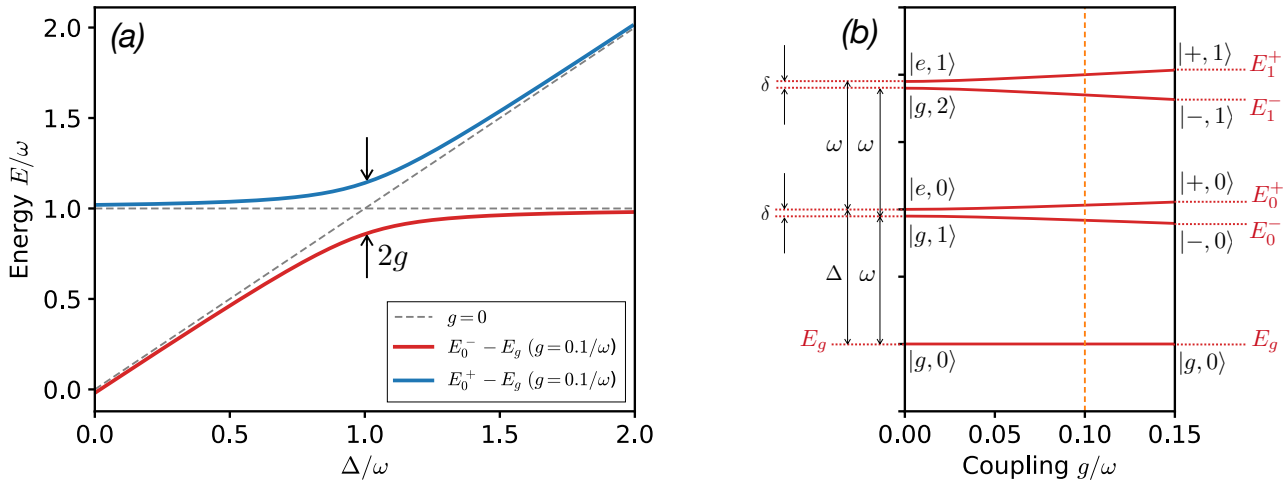

Figure 2.7: Eigenenergies of the Jaynes-Cummings model: **(a)** The hybridization between $|0,+\rangle$ and $|0,-\rangle$ is revealed by the anti-crossing between the eigenvalues $E_0^+ - E_g$ and $E_0^- - E_g$. The energy of the ground state $E_g = -\Delta/2$ was here subtracted for convenience. **(b)** Ladder of hybridized eigenenergies versus coupling. The orange-dashed line indicates the coupling at which the anti-crossing in (a) was plotted.

From this expression, it appears as if the coupling is proportional to the inverse square-root of the characteristic impedance of the effective resonator $Z_{\text{eff}} = \sqrt{L_1/C_{\text{eff}}}$. In practice however, it is only really meaningful to quantify the coupling relatively to the energy of the resonator $\hbar\omega_{\text{eff}}$ (2.78), by taking the ratio of the two energy scales:

$$\frac{g}{\hbar\omega_{\text{eff}}} = \sqrt{\frac{2e^2 Z_{\text{eff}}}{\hbar}} \frac{C}{C_g + C_J + C}. \tag{2.83}$$

It turns out therefore, that the coupling relative to $\hbar\omega_{\text{eff}}$ scales proportionally to the square-root of the characteristic impedance of the effective resonator.

Finally, to recover the standard form of the Rabi Hamiltonian, we remove the minus sign in front of the qubit term by applying a π-rotation around σ_z:

$$H = \frac{E_J}{2}\hat{\sigma}_x - \frac{g}{2}\hat{\sigma}_z(\hat{a}^\dagger + \hat{a}) + \omega_{\text{eff}}\hat{a}^\dagger\hat{a}. \tag{2.84}$$

Up to a $\pi/2$ rotation of the qubit basis around the y-axis, Eq. (2.81) is precisely in the same form as Eq. (2.73). Although we will mostly be working in the Cooper-pair box basis in this thesis, with $\hat{\sigma}_x$ as the qubit tunneling term, the next paragraph will consider the qubit eigenbasis.

2.3.3 The rotating-wave approximation

As long as $g \ll \Delta$ and $g \ll \omega$, it is safe to neglect the off-resonant terms of the interaction. Those are the ones that either involve a jump to the excited state together with the emission of a photon ($\hat{\sigma}^+\hat{a}^\dagger$), or the relaxation to the ground state together with the absorption of a photon ($\hat{\sigma}^-\hat{a}$). Within this approximation, known as the rotating-wave approximation (RWA), the Rabi Hamiltonian (2.84), now expressed in the eigenbasis of the qubit, becomes the Jaynes-Cummings Hamiltonian:

$$H_{\text{JC}} = \frac{\Delta}{2}\hat{\sigma}_z - \frac{g}{2}(\hat{a}^\dagger\hat{\sigma}^- + \hat{a}\hat{\sigma}^+) + \omega\hat{a}^\dagger\hat{a}. \tag{2.85}$$

By explicitly writing the matrix for this Hamiltonian we see that it is block-diagonal (except for the H_{00} element, which corresponds to the uncoupled ground state):

$$H = \begin{pmatrix} -\frac{1}{2}\Delta & & & \\ & H_0 & & \\ & & H_1 & \\ & & & \ddots \end{pmatrix}, \tag{2.86}$$

with the blocks given by the following 2×2 matrices that mix the neighboring energy levels $|g, n+1\rangle$ and $|e, n\rangle$:

$$\begin{aligned} H_n &= \omega(n+1/2)\mathbb{1} + \begin{pmatrix} \delta/2 & -g\sqrt{n+1} \\ -g\sqrt{n+1} & -\delta/2 \end{pmatrix} \\ &= \frac{\delta}{2}\hat{\sigma}_z - g\sqrt{n+1}\hat{\sigma}_x + \omega(n+1/2)\mathbb{1}, \end{aligned} \tag{2.87}$$

In the above equation, we have defined $\delta = \Delta - \omega$, the detuning between the field mode frequency and the resonance of the qubit. Diagonalizing this system yields the eigenenergies

$$E_g = -\Delta/2, \tag{2.88}$$

$$E_n^{\pm} = \omega(n+1/2) \pm \frac{1}{2}\sqrt{4(n+1)g^2 + \delta^2}, \tag{2.89}$$

and the eigenstates, often referred to as the "dressed" states of the atom:

$$\begin{aligned} |+, n\rangle &= \cos(\theta_n/2)\,|e, n\rangle + \sin(\theta_n/2)\,|g, n+1\rangle\,, \\ |-, n\rangle &= \sin(\theta_n/2)\,|e, n\rangle - \cos(\theta_n/2)\,|g, n+1\rangle\,. \end{aligned} \tag{2.90}$$

For convenience, we have here introduced θ_n, a "mixing angle" defined by

$$\tan(\theta_n) = g\sqrt{n+1}/\delta. \tag{2.91}$$

The eigenenergies (2.89) are plotted versus coupling in Fig. 2.7b, to illustrate the progressive hybridization of $|e, n-1\rangle$ and $|g, n\rangle$ into $|+, n\rangle$ and $|-, n\rangle$. If one sweeps the detuning δ, let's say by varying the qubit energy Δ while keeping ω constant, this hybridization appears as an avoided crossing centered at the point of no detuning ($\Delta/\omega = 1$). As an example, we show in Fig. 2.7a the avoided crossing between $E_0^- - E_g$ and $E_0^+ - E_g$, which reveals the hybridization of $|e, 0\rangle$ and $|g, 1\rangle$ (in grey-dashed lines) into $|+, 0\rangle$ and $|-, 0\rangle$.

2.3.4 Rabi oscillations induced by n photons

Rabi oscillations is a phenomenon occurring when the field mode is resonant with the qubit, and that involves the coherent exchange of quanta between the atom and the field. For $\delta = 0$, the hybridized modes take the following form:

$$|\pm, n\rangle = \big(\,|e, n\rangle \pm |g, n+1\rangle\,\big)/\sqrt{2}. \tag{2.92}$$

Let us assume that at $t = 0$ the atom-cavity system is in the $|e, n\rangle$ state. We can then rewrite this initial state in terms of the eigenstates as

$$|\Psi(0)\rangle = |e, n\rangle = \big(\,|+, n\rangle + |-, n\rangle\,\big)/\sqrt{2}, \tag{2.93}$$

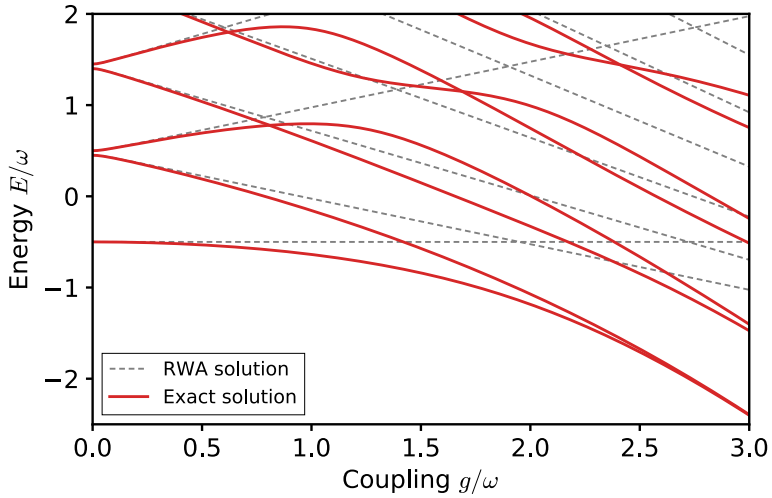

Figure 2.8: Energy spectrum of the Rabi model. In dashed-grey is the spectrum from the Jaynes-Cummings model, which was shown in Fig. 2.7b. Note that within the full Rabi model, the ground state energy is no longer constant as coupling is increased.

and apply the time-evolution operator $\hat{U}^\dagger = e^{-\frac{i}{\hbar}\hat{H}t}$ to obtain the state of the system at time t:

$$|\Psi(t)\rangle = \left(|+,n\rangle\, e^{-ig\sqrt{n+1}t} + |-,n\rangle\, e^{ig\sqrt{n+1}t}\right)/\sqrt{2}. \tag{2.94}$$

Finally, reverting to the uncoupled basis, we obtain:

$$|\Psi(t)\rangle = \cos(g\sqrt{n+1}t)\,|e,n\rangle + \sin(g\sqrt{n+1}t)\,|g,n+1\rangle \tag{2.95}$$

Thus, we see that a periodic coherent exchange of quanta takes place, with $\tau = \frac{\pi}{2g\sqrt{n+1}}$ being the time required for the atom to emit/absorb a complete photon.

2.3.5 Beyond the rotating-wave approximation - the Rabi model

Briefly, we consider the full Rabi model, including the off-resonant terms dropped in the Jaynes-Cummings formalism:

$$H_{\text{Rabi}} = \frac{\Delta}{2}\hat{\sigma}_x - \frac{g}{2}\hat{\sigma}_z(\hat{a}^\dagger + \hat{a}) + \omega\hat{a}^\dagger\hat{a}.$$

This Hamiltonian can easily be diagonalized numerically after truncating the Fock space to $n \sim 100$, as long as g/ω is not too large. We denote the eigenstates as the set $\{|\psi_n\rangle\}$, and the corresponding energy spectrum $\{E_n\}$, which is plotted in red in Fig. 2.8. To provide a comparison and visualize the break-down of the rotating-wave approximation, we show in dashed-grey lines the Jaynes-Cummings spectrum from Fig. 2.7b.

Performing a time evolution is then just a matter of re-writing the initial state $|\Psi(0)\rangle$ in the diagonal basis,

$$|\Psi(0)\rangle = \sum_n c_n\,|\psi_n\rangle\,, \tag{2.96}$$

and then applying the time-evolution operator:

$$|\Psi(t)\rangle = \hat{U}^\dagger\,|\Psi(0)\rangle = e^{-\frac{i}{\hbar}\hat{H}t}\,|\Psi(0)\rangle = \sum_n c_n e^{-\frac{i}{\hbar}E_n t}\,|\psi_n\rangle\,. \tag{2.97}$$

This exact time-evolution (up to numerical error) will be useful to us in chapter 3 to provide a benchmark of our multi-coherent state technique applied to the Rabi model.

Note that no complete exact solution to the Rabi model has been found in compact analytical form, although transcendental equations can be written using integrability [57]. Numerically, its spectrum and dynamics have been explored in great detail, including the ultra-strong coupling regime, in several studies (here is a non-exhaustive list of recent references [58, 59, 60, 61, 62, 63]).

2.4 Many-mode ultra-strong coupling: waveguide QED

In this section, we generalize the single-mode circuit to the many-mode chain interacting with a superconducting qubit. In particular, following the derivation by Snyman and Florens [27], we show that the spin-boson model can describe a Cooper-pair box coupled to a chain of Josephson junctions. Finding the solution to this complicated many-body model will then be the topic of the next chapter. Note that there are various possible architectures for coupling qubits to waveguides that can also be mapped on the spin-boson model. Several theoretical papers for example consider a double-island quantum impurity [64, 29] instead of a Cooper-pair box. Another example is the coupling of flux qubit to a 50 Ω transmission line which can also be described by the spin-boson Hamiltonian [17].

2.4.1 Hamiltonian of the Josephson waveguide

We start with the Hamiltonian of the circuit illustrated in Fig. 2.9:

$$\hat{H} = \hat{H}_0 + \hat{H}_1, \tag{2.98}$$

where the quadratic part H_0 describes the linearized semi-infinite Josephson junction chain:

$$\hat{H}_0 = \frac{1}{2}\sum_{m,n=0}^{+\infty} \hat{N}_m \left(M^{-1}\right)_{mn} \hat{N}_n + \frac{1}{2}\sum_{m,n=0}^{+\infty} \hat{\varphi}_m V_{mn} \hat{\varphi}_n. \tag{2.99}$$

The impurity, located at the end of the chain, contains the only source of non-linearity of the problem, encoded in the Josephson energy:

$$\hat{H}_1 = -E_{Jd}\cos(\hat{\varphi}_0 - \hat{\varphi}_1). \tag{2.100}$$

Similarly to how we derived the Rabi model in paragraph 2.3.2, we can write down the capacitance matrix M by applying prescription (2.76):

$$M = \frac{1}{(2e)^2}\begin{pmatrix} C_{gd}+C_d & -C_d & & & & \\ -C_d & G_g+C_d+C & -C & & & \\ & -C & C_g+2C & -C & & \\ & & -C & C_g+2C & -C & \\ & & & \ddots & \ddots & \ddots \end{pmatrix}. \tag{2.101}$$

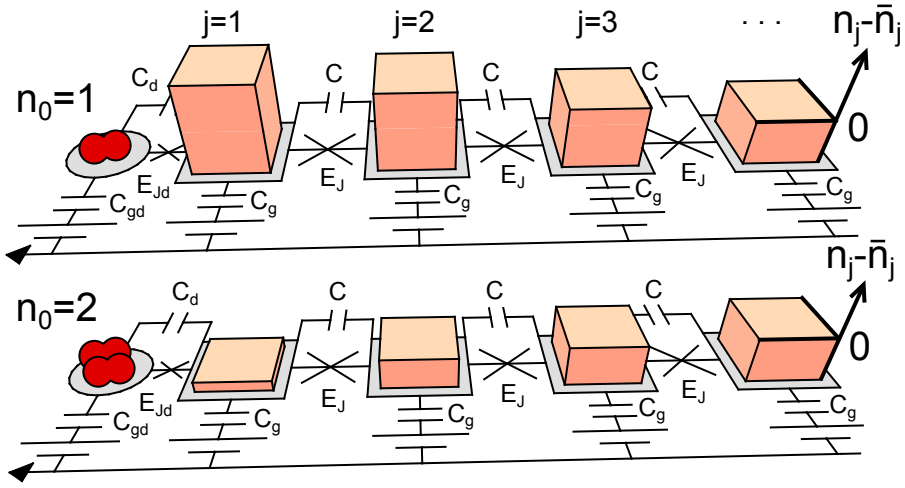

Figure 2.9: Schematic view of the studied superconducting circuit supporting two dressed qubit states, where one or two Cooper-pairs in excess on the leftmost island are each accompanied by a different charge polarization cloud, illustrated by the orange cubes symbolizing the charge accumulated at each site. Josephson tunneling between the two configurations generates entanglement between the qubit and its environment. This illustration is from [27].

The inductance matrix V is easily deduced by considering the linearized Josephson terms $-E_J\cos(\hat{\varphi}_i-\hat{\varphi}_j)\simeq E_J(\hat{\varphi}_i-\hat{\varphi}_j)^2/2$ that couple site i to site j:

$$V = E_J\begin{pmatrix} 0 & 0 & & & & \\ 0 & 1 & -1 & & & \\ & -1 & 2 & -1 & & \\ & & -1 & 2 & -1 & \\ & & & \ddots & \ddots & \ddots \end{pmatrix}, \tag{2.102}$$

which excludes the flux $\hat{\varphi}_0$ at the beginning of the array. The indexing convention is such that the upper-left entries of these matrices are labeled by M_{00} and V_{00}. One would like to express H_0 as a bath of independent oscillators that are linearly coupled to the impurity at site 0. This is achieved by expressing the set of harmonic variables in terms of bosonic operators:

$$\hat{N}_m = \frac{1}{\sqrt{2}}\int_0^{+\infty} dk\ \theta_{mk}(\hat{b}_k+\hat{b}_k^\dagger) \qquad m=1,2,\ldots,+\infty \tag{2.103}$$

$$\hat{\varphi}_m = \frac{i}{\sqrt{2}}\int_0^{+\infty} dk\ \xi_{mk}(\hat{b}_k-\hat{b}_k^\dagger) \qquad m=1,2,\ldots,+\infty \tag{2.104}$$

where ξ_{mk} and θ_{mk} are real numbers. We stress that the coordinates $(\hat{N}_0,\hat{\varphi}_0)$ at the end of the chain (site $m=0$) are not part of this decomposition, which will facilitate the later projection onto the two-level system. A first important relation follows from (2.103-2.104) by imposing the commutation relation $[\hat{\varphi}_m,\hat{N}_n]=i\delta_{m,n}$ and assuming standard algebra of the bosonic operators, namely $[\hat{b}_k,\hat{b}_k]=0$, $[\hat{b}_k,\hat{b}_k^\dagger]=\delta(k-k')$:

$$\int_0^{+\infty} dk\ \xi_{mk}\theta_{nk}=\delta_{m,n}. \tag{2.105}$$

The eigenfrequencies and eigenmodes of the chain are then obtained by imposing that the

quadratic part of the Hamiltonian, excluding site $m = 0$, is diagonalized by the bosonic operators:

$$\hat{H}_0^{\text{chain}} = \frac{1}{2}\sum_{m,n\neq 0} \hat{N}_m \left(M^{-1}\right)_{mn} \hat{N}_n + \frac{1}{2}\sum_{m,n\neq 0} \hat{\varphi}_m V_{mn} \hat{\varphi}_n \equiv \int_0^{+\infty} dk\ \omega_k \hat{b}_k^\dagger \hat{b}_k, \tag{2.106}$$

with ω_k the positive frequencies of the normal modes. Here we will simply state the result for the eigenvalues:

$$\omega_k = \sqrt{\frac{4(2e)^2 E_J \sin^2(k/2)}{C_g + 4C\sin^2(k/2)}}. \tag{2.107}$$

The complete derivation of this expression, and of the coefficients θ_{mk} and ξ_{mk} defining the eigenmodes in Eq. (2.103), is given in appendix A.

2.4.2 Hamiltonian of the full system: the spin-boson model

To obtain the full Hamiltonian we need to include the degrees of freedom of the impurity at site $m = 0$, which have been excluded in Eq. (2.106). The impurity part of the quadratic Hamiltonian (2.99) related to the site $m = 0$ reads:

$$\hat{H}_0^{\text{imp}} = \frac{1}{2}\left(M^{-1}\right)_{00} \hat{N}_0^2 + \hat{N}_0 \sum_{m=1}^{+\infty} \left(M^{-1}\right)_{0m} \hat{N}_m. \tag{2.108}$$

As shown in appendix A, we can obtain an exact and remarkably compact expression for the full Hamiltonian in terms of the normal modes and of the variables at the first two sites of the Josephson chain:

$$\hat{H} = \frac{1}{2}\left(M^{-1}\right)_{00} \hat{N}_0^2 + \int_0^\pi dk\ \omega_k \hat{b}_k^\dagger \hat{b}_k + \hat{N}_0 \int_0^\pi dk\ g_k(\hat{b}_k + \hat{b}_k^\dagger) - E_{Jd}\cos(\hat{\varphi}_0 - \hat{\varphi}_1), \tag{2.109}$$

where we have introduced the mode-dependent coupling constant

$$g_k = \frac{1}{2}\frac{C_d}{C_{gd} + C_d}\frac{1}{\sin(k/2)}\sqrt{\frac{\omega_k^3}{2\pi E_J}}\cos\left[\frac{k}{2} - \arctan\left(\frac{(1 - C_g/C_{\text{eff}})\sin(k)}{(1 - C_g/C_{\text{eff}})\cos(k) - 1}\right)\right]. \tag{2.110}$$

To get rid of the factors containing $\hat{\varphi}_1$, we perform a unitary transformation $\widetilde{H} = UHU^\dagger$, with $U = e^{i\hat{N}_0\hat{\varphi}_1}$. The transformed Hamiltonian reads

$$\widetilde{H} = \frac{(2e)^2}{2C_{\text{imp}}}\hat{N}_0^2 + \int_0^\pi dk\ \omega_k \hat{b}_k^\dagger \hat{b}_k - \frac{1}{\sqrt{2}}\hat{N}_0 \int_0^\pi dk\ \omega_k \xi_{0k}(\hat{b}_k^\dagger + \hat{b}_k) - \frac{E_{Jd}}{2}\left[e^{i\hat{\varphi}_0} + e^{-i\hat{\varphi}_0}\right] \tag{2.111}$$

where

$$\frac{(2e)^2}{C_{\text{imp}}} = \left(M^{-1}\right)_{00} + \left(1 - \frac{2C_d}{C_d + C_{dg}}\right)\int_0^\pi dk\ \omega_k \xi_{1k}^2. \tag{2.112}$$

Now we assume that we are at a degeneracy point of the uncoupled impurity, and project the impurity part of the Hilbert space onto the two degenerate states. This results in $\hat{N}_0 \to -\hat{\sigma}_z/2$ and $(e^{i\hat{\varphi}_0} + e^{-i\hat{\varphi}_0}) \to \hat{\sigma}_x$, as discussed in paragraph 2.2.4. Dropping the constant term $\hat{\sigma}_z^2$, it follows that Eq. (2.111) takes the form of a spin-boson Hamiltonian:

$$\tilde{H} \simeq \int_0^\pi \omega_k \hat{b}_k^\dagger \hat{b}_k - \frac{\hat{\sigma}_z}{2}\int_0^\pi dk\ g_k(\hat{b}_k^\dagger + \hat{b}_k) - E_{Jd}\frac{\hat{\sigma}_x}{2}. \tag{2.113}$$

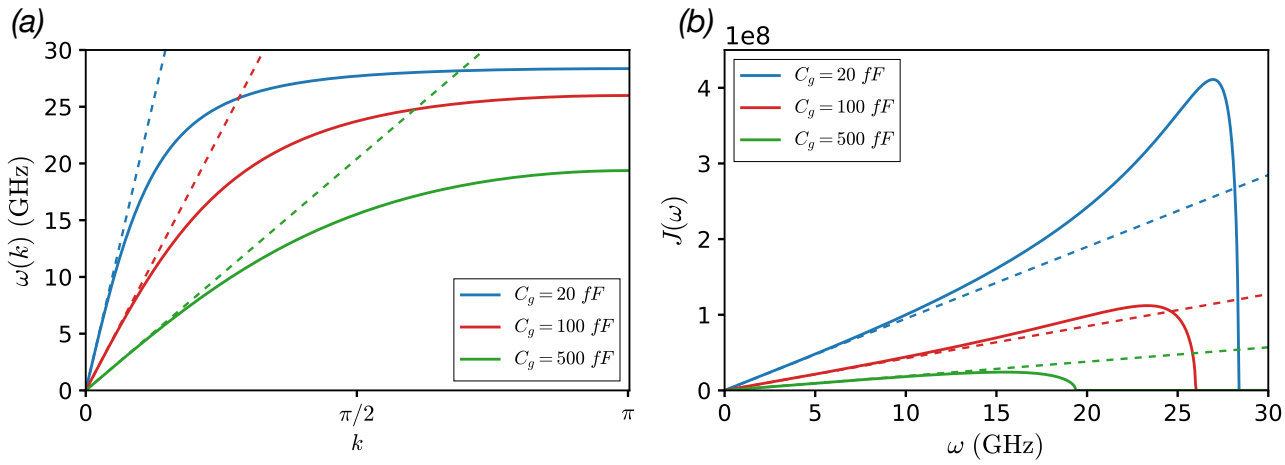

Figure 2.10: **(a)** Dispersion relation of the chain and **(b)** spectral function for three different values of the ground capacitance C_g and for $C = 100$ fF, $C_\mathrm{d} = C_\mathrm{gd} = 100$ fF, $L_\mathrm{J} = 0.3$ nH. The solid lines are the exact results while the dashed lines correspond to the low-frequency approximation. Note that as C_g becomes very small, the density of states at the cutoff frequency becomes very large, which is why the spectral function is peaked close to the cutoff frequency.

Performing a π-rotation around $\hat{\sigma}_z$, we remove the minus sign on the σ_x operator to obtain the standard form of the Hamiltonian:

$$\tilde{H} \simeq \int_0^\pi \omega_k \hat{b}_k^\dagger \hat{b}_k - \frac{\hat{\sigma}_z}{2} \int_0^\pi dk\, g_k(\hat{b}_k^\dagger + \hat{b}_k) + E_{Jd}\frac{\hat{\sigma}_x}{2}. \tag{2.114}$$

In the low-frequency approximation, with $k \ll \sqrt{C_g/C}$,

$$\omega_k \simeq E_0 k, \tag{2.115}$$

$$g_k \simeq \sqrt{\left(\frac{C_{dg}}{C_{dg}+C_d}\right)^2 \frac{E_0^3}{\pi E_J} k}, \tag{2.116}$$

where $E_0 = \sqrt{(2e)^2 E_J/C_g}$. We can thus identify the Ohmic spin-boson model parameter

$$\alpha = \frac{1}{2\pi}\left(\frac{C_{dg}}{C_{dg}+C_d}\right)^2 \frac{E_0}{E_J}, \tag{2.117}$$

which brings g_k into a more concise form:

$$g_k = \sqrt{2\alpha E_0 \omega_k}. \tag{2.118}$$

By calculating the spectral function, we can further characterize the interaction between the chain modes and the qubit:

$$J(\omega) = \pi \int_0^\pi dk\ g_k \delta(\omega - \omega_k) = \pi \left|\frac{dk}{d\omega}\right| |g_k(\omega)|^2. \tag{2.119}$$

In the low-frequency approximation (2.116) this is simply:

$$J(\omega) \simeq 2\pi\alpha\omega \tag{2.120}$$

In Fig. 2.10, we plot the spectral function and the dispersion relation using the exact expressions (2.107) and (2.110), for the realistic parameters $C = 100$ fF, $C_\mathrm{d} = C_\mathrm{gd} = 10$ fF, $L_\mathrm{J} = 0.3$ nH,

and for three different values of the ground capacitance C_g. These curves are compared with the low frequency approximation given by Eq. (2.116) (dashed curves). Clearly, the low frequency approximation best matches the exact curve for $C_g > 100$ fF (in red and green). For the lower value $C_g = 20$ fF (in blue) however, ω_k quickly reaches the plasma frequency, resulting in a very high density of states close to this frequency, which in turn leads to the sharply peaked spectral function of Fig 2.10b. Note that in the work of this thesis we will apply an exponential cutoff to the spectral function to model the sharp decrease observed in Fig. 2.10b. This is a common approach in the literature [30]. The other approach [28] is to apply a sharp cutoff to the spectral function above at certain frequency ω_c. It is worth noting at this point that in this thesis we will be working with qubit frequencies typically of the order of $\omega_c/10$, well within the range where the low-frequency approximation (2.116) is close to exact (i.e. the solid lines and the dashed lines agree in Fig. 2.10b).

2.4.3 The discretized spin-boson model

In view of solving the system numerically, let us discretize the spin-boson Hamiltonian to a number of modes N_{modes}. In the low-frequency approximation, the discrete version of the spectral function (2.120) is

$$J(\omega) = 2\pi\alpha\omega e^{-\omega/\omega_c} = \lim_{N_{\text{modes}}\to\infty} \pi \sum_{k>0}^{N_{\text{modes}}} g_k^2 \, \delta(\omega - \omega_k) \tag{2.121}$$

to which we have added the exponential cutoff that was discussed above. To obtain the coupling g_k corresponding to a given discrete mode, with the assumption that the mode separation δk is small, we integrate Eq. (2.121) around a certain mode k_1:

$$\int_{k_1-\delta k/2}^{k_1+\delta k/2} J(\omega) d\omega_k = 2\pi\alpha \int_{k_1-\delta k/2}^{k_1+\delta k/2} \omega e^{-\omega/\omega_c} d\omega_k \simeq 2\pi\alpha k_1 \delta k e^{-\omega_{k_1}/\omega_c} \tag{2.122}$$

$$= \pi g_{k_1}^2, \tag{2.123}$$

It follows that

$$g_k = \sqrt{2\,\alpha\,k\,\delta k\,e^{-\omega_k/\omega_c}}. \tag{2.124}$$

Therefore, the discretized spin-boson model [26] reads

$$H = \frac{\Delta}{2}\hat{\sigma}_x - \frac{\hat{\sigma}_z}{2} \sum_{k>0}^{N_{\text{modes}}} g_k(\hat{a}_k + \hat{a}_k^\dagger) + \sum_{k>0}^{N_{\text{modes}}} \omega_k \hat{a}_k^\dagger \hat{a}_k \,, \tag{2.125}$$

where we have renamed the bare splitting of the qubit levels $\Delta \equiv E_{Jd}$. We stress again that we do not work in the qubit eigenbasis here, but rather in a basis that makes the qubit-waveguide coupling diagonal, as described by the $\hat{\sigma}_z$ term above. This choice allows a natural description of the driving force behind the entanglement between the qubit and the waveguide, and sets the natural language for the numerical technique based on coherent states we will now present.

Note that an important assumption that we have made in this study is the restriction of the atom to a perfect two-level system. This hypothesis is perfectly legitimate for strongly non-linear qubits, such as the Cooper-pair box or the flux qubit [5, 65, 17, 66]. Focusing on a two-level system allows to capture the maximum inelastic scattering cross-sections, due to its intrinsically high non-linearity. It is thus an excellent testbed to examine physics that is already quite rich, and to develop methodologies in the most challenging situation from a computational point of view.

Chapter 3

Solving the Spin-Boson Model at Ultra-Strong Coupling

In this chapter, we introduce a key element of this thesis: a variational method based on a coherent state ansatz for solving the spin-boson model in the ultra-strong coupling regime [67, 68]. Although the usual approach consists in making use of the Fock basis to describe the quantized bath excitations, this technique is based on the expansion of the bosonic degrees of freedom in terms of a finite number of coherent states. In other words, we use an adaptable basis, wherein both the amplitude *and* the displacement of the coherent state Gaussians are variational parameters. It was previously demonstrated that for calculating of the ground state of the spin-boson model, the use of this basis can provide a tremendous computational gain [69, 70]. In this chapter, we will extend this result to the dynamics.

Interestingly, work on Gaussian-based techniques can be traced all the way back to the work of E. J. Heller in 1975 on a semiclassical method aimed at describing molecular dynamics [71]. Since then, many methods have been introduced, mostly on the side of theoretical chemistry, to tackle the interaction of a strongly non-linear system with a large bath. After we have presented the multi-coherent state technique and introduced the framework we will be working in, an account of previous work will be given and compared to the new approach proposed in this thesis.

An important characteristic of the multi-coherent state technique, as we will see, is the surprisingly small number of coherent states required to tackle systems that would otherwise require an unmanageably huge Hilbert space in the Fock state basis. The reader will however quickly realized that the underlying physical machinery of our variational algorithm is greatly obscured by the complexity of the many-body systems we study in this thesis. For this reason, after laying out the framework of the variational method, we will begin by revisiting the spin-boson model with a single mode, which will provide some insight regarding the physics dictating the qubit-bath dynamics within the coherent state framework. We will then move on to the full many-mode spin-boson model and provide a first demonstration of our technique by identifying the quantum states of spontaneous emission in a wave-guide in the ultra-strong coupling regime [67].

3.1 Variational dynamics with coherent states

3.1.1 The ansatz: a superposition of multi-mode coherent states

The strategy is to write the state vector as a coherent state expansion, also referred to in the following as the MCS ansatz [69, 70, 72, 67, 68]:

$$|\Psi(t)\rangle = \sum_{m=1}^{N_{\text{cs}}} \Big[p_m(t)|f_m(t)\rangle|\uparrow\rangle + q_m(t)|h_m(t)\rangle|\downarrow\rangle \Big], \tag{3.1}$$

We have introduced here the complex and time-dependent amplitudes $p_m(t)$ and $q_m(t)$ for each qubit component, as well as a set of discrete multi-mode coherent states for each qubit component:

$$|f_m(t)\rangle = \prod_{k=1}^{N_{\text{modes}}} e^{f_m^k(t)a_k^\dagger - f_m^{k*}(t)a_k} |0\rangle, \tag{3.2}$$

and similarly for $|h_m(t)\rangle$. The index m labels the N_{cs} coherent states of the superposition, each defined with the correponding set of N_{modes} displacements $\{f_m^k\}$ (or $\{h_m^k\}$).

This ansatz allows in principle to target an arbitrary state of the full Hilbert space (with an exponential cost). One must note a strong difference here with the standard Glauber-Sudarshan decomposition (2.27), which relies on a continuous expansion of the state vector onto coherent states. Because of the large number of modes involved in waveguide QED at ultra-strong coupling, the continuous representation is not suitable for numerical purposes. Our discrete expansion (3.1) can however be understood as a discretized version of the continuous integral representation of an arbitrary wave-function onto coherent states. Most importantly, we will demonstrate that physical states obtained from standard protocols, including spontaneous emission (section 3.3) and coherent state scattering (chapter 4), can be efficiently simulated with a discrete set of coherent states, showing only a polynomial cost in the number of modes N_{modes} and coherent states N_{cs}.

3.1.2 Equations of motion

We choose to approach the problem with a variational technique. Just as in the classical case where minimizing the action $S = \int \mathcal{L}\, dt$ is equivalent to Newton's 2nd law, one can show that the Shrödinger equation is equivalent to minimizing the action defined with the following Lagrangian density [73]:

$$\mathcal{L} = \langle\Psi(t)|\frac{i}{2}\overrightarrow{\partial_t} - \frac{i}{2}\overleftarrow{\partial_t} - \mathcal{H}\,|\Psi(t)\rangle\,. \tag{3.3}$$

Here, we have introduced the short-hand notation $\overleftarrow{\partial_t}$ and $\overrightarrow{\partial_t}$ defined as:

$$\overrightarrow{\partial_t}\,|\Psi(t)\rangle = \frac{d}{dt}\,|\Psi(t)\rangle \qquad \text{and} \qquad \langle\Psi(t)|\,\overleftarrow{\partial_t} = -\Big(\frac{d}{dt}\,|\Psi(t)\rangle\Big)^\dagger. \tag{3.4}$$

This leads to the Euler-Lagrange equations for the set of variables $v = \{p_n, q_n, f_n^k, h_n^k\}$ that characterize the MCS state vector (3.1):

$$\frac{d}{dt}\frac{\partial\mathcal{L}}{\partial\dot{p_n}} = \frac{\partial\mathcal{L}}{\partial p_n} \qquad \frac{d}{dt}\frac{\partial\mathcal{L}}{\partial\dot{f_n^k}} = \frac{\partial\mathcal{L}}{\partial f_n^k}. \tag{3.5}$$

Taking H in Eq. (3.3) to be the spin-boson Hamiltonian (2.125), and after a few lines of algebra, these equations explicitly read:

$$-i\frac{\partial E}{\partial p_j^*} = \sum_m \left(\dot{p}_m - \frac{1}{2}p_m\kappa_{mj}\right)\langle f_j|f_m\rangle\,, \tag{3.6}$$

$$-i\frac{\partial E}{\partial f_j^{k*}} - \frac{i}{2}\Big(\frac{\partial E}{\partial p_j^*}p_j^* + \frac{\partial E}{\partial p_j}p_j\Big)f_j^k = \sum_m \left[p_m\dot{f}_m^k + \left(\dot{p}_m - \frac{1}{2}p_m\kappa_{mj}\right)f_m^k\right]\langle f_j|f_m\rangle\,, \tag{3.7}$$

$$\kappa_{mj} = \sum_{k>0}\Big[\dot{f}_m^k f_m^{k*} + \dot{f}_m^{k*}f_m^k - 2f_j^{k*}\dot{f}_m^k\Big]. \tag{3.8}$$

Identical equations (up to a minus sign in g_k) are obtained for the variables q_n and h_n^k. Let us recall that the notation $\langle\alpha|\beta\rangle$ used here denotes the inner product between two multimode coherent states $|\alpha\rangle$ and $|\beta\rangle$, and is given by:

$$\langle\alpha|\beta\rangle \equiv \exp\Big[-\frac{1}{2}\sum_k |\alpha_k|^2 + |\beta_k|^2 - 2\alpha_k^*\beta_k\Big]. \tag{3.9}$$

Note also that we have denoted $E = \langle\Psi|H|\Psi\rangle$ the expectation value of the energy, whose explicit expression is:

$$\begin{aligned} E =& \frac{\Delta}{2}\sum_{n,m}\Big(p_n^*q_m\langle f_n|h_m\rangle + p_mq_n^*\langle h_n|f_m\rangle\Big) + \sum_{n,m}\Big(p_n^*p_m\langle f_n|f_m\rangle\Omega_{nm}^f + q_n^*q_m\langle h_n|h_m\rangle\Omega_{nm}^h\Big) \\ &- \frac{1}{2}\sum_{n,m}\Big(p_n^*p_m\langle f_n|f_m\rangle G_{nm}^f - q_n^*q_m\langle h_n|h_m\rangle G_{nm}^h\Big) \end{aligned} \tag{3.10}$$

where we have defined the shorthand notation $\Omega_{nm}^f = \sum_{k>0}\omega_k f_n^{k*}f_m^k$, $\Omega_{nm}^h = \sum_{k>0}\omega_k h_n^{k*}h_m^k$, $G_{nm}^f = \sum_{k>0}g_k(f_n^{k*} + f_m^k)$, $G_{nm}^h = \sum_{k>0}g_k(h_n^{k*} + h_m^k)$.

3.1.3 The numerical algorithm

In contrast to the dynamics with a single coherent state [74, 75], one encounters here a computational difficulty [76], because the time-derivatives $\dot{f}_m^{k'}$ of all the possible coherent state amplitudes enter Eq. (3.7) dictating the value of a given field f_j^k through the parameter κ_{mj} in Eq. (3.8). Indeed, for stability reasons it is crucial to formulate the dynamical equations in an explicit form $\dot{f}_j^k = F[v]$, where F is only a functional of the variables $v = \{p_n, q_n, f_n^k, h_n^k\}$, without reference to their time derivatives. Numerical inversion in order to bring the system into explicit form is however prohibitive as it would cost $(N_{\text{modes}} \times N_{\text{cs}})^3$ operations (unless the number of modes is small, for instance in the case of the Wilson discretization [74], which is not adapted to study the bath dynamics). It turns out that a very convenient trick allows to make the inversion in $(N_{\text{cs}})^6$ operations. This is favorable provided $N_{\text{cs}} \ll N_{\text{modes}}$, which is the case for very long Josephson arrays or broadband environments.

First, let us cast Eq. (3.6-3.7) into the following more concise form:

$$\sum_m \left(\dot{p}_m - \frac{1}{2}p_m\kappa_{mj}\right)M_{jm} = P_j, \tag{3.11}$$

$$\sum_m \left(p_m\dot{f}_m^k + \left(\dot{p}_m - \frac{1}{2}p_m\kappa_{mj}\right)f_m^k\right)M_{jm} = F_j^k \tag{3.12}$$

where we have defined the overlap matrix

$$M_{ij} = \langle f_i | f_j \rangle \,, \tag{3.13}$$

as well the shorthands

$$P_j = -i\frac{\partial E}{\partial p_j^*}, \tag{3.14}$$

$$F_j^k = -i\frac{\partial E}{\partial f_j^{k*}} - \frac{i}{2}\left(\frac{\partial E}{\partial p_j^*}p_j^* + \frac{\partial E}{\partial p_j}p_j\right) f_j^k. \tag{3.15}$$

By multiplying Eqs. (3.11-3.12) by the inverse of the overlap matrix, we obtain:

$$\begin{aligned}\sum_j M_{nj}^{-1} P_j &= \dot{p_n} - \frac{1}{2}\sum_{mj} p_m \kappa_{mj} M_{nj}^{-1} M_{jm} \\ &= \dot{p_n} - \frac{1}{2}p_n\left(\sum_k \dot{f_n^k} f_n^{k*} + \dot{f_n^{k*}} f_n^k\right) + \sum_{mjk} p_m M_{nj}^{-1} M_{jm} f_j^{k*} \dot{f_m^k},\end{aligned} \tag{3.16}$$

and

$$\begin{aligned}\sum_j M_{nj}^{-1} F_j^k = p_n \dot{f_n^k} + \dot{p_n} f_n^k - \frac{1}{2}p_n\left(\sum_k \dot{f_n^k} f_n^{k*} + \dot{f_n^{k*}} f_n^k\right) f_n^k \\ + \sum_{jmq} p_m M_{nj}^{-1} M_{jm} f_n^k f_j^{q*} \dot{f_m^q}.\end{aligned} \tag{3.17}$$

Combining Eqs. (3.16) and (3.17), we can easily remove the dependance on $\dot{p}_n$, and thus obtain an equation in terms of $\dot{f_n^k}$ only:

$$p_n \dot{f_n^k} + \sum_{mjq} M_{nj}^{-1} M_{jm} p_m f_j^{q*} \dot{f_m^q} \left(f_m^k - f_n^k\right) = \sum_j M_{nj}^{-1} F_j^k - f_n^k M_{nj}^{-1} P_j. \tag{3.18}$$

The next step is then to define the mode-independent matrix

$$a_{in} = p_n \sum_k f_i^{k*} \dot{f_n^k}, \tag{3.19}$$

and use it to re-express Eq. (3.18) as:

$$p_n \dot{f_n^k} + \sum_{mj} M_{nj}^{-1} M_{jm} a_{jm} (f_m^k - f_n^k) = \sum_j M_{nj}^{-1} F_j^k - f_n^k M_{nj}^{-1} P_j. \tag{3.20}$$

Multiplying (3.20) by f_i^{k*}, and summing over k, we obtain an equation for a_{in} alone:

$$a_{in} + \sum_{mj} a_{jm} M_{nj}^{-1} M_{jm} \left(b_{im} - b_{in}\right) = A_{in}, \tag{3.21}$$

where for convenience we have defined the variables

$$A_{in} = \sum_{jk} f_i^{*k} \left(M_{nj}^{-1} F_j^k - f_n^k M_{nj}^{-1} P_j\right) \qquad \text{and} \qquad b_{in} = \sum_k f_i^{k*} f_n^k. \tag{3.22}$$

Eq. (3.21) is a linear system of $(N_{\text{cs}})^2$ equations that can be solved numerically. Once the matrix a_{in} is obtained, one can straightforwardly use Eqs. (3.20) and (3.16) to deduce the sets of derivatives $\{\dot{p}_n\}$ and $\{\dot{f}_n^k\}$ corresponding to the N_{cs} coherent states of the $\uparrow$ qubit sector. The same procedure is applied to obtain the derivatives $\{\dot{q}_n\}$ and $\{\dot{h}_n^k\}$ of the $\downarrow$ qubit sector. The Fortran 98 code written to perform these numerics makes an extensive use of the highly optimized Math Kernel Libraries (MKL) from Intel[1].

Remarkably, Eq. (3.21) allows us to bypass the gigantic system of $(N_{\text{modes}} \times N_{\text{cs}})$ Euler-Lagrange equations (3.5) that would have involved a numerical cost scaling as $(N_{\text{modes}} \times N_{\text{cs}})^3$. Instead, the cost of solving Eq. (3.21) only scales as $(N_{\text{cs}})^6$, which is a tremendous advantage as long as $N_{\text{modes}} \gg N_{\text{cs}}$.

3.1.4 Quantifying the error

Theoretically, the multi-mode coherent state technique becomes exact only when the number of coherent states $N_{\text{cs}} \to \infty$. It turns out however that only a small number of coherent states are required to converge the solution with high precision. The precise number required will depend on the regime of coupling considered and on the degree of precision required to calculate the quantities of interest. As we will see in the next chapter, calculating second-order correlation functions in the radiation scattered by the qubit requires many more coherent states to obtain adequate accuracy, as compared to calculating power spectra.

We therefore need a reliable tool to quantify the degree of convergence of the dynamical solutions that we find. In this work, we define an error by the squared norm

$$\text{Err}(t) \equiv \big\langle \Phi(t) | \Phi(t) \big\rangle \tag{3.23}$$

of the auxiliary state

$$|\Phi(t)\big\rangle \equiv (i\partial_t - H)|\Psi(t)\big\rangle. \tag{3.24}$$

The full expression for $\text{Err}(t)$ is given in appendix B. Clearly, if $|\Psi(t)\rangle$ satisfies the Schrödinger equation, then $\text{Err}(t) = 0$. With only a finite number of coherent states N_{cs} in the state vector, $\text{Err}(t)$ can only be finite, but will steadily decrease as more coherent states are included in the state vector and the dynamics converge closer to the exact solution. In the following, we will systematically demonstrate this steady decrease to show that our technique is well-controlled.

3.1.5 Precursors of the MCS technique

Historically, the use of Gaussian-like state functions can be traced back to the work on semi-classical approaches of E. J. Heller in the mid 1970s. Motivated by an effort to describe molecular nuclei dynamics, his first proposal was to describe heavy-particles by a single Gaussian wavepacket with a centre and a width that evolved variationally [71]. This approximation is referred to as the "thawed" Gaussian ansatz, because the shape of the Gaussian evolves to adapt to the requirement of the dynamics. This ansatz however turned out to be too limited for the description of the dynamics of a real molecular system, which prompted E. J. Heller to introduce a variant where nuclei are this time described by a superposition of multiple Gaussians. In this improved version, known as the "frozen" Gaussian method [77], the centers of the different Gaussians now follow classical trajectories, and their shapes are frozen. At the level of molecules, where most of the quantum dynamics falls into the semiclassical domain, these

[1] https://software.intel.com/en-us/mkl

Gaussian-based approximations conveniently offer a link between the localized classical particle trajectory, and the delocalization due to the unavoidable quantum uncertainty. The frozen Gaussian ansatz became most powerful in combination with the time-dependent semiclassical Green's function approaches later developed [78, 79, 80].

Although these Gaussian techniques proved astoundingly effective for semiclassics, they remain a trade-off between quantum and classical that is bound to fail as we go deeper into the quantum domain. The next stride forward was made with the advent of the multi-configuration time-dependent Hartree technique (MCTDH) aimed at solving variationally the time-dependent Schrödinger equation [81]. This method consists in expanding the state vector onto a set of time-evolving functions, which can in principle be anything. More powerful than the MCTDH however, is an improved version of it known as the ML-MCTDH, that is the *multi-layer* MCTDH [82]. In this version of the method, the functions on which the state vector was already expanded, are *themselves* expanded on another set of functions, leading to 'layers' of expansions. This method proved particularly powerful at describing condensed matter processes taking place in large systems, such as photo-induced electron-transfer in semiconductors [83], or proton transfer reactions in condensed-phase environments [84]. Furthermore, Wang and Thoss used the ML-MCTDH technique [82, 31] to calculate for the first time the complete dynamics of the spin-boson model. Remarkably, they were able to include hundreds of bath modes, and thus study spin dynamics without tracing on the bath degrees of freedom entangled with the qubit, a necessary condition for accurately describing the strong coupling regime.

The next theoretical development, brings us nearest to the description that we have described in this section. Introduced by Burghardt *et. al.* in 1999 [85, 86], the variational multi-configuration Gaussian method (vMCG), is a variation of the MCTDH (the single layer version), in which the linear degrees of freedom, such as a those of a bath, are expanded on either frozen or thawed Gaussian wave-functions. Although reminiscent of Heller's frozen Gaussian method, the vMCG technique here entails the full quantum treatment of the MCTDH, as opposed to the frozen Gaussian's semiclassical approximation.

Our approach in this thesis, although aimed specifically at solving the spin-boson model, bears some similarities with the vMCG method in that we have also described the bath degrees of freedom in terms of a superposition of Gaussians, and have used the Euler-Lagrange equations to derive the equations of motion. Instead of considering a generic type of Gaussians however, we have specified our derivation to an expansion in terms of coherent states, which are basically Gaussians that present just enough widths in position and momentum that they verify the Heisenberg uncertainty relations. As we saw, this specific choice of parametrization, leads to an astonishing simplification of the dynamical equations which allows our simulations to run orders of magnitude faster than the vMCG for large systems. In particular, whereas the bottleneck of the vMCG is a system of $(N_{\text{dof}} \times N_{\text{Gaussians}})$ equations, with $N_{\text{Gaussians}}$ the number of Gaussians and N_{dof} the number of bath degrees of freedom, our method's bottleneck is a system of only N_{cs}^2 equations (Eq. 3.21).

Although this drastic simplification that we witness seems surprising at first, let us point out that our ansatz appears particularly well motivated if we think in the lines of the philosophy of Heller's Gaussian approach. Indeed, in the ultra-strong coupling regime, one expects the macroscopic dynamics that emerge from the intense qubit-bath coupling to lead to classical-like bath trajectories with minimum quantum uncertainty, which is most appropriately described by our Gaussian coherent states. In parallel, the tunneling effect from the qubit will induce coherent superpositions of these macroscopic trajectories, similar to the superposed frozen Gaussians. In a way therefore, the ultra-strong coupling regime bears some similarity with the semiclassical realm, in that it requires classical-like states to describe emerging classical-like

dynamical effects within a more general quantum description.

Another notable difference of our approach is that it is expressed in the second-quantization formalism, the natural language of quantized harmonic modes, whereas the MCTDH and the vMCG methods have systematically been expressed using real-space wave-functions. Second-quantization will prove most appropriate for the study of the bath dynamics on which we will be focusing our study of spin-boson physics.

3.2 Dynamics of the Rabi model

The aim here is to demonstrate how to implement the MCS algorithm on the simpler single-mode Rabi model before we move on to the many-mode spin-boson model. In particular, having only one mode will make it possible to visualize field states using Husimi or Wigner functions and to gain some insight in the way the different coherent states from the MCS state vector evolve dynamically. The simplicity of this model will also allow us to provide a benchmark for the multi-coherent state dynamics by comparing our technique with a direct diagonalization in the usual Fock state basis. Remarkably in fact, we will see that very few degrees of freedom need to be considered in the coherent state basis, which clearly seems to indicate that quantum superpositions of classical-like states are more representative of the physical reality in the ultra-strong coupling regime than the usual number-state representation.

3.2.1 Hamiltonian and dynamical equations

The Hamiltonian for the Rabi model is given by:

$$H_{\text{rabi}} = \frac{\Delta}{2}\sigma_x + \omega a^\dagger a - \frac{g}{2}\sigma_z(a^\dagger + a). \tag{3.25}$$

Following the strategy outlined in the previous section but with a single mode, we start with the multi-coherent state ansatz defined in Eq. (3.1):

$$|\Psi(t)\rangle = \sum_{n=1}^{N_{\text{cs}}} \Big[p_n(t)|f_n(t)\rangle|\uparrow\rangle + q_n(t)|h_n(t)\rangle|\downarrow\rangle \Big],$$

where $|f_n\rangle$ ($|h_n\rangle$) are here the familiar one-mode coherent states described by a single displacement f_n (h_n). With only one frequency involved in the system, the variational method introduced in paragraph 3.1.2 leads to only N_{cs} Euler-Lagrange equations, for each sector of the spin:

$$\frac{d}{dt}\frac{\partial \mathcal{L}}{\partial \dot{p_n}} = \frac{\partial \mathcal{L}}{\partial p_n} \qquad \frac{d}{dt}\frac{\partial \mathcal{L}}{\partial \dot{f}_n} = \frac{\partial \mathcal{L}}{\partial f_n}, \tag{3.26}$$

and the same for $\{q_n\}$ and $\{h_n\}$. As long as the couplings are not too large, the number N_{cs} of Lagrange-Euler equations will remain small enough that one can obtain the set of values of $\{\dot{p}_n, \dot{q}_n, \dot{f}_n, \dot{h}_n\}$ by directly solving the equations numerically.

In order to provide a benchmark of our simulations, we will be comparing this solution with the one obtained by directly diagonalization the Rabi Hamiltonian in the Fock state basis, which is described in paragraph 2.3.5.

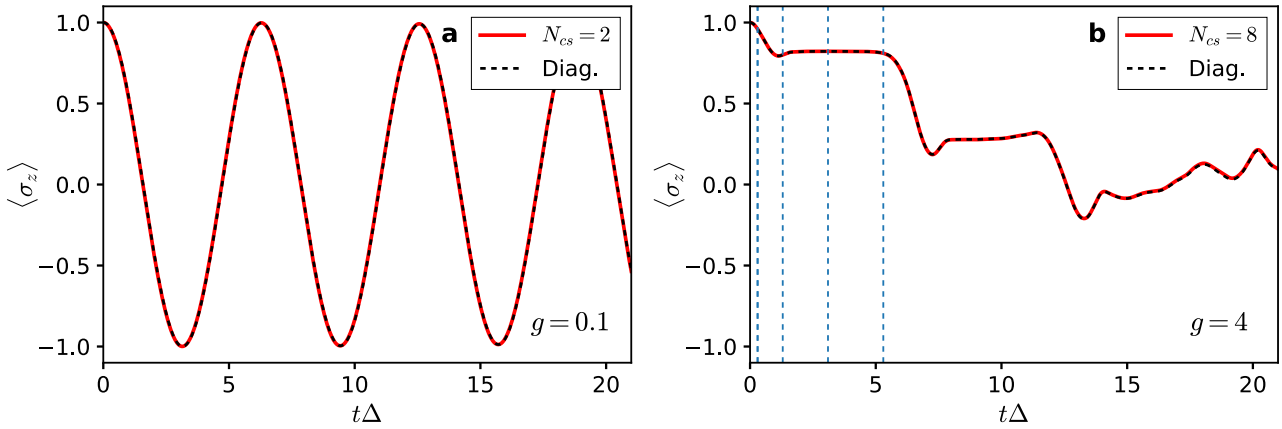

Figure 3.1: Dynamics of the expectation value of the $\langle \sigma_z \rangle$ operator for two different values of the coupling g upon preparing the qubit in the $|\uparrow\rangle$ state. For those simulations we took the qubit energy $\Delta = 0.1$ and the mode frequency $\omega = 1.0$. The dynamics obtained from the MCS technique in shown in red, while the dashed black curve is obtained by directly diagonalizing the Hamiltonian and by performing a unitary evolution. The blue dashed lines correspond to the 4 snapshots of the field shown in Fig. 3.2.

3.2.2 Quench dynamics

We start by considering a standard protocol in quantum optics: the quantum quench. The idea is that initially the spin and the qubit are decoupled ($g = 0$), while the qubit is prepared in a superposition of the two bare atomic levels $|\mathrm{g}\rangle = \big[\,|\uparrow\rangle - |\downarrow\rangle\,\big]/\sqrt{2}$ and $|\mathrm{e}\rangle = \big[\,|\uparrow\rangle + |\downarrow\rangle\,\big]/\sqrt{2}$, and the bath is left in the vacuum:

$$|\Psi(t=0)\rangle = |\uparrow\rangle\,|0\rangle = \frac{|g\rangle + |e\rangle}{\sqrt{2}} \otimes |0\rangle\,. \tag{3.27}$$

Let us then assume that at $t = 0$ the coupling is switched on and that the system is left to evolve dynamically. The subsequent spin evolution as obtained using the MCS technique is shown in solid-red on Fig. 3.1, for two values of the coupling g. The result obtained from direct diagonalization (2.97) is given by the black-dashed line, showing very good agreement with our simulations in both cases. In the low coupling regime with $g = 0.1$, in the left panel, the spin is almost uncoupled from the bath, and is performing nearly free Purcell oscillations driven by the tunneling operator σ_x in the Hamiltonian. Note that in this regime, using only two coherent states in the MCS state vector is enough to obtain the correct spin dynamics.

At strong coupling with $g = 4$, in the right panel, the spin dynamics becomes much more complex, and requires at least $N_{\mathrm{cs}} = 8$ coherent states to reach convergence. Note some very peculiar features of the evolution: after initially decaying gradually, as in the low-coupling case, the spin tunnels back up to $|\uparrow\rangle$ for a short time at $t\Delta \simeq 1.3$ before it suddenly reaches a plateau [87]. To understand this behavior we need to consider the corresponding dynamics of the bath. We do so by calculating the Husimi Q functions of the bath $\mathrm{Q}_{|\uparrow\rangle}(\alpha)$ and $\mathrm{Q}_{|\downarrow\rangle}(\alpha)$ in the two spin sectors, which in the coherent state basis are given by the following concise expressions:

$$\mathrm{Q}_{|\uparrow\rangle}(\alpha) = \langle\alpha|\,\langle\uparrow|\Psi\rangle\,\langle\Psi|\uparrow\rangle\,|\alpha\rangle = \sum_{m,n} p_m^* p_n\,\langle\alpha|f_n\rangle\,\langle f_m|\alpha\rangle\,, \tag{3.28}$$

$$\mathrm{Q}_{|\downarrow\rangle}(\alpha) = \langle\alpha|\,\langle\downarrow|\Psi\rangle\,\langle\Psi|\downarrow\rangle\,|\alpha\rangle = \sum_{m,n} q_m^* q_n\,\langle\alpha|h_n\rangle\,\langle h_m|\alpha\rangle\,. \tag{3.29}$$

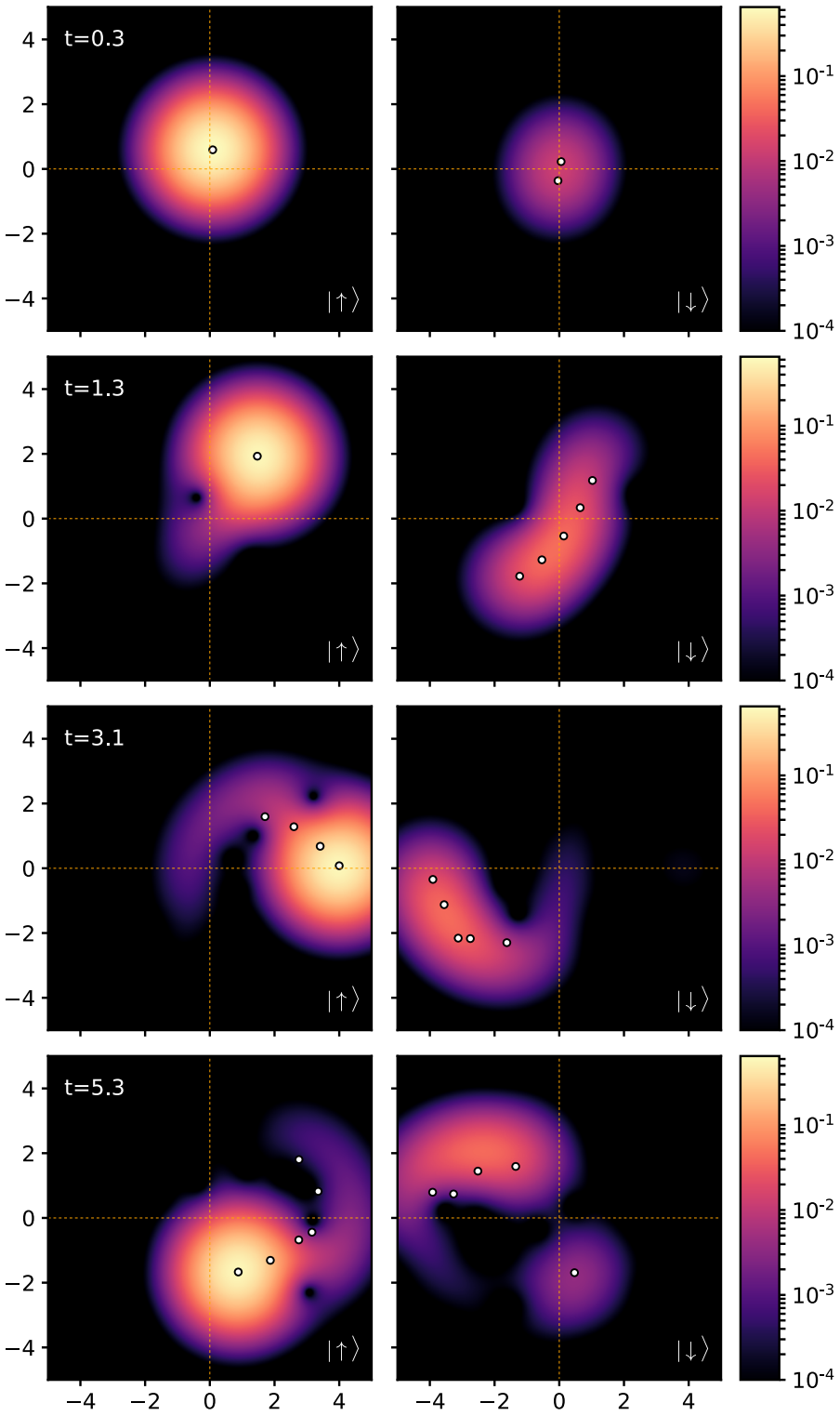

Figure 3.2: Husimi Q functions of the field state of the $|\uparrow\rangle$ sector (left panels) and of the $|\downarrow\rangle$ sector (right panels) at 4 different times of the quench dynamics for $g = 4, \Delta = 1.0$, and $\omega = 1.0$. The displacement of the coherent states $f_n(h_n)$ with weight $|p(n)| > 0.05$ ($|q(n)| > 0.05$) are indicated by white dots. Note in particular the trailing tail of the field excitation due to the σ_x tunneling of the coherent states together with their qubit states, as depicted in Fig. 3.3a.

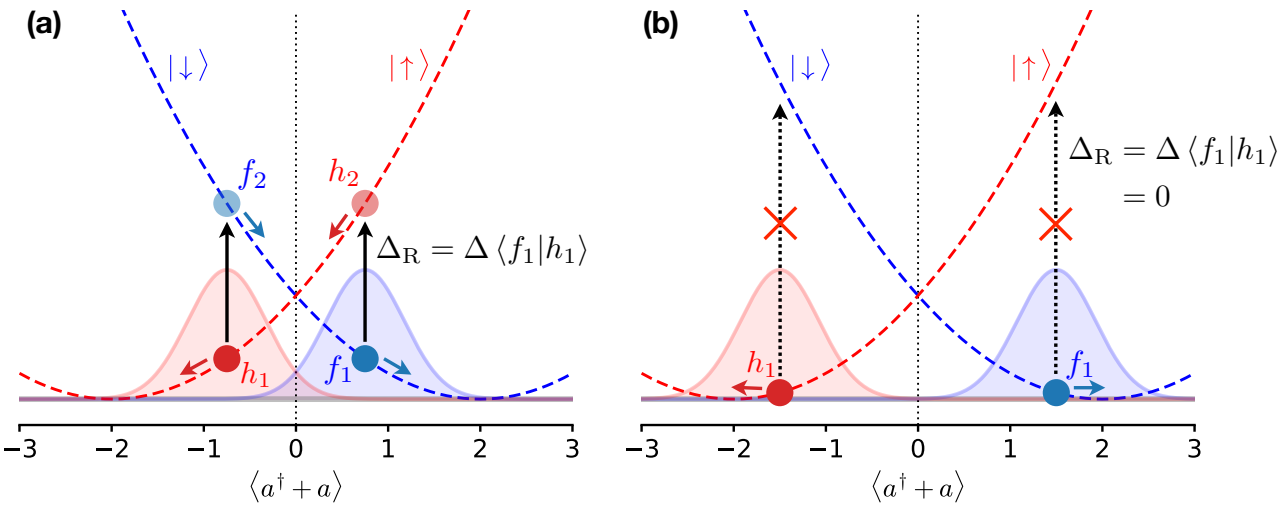

Figure 3.3: Illustration of the physics involved in the tunneling regime (until $\omega_c t \simeq 1.3$) and in the localized regime ($\omega_c t \simeq 3.1$) of the coherent state dynamics shown in Fig. 3.2. As indicated by Eq. (3.30), the renormalized tunneling rate is strongly dependent on the overlap between the different coherent states. If, as in panel (a), there is an overlap between the coherent states of the opposite sectors then tunneling is allowed from $|\uparrow\rangle$ to $|\downarrow\rangle$ at a rate Δ_R. Note that the coherent states of each sector tunnel via their spin states, in other words: $|\uparrow\rangle|f_1\rangle$ tunnels into $|\downarrow\rangle|h_2\rangle$. Similarly, $|\downarrow\rangle|h_1\rangle$ tunnels into $|\uparrow\rangle|f_2\rangle$. Because $|f_2\rangle$ and $|h_2\rangle$ end up in the opposite sector, they become subject to a strong force that reverses their momentum and directs them to the minimum of the new potential landscape. If on the other hand, as in panel (b), the overlap between the two coherent states is nearly zero, then the tunneling rate Δ_R is completely suppressed.

These functions are plotted in Fig. 3.2 at the four times indicated by the vertical dashed lines in Fig. 3.1b. White dots have also been added on top of the color plots to indicate the displacements of the coherent states with weight $|p_n| > 0.05$ ($|q_n| > 0.05$). The key to understanding the physics of this time-evolution, is to note that the tunneling rate is strongly dependent on the coherence $\langle\sigma_x\rangle$ between the two spin states, and therefore on the amount of overlap between the field states of the $\uparrow$ and $\downarrow$ sectors. To see this, consider the renormalized tunneling rate:

$$\Delta_R \equiv \Delta\,\langle\sigma_x\rangle = \Delta \sum_{m,n} p_n^* q_m\,\langle f_n|h_m\rangle + c.c., \tag{3.30}$$

which is the effective tunneling rate in the presence of non-vacuum field states. Clearly, as the overlap $\langle f_n|h_m\rangle \to 0$, tunneling is blocked, and it is maximum when $\langle f_n|h_m\rangle \to 1$.

Moving on to a detailed analysis, we note that at $\omega_c t = 0.3$, the Husimi functions of both sectors overlap almost completely, thus leading to maximum tunneling, consistent with the rapid $\langle\sigma_z\rangle$ decay in Fig. 3.1b. Later, at $\omega_c t = 1.3$, one can see that the fields have had time to precess for about $\frac{1}{6}$ of a period, and interestingly, both field states are developing a tail that extends all the way to the opposite sector (especially in the down sector). This happens because coherent states, which have already been displaced according to their spin orientation through the coupling term $\sigma_z(a + a^\dagger)$, tunnel together with their spin state, and thus end up in the opposite spin sector. Now located in the opposite sector, these coherent states are suddenly endowed with a very high potential energy that directs them towards the minimum of their new potential landscape. This process is depicted in a cartoon in Fig. 3.3a, where the spin-up coherent state f_1 tunnels to a spin-down coherent state h_2. This tunneled coherent state is what forms the peculiar tail in the Husimi function.

After half a period of precession, at $\omega_c t = 3.1$, the fields of the two sectors are now at their maximum displacement and have minimum overlap, hence preventing any tunneling from happening, as depicted in Fig. 3.3b. In other words $\langle\sigma_z\rangle$ becomes localized, which explains the plateau in Fig. 3.1b.

Finally, at $\omega_c t = 5.3$, as the field states are about to complete one period, the overlap between the two sectors is progressively recovered which allows the tunneling to resume. This is clearly demonstrated by the smear in the lower right quadrant of the $\downarrow$ field, which corresponds to coherent states that have tunneled from the lower-right quadrant of the $\uparrow$ field. This is also consistent with the beginning of the second phase of $\langle\sigma_z\rangle$ decay in Fig. 3.1b.

It is clear from this analysis of the Rabi model at strong coupling, that spin tunneling and coherent state tunneling from one sector to the other are heavily inter-dependent: coherent states can of course only tunnel via the spin tunneling, but spin tunneling can only occur provided that the field states of both sectors are overlapping.

3.2.3 Convergence and coherent state spawning

The convergence of the quench dynamics with the number of coherent states in the MCS ansatz (3.1) is extremely fast, as can be see in Fig. 3.4a: with only $N_{\text{cs}} = 8$ coherent states in the state vector, our algorithm is able to converge the $\langle\sigma_z\rangle$ trajectory for $g = 4$. That same trajectory required including all Fock states up to the 30-photon state $|n = 30\rangle$ (that is a 60-dimensional Hilbert space for the whole system), in order to converge the solution in Fock space using direct diagonalization. The MCS algorithm therefore provides a huge gain in terms of the number of degrees of freedom that one needs to keep track of. We can of course further increase the number of coherent states to decrease the error beyond the level at which the MCS solution simply "matches" the exact result. This is clear from the right panel of Fig. 3.4 which shows that by using 14 coherent states, we can further reduce the error obtained with 8 coherent states by about 3 orders of magnitude.

One can also check the field convergence by comparing the Husimi and Wigner functions [18] obtained with the two different approaches. The expression for the Wigner distribution for our ansatz is given in appendix C. In the left panels of Fig. 3.6 we plotted the two functions in log scale corresponding to the $|\uparrow\rangle$ sector at time $\omega_c t = 20$ of time-evolution, and in the right panels the same but obtained via direct diagonalization. They are clearly almost identical, and it is in fact quite remarkable how the right arrangement of a few simple coherent states is capable of describing the high complexity of this field state.

A subtle point of the MCS technique is that because the coherent state basis we are working in is over-complete, when different coherent states in the state vector overlap exactly, that is to say $f_n = f_m$ for some n and m, the matrix representing the linear system of equations (3.26) becomes non-solvable. For this reason, only one coherent state of the expansion (3.1) may be initialized in the vacuum state $|0\rangle$ at $t = 0$, and the other coherent states should be spawned in the vacuum at a later point of the dynamics. The weight of the new coherent states p_{new} and q_{new} cannot be zero, as this would also result in a singularity in the equations (3.26). However, as long as $p_{\text{new}} = q_{\text{new}} \simeq 0$, the vacuum values of f_{new} and h_{new} will only affect the state vector negligibly.

A spawning algorithm was first introduced by Martínez, BenNun and Levine [88, 89, 90], in the context of the frozen Gaussian method that we discussed in paragraph 3.1.5. Similarly to our technique, by generating Gaussian states at the right time of the dynamics, they were able to allow Gaussian-based classical trajectories to bifurcate into quantum superpositions of

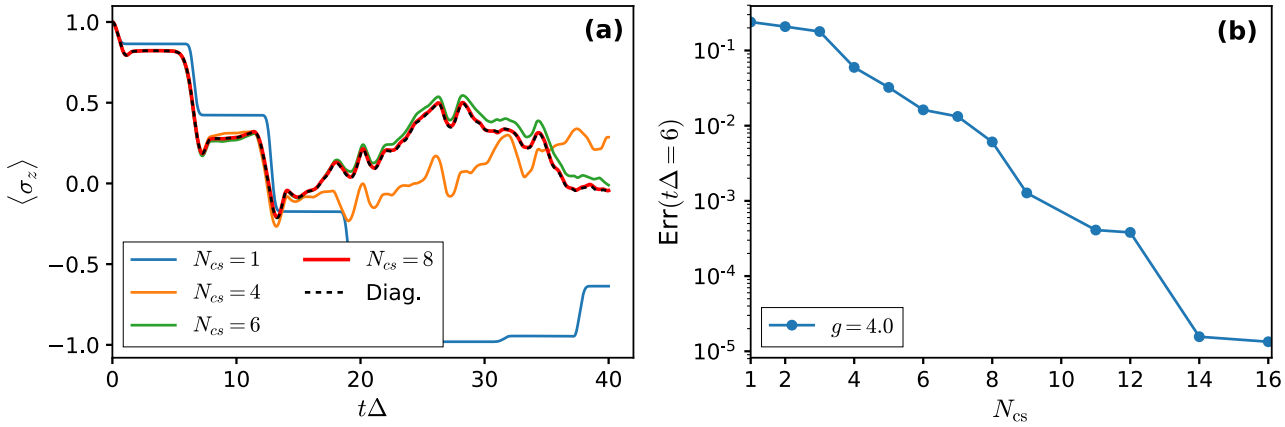

Figure 3.4: In the left panel we show the convergence of $\langle\sigma_z\rangle$ with the number of coherent states for $g = 4$ with up to $N_{cs} = 8$ coherent states in the MCS state vector. In the right panel we show the error $\mathrm{Err}(t\Delta = 6)$ at time $t = 6$ as a function of the number coherent states used in the state vector. The fast decrease of the error demonstrates the appropriateness of the coherent state basis for studying regimes of high coupling.

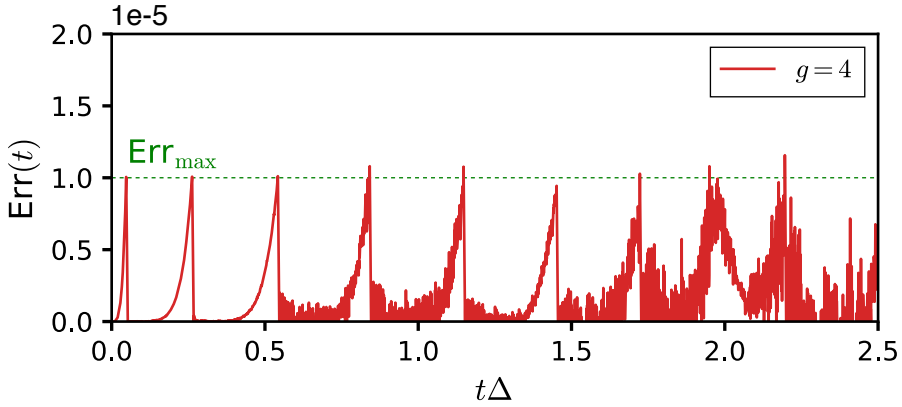

Figure 3.5: Evolution of error $\mathrm{Err}(t)$ with time during the addition of the first 8 coherent states. The threshold error at which an additional coherent is to be added in indicated by the green dashed line. The drop of the error to 0, signals that a coherent state was added.

classical trajectories. This "right time" at a which an additional coherent state should to be spawned depends on the specificities of the physical framework, and our solution for defining that time is in fact different from the one used for frozen Gaussians.

One simple way to time the spawning of coherent states would have been to wait a time δt for the initial (or previously spawned) coherent state to be pulled into the dynamics, so that it moves away from its zero displacement state, and then to add a new zero-displacement coherent state. This procedure would however not have taken into account the *rate* at which new coherent states are required in the dynamics. A better way is to use the error $\mathrm{Err}(t)$ defined in paragraph 3.1.4 and to trigger the addition of a coherent state whenever $\mathrm{Err}(t) > \mathrm{Err}_{\max}$, where $\mathrm{Err}_{\max}$ is an error threshold that we set. To illustrate this, the error versus time for the $g = 4$ regime is plotted in middle panel of Fig. 3.5, where one can see that as soon that $\mathrm{Err}(t) > \mathrm{Err}_{\max} = 10^{-5}$, $\mathrm{Err}(t)$ drops to 0, indicating that a coherent state was spawned. It is important to point out here that the error we defined is *instantaneous*, meaning that $\mathrm{Err}(t)$ does not account for the error accumulated since the beginning of the dynamics. This is why also the error returns to 0 as soon as a coherent state is added, because the coherent state

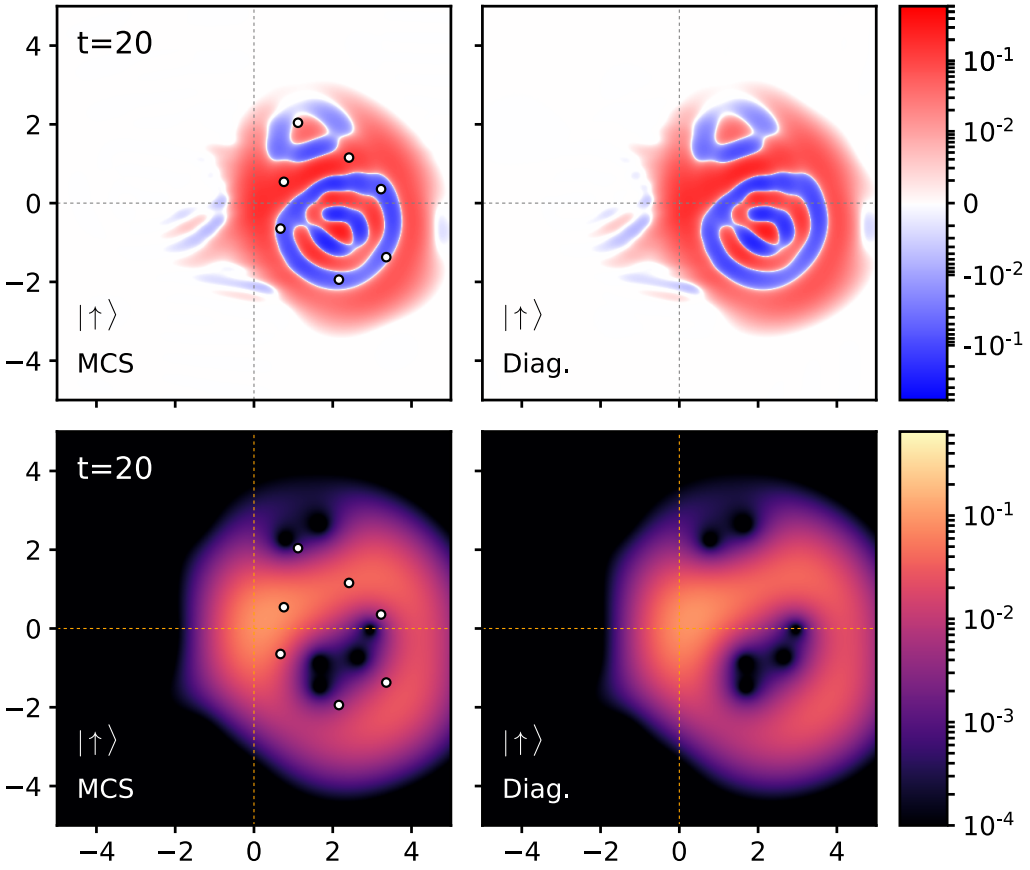

Figure 3.6: Comparison of the Wigner and Husimi functions at $\omega_c t = 20$ obtained using the MCS technique (left panels) and the one obtained using direct diagonalization in Fock space (right panels). The simulation parameters are the same as in Fig. 3.2. White dots indicate the center of the coherent states with weight $|p(n)|, |q(n)| > 0.05$.

provides the extra degree of freedom required by that precise instant of dynamics.

This procedure thus ensures that coherent states will be added only when required, and that the added coherent state does not end up on top of one another.

3.3 Qubit and bath dynamics in the spin-boson model

Having demonstrated the multi-coherent state technique on the Rabi model, we are now ready to tackle the full many-mode spin-boson model that we introduced in paragraph 2.4.2:

$$H = \frac{\Delta}{2}\sigma_x - \frac{\sigma_z}{2}\sum_{k>0} g_k(a_k \ + a_k^\dagger) + \sum_{k>0}\omega_k a_k^\dagger a_k \ , \tag{3.31}$$

We will first study the dynamics of the qubit following its preparation in the $|\uparrow\rangle$ state and characterize the time scales at play as we go from the onset of the ultra-strong coupling regime ($\alpha \simeq 0.1$) to the deep ultra-strong coupling regime ($\alpha \simeq 1.0$). We will then move on to characterize the light emitted by spontaneous emission upon preparing the qubit in the excited state. Using the Wigner function, we will see that the emission happens in the form of a Schrödinger cat state of light, which however is not fully coherent, due to the slow decoherence time scale T_2 in the ultra-strong coupling regime.

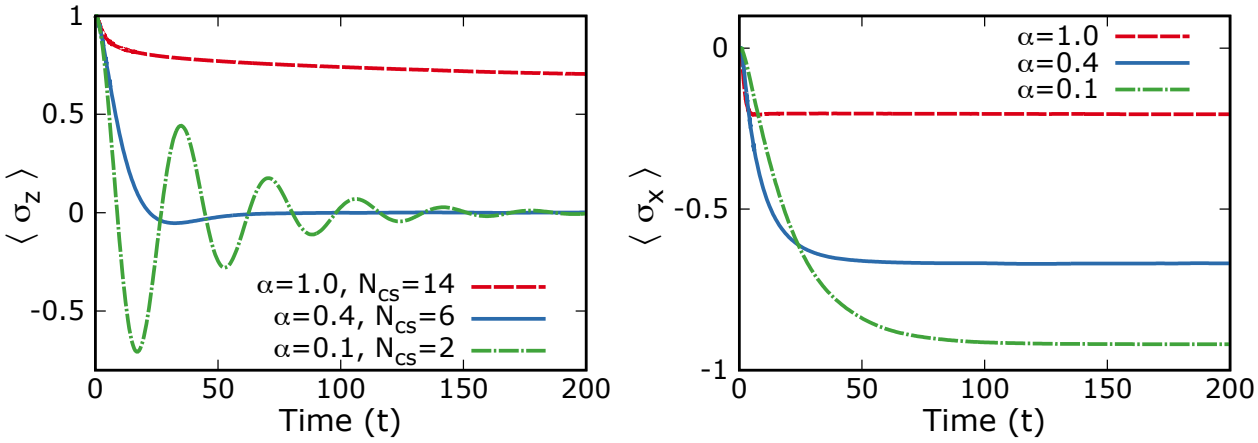

Figure 3.7: (Color online) Left panel: decoherence process $\langle\sigma_z(t)\rangle$ with typical decay time T_2, for increasing dimensionless coupling $\alpha = 0.1, 0.4, 1.0$ (with coherent state number $N_{\rm cs} = 2, 6, 14$, as required to reach convergence in the respective regimes). In all computations, $\Delta/\omega_{\rm p} = 0.2$ and $N_{\rm modes} = 800$. Right panel: energy relaxation process $\langle\sigma_x(t)\rangle$ with typical decay time T_1, for the same parameters. For $\alpha \ll 1$, decoherence and relaxation times fulfill the usual relation $T_2 = 2T_1$, but for $\alpha = 1.0$ the two time scales are widely different, with $T_2 \gg T_1$.

3.3.1 Quench dynamics and relaxation time scales

We consider first the important issue of the time scales governing the qubit dynamics in the ultra-strong coupling regime. For this purpose, we prepare the initial state in the same way as we did for the Rabi model with the qubit in a superposition of the two bare atomic levels, and with the bath modes in the vacuum:

$$|\Psi(t=0)\rangle = |0\rangle \otimes |\uparrow\rangle = |0\rangle \otimes \frac{|g\rangle + |e\rangle}{\sqrt{2}}. \tag{3.32}$$

An important point is that, unlike the Rabi model we studied in the previous section, here the system has a finite length $L = 1/\delta k$, where δk is the smallest wave-vector of the system. It follows that within this finite size, our system is effectively an open system, in which the qubit is allowed to relax to the ground state by releasing its extra energy outwards in the waveguide. Since the qubit energy gap is described by the σ_x operator in Eq. (3.31) (as opposed to standard quantum optics), one expects relaxation to happen over a time T_1 for the longitudinal term $\langle\sigma_x(t)\rangle$, and over a time T_2 for the transverse spin component $\langle\sigma_z(t)\rangle$ as it precesses and decays to 0. This standard behavior is well obeyed in the weak-coupling regime $\alpha \ll 1$, with $T_2 = 2T_1$, as seen from the dot-dashed green curve in the two panels of Fig. 3.7. For the intermediate value $\alpha = 0.4$ (full blue curve), precession of $\langle\sigma_z(t)\rangle$ is nearly over-damped, as is well established [26].

Remarkably, the ultra-strong coupling regime $\alpha = 1.0$ (dashed red curve) shows a striking decoupling between the decoherence time T_2 and the energy relaxation time T_1, with $T_2 \gg T_1$. The underlying physics can be anticipated: rapid decoherence is prohibited because the atom is dressed by its electromagnetic environment [27] on a large spatial scale

$$L_K = (\omega_{\rm p}/\Delta)^{\alpha/(\alpha_c-\alpha)} \tag{3.33}$$

(here $\alpha_c = 1 + \Delta/\omega_{\rm p}$, corresponding to the threshold of full localization). Decoherence thus takes a considerable time $T_2 \simeq L_K$ for the complete relaxation of all quantum correlations between the dressed atom and the radiated field. This effect is seen by the very slow decay of

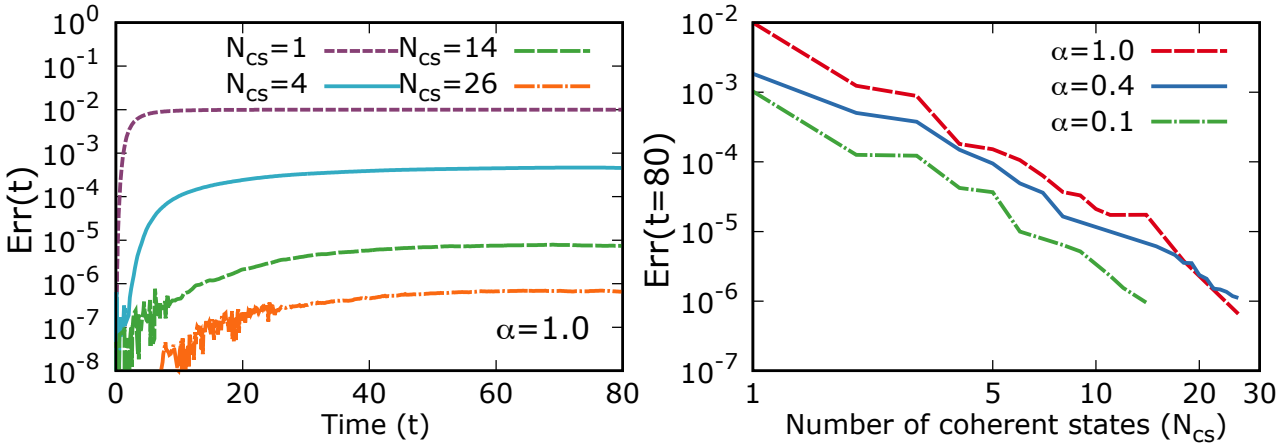

Figure 3.8: (color online) Left panel: error $\mathrm{Err}(t)$ as a function of time with respect to the exact Schrödinger dynamics for the challenging case $\alpha = 1.0$ (here the atomic splitting is $\Delta/\omega_c = 0.2$), which drops rapidly to zero with increasing N_{cs}. Right panel: error $\mathrm{Err}(t = T)$ at a fixed time $T = 80$, as a function of the number of coherent states for $\alpha = 0.1$, $\alpha = 0.4$ (intermediate ultra-strong coupling regime) and $\alpha = 1.0$ (deep ultra-strong coupling regime), showing a scaling $[N_{\mathrm{cs}}]^{-2}$.

$\langle\sigma_z(t)\rangle$ (dashed red curve in the left panel of Fig. 3.7). Indeed, for $\alpha = 1.0$ and $\Delta/\omega_{\mathrm{p}} = 0.2$, $T_2 \simeq 3000$, which was not reached at the final time of our simulations. It is worth noting, that this slow decoherence is in essence the same as the one that led to the temporary freezing of the decay of $\langle\sigma_z(t)\rangle$ in Fig. 3.1(b) in the case of the Rabi model: the entanglement between the spin and its cloud drastically reduces the spin coherence that was allowing the spin to decay. As we will see in the following, this damping of the qubit decay by the cloud is key to understanding the physics at play, due to its strong impact on the structure of the emitted light.

Similarly to how we proceeded with the Rabi model in the previous section, we can study the convergence of our solution by using the error $\mathrm{Err}(t)$ defined in Eq. (3.23). Clearly, the error is already small at all times for a single coherent state $N_{\mathrm{cs}} = 1$, and goes quickly to zero as number of terms in the decomposition Eq. (3.1) increases. The precise scaling of the algorithm with N_{cs} is demonstrated in the right panel of Fig. 3.8. We find that the error (here computed at a fixed time $T = 80$) decreases typically with an inverse square power $[N_{\mathrm{cs}}]^{-2}$, independently of the coupling strength α. This shows that our methodology is based on a physically well-motivated decomposition of the state vector, and is not tied to a particular regime of the spin-boson model. The coherent state expansion of the time-dependent state vector (3.1) thus provides numerically accurate results in all regimes of coupling for a small computational effort.

3.3.2 Quantum states of spontaneous emission

We turn to the emission protocol, taking now the bare excited level of the atom

$$|\Psi(t=0)\rangle = |0\rangle \otimes \frac{|\uparrow\rangle + |\downarrow\rangle}{2} = |0\rangle \otimes |e\rangle\,, \tag{3.34}$$

as the initial state. According to Wigner-Weisskopf theory [34] valid at weak coupling $\alpha \ll 1$, one expects spontaneous emission of a single photon and decay of the atom towards its bare ground state. Although our theory (3.1) is based on coherent states and not Fock excitations, we can show that it does recover the standard quantum optics results at $\alpha \to 0$, while providing

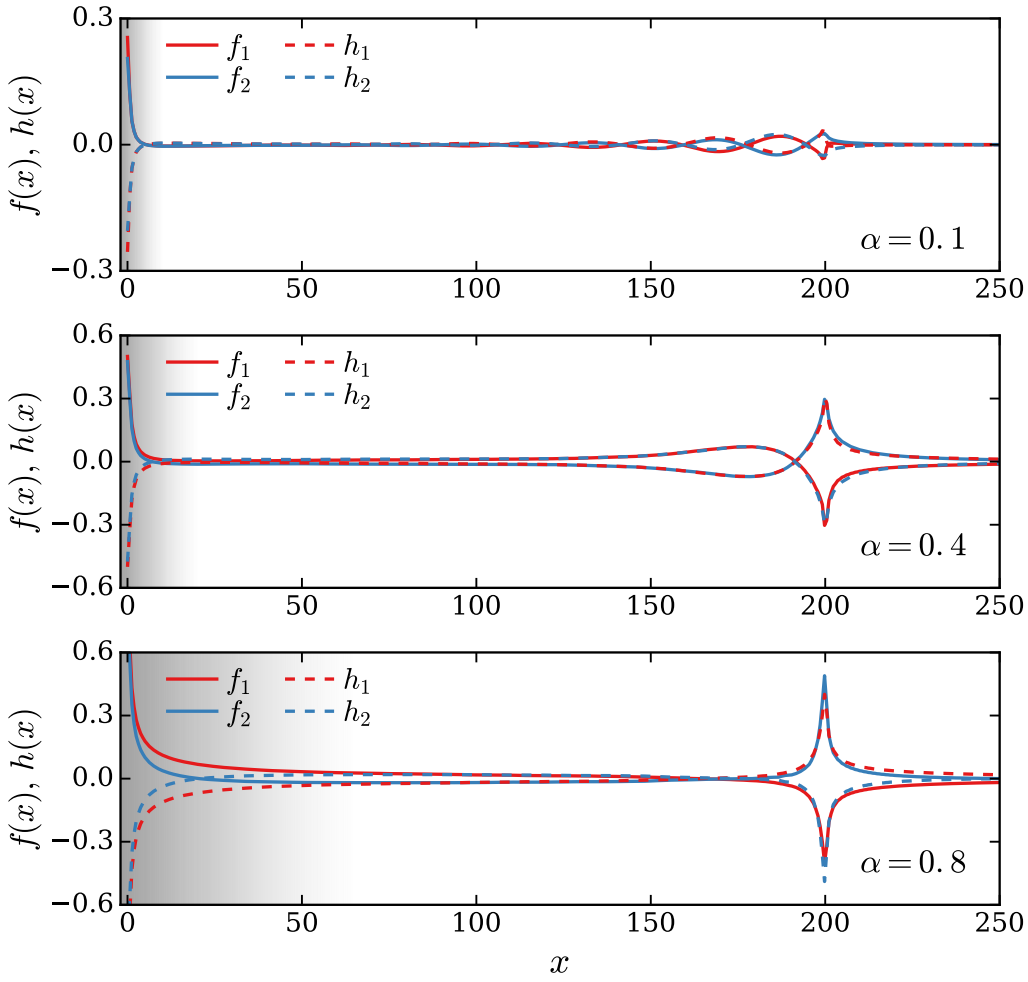

Figure 3.9: (Color online) Real part of the coherent state amplitudes in real space $f_m(x,T)$ and $h_m(x,T)$ (for $m=1,2$) at a time $T=200$ long enough that the emitted wavepacket is uncorrelated from the entanglement cloud associated to the dressed atomic ground state (denoted as a shaded area). Here $\Delta/\omega_{\rm p}=0.2$, and $N_{\rm cs}=2$, with $\alpha=0.1$ (top panel), $\alpha=0.4$ (middle panel), and $\alpha=0.8$ (bottom panel).

a simple physical picture in the ultra-strong coupling regime. For this purpose, we plot in Fig. 3.9 the real part of the coherent state amplitudes $f_m(x,T)$ and $h_m(x,T)$ (of the first two coherent states $m=1,2$) as a function of the spatial separation x along the waveguide (the atom is located at $x=0$). Here we choose a time $T\gg T_2\simeq L_K$ long enough that the system has had time to fully relax to its dressed ground state. The emitted wavepacket is clearly seen at a distance $x\simeq T$, due to ballistic propagation of the wavefront, and the displacements weights satisfy the following relations:

$$\begin{aligned} &f_1(x,t)\simeq -f_2(x,t)\simeq -h_1(x,t)\simeq h_2(x,t)\equiv f_{\rm wp}(x-t),\\ &p_1=-p_2=q_1=-q_2\equiv p. \end{aligned} \tag{3.35}$$

Within the spatial region $x<L_K$, where the atom is dressed by its static surrounding cloud, a different set of relations is observed:

$$\begin{aligned} &f_1(x,t)\simeq f_2(x,t)\simeq -h_1(x,t)\simeq -h_2(x,t)\equiv f_{\rm cl}(x),\\ &p_1=-p_2=q_1=-q_2\equiv p \quad \text{(amplitudes are the same as above)}. \end{aligned} \tag{3.36}$$

Using these relations we can then separate spatially the coherent states into their cloud and wave-packet components, which gives:

$$\begin{aligned}
|f_1\rangle &= |f_{\rm cl}\rangle \otimes |f_{\rm wp}\rangle \\
|f_2\rangle &= |f_{\rm cl}\rangle \otimes |-f_{\rm wp}\rangle \\
|h_1\rangle &= |-f_{\rm cl}\rangle \otimes |-f_{\rm wp}\rangle \\
|h_2\rangle &= |-f_{\rm cl}\rangle \otimes |f_{\rm wp}\rangle .
\end{aligned} \tag{3.37}$$

These four relations can then be used to simplify the MCS state vector (3.1) for $N_{\rm cs} = 2$:

$$\begin{aligned}
|\Psi(T)\rangle &\simeq \Big[p_1|f_1\rangle + p_2|f_2\rangle\Big]|\uparrow\rangle + \Big[q_1|h_1\rangle + q_2|h_2\rangle\Big]|\downarrow\rangle \\
&\simeq \Big[p|f_{\rm cl}\rangle|f_{\rm wp}\rangle - p|f_{\rm cl}\rangle|-f_{\rm wp}\rangle\Big]|\uparrow\rangle + \Big[p|-f_{\rm cl}\rangle|-f_{\rm wp}\rangle - p|-f_{\rm cl}\rangle|f_{\rm wp}\rangle\Big]|\downarrow\rangle \\
&\simeq \Big[|f_{\rm cl}\rangle|\uparrow\rangle - |-f_{\rm cl}\rangle|\downarrow\rangle\Big] \otimes p\Big[|f_{\rm wp}\rangle - |-f_{\rm wp}\rangle\Big].
\end{aligned} \tag{3.38}$$

The last line in (3.38) is straightforwardly interpreted as the absence of correlations between the dressed qubit

$$|\Psi_{\rm cl}\rangle \equiv \Big[|f_{\rm cl}\rangle|\uparrow\rangle - |-f_{\rm cl}\rangle|\downarrow\rangle\Big]/\sqrt{2}, \tag{3.39}$$

and the emitted wavepacket

$$|\Psi_{\rm wp}\rangle \equiv \sqrt{2}p\Big[|f_{\rm wp}\rangle - |-f_{\rm wp}\rangle\Big]. \tag{3.40}$$

This is physically expected as the system relaxes at long times to a unique dressed ground state, while emitting a stream of electromagnetic radiation carrying the excess energy but no quantum correlations with the atom. We stress that the above expressions for $|\Psi_{\rm cl}\rangle$ (3.39) and $|\Psi_{\rm wp}\rangle$ (3.40) are only approximate, as quantum corrections arise at increasing α [69, 70] that are accounted for by other coherent states in the MCS state vector (3.1).

The approximate state vector (3.38) nicely recovers the result of Wigner-Weisskopf theory in the quantum optics regime $\alpha \to 0$. Indeed, in this case the displacements $f_{\rm cl}(x)$ in the dressing cloud $|\Psi_{\rm cl}\rangle$ are vanishingly small, and thus

$$|\Psi_{\rm cl}\rangle = |0\rangle\big[|\uparrow\rangle - |\downarrow\rangle\big]/\sqrt{2} \equiv |0\rangle|g\rangle, \tag{3.41}$$

so that the atom has correctly relaxed to its bare ground state. The quantum state describing the emitted light also simplifies, since the displacements $f_{\rm wp}(x)$ in the wavepacket $|\Psi_{\rm wp}\rangle$ are also small. A first-order Taylor expansion of the coherent states in (3.40) gives

$$\begin{aligned}
|\Psi_{\rm wp}\rangle &= \sqrt{2}p\Big[|f_{\rm wp}\rangle - |-f_{\rm wp}\rangle\Big] \\
&= \sqrt{2}p\Big[e^{\sum_k f^k_{\rm wp}a^\dagger_k - f^{k*}_{\rm wp}a_k} - e^{\sum_k -f^k_{\rm wp}a^\dagger_k + f^{k*}_{\rm wp}a_k}\Big]|0\rangle \\
&\simeq \sqrt{2}p\Big[1 + \Big(\sum_k f^k_{\rm wp}a^\dagger_k - f^{k*}_{\rm wp}a_k\Big) - 1 - \Big(\sum_k -f^k_{\rm wp}a^\dagger_k + f^{k*}_{\rm wp}a_k\Big)\Big]|0\rangle \\
&\simeq 2\sqrt{2}p\sum_k f^k_{\rm wp}a^\dagger_k|0\rangle,
\end{aligned} \tag{3.42}$$

which is the expected one-photon Fock state. The monochromatic nature of the emitted light can be seen from the spatiotemporal oscillations of the fields in the upper panel of Fig. 3.9, with

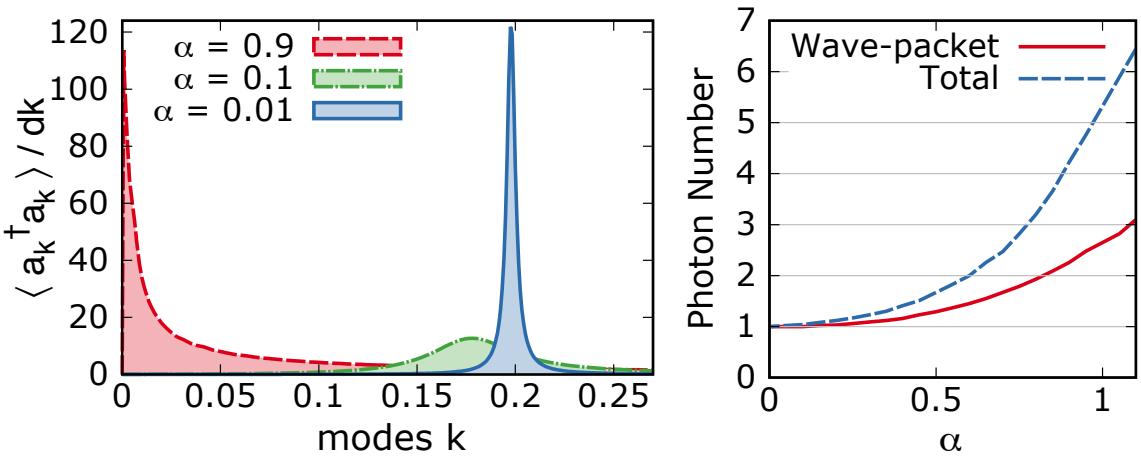

Figure 3.10: (Color online) Left: photon number density $\langle a_k^\dagger a_k \rangle / dk$ as a function of mode number k, for $\alpha = 0.01, 0.1, 0.9$, with $\Delta/\omega_p = 0.2$. Right: photon number in the wavepacket (solid line) and in the total wave-function (dashed line).

an envelope controlled by the underdamped dynamics of the qubit (left panel of Fig. 3.7 for $\alpha = 0.1$). Moving towards the ultra-strong coupling regime for increasing α values (middle and lower panel in Fig. 3.9), two major changes occur. First, the displacements in the entanglement cloud $x < L_K$ penetrate deeper and deeper within the waveguide, due to the increase of the screening length L_K with α, as shown by the shaded area in Fig. 3.9. Second, the emitted wavepacket becomes very localized temporally, with associated displacements that clearly grow in magnitude.

We can further analyze the emitted wave-packets by studying the spectrum of the radiation, which we show in the left panel of Fig. 3.10. In the quantum optics regime $\alpha = 0.01$, the line-shape is a narrow Lorentzian centered at the bare transition frequency Δ, which confirms the monochromatic nature of the photon we pointed out in the previous paragraph. For increasing α, the peak is shifted to lower frequencies due to the dressing of the atom by the bosonic bath. But more remarkably, its line-shape becomes spectrally broad, which indicates the presence of a large number of photons in the emitted wave-packet. This observation is confirmed by the integrated number of photons in the wavepacket, shown in solid red in the right panel of Fig. 3.10: as expected, the number of emitted quanta at very low coupling is exactly $n_{\rm wp} = 1$, it then increases steadily to reach $n_{\rm wp} \simeq 3$ photons at $\alpha = 1$. On the same plot, the dashed blue curve shows the total number of photons in the system, that combines the $\bar{n}_{\rm cl}$ photons in the cloud and the $n_{\rm wp}$ in the wave-packet. The total of 6 photons reached at $\alpha = 1$ highlights the complexity of the quantum problem at play, involving more than $1000^{\bar{n}_{\rm tot}} \simeq 10^{18}$ quantum states.

These coherent state spatial profiles and the photon spectra certainly give us detailed information concerning the photon and frequency content of the radiation, but what about the profile of the quadratures of the field themselves? Indeed, due to the over-completeness of the coherent state basis, it is very hard to get an intuitive idea of the field quadrature profile, as the overlaps between the different coherent states shown in Fig. 3.9 carry as much physical meaning as the coherent states individually. In the next paragraph, we therefore turn to a detail study of the field quadratures to gain more insight regarding the quantum nature of emitted radiation.

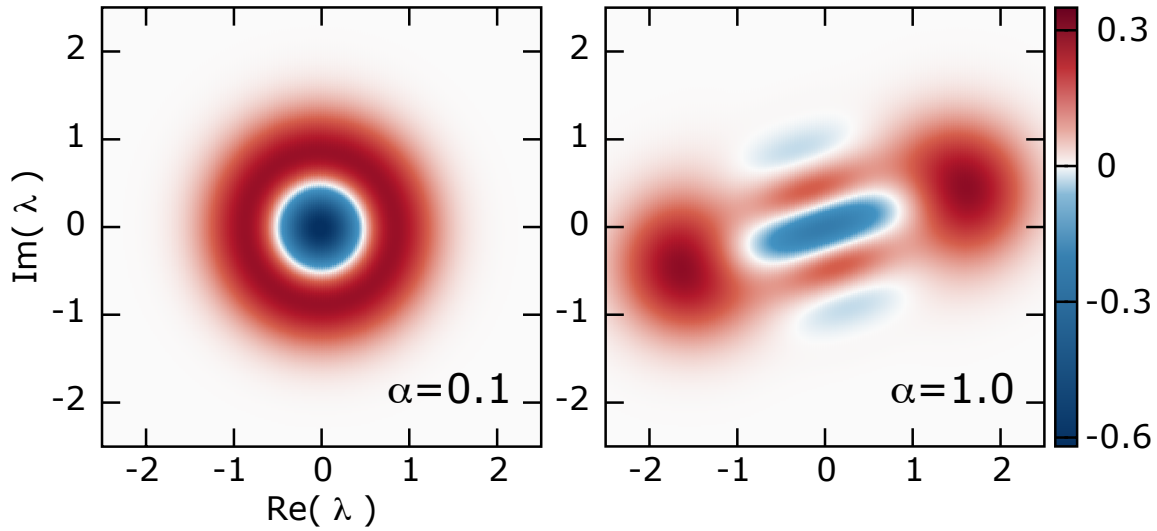

Figure 3.11: Wigner distribution $W(\lambda)$ at $t = 900$ identifying a one-photon state at $\alpha = 0.1$ (left panel) and a partially coherent cat state at $\alpha = 1$ (right panel) with two positive classical lobes and a negative region with reduced amplitude compared to $-2/\pi$ for a fully coherent cat. The function was computed with $N_{\rm cs} = 14$ and $N_{\rm modes} = 1800$.

3.3.3 Nature of the spontaneously emitted cats

Let us consider again the approximate expression of the emitted wavepacket we gave in Eq. (3.40):

$$|\Psi_{\rm wp}\rangle = \sqrt{2}p\Big[|f_{\rm wp}\rangle - |-f_{\rm wp}\rangle\Big]. \tag{3.43}$$

As we saw in Eq. (3.42), when $\alpha \to 0$, this expression becomes the 1-photon Fock state. As the displacements grow large however, as can be seen for $\alpha = 0.8$ in the lower panel in Fig. 3.9, this state clearly turns into an odd parity Schrödinger cat state of the field.

In order to check this idea on the converged state vector at $\alpha = 1.0$, which includes $N_{\rm cs} = 14$ coherent states, we computed the Wigner distribution. In contrast to photons released into a cavity [91, 18], we stress again that the radiation is not purely monochromatic, due to the significant damping effect on the atom caused by the strong coupling to the waveguide. Accordingly, following standard practice [10], one uses an optimized temporal filter $w(t)$ of the output signal to define an effective creation operator

$$b^\dagger = \sum_x w(x)a^\dagger(x)\Theta(x - L_K), \tag{3.44}$$

in which a Θ-function is used to filter out the static bound component of the screening cloud. The Wigner distribution [18] is then computed using the standard expression

$$W(\lambda) = \frac{1}{\pi^2}\int {\rm d}^2\beta\ C_s(\beta)e^{\lambda\beta^* - \lambda^*\beta}, \tag{3.45}$$

with the symmetrized correlation function $C_s(\beta) = \big\langle\Psi|e^{\beta b^\dagger - \beta^* b}|\Psi\big\rangle$. The full expression is given in appendix C. For $\alpha = 0.1$, the phase space distribution in the left panel of Fig. 3.11 shows the characteristic circular form of the $n = 1$ Fock state with negative quasi-probability $-2/\pi$ at the origin.

At ultra-strong coupling for $\alpha = 1.0$, the emitted radiation undergoes radical changes, as shown in the right panel of Fig. 3.11. The Wigner distribution now presents two positive lobes (signature of the two classical configurations of the cat), but also a negative region near the origin, fingerprint of the characteristic quantum interference, or "whiskers", of a Schrödinger cat. The strongly displaced lobes are consistent with the large number of photons accumulated in the wave-packet at $\alpha = 1$, as we saw in the previous paragraph. Surprisingly, the maximum negative amplitude does not reach the expected value $-2/\pi$ of a perfectly coherent cat, although our system does not present any extrinsic source of decoherence for the optical modes (such as leaks into a 3D continuum). We argue that the physical source of decoherence is the dressed qubit itself, which can be understood from the qubit dynamics shown in Fig. 3.7, in relation to the separation of time scales $T_2 \gg T_1$. Indeed, the cat state is emitted on a short scale $T_1 \simeq 1/\omega_p$ in the ultra-strong coupling regime, due to the sudden release of energy. But the atom maintains its coherence on a longer time scale T_2, due to the entanglement between the spin states and the cloud that prevents $\langle \sigma_z(t) \rangle$ from decaying. From the no-cloning theorem [34], the quantum information stored in the dressed atom state cannot be fully transferred to the wavepacket for times $t \ll T_2$, and thus the coherence of the emitted cat state is only partial at intermediate timescales.

In this chapter, we have thus demonstrated the power of a variational method, dubbed the MCS technique, that harnesses coherent states to describe the complex dynamics between a qubit and a waveguide in the ultra-strong coupling regime. In particular, we have shown here that we are able to describe accurately the process of spontaneous emission in a waveguide by using a very small number of coherent states ($N_{cs} \simeq 10$), as opposed to an unmanageably large number of states that we would have needed to consider in order the solve the problem in the number state basis. A key to the success of this technique is the adaptability of the coherent state basis, which allows the coherent state displacements to evolve in time, and therefore to span different parts of the Hilbert space at different moments of the dynamics. It should be noted, however, that the protocol presented to create the Schrödinger cat states of light is very difficult to implement experimentally, and it is therefore unlikely that the phenomenon we predict will be observed in the near future. In the next chapter on the other hand, we will be looking at the more common and accessible protocol, namely the scattering of coherent states on a qubit, which will allow us to probe the physics of the ultra-strong coupling regime in greater detail.

Chapter 4

Particle Production in Ultra-Strongly Coupled Waveguides

In waveguide QED, many-body effects are expected to occur at ultra-strong coupling that have no counterpart in standard quantum optics. An example is the spontaneous emission of cat states that we demonstrated in the previous chapter, which involves the emission of many light quanta over a large range of frequencies. There are many other examples of theoretical predictions of phenomena taking place at ultra-strong coupling including giant Lamb shifts [26, 64, 92, 69, 93], single-photon down-conversion [29, 94], non-RWA transmission line-shapes [64, 75, 95], and multi-mode entanglement [70, 27, 96]. The origin of all these phenomena is rooted in the non-conservation of quanta occurring when the waveguide-qubit coupling energy becomes of the same order as that of the qubit level spacing. It is therefore worthwhile that we focus directly on physical measures of this non-conservation.

In this chapter, we will investigate particle production by analyzing the scattered output of coherent wave-packets impinging on a qubit, the most common experimental protocol. The scenario we consider is shown in Fig. 4.1, where a right-going coherent state pulse is injected into a waveguide to which a qubit is side-coupled in the centre. We consider that the waveguide-qubit system is initially in its ground state, meaning that the qubit is dressed by a cloud of waveguide photons [27]. The scattering of the coherent state on this dressed qubit then results in an outgoing transmitted pulse and a reflected pulse, that have acquired on general grounds a many-body character [97].

After an overview of the state-of-the-art RWA solutions for this problem, we will first develop a general many-body wavefunction approach for the study of inelastic photon emission by a single two-level system. Detailed inelastic emission spectra will then be presented, in connection with the relevant physical processes. Following this, we will provide a comparison of our results to standard results in quantum optics based on the RWA. Finally, we will close the discussion by analyzing the temporal correlations of the emitted light, which will reveal several qualitative features of the ultra-strong interaction.

4.1 Coherent state scattering within the RWA

Before making use of the multi-coherent state (MCS) technique that has proven very effective in tackling spontaneous emission in the previous chapter, let us begin by making a simple assessment of the non-linear processes that can be readily described by the rotating-wave approximation (RWA). This will allow the reader to get familiar with a simpler version of the problem and to understand the necessity of going beyond the RWA. As illustrated in Fig. 4.1(b),

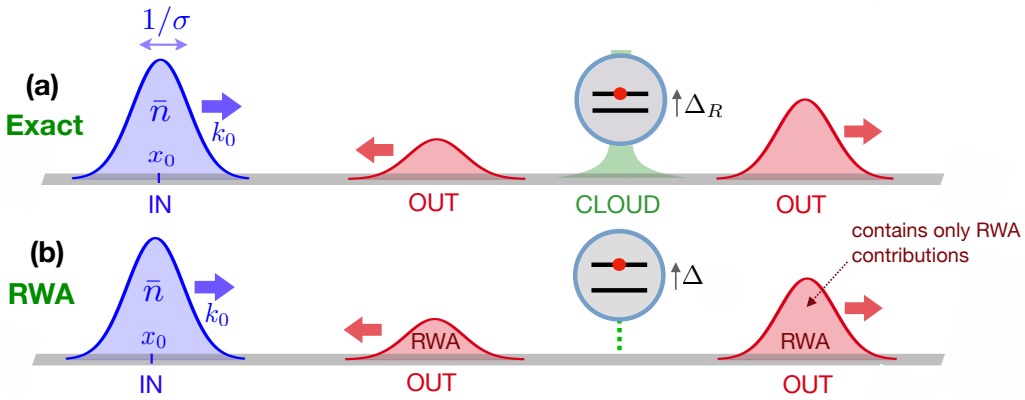

Figure 4.1: Illustration of the setup considered in this chapter: a long transmission waveguide (grey horizontal line) is side-coupled to a two-level system, allowing the measurement of multi-photon scattering matrices in a typical two-terminal geometry from the reflection and transmission (in red) of a coherent state Gaussian wavepacket (in blue). (a) Complete problem, where non-RWA terms cause the interaction with the qubit to spread within the wave-guide, leading to the presence of a many-body polarization cloud tied to the qubit (in green) [27], which in turn renormalizes the qubit resonance Δ to Δ_R . (b) RWA approximation: point-like interaction and no qubit renormalisation. The contents of the outgoing wave-packets is limited to RWA contributions.

dropping the counter-rotative terms simplifies the problem by removing the qubit polarization cloud and the renormalisation of the qubit energy altogether (when the RWA is performed using an approximate point contact interaction [98]). In addition, scattering of Fock states can be described within a smaller subspace of number-conserving states [15], which is easier to handle theoretically. However, the fact that the RWA misses out on the qubit renormalisation requires to set "manually" the qubit frequency to be the renormalized frequency Δ_R (found numerically with the full MCS calculation), if one is to obtain any quantitative result within the RWA. The complete RWA calculation on which the following results are based is beyond the scope of this discussion. For a detailed derivation using the input-output formalism, the reader may refer to appendix D.

In the left panels of Fig. 4.2, we show the scattered radiation spectrum for an incoming off-resonant beam with $k_0 = 0.16 \simeq 2\Delta_R$. In these simulations, the renormalized qubit energy was taken to be $\Delta = \Delta_R = 0.083\omega_c$, while the wavepacket was given a mean photon number $\bar{n} = 0.5$ and a linewidth $\sigma = 0.005\omega_c$. Note that although the incoming beam is far detuned from resonance, a small fraction of the signal is still reflected due to the high coupling ($\alpha = 0.1$). More interesting however, is the conversion of the incoming frequency k_0 to two lateral frequencies, located at $k = \Delta_R$ and $k = 2k_0 - \Delta_R$. Having in mind that we are only considering the rotating terms, the physics here is clear: a 2-photon process is occurring which redistributes the energy of two photons incoming at k_0 into a spontaneously emitted photon at Δ_R and another at energy $2k_0 - \Delta_R$. As shown in Fig. 4.3, this is clearly an RWA process, as its vertices only involve the quanta-conserving processes.

If we now consider an on-resonant drive with $k_0 = \Delta_R$, as shown in the right panels, the major part of the beam is reflected, but an important part of the signal is still transmitted due (in part) to a significant fraction of $N > 1$ Fock states in the incoming state (the RWA cannot reflect 2 photons at once). The inelastic contribution to the spectrum can also be seen in the on-resonant case (Fig. 4.2b), as shown in the bottom panel by the long tails that extend beyond the width on the incoming wave-packet, and that account for up to 10% of the transmitted signal. These tails can be explained by the same 2-photon process (Fig. 4.3): this time the

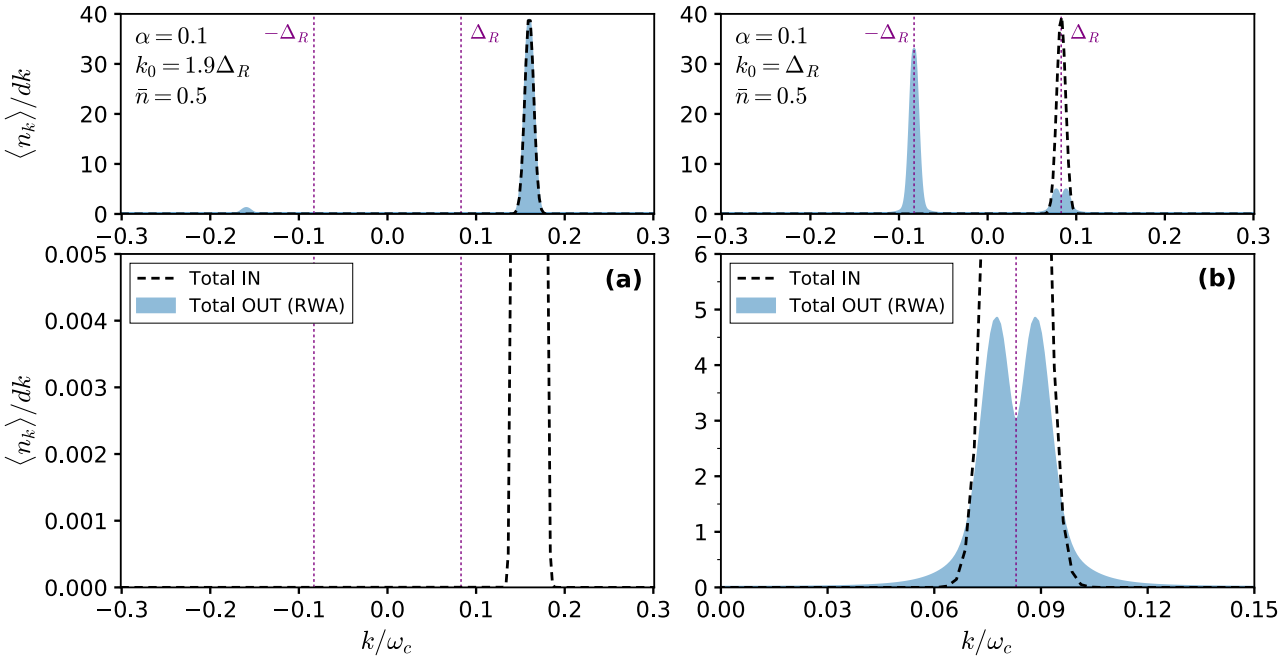

Figure 4.2: Mean density of photons at momentum k in the outgoing left/right wavepackets (in blue) within the RWA approximation. The parameters for this simulations are the qubit energy $\Delta_R = 0.1\omega_c$, the coupling $\alpha = 0.1$, the mean photon number $\bar{n} = 0.5$ and bandwidth $\sigma = 0.005\omega_c$. Left panels: off-resonant drive with momentum $k_0 \simeq 1.9\Delta_R$, leading to inelastic bands at $k = \Delta_R$ and $k = 2k_0 - \Delta_R$. Right panels: on-resonant drive with $k_0 = \Delta_R$. The inelastic RWA process (shown below) gives rise to wings reaching beyond the width of the incoming wave-packets.

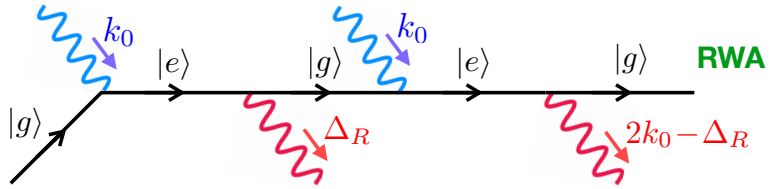

Figure 4.3: Diagrammatic representation of an RWA frequency converting 2-photon process.

qubit is absorbing two on-resonant photons at $k_0 = \Delta_R$ and reemitting two photons laterally within the extent of its linewidth at $\Delta_R + \delta k$ and $\Delta_R - \delta k$.

It is common knowledge that the RWA becomes exact as $\alpha \to 0$, but how well does it actually fare in this finite α regime, already at the onset of the ultra-strong coupling? Indeed, in the ultra-strong coupling regime, where the linewidth of the qubit energy becomes of the order of its energy splitting, one expects many-photon processes to become increasingly likely, which includes particle non-conserving processes. In fact, an off-resonant photon-producing process which "splits" a single incoming photon into three lower energy ones, was recently discovered by Goldstein *et al.* using perturbation theory [29], and is predicted to lead to a broad low-energy continuum in the scattered spectrum (see Fig. 1.6, and the related discussion in section 1.3). Clearly, this splitting is an example of a process that cannot be described by an RWA quanta-conserving process, which points to a severe limitation of the RWA regarding its potential to describe inelastic scattering in the ultra-strong coupling regime.

Having demonstrated in the previous chapter that the multi-coherent state technique is capable of tackling the waveguide-qubit interaction all the way up to the deep ultra-strong coupling regime ($\alpha \simeq 1$), it appears to be a good candidate for taking over where the RWA seems

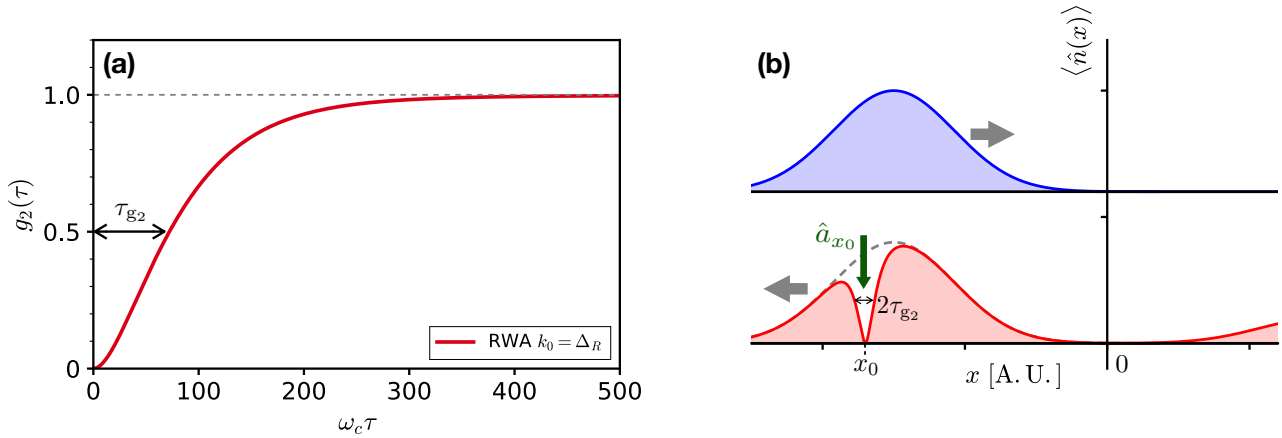

Figure 4.4: **(a)** Second order correlation function $g_2(\tau)$ calculated in reflected wave-packet, for the same parameters as Fig. 4.2(b). Note that $g_2(0) = 0$, implying at at any point in the wave-packet, there is at most one photon. This is known in the literature photon anti-bunching. We have also denoted τ_{g_2} the time required for $g_2(\tau)$ to reach 0.5. **(b)** Illustration of the expectation value of the local photon number $\langle n(x) \rangle$ at the beginning of the simulation (in blue) and at the end of the simulation right after annihilation of a photon at x_0 (in red). The qubit is located at $x = 0$. As shown, the annihilation results in a dip in the photon density centered at x_0 and of width twice the time scale τ_{g_2} of the g_2 function. The reflected signal before annihilation is shown by the grey dashed lines.

to be failing. It should be noted however, that the scattering of a coherent state on a two-level system is a significantly more complex and challenging problem than our idealistic description of spontaneous emission in chapter 3. For one, scattering involves both the absorption of part of the signal by the qubit, followed by re-emission, implying that the emission process is only a *subpart* of the physics involved. Secondly, since we are interested in long enough wave-packets (i.e. a small wave-packet linewidth) in order to define a nearly monochromatic drive, the scattering will involve a continuous sequence of excitation and reemission by the qubit which will lead to a highly non-trivial scattered quantum state. The complexity and quantum nature of this state of light is best revealed in the second-order correlations as measured by the g_2 function given by:

$$g_2(x,\tau) = \frac{\langle a_x^\dagger(t) a_x^\dagger(t+\tau) a_x(t+\tau) a_x(t) \rangle}{\langle a_x^\dagger(t+\tau) a_x(t+\tau) \rangle \langle a_x^\dagger(t) a_x(t) \rangle}, \tag{4.1}$$

which gives the probability of measuring a photon at the point x of the waveguide and at time $t + \tau$, provided that a photon was already measured at time t. To get an idea of this complexity, we calculated this $g_2(\tau)$ in the reflected wave-packet of the on-resonant RWA-simulation corresponding to Fig. 4.2(b), and plotted that function in Fig. 4.4a. In particular, we see that at $\tau = 0$, the g_2 function vanishes, meaning that the simultaneous measurement of two photons is impossible (at least within the RWA). In the literature, photons anti-correlated in this fashion are often referred to as *anti-bunched*. Note that the time scale giving the shape of the g_2 is a non-trivial function of the qubit relaxation rate $\Gamma = \pi \Delta_R \alpha$ and of the drive power [99]. For convenience therefore, let us simply denote τ_{g_2} the time required for $g_2(\tau)$ to reach 0.5.

Finally, to get some insight into the structure of the anti-bunched radiation, we show in Fig. 4.4b the mean number of scattered photons in the waveguide, *right after* the first photon was measured, say at x_0 by applying the annihilation operator a_{x_0}. Although in circuit QED

measurement is generally performed by measuring the voltage of the signal $(a + a^\dagger)/2$, it is instructive to consider what would be the effect of the direct destruction of a photon in the emitted signal. What we see is that a dip entirely depleting the photon density at x_0 is created, which has a spatial width of twice the time scale of $g_2(\tau)$ (since we took $c = 1$, the time scale is also a spatial scale).

In the following, we move on to the investigation of contributions beyond the RWA to obtain a full solution to the scattering problem by making use of the MCS technique introduced in the previous chapter.

4.2 Many-body coherent state scattering formalism

4.2.1 Two-level system coupled to a double-sided waveguide

Until now, we have only been working with right-propagating waves when studying spontaneous emission, and have therefore only needed to take into account the positive k modes in the spin-boson model. Since we are now interested in simulating a wave-guide on both sides of the qubit, with reflected waves traveling to the left and transmitted waves traveling to the right, we now need to consider the full range of positive and negative momenta k (with $\omega(k) = |k|$) in the spin-boson model:

$$H = \frac{\Delta}{2}\sigma_x - \frac{\sigma_z}{2}\sum_{k\in\mathbb{R}} g_k^{\text{full}}(a_k \ + a_k^\dagger) + \sum_{k\in\mathbb{R}} \omega_k a_k^\dagger a_k \ , \tag{4.2}$$

where g_k^{full} here stands for the coefficient of interaction between mode a_k and the full double-sided waveguide.

In order to simplify the problem, we start by folding the bosonic modes onto a half-line, by defining even and odd modes:

$$a_k^e = \frac{1}{\sqrt{2}}(a_k + a_{-k}) \quad \text{and} \quad a_k^o = \frac{1}{\sqrt{2}}(a_k - a_{-k}) \, , \tag{4.3}$$

so that the Hamiltonian (4.2) can be rewritten as

$$H = \frac{\Delta}{2}\sigma_x - \frac{\sigma_z}{2}\sum_{k>0} g_k(a_k^e \ + a_k^{e\dagger}) + \sum_{k>0} \omega_k \left[a_k^{e\dagger} a_k^e + a_k^{o\dagger} a_k^o \ \right], \tag{4.4}$$

with the coupling constant to the even modes, $g_k = \sqrt{2} g_k^{\text{full}}$. With this simple manipulation, we have recovered the form of the spin-boson model we had derived in paragraph 2.4.2. The value of g_k is the one given by Eq. (2.124).

According to Hamiltonian (4.4), only the even modes are interacting with the qubit, while the odd modes are freely propagating. This allows us to write the state vector $|\Psi\rangle$ as the direct product of the even sector $|\psi^e\rangle$ and the odd sector $|\psi^o\rangle$:

$$|\Psi\rangle = |\psi^e\rangle_e \otimes |\psi^o\rangle_o = |\psi^e\rangle_e \, |\psi^o\rangle_o \, , \tag{4.5}$$

provided the initial state can be decomposed accordingly. The dynamics in the odd sector is essentially trivial, while many-body effects have to be considered to capture the dynamics in the even sector. The strategy will therefore be to use the MCS ansatz to describe the even

sector $|\psi^e\rangle_e$ only, while the odd sector $|\psi^o\rangle_o$, detailed in the next paragraph, maintains a very simple form:

$$|\psi\rangle = \sum_{m=1}^{N_{\rm cs}} \Big[p_m(t)|f_m(t)\rangle|\uparrow\rangle + q_m(t)|h_m(t)\rangle|\downarrow\rangle \Big] \otimes |\psi^o\rangle_o \,, \tag{4.6}$$

The details of the preparation of this state for performing scattering simulations is a topic we address now.

4.2.2 General coherent state scattering formalism

We now process to prepare the initial state in order to perform scattering simulations according to the scheme in Fig. 4.1(a). The generic difficulty is that the qubit is dressed non-perturbatively by a cloud of photons in the ultra-strong coupling regime [26, 92, 70, 94, 27, 93], so that this ground state assumes a many-body character. Thanks to the MCS ansatz introduced in eq. (4.6), we can efficiently express the static ground state of the joint qubit and waveguide system in terms of multi-mode coherent states:

$$|\Psi^{\rm GS}\rangle = \sum_{m=1}^{N_{\rm cs}^{\rm GS}} p_m^{\rm GS} \Big[|f_m^{\rm GS}\rangle_e|\uparrow\rangle - |-f_m^{\rm GS}\rangle_e|\downarrow\rangle \Big] |0\rangle_o, \tag{4.7}$$

where we enforced the $\mathbb{Z}_2$ spin-symmetry of the spin-boson Hamiltonian (4.4) to simplify the expression. We have also used the fact that the odd modes do not interact with the qubit, which is why in (4.7) the ground state displacements involve only even modes, while odd modes are kept in the vacuum state.

By implementing numerically a variational optimization [70, 69], one can determine the set of weights $p_m^{\rm GS}$ and displacements $f_{k,m}^{\rm GS}$, and thus obtain an exact result for the ground state up to negligible numerical error. Conveniently, only a small number of coherent states $N_{\rm cs}^{\rm GS}$, typically less than 10, are required in the realistic domain of parameters of the spin-boson model.

The second step in the scattering picture of Fig. 4.1 is to include a wavepacket (in blue) impinging on the dressed ground state. We will work in what follows with a single coherent state pulse as input, which is realistic in terms of the classical sources used in actual experiments. Let us denote z_k the displacement of the incoming wave-packet in mode k of the physical waveguide, and z_x its Fourier transform to real space:

$$z_x = \int_{-\infty}^{\infty} \frac{dk}{\sqrt{2\pi}} e^{+ikx} z_k. \tag{4.8}$$

We choose to use here a Gaussian-shaped wavepacket

$$z_k = \sqrt{\bar{n}} \left(\frac{1}{2\pi\sigma^2} \right)^{\frac{1}{4}} e^{-\frac{(k-k_0)^2}{4\sigma^2}} e^{-i(k-k_0)x_0} e^{-ik_0x_0/2}, \tag{4.9}$$

corresponding to a signal initially centered around position x_0 in the waveguide, with mean wavenumber k_0, spatial extent $1/\sigma$, and total intensity corresponding to $\bar{n}$ photons on average, as indicated on Fig. 4.1. The associated real space wavepacket is then

$$z_x = \sqrt{\bar{n}} \left(\frac{2\sigma^2}{\pi} \right)^{\frac{1}{4}} e^{-(x-x_0)^2\sigma^2} e^{+ik_0(x-x_0)} e^{+ik_0x_0/2}. \tag{4.10}$$

Note that these amplitudes are both normalized so that $\int_{-\infty}^{\infty} dx|z_x|^2 = \int_{-\infty}^{\infty} dk|z_k|^2 = \bar{n}$.

The even and odd parts of the incoming wavepacket are then defined strictly for $k > 0$ as

$$z_k^e = \frac{1}{\sqrt{2}}\left(z_k + z_{-k}\right) \quad \text{and} \quad z_k^o = \frac{1}{\sqrt{2}}\left(z_k - z_{-k}\right). \tag{4.11}$$

Since even and odd modes commute, we can then define a displacement operator $D(z)$ for the initial incoming wave-packet which verifies:

$$\begin{aligned} |z^e, z^o\rangle &= D(z)\,|0\rangle = D(z^e)D(z^o)\,|0\rangle \\ &= e^{\sum_{k>0}\left(z_k^e a_k^{e\dagger} - z_k^{e*} a_k^e\right)} e^{\sum_{k>0}\left(z_k^o a_k^{o\dagger} - z_k^{o*} a_k^o\right)}\,|0\rangle\,. \end{aligned} \tag{4.12}$$

The final step in the initialization of the state vector is to combine the incoming wavepacket coherent state $|z_k\rangle$ in Eq. (4.9) with the displacements entering the full many-body ground state (4.7). Using the operator $D(z)$ we just defined, we readily find for the spin-up projection of the wavefunction

$$\begin{aligned} |\Psi_\uparrow\rangle &= D(z^e)D(z^o)\,|\Psi_\uparrow^{\mathrm{GS}}\rangle \\ &= e^{\sum_{k>0} z_k^e a_k^{e\dagger} - \text{c.c.}} \sum_m^{N_{\mathrm{cs}}^{\mathrm{GS}}} p_m^{\mathrm{GS}} e^{\sum_{k>0} f_{k,m}^{\mathrm{GS}} a_k^{e\dagger} - \text{c.c.}}\,|0\rangle_e\,|z^o\rangle_o\,, \end{aligned} \tag{4.13}$$

which can be recombined using the standard relation $e^A e^B = e^{A+B} e^{\frac{1}{2}[A,B]}$, valid as the commutator here is only a number. The initial state associated to the $\uparrow$ qubit state thus reads:

$$|\Psi_\uparrow\rangle = \sum_m^{N_{\mathrm{cs}}^{\mathrm{GS}}} p_m^{\mathrm{GS}} e^{\frac{1}{2}\sum_{k>0}\left(z_k^e f_{k,m}^{\mathrm{GS}*} - z_k^{e*} f_{k,m}^{\mathrm{GS}}\right)} e^{\sum_{k>0}\left[\left(f_{k,m}^{\mathrm{GS}} + z_k^e\right)a_k^{e\dagger} - \left(f_{k,m}^{\mathrm{GS}} + z_k^e\right)^* a_k^e\right]}\,|0\rangle_e\,|z^o\rangle_o\,. \tag{4.14}$$

For the spin-down projection, one simply replaces $f_{k,m}^{\mathrm{GS}}$ by $-f_{k,m}^{\mathrm{GS}}$ without changing the sign of z_k^e, so that our total initial wavefunction is given by

$$\begin{aligned} |\Psi^{\mathrm{IN}}\rangle = \sum_{m=1}^{N_{\mathrm{cs}}^{\mathrm{GS}}} p_m^{\mathrm{GS}} \Big[&|\uparrow\rangle\, e^{\frac{1}{2}\sum_{k>0}\left(z_k^e f_{k,m}^{\mathrm{GS}*} - z_k^{e*} f_{k,m}^{\mathrm{GS}}\right)} e^{\sum_{k>0}\left[\left(f_{k,m}^{\mathrm{GS}} + z_k^e\right)a_k^{e\dagger} - \left(f_{k,m}^{\mathrm{GS}} + z_k^e\right)^* a_k^e\right]} \\ &- |\downarrow\rangle\, e^{\frac{1}{2}\sum_{k>0}\left(-z_k^e f_{k,m}^{\mathrm{GS}*} + z_k^{e*} f_{k,m}^{\mathrm{GS}}\right)} e^{\sum_{k>0}\left[\left(-f_{k,m}^{\mathrm{GS}} + z_k^e\right)a_k^{e\dagger} - \left(-f_{k,m}^{\mathrm{GS}} + z_k^e\right)^* a_k^e\right]} \Big]\,|0\rangle_e\,|z^o\rangle_o\,. \end{aligned} \tag{4.15}$$

The many-body scattering theory thus amounts to use state (4.15) as the initial condition for the dynamical equations of motion (3.11)-(3.12). During the dynamics, as the incoming wavepacket impinges on the qubit, the necessary number of coherent states N_{cs} will sensibly grow from the initial value $N_{\mathrm{cs}}^{\mathrm{GS}}$ due to non-classical emission, therefore requiring to add extra coherent states to the state vector when needed (the procedure is the same as for the Rabi model, which was detailed in paragraph 3.2.3). In the odd sector, which is completely decoupled from the qubit, the related displacements are trivially evolving in time according to $i\dot{z}_k^o = \omega_k z_k^o$, and a single coherent state is enough for the whole time-evolution.

After a given time T long enough to ensure interaction of the wavepacket with the qubit and subsequent decoupling of the reflected and transmitted wavepackets from the many-body cloud surrounding the qubit, one expects on general grounds a factorization of the final wavefunction as:

$$|\Psi(T)\rangle = |\Psi^{\mathrm{GS}}\rangle \otimes |\Psi^{\mathrm{OUT}}\rangle\,, \tag{4.16}$$

where $|\Psi^{\rm GS}\rangle$ is the many-body ground state of the spin-boson model and $|\Psi^{\rm OUT}\rangle$ a many-body outgoing wavepacket that contains a non-trivial decomposition of the emitted signal in terms of a large number of multi-mode coherent states (typically $N_{cs}^{\rm OUT} \sim 20-30$):

$$|\Psi^{\rm OUT}\rangle = \sum_{m=1}^{N_{\rm cs}^{\rm OUT}} p_m^{\rm OUT} \prod_{k=1}^{N_{\rm modes}} e^{[f_{k,m}^{\rm OUT} a_k^{e\dagger} - f_{k,m}^{\rm OUT*} a_k^e]} |0\rangle. \tag{4.17}$$

Clearly the quantum many-body character of the scattering process is encoded in the sum over more than a unique coherent state, in contrast to the incoming wavepacket (4.12) that is characterized by a single coherent state (namely a classical-like signal).

Extracting the wavepacket contribution (4.17) from the long-time wavefunction (4.16) can be performed as follows. The complete set of displacements $\{f_{k,n}^e(T), h_{k,n}^e(T)\}$ in the even sector at a fixed long time T for the full wavefunction (4.6) are first Fourier transformed to real space using (4.8). The local photon density $n(x)$ associated to these displacements is sketched in Fig. 4.1: photons are either bound statically near the qubit (associated to the dressed vacuum, in green) or travel in the outgoing wavepackets (in red). The displacements are then simply set to zero in the region surrounding the qubit, and Fourier transformed back to the momentum basis. Due to factorization (4.16), the outgoing wavefunction is recovered up to a normalization factor, which is supplemented accordingly. The even modes thus obtained and the trivial odd mode wave-functions are finally combined together, allowing reconstruction of the full outgoing wavefunction for the physical waveguide.

4.2.3 Number resolved spectra

In order to analyze the content of the scattered wavepackets, we will need to assess the nature of the particle production in the scattering process. For this purpose, we derive the inelastic spectrum in terms of Fock states $|N\rangle$. First, consider the general expansion of the multi-mode outgoing wavefunction (4.17) in terms of number states:

$$\begin{aligned} |\Psi^{\rm OUT}\rangle = \gamma\,|0\rangle + \sum_k \alpha_k a_k^\dagger\,|0\rangle + \sum_{k_1,k_2} \alpha_{k_1,k_2} a_{k_1}^\dagger a_{k_2}^\dagger\,|0\rangle \\ + \sum_{k_1,k_2,k_3} \alpha_{k_1,k_2,k_3} a_{k_1}^\dagger a_{k_2}^\dagger a_{k_3}^\dagger\,|0\rangle + \quad ... \end{aligned} \tag{4.18}$$

It can then easily be verified that the 1-photon amplitude is given by:

$$\alpha_k = \langle 0|\, a_k\, |\Psi^{\rm OUT}\rangle = \sum_n p_n f_{k,n}\, \langle 0|f_n\rangle\,, \tag{4.19}$$

and that the scattering amplitude for a generic N-photon state is:

$$\alpha_{k_1,...,k_N} = \frac{1}{N!}\,\langle 0|\, a_{k_1}... \, a_{k_N}\, |\Psi^{\rm OUT}\rangle = \frac{1}{N!}\sum_n p_n f_{k_1,n}...f_{k_N,n}\, \langle 0|f_n\rangle\,, \tag{4.20}$$

which can be obtained straightforwardly from the algebraic identities of coherent states. For the sake of clarity, we have dropped the OUT labels on p_n and $f_{n,k}$. From the multi-photon amplitudes, we can then compute the probability distribution for finding a photon in a given

k mode, according to the various Fock contents of the total wavefunction:

$$\begin{aligned} \langle n_k \rangle_{1\text{photon}} &= |\alpha_k|^2, \\ \langle n_k \rangle_{2\text{photon}} &= 4 \sum_{k1} |\alpha_{k,k1}|^2, \\ \langle n_k \rangle_{3\text{photon}} &= 18 \sum_{k2,k3} |\alpha_{k,k2,k3}|^2. \end{aligned} \tag{4.21}$$

4.3 Multi-photon inelastic scattering

4.3.1 Elastic emission and high power saturation

As a first illustration for our dynamical many-body scattering method, we investigate reflection as a function of the frequency and power of the incoming signal. This problem is particularly challenging because of the combination of non-perturbative ultra-strong coupling with non-equilibrium effects that arise at finite input power. Ultra-strong coupling scattering at non-vanishing power has been addressed previously with approximate techniques [64, 75, 95, 66] and with more advanced numerical methods [92, 94]. However, systematic extraction of many-body scattering matrices has not been performed to our knowledge.

Our calculation scheme proceeds similarly to an experimental setup: the incoming Gaussian coherent-state wavepacket, shown schematically in blue as a distribution of photons in real space in Fig. 4.1(a), is initialized to the left of the qubit. The qubit is placed at position $x = 0$ as seen from its sharply decreasing photonic cloud [27] which is present in both the input and output ports, but remains statically bound to the central impurity. After propagation towards the qubit and subsequent interaction, the photon flux decouples at long times, and is separated into a reflected left going ($k < 0$) signal and a transmitted right going ($k > 0$) signal, both shown in red in Fig. 4.1(a). Note that in all the simulations made in this paper, we have considered the linewidth σ of the wavepacket in k-space to be smaller than the qubit linewidth Γ (in order to achieve high spectroscopic resolution), but large enough to keep the simulations on a reasonable system size (typically we consider from $N_{\text{modes}} = 1000$ to $N_{\text{modes}} = 3000$ modes for the chain in the even sector). All calculations are done in units of the plasma frequency ω_c as defined in the spectral density (2.121), and the wavepacket linewidth appearing in Eq. (4.9) is taken as $\sigma = 0.005\omega_c$, unless indicated otherwise.

We define the reflection and transmission coefficients in the following way:

$$T = \frac{\sum_{k>0} \langle a_k^\dagger a_k \rangle_{\text{out}}}{\sum_{k>0} \langle a_k^\dagger a_k \rangle_{\text{in}}} \quad \text{and} \quad R = \frac{\sum_{k<0} \langle a_k^\dagger a_k \rangle_{\text{out}}}{\sum_{k>0} \langle a_k^\dagger a_k \rangle_{\text{in}}}, \tag{4.22}$$

where we have denoted $\langle \ldots \rangle_{\text{in}}$ the average over the state vector corresponding to the coherent incoming wave-packet before scattering, and $\langle \ldots \rangle_{\text{out}}$ the average over the many-body outgoing wave-packet after scattering. Both are obtained from the full state vector (4.17) by simply filtering out in real-space the polarization cloud associated with the ground state, as explained in paragraph 4.2.2.

Results for different values of the incoming power are shown in Fig. 4.5. The probability of reflection generally increases on resonance; indeed, for elastically scattered photons, inference effects cause the near extinction of the transmission signal, leading to an almost complete reflection when exactly on resonance. For small values of the incoming power ($\bar{n} = 0.01$ and $\bar{n} = 0.1$), for which the initial coherent state wavepacket has a very small probability of

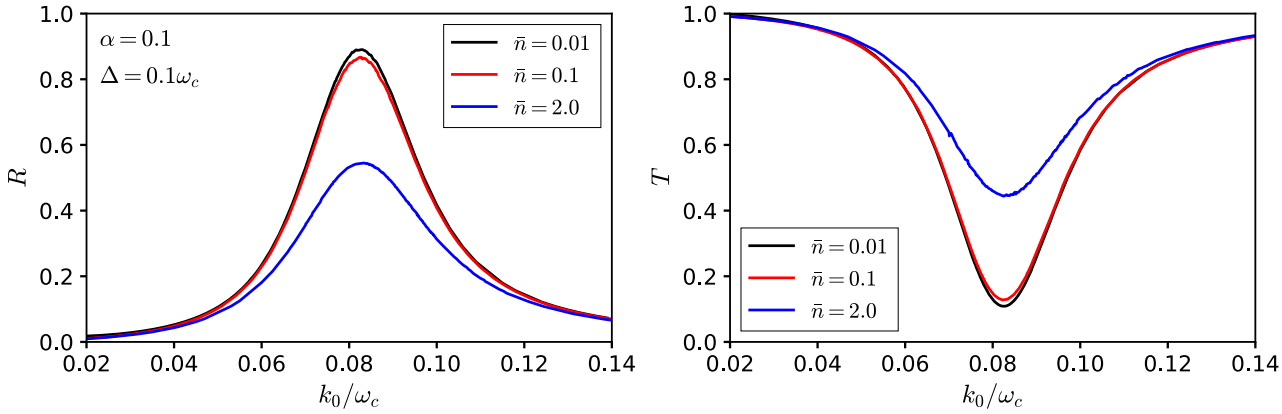

Figure 4.5: Saturation effects in the reflection and transmission coefficients as a function of the incoming wave-vector k_0, for three different amplitudes $\bar{n} = 0.01, 0.1, 2.0$ of the input, with a wavepacket width $\sigma = 0.005\omega_c$. These curves correspond to converged numerical data with up to $N_{\rm cs} = 16$ coherent states in the MCS wavefunction (4.6). The bare qubit frequency is $\Delta = 0.1\omega_c$ and the dimensionless light-matter interaction is $\alpha = 0.1$, leading to a sizable renormalized qubit frequency $\Delta_R \simeq 0.08\omega_c$.

containing Fock states with more than 1 photon, one can note that the reflection only reaches $R \simeq 0.9$ at peak value. This incomplete reflection of the photons arises from the finite linewidth of the incoming wavepacket, and not from inelastic losses. Since our incoming Gaussian pulse is not perfectly monochromatic, the modes at the edge of a resonant incoming beam (centered at $k_0 = \Delta_R$) are slightly off-resonant and do not get fully reflected by the qubit.

Even in the present case of a relatively small light matter coupling $\alpha = 0.1$, many-body effects due to the ultra-strong coupling are apparent in the reflection curve of Fig. 4.5. First, a non-Lorentzian asymmetric line-shape is obtained, with a high energy tail more prominent than at low energy. In addition, we clearly observe a substantial renormalisation of the qubit frequency $\Delta_R \simeq 0.08\omega_c$ from its bare value $\Delta = 0.1\omega_c$.

For higher incoming power, one physically expects saturation effects to take place, and these are clearly evidenced by the curve with average number of photons $\bar{n} = 2.0$ in Fig. 4.5. We stress that converging such computations in the high power regime is quite challenging, and approximate techniques such as single coherent state truncation lead to uncontrollable noise levels, as found in previous work [75]. It will be shown in paragraph 4.3.5 that the reflection curve converges smoothly at $\bar{n} = 2.0$ for about $N_{\rm cs} = 16$ coherent states in the MCS state vector (4.6).

4.3.2 Off-resonant particle frequency-conversion spectra

We now turn to the analysis of the emitted radiation in the off-resonant case, in which the system is excited at a frequency k_0 above the renormalized qubit transition frequency Δ_R. A typical inelastic spectrum is shown in Fig. 4.6(a), here for $k_0 = 0.16\omega_c$, $\Delta_R = 0.08\omega_c$, and an injected $\bar{n}$ of 0.5. The stronger transmission relative to reflection (upper panel) is simply a result of the off-resonant situation $k_0 \approx 2\Delta_R$, in agreement with the reflection curve in Fig. 4.5. The vertical scale is expanded in the lower panel, so that the inelastic contributions are made apparent at the foot of the large reflection and transmission elastic peaks located at $\pm k_0$. Note that the actual linewidth of this elastic peak, set by $\sigma = 0.005\omega_c$, is in fact much smaller than what the lower panel seems to indicate, because the maximum peak amplitude is 2000 times higher than the scale of the graph. The grey-shaded curve displays the expectation value of the

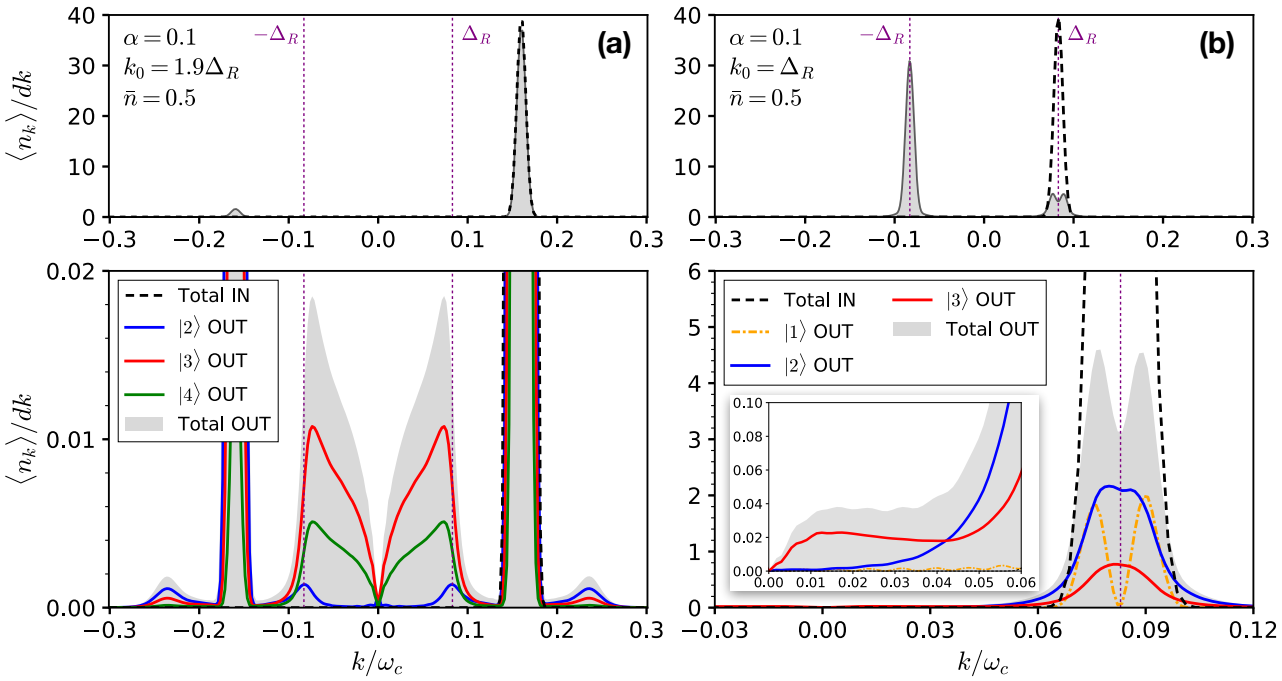

Figure 4.6: Mean density of photons at momentum k in the outgoing wave-packet calculated with the MCS technique, with the same parameters as in Fig. 4.2 ($\alpha = 0.1$, $\sigma = 0.005$, $\bar{n} = 0.5$). The total outgoing signal (grey shaded) is decomposed into Fock resolved excitations with $N = 2, 3, 4$ photons (blue, red, green curves), in order to highlight the processes of Fig. 4.9. Left panels: off-resonant drive with $k_0 = 1.9\Delta_R$. The simulations were performed by considering a wavefunction containing $N_{\rm cs} = 30$ coherent states, and $N_{\rm modes} = 1200$ modes. Right panels: on-resonant drive with $k_0 = \Delta_R$. Because of the wavepacket finite linewidth σ, a small fraction of one-photon states is still transmitted (orange dot-dashed line), despite being on resonance. Besides the wide inelastic wings, the two-photon contribution (in blue) presents a 3-photon continuum (in red) magnified in the inset.

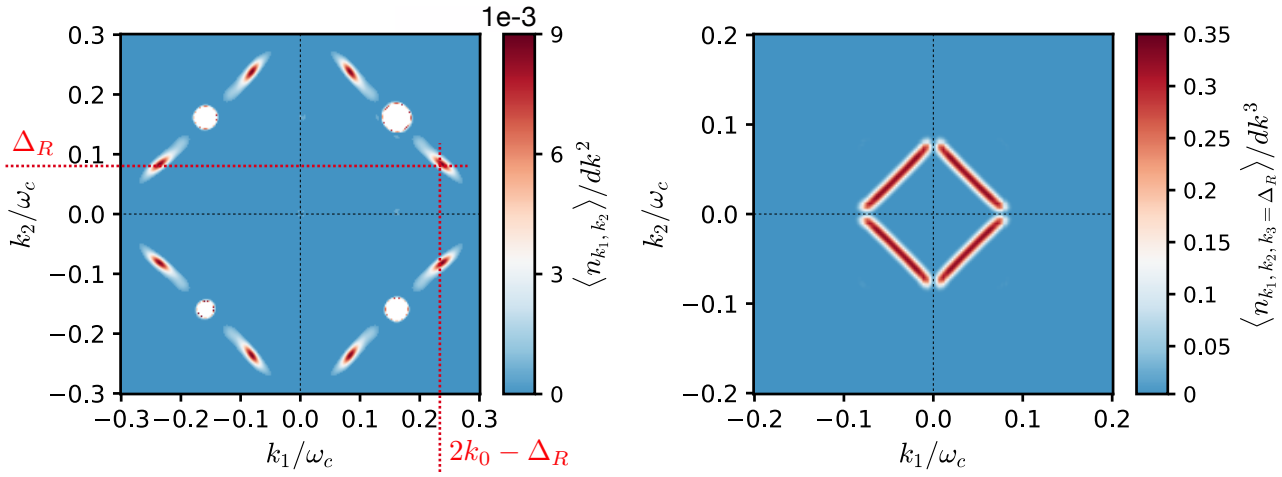

Figure 4.7: Left panel: probability distribution of the two-photon states $|\alpha_{k_1,k_2}|^2/dk^2$ corresponding to the 2-photon curve in Fig. 4.6(a). The clear inelastic sidebands correspond to frequency exchange between 2 photons. Right panel: probability density distribution $|\alpha_{k_1,k_2,k_3=\Delta_R}|^2/dk^3$ of the three-photon states in which one photon is at the resonance frequency $k_3 \approx \Delta_R$, corresponding to the 3-photon curve in Fig. 4.6(a). The emission continuum associated to particle production is revealed by the diamond-shaped line.

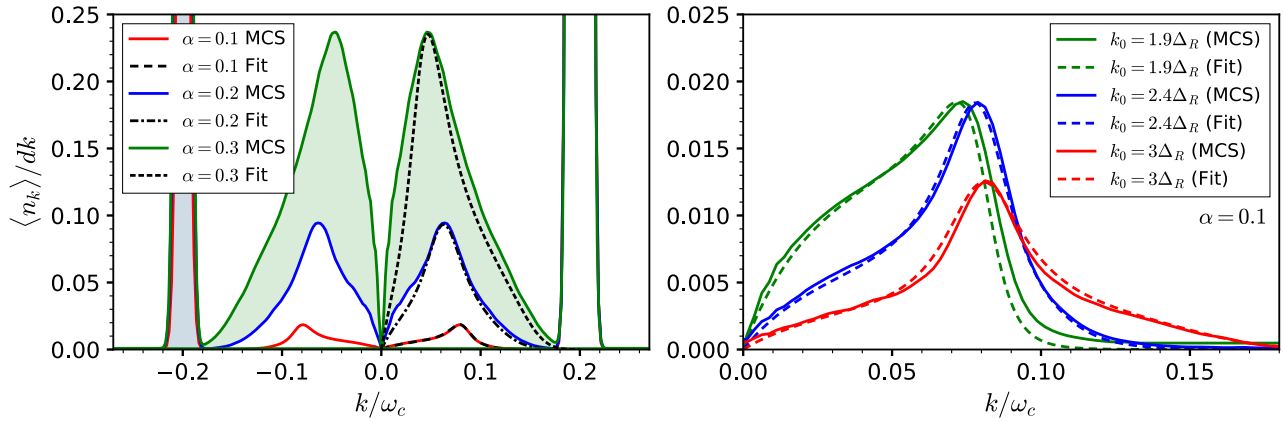

Figure 4.8: Left panel: Frequency conversion spectrum by going deeper in the ultra-strong coupling regime ($\alpha = 0.1, 0.2, 0.3$) for an off-resonant incoming wave-vector $k_0 = 0.2\omega_c$. Although the resonance frequency Δ_R and inelastic linewidth γ_R^{inel} were optimized, one observes increasing deviations to the fitting formula (E.1) at larger α. Enhanced scattering of low-energy modes, precursor of the Kondo regime, originate from non-perturbative many-body corrections beyond the lowest order perturbation theory of Ref. [29]. Right panel: Low-energy inelastic spectrum for several off-resonant values of the incoming momentum $k_0 = 0.16, 0.20, 0.25\omega_c$ obtained using the MCS technique, together with a comparison to the analytical formula (E.1), using a fitted and momentum-dependent linewidth $\gamma_R(k_0)$. [*Unspecified parameters on both plots are the same as in Fig. 4.6(a)*].

total number of outgoing photons $\langle a_k^\dagger a_k \rangle_{\text{out}}$ while the dashed line indicates the total number of incoming photons $\langle a_k^\dagger a_k \rangle_{\text{in}}$ centered around k_0. The first striking result is the broad spectrum of emission extending from the qubit frequency Δ_R all the way down to $k = 0$.

The solid, colored lines display how the total outgoing photon contribution is distributed among different Fock states $|N\rangle$ with photon number $N = 2, 3, 4$, allowing us to assess the nature of particle production. (see paragraph 4.2.3 for details on the method). Note that the majority of the inelastic emission involves 3 and 4 photon contributions. Since the incoming average photon number is only 0.5, clearly substantial particle production is occurring. Both the broad inelastic spectrum and particle production are quintessentially ultra-strong coupling phenomena. The two-photon scattered spectrum, in blue, is the two photon inelastic RWA process (Fig. 4.3) that was identified in the RWA spectrum in Fig 4.2 that occurs by distributing the total incoming energy $2k_0$ into a resonant photon at Δ_R and another at $2k_0 - \Delta_R$. On the other hand, for a *single* incoming photon with momentum k_0, since the emission is still maximum at the (renormalized) resonant qubit frequency Δ_R, an excess energy of $k_0 - \Delta_R$ must be distributed between *two extra* outgoing photons (in order to properly relax to the ground state). The accessible non-resonant states thus lead to the non-RWA 3-photon emission process shown in Fig. 4.9(a). In general, the two extra photons that are produced are not resonant, and the amplitude of the total process is sizable only because of the ultra-strong coupling regime. Indeed, the elastic reflection curve of Fig. 4.5 is spectrally very broad, and emission does not necessarily involve strictly resonant photons.

The non-RWA nature of the particle production process is obvious from the non-conservation of excitations: the middle red arrow in Fig. 4.9(a) corresponds to the *emission* of a photon upon *excitation* of the two-level system (instead of the usual de-excitation). Four-photon production is also displayed in panel (a) for an input state with two photons. In this case, one input photon is elastically scattered at k_0, while the second input photon splits into three photons similar to the process in panel (b). Since the RWA $2 \to 2$ process in panel (a) and the non-RWA $2 \to 4$ process in panel (b) come at the same order in the input power, they can be

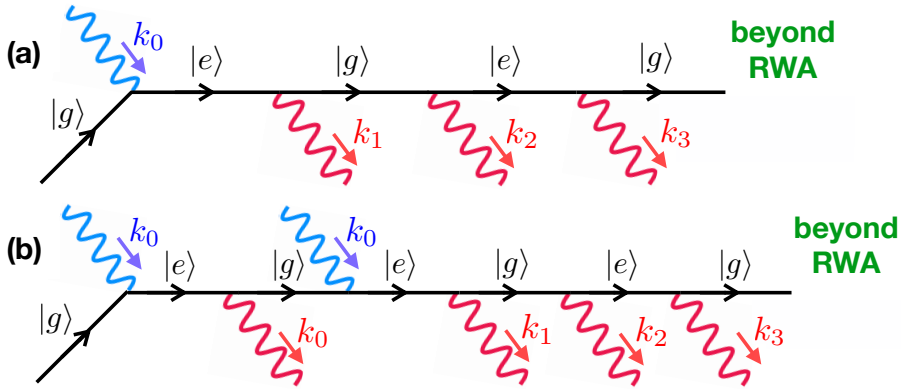

Figure 4.9: Diagrammatic representation of some non-RWA non-linear photon processes occurring during scattering onto a two-level system. Panel (b) shows the one photon to three photon conversion [29], which leads to a broad emission continuum, sharply peaked at the resonance Δ_R in the case of an off-resonant drive. Panel (c) is a similar particle producing process, now with two input photons, one being down converted to three photons, the other photon being elastically scattered.

used to directly compare the relative strength of RWA and non-RWA processes. Note that all three processes of Figs. 4.9 and 4.3 are clearly observed in the spectrum shown in Fig. 4.6(a), as the emission amplitude is decomposed into photon number states $N = 2, 3, 4$. In view of the wide use of the RWA in the quantum optics context, the main surprise in these results (to be discussed in more detail below) is that non-RWA processes strongly dominate in amplitude the RWA processes.

Some of the off-resonant processes were previously predicted perturbatively [29] in the $\alpha \to 0$ limit and at the Toulouse limit. Using the MCS method, we are able to characterize quantitatively the non-linear emission for the first time up to $\alpha = 0.3$, as shown in the left panel of Fig. 4.8. The main effect brought by stronger coupling is a further renormalisation of the spontaneous emission line Δ_R down to lower values, as well as a global increase of the probability for inelastic conversion. Interestingly, we find that the perturbative formula (E.1), given in appendix E, cannot quantitatively describe our data anymore in this regime, even when allowing to fit the inelastic linewidth. Perturbation theory thus fails to capture the pile-up of low-energy photons found in the numerical simulations, which signals the approach to the incoherent Kondo regime, in which the qubit resonance is fully washed out.

Note nonetheless, that for $\alpha = 0.1$ and for various values of the incoming momentum k_0, the results from perturbation theory match our results quantitatively when allowing to fit the inelastic linewidth, as shown in the right panel of Fig. 4.8. More details are given in appendix E.

4.3.3 On-resonant frequency-conversion spectra

We now consider the resonant case where the incoming photon energy $k_0 = \Delta_R$ matches the renormalized atomic transition energy. Fig. 4.6(b) shows the total transmitted signal as well as its decomposition in terms of number states with $N = 1, 2, 3$ photons. As we had observed on Fig. 4.2(b), the two-photon amplitude in this regime is strongly enhanced with respect to the off-resonant situation of Fig. 4.6(a). One-photon contributions are also observed as two side-bands away from the resonance Δ_R, which are due to the finite width of the incoming wave-packet. The resonant 1-photon state (at exactly $k = k_0$) is completely reflected, as expected. The on-resonant regime is a promising one to observe experimentally non-linear

effects, because of the enhanced magnitude of the inelastic signal, as compared to the weaker off-resonant situation of Fig. 4.6(a). Note also, that the blue curve in Fig. 4.6(b), gives us confirmation that the long inelastic tails in Fig. 4.2(b), which corresponded the total mean number of photons, are indeed due to the 2-photon RWA process.

As in the off-resonant case, the resonant scattered spectrum also presents a 3-photon low energy continuum, as can be seen from the inset. The shape however does not present any sharply peaked feature, since this time the continuum does not contain the resonant frequency $k = \Delta_R$ at which the qubit spontaneously reemits. Instead, the spectrum is more flat, implying the single photon splits more uniformly into all the possible (k_1, k_2, k_3) allowed by the $1 \to 3$ process of Fig. 4.9. Interestingly, the magnitude of this 3-photon continuum is of the same order of magnitude as in the off-resonant case of Fig. 4.6(a), since non-linear processes are here intensified by having an on-resonant input, which compensates for the absence of an enhancing resonant frequency in the output below k_0. Again, this particle production process dominates the RWA contribution, but here only away from the probe frequency. The spectral line-shape of this resonant inelastic signal will be further analyzed in section 4.4.

4.3.4 Particle production processes

We now investigate more precisely the photonic content of the emitted radiation in the inelastic channel. Let us start with the 2-photon particle-conserving RWA contribution (blue line in Fig. 4.6(a)) forming two lobes symmetrically arranged around the main elastic peak (at $k_0 = 0.16\omega_c$). The lowest energy lobe is centered around $k \simeq 0.08\omega_c \simeq \Delta_R$ corresponding to the spontaneous reemission of the qubit, while the high energy lobe is located around $k \simeq 0.24\omega_c \simeq 2k_0 - \Delta_R$, as expected from energy conservation (panel (a) in Fig. 4.9). A closer view into this two-photon joint emission process is given by the complete two-photon probability distribution $|\alpha_{k_1\,k_2}|^2$ that is plotted in the left panel of Fig. 4.7 (see paragraph 4.2.3 for details).

The main 2-photon elastic peaks are the white disks located at $[\pm k_0, \pm k_0]$, that have been cut-off in order to magnify the small inelastic contributions. From the lateral inelastic peaks, one can immediately read-off the two-photon frequency conversion process in which two photons with energy k_0 redistribute their energy into one photon with momentum Δ_R and another with energy $2k_0 - \Delta_R$.

The inelastic spectrum originating from the conversion of a single incoming photon into three outgoing photons, with probability $\langle n_k \rangle_{3\text{photon}}$ of measuring one of these photons at energy k, is represented by the green curve in Fig. 4.6(a). This inelastic line-shape presents quite unusual features: a sharp resonance at the qubit frequency Δ_R, a broad continuum extending from zero energy up to the foot of the elastic peak, and a small lobe at the same energy $2k_0 - \Delta_R$ as the previous two-photon conversion process. The latter is easily understood as an input of three photons with momentum k_0, out of which one photon is elastically scattered, while the other two are RWA frequency converted to Δ_R and $2k_0 - \Delta_R$ (similar to the previous $2 \to 2$ RWA process). We have checked that this $3 \to 3$ RWA process becomes relatively weaker in amplitude as the input power $\bar{n}$ is turned down, and is indeed therefore associated to a three-photon input.

The broad low-energy continuum is readily explained by the 1-photon to 3-photon non-RWA conversion process shown in Fig. 4.9(a). This interpretation is backed up by studying in the right panel of Fig. 4.7 the probability distribution $|\alpha_{k_1 k_2 k_3 = \Delta_R}|^2$ of 3-photon outgoing states for which one of the three outgoing modes is resonant, $k_3 = \Delta_R$. To understand the diamond pattern, one can observe that the process leading to the diagonal line in the top-left

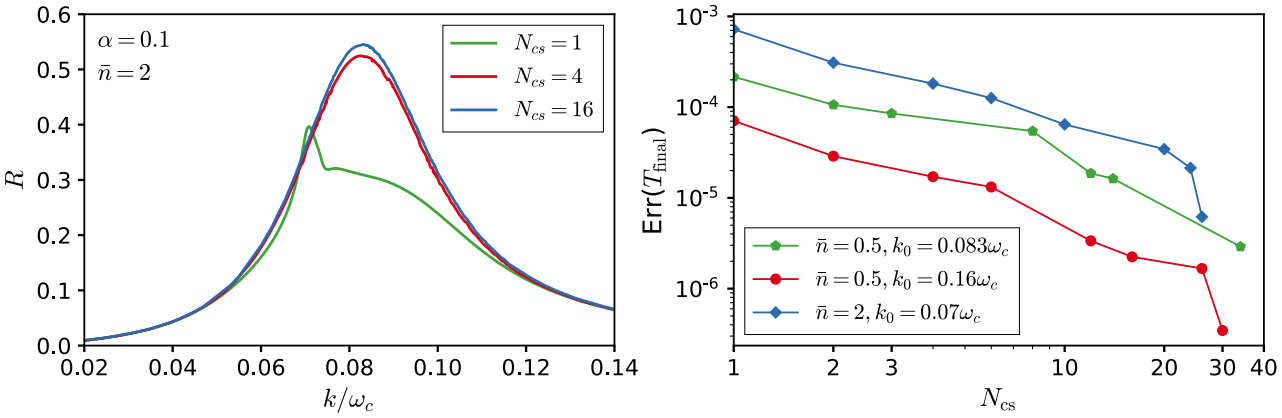

Figure 4.10: Left panel: Power reflection spectrum shown for different number of coherent states $N_{\mathrm{cs}} = 1, 4, 16$ included in the MCS wavefunction (4.6), with the same parameters as in Fig. 4.5 in the case of $\bar{n} = 2$ photons in the incoming beam. Right panel: Convergence of the error defined in the text at the final time T_{final} of the simulations, as a function of coherent state number in the wavefunction for the off-resonant case (red) of Fig. 4.6(a) and the high-power regime of the upper panel (blue).

quadrant can easily be parametrized as:

$$|k_0\rangle \to |\Delta_R\rangle\,|\Omega\rangle\,|k_0 - \Delta_R - \Omega\rangle \;\text{ with } \Omega \in [0 : k_0 - \Delta_R], \tag{4.23}$$

which expresses conservation of energy between the input and the output. Again, it is not necessary to have one of the three photons emitted at the resonance frequency for the process to occur, as we saw in the on-resonant situation (Fig. 4.6b), where the complete 3-photon continuum is below $k = \Delta_R$. In the *off*-resonance case on the other hand, the three-photon process has largest amplitude only when it allows the qubit to reemit at $k = \Delta_R$, as in process (4.23).

4.3.5 Convergence properties

Assessing the good convergence of the numerical results is important to gain confidence in the time-dependent variational MCS technique Indeed, we find that using too few variational parameters imposes strong constraints on the dynamics, which may result in unphysical behavior and numerical artifacts. One delicate test is the strong power saturation spectrum shown in Fig. 4.5. Indeed, the calculations that use only a single coherent state, as done in a previous publication [75], are found to be problematic in the strong power regime. This behavior is illustrated in the left panel of Fig. 4.10, showing the power reflection spectrum as a function of incoming frequency at a strong input power ($\bar{n} = 2$) for three different values of the number of coherent states $N_{\mathrm{cs}} = 1, 4, 16$. The computation with $N_{\mathrm{cs}} = 1$ is indeed quite noisy and imprecise, and a smooth and converged curve is only obtained at $N_{\mathrm{cs}} = 16$. We find that the inelastic spectra shown in Fig. 4.6(a) are also delicate to compute, because they consist of a tiny fraction of the total signal, and encode complex quantum states. A relatively large number of coherent state is also necessary here for success, even at small input power.

The next section investigates how the complete inelastic emission spectra compare with the standard RWA prediction in quantum optics. This comparison will provide not only a benchmark of our simulations, but will also reveal several physical features that cannot be captured without the inclusion of particle production processes.

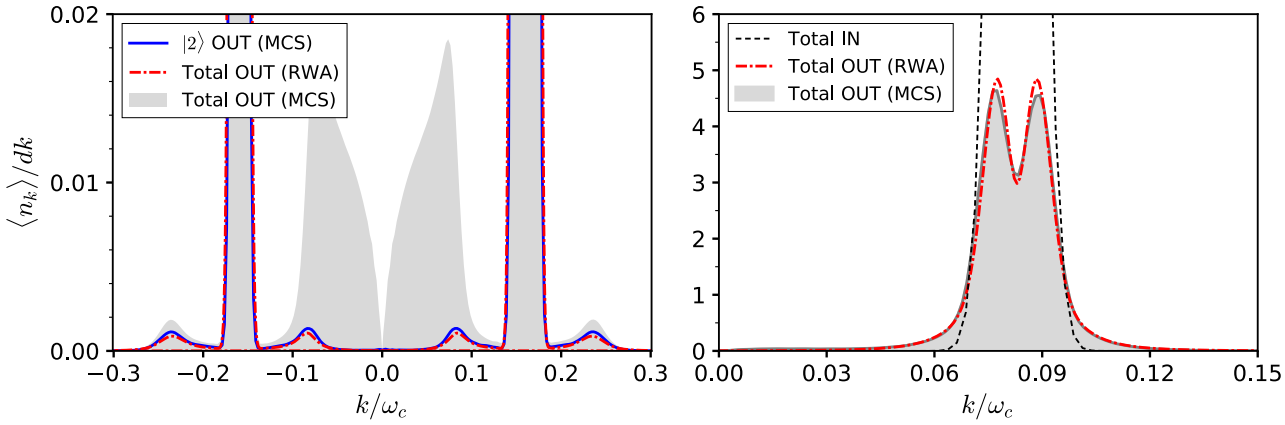

Figure 4.11: Comparison of MCS simulations to RWA input-output theory with regard to frequency conversion spectra for the off-resonant case (left panel) and on-resonant case (right panel). The parameters are the same as in Figs. 4.6(a) and 4.6(b). This confirms the previous interpretation that RWA inelastic processes dominate only on-resonance, and miss the main contributions to the off-resonant signal.

4.4 Success and failure of the RWA for inelastic emission

4.4.1 RWA inelastic conversion

To highlight particle production that arises at ultra-strong coupling, we now compare our MCS simulations to the direct treatment within the RWA that we had presented at the beginning of this chapter. As we saw in the scattered spectra of Fig. 4.2, the approximation can only describe particle-conserving inelastic processes and therefore misses all the particle production processes that occur in the complete theory.

Comparison to the RWA power spectrum in the off-resonant and resonant cases is shown in the left and right panels of Fig. 4.11 respectively. The dominant inelastic process within the RWA is the scattering of two incoming photons into two outgoing photons, see panel (a) of Fig. 4.2. One sees that this process explains most of the total scattered spectrum in the resonant case. Indeed, the right panel in Fig. 4.11 shows that the RWA and numerical MCS results are nearly identical on the scale shown. In particular both the overall width and shape of the inelastic power spectrum agree well. However, it is clear that the RWA prediction is only a small fraction of the total inelastic scattering in the off-resonant case (left panel in Fig. 4.11), as particle production leads to qualitatively different and much larger cross-sections. Thus for these parameters, the RWA fails badly, even though the coupling constant $\alpha = 0.1$ is not very large.

4.4.2 Temporal correlations associated to particle production

It is interesting to study photon number temporal correlations, a standard measure of non-linearities, but now in light of the large inelastic effects that we uncovered in the ultra-strong coupling regime. In section 4.1, we have defined the autocorrelation function of the reflected wavepacket ($x < 0$, $k < 0$) as

$$g_2(x,\tau) = \frac{\langle a_x^\dagger(t) a_x^\dagger(t+\tau) a_x(t+\tau) a_x(t) \rangle}{\langle a_x^\dagger(t+\tau) a_x(t+\tau) \rangle \langle a_x^\dagger(t) a_x(t) \rangle}. \tag{4.24}$$

An equivalent way to express this correlation function is by fixing a time t at which the reflected signal is completely dissociated from the qubit cloud, and to calculate the correlation between two *spatial* points of the wave-packet. This is clearly the same as to calculate the correlation according to Eq. (4.24), where the g_2 is calculated between point x at time t, and point x after the wavepacket has been translated in time by τ. Although both strategies are equivalent, the former is more convenient as it allows to access the correlation in one go without additional time evolution from t to $t+\tau$. Accordingly therefore, we re-write Eq. (4.24) as:

$$g_2(\tau) = \frac{\langle a_x^\dagger a_{x+\tau}^\dagger a_{x+\tau} a_x \rangle}{\langle a_{x+\tau}^\dagger a_{x+\tau} \rangle \langle a_x^\dagger a_x \rangle}, \tag{4.25}$$

where x is such that both x and $x+\tau$ are within the reflected wavepacket. In principle, $g_2(\tau)$ also depends on x, but this dependence is weak provided the wavepacket is almost monochromatic, and the location x is taken deep within the outgoing wavepacket. Note that since we take the speed of light $c = 1$, τ is just the distance traveled by radiation in time τ.

To obtain an expression for the g_2 function (4.25) in terms of our coherent state degrees of freedom, we insert the MCS expansion Eq. (4.6) into Eq. (4.25). Since coherent states are eigenstates of the annihilation operator, we immediately obtain a very compact expression for the autocorrelation function in terms of the real space displacements f_n^x:

$$g_2(\tau) = \frac{\sum_{m,n} p_n^* p_m (f_n^x)^* (f_n^{x+\tau})^* f_m^{x+\tau} f_m^x \langle f_n | f_m \rangle}{\langle n(x) \rangle \langle n(x+\tau) \rangle}, \tag{4.26}$$

with the local photon number defined as:

$$\langle n(x) \rangle = \langle a_x^\dagger a_x \rangle = \sum_{m,n} p_n^* p_m (f_n^x)^* f_m^x \langle f_n | f_m \rangle \,. \tag{4.27}$$

In the simulations performed to compute this quantity we used a sharp cutoff $\Theta(\omega_c - \omega)$ for the dispersion relation instead of the exponential cutoff $\mathrm{e}^{-\omega/\omega_c}$. Note that using the hard cut-off results in a slightly lower value of the renormalized qubit energy Δ_R, than with the exponential cutoff. This allowed us to decrease the numerical cost and therefore attain a higher number of coherent states, $N_{\mathrm{cs}} = 40$, which was necessary, as second-order correlations are more challenging to converge than average photon numbers. The simulations were stopped at a timescale $T = 1250/\omega_c$ long enough that the wavepacket is located far away from the dressed qubit, and we chose the spacial point $x = -681$ in Eq. (4.25), so as to keep the range of the function near the centre of the wavepacket. We finally note that spurious effects associated with the finite spatial extension of the wavepacket (due to $\sigma \neq 0$) lead to the small oscillations seen in Fig. 4.12 at longer times.

We find that temporal correlations are a very sensitive measure of ultra-strong coupling effects. In the resonant case (see the top panel of Fig. 4.12), the correlations are typical of single photon emission. The comparison to the RWA is globally quantitative, as expected from the previous agreement in the inelastic spectrum on-resonance (small oscillations at long time in $g_2(\tau)$ reflect the improper convergence of our MCS numerics near the edges of the outgoing wavepacket). In disagreement with the RWA however, we notice that the numerical data shows partial anti-bunching at zero delay, $g_2(0) > 0$, signaling the production of particles, as was revealed by the low-energy spectrum in Fig. 4.6(b). Thus particle production leads to physical effects that are potentially observable experimentally even when on resonance. This offset, which is zero in the RWA, is found to increase with α (see the upper middle of Fig. 4.12 for $k_0 = \Delta_R$). The incomplete cancellation here can be readily interpreted as a probability of emitting

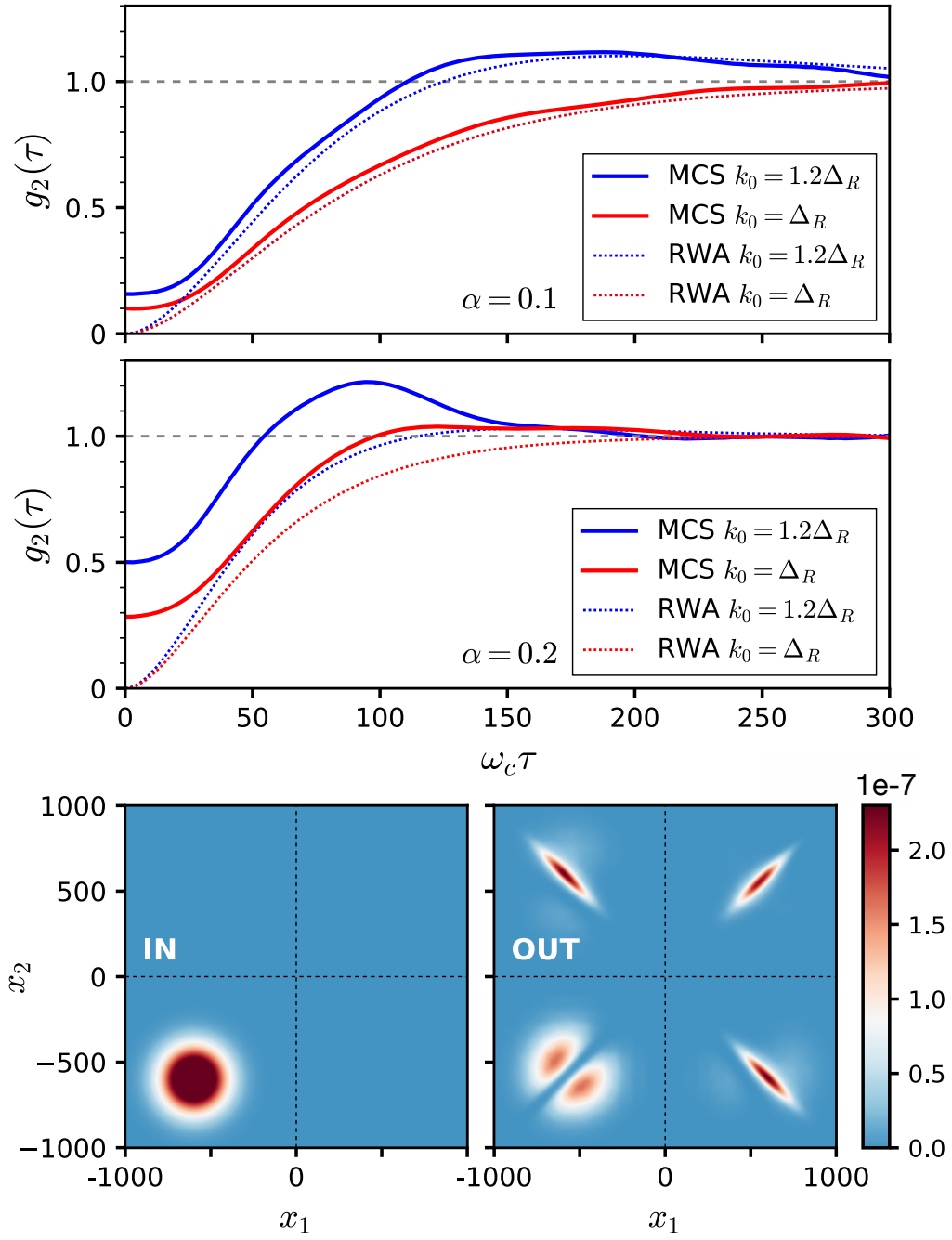

Figure 4.12: Second-order correlation function $g_2(\tau)$ in reflection, at $\alpha = 0.1$ (upper panel) and $\alpha = 0.2$ (middle panel). The dip at $\tau = 0$ is a standard signature of anti-bunching, but multiple photon emission seen in Fig. 4.6(a) at ultra-strong coupling leads to an incomplete cancellation, $g_2(0) > 0$. In the off-resonant case ($k_0 = 1.2\Delta_R$), particle production is enhanced relative to the single photon reflection, resulting in a stronger bunching ($g_2(\tau) > 1$) than predicted in the RWA. The MCS simulations were performed with the same parameters as in Fig. 4.6(b), except for the stronger coupling $\alpha = 0.2$, $\sigma = 0.004\omega_c$ and a hard cut-off that was used (see text). Bottom panel: Real space probability distribution of the two-photon states $|\alpha_{x_1,x_2}|^2/dx^2$ at the initial (left panel) and final (right panel) times of the simulation. One remarks the absence of reflection for two photons arriving at the same time on the qubit, as seen by the dip within the probability distribution located in the bottom left quadrant of the right panel.

many-photon states due to frequency down-conversion. Even more striking is the appearance of a large bunching signal at intermediate times in the off-resonant case (see the middle panel of Fig. 4.12 for $k_0 = 1.2\Delta_R$), which was not reported to our knowledge for the radiation of a *single* level qubit (bunching can be observed in spontaneous emission from multilevel atoms [100], due to a simpler cascade effect [14], or from multiqubit systems [15, 101, 102]). Here, bunching originates from the single-shot emission of three photons by the two-level system, a property that is only allowed at ultra-strong coupling. Even though particle production is comparable in the resonant case and the off-resonant case, the bunched signal only becomes sizable off-resonance, because the amplitude for a single photon to be reflected is strongly reduced.

As a nice illustration of the partitioning of the incoming beam by the two-level system, we show in the bottom panels of Fig. 4.12 the real space probability distribution of the two-photon states $|\alpha_{x_1,x_2}|^2/dx^2$ at the beginning and at the end of the time evolution. These results were obtained in the on-resonant case with $\alpha = 0.1$, by Fourier transforming to real space the k-space displacements. One can clearly see within the reflected signal (bottom-left quadrant in the right panel) a deep trench on the diagonal $x_1 = x_2 < 0$ with vanishing photon content (the incoming coherent state is shown in the bottom left panel for comparison). Two photons impinging simultaneously on the qubit have thus very low likelihood of both being reflected. This provides a direct visualization of photon anti-bunching, which arises because a single emitter can only reflect one photon at a time.

Thus, in this chapter we extended the MCS technique introduced in the chapter 3 to address the many-body scattering properties of a two-level system embedded in a waveguide in the regime of ultra-strong coupling. This problem is intrinsically non-perturbative in nature due to the large production of particles, and cannot be reliably addressed by the standard methods of quantum optics.

We have been able to characterize precisely the output field, by decomposing the reflected and transmitted photon wave-packets into Fock states, and also by computing temporal correlations. The main results are as follows. (i) The process by which one photon is absorbed and three photons are emitted dominates in the off-resonant low-power limit and leads to a broad spectrum of emission extending from zero frequency to the renormalized qubit frequency. (ii) In the resonant case as well, where the dominant inelastic emission near the resonant frequency is captured by the rotating wave approximation, there is a broad spectrum of weak inelastic transmission produced by the counter-rotating terms. (iii) The correlation function $g_2(\tau)$ in reflection is a sensitive measure of ultra-strong coupling physics. In particular, particle production implies that it needs not vanish at zero delay, $g_2(0) > 0$, and that it shows a bunching effect at a delay of the order of the inverse lifetime. (iv) Finally, we have found that perturbative predictions for the inelastic response [29] cannot be used simply by renormalizing the bare qubit resonance frequency and linewidth when the coupling becomes ultra-strong. A more consistent theory including self-energy effects should be developed for the future.

All our quantitive predictions have relevance for the ongoing experimental effort in pushing waveguide quantum electrodynamics to the ultra-strong coupling regime. The connection to future experiments opens in addition various research directions. One important issue is that superconducting qubits are rarely operated as truly perfect two-level systems. Reducing the non-linearity of the qubit is typically important to minimize the effect of random noise from the circuit, but this strongly diminishes of course the amplitude of the interesting non-linear signals, a topic we discuss in chapter 6. Thus, extending our methodology to fully realistic superconducting quantum circuits will be crucial to address whether particle-production can be sizable in practice.

Chapter 5

Photon Statistics in a Microwave Signal

In this chapter, we describe an experiment aimed at measuring the anti-bunching of photons in the signal reflected by a qubit strongly coupled to a waveguide. Here, we use the word "strong" in accordance with its common use in the literature: strong compared to the so-called "weak" coupling regime, so that the energy relaxation rate Γ due to the waveguide dominates the losses Γ_ϕ, but still small compared to the ultra-strong couplings investigated in the previous two chapters, where the rate Γ ranged from 10% to 90% of the qubit energy. More specifically, in this chapter we will be considering a coupling of the order of $\Gamma/2\pi = 30$ MHz, with $\Gamma/2\pi \gg \Gamma_\phi/2\pi \simeq 1$ MHz.

In section 4, we introduced the second-order correlation function g_2, and discussed how measuring $g_2[0] = \langle {a^\dagger}^2 a^2 \rangle / \langle a^\dagger a \rangle^2 = 0$ is evidence that a signal is anti-bunched. Previously, Hoi *et. al* succeeded in measuring $g_2[0] < 1$ in the signal reflected by a strongly coupled qubit [8], but due to limited measurement bandwidth, the measured value of $g_2[0]$ was only of the order of 0.5, as shown in Fig. 1.1e. As a reminder, the ideal $g_2[\tau]$ for a perfectly anti-bunched signal is a function that goes all the way to zero at $\tau = 0$, as shown by the g_2 curve in Fig. 4.4a, calculated using Eq. (D.11). The use of a parametric amplifier would have considerably increased the signal to noise ratio of that experiment, but at the time, parametric amplifiers did not have the required bandwidth to amplify the wide spectrum of the signal emitted by a qubit at a rate of 30 MHz.

With the recent development of *broadband* parametric amplifiers [103], it has become possible to perform this experiment with a much better signal to noise ratio. The aim of the experiment described in this chapter is therefore to measure, using a broadband parametric amplifier, a value of $g_2[0]$ very close to 0. It should be noted that the experiment is still ongoing, and that final results are not yet available. We will nonetheless present the developed simulation tools and the results obtained so far.

In the first section, we will present the qubit-waveguide design developed using a simulation software, and the characterization of sample properties after fabrication. In the second section, we will explain the various steps involved in demodulating the signal reflected from or transmitted through the qubit, and the extraction of the signal quadratures of interest. In the third section, we will provide the basic background required for calculating signal correlators, according to the chosen experimental setup. Following this, we will present the calculation of the g_1 and g_2 correlation functions on simple numerically-generated signals, in order to show that our code is working as expected for these simple signals. Finally, we will present our preliminary measurements of the g_1 and g_2 correlation functions.

The work presented in this chapter was carried out at the Tata Institute of Fundamental Research (TIFR), in Mumbai (India).

5.1 Sample fabrication and characterization

The qubit-waveguide system was designed based on simulations performed with AWR microwave office, a software that simulates the electromagnetic behavior of an electronic structure by solving Maxwell's equations using a finite element method (FEM). The samples were fabricated by depositing aluminum thin films on an intrinsic silicon chip in either a micro-strip design or a coplanar waveguide design (CPW) [104].

The final design of the CPW qubit-waveguide system is shown in Fig. 5.1a, where the grey area is the aluminum structure, and the white area the silicon chip. The waveguide is composed of 3 elements: the central strip and the two lateral ground planes. In this architecture, the electromagnetic field oscillates between the central strip and the outer ground planes, coplanar to the chip. The qubit, in the centre, is made of the two large rectangular capacitor plates and a SQUID joining them in-between, of which the linearized inductance is equal to 8 nH (drawn schematically on top of the design). In our AWR simulations, which are of course purely classical, the SQUID was modeled by a regular linear inductance corresponding to that of the SQUID at superconducting temperatures, that is as given by Eq. (2.52). The capacitors of the qubit were then shaped and positioned in AWR in such a way as to impose a coupling of about 30 MHz. In designing the qubit, care was also taken to keep it within the transmon regime ($E_J/E_C \sim 100$), so that the sensitivity to charge fluctuations remains low while at the same time allowing enough non-linearity for the qubit to behave as a good two-level quantum system. The reflection S_{11} and transmission S_{12} by the qubit as simulated by AWR are shown in Fig. 5.2a-b, from which we can read-off the resonance frequency $\omega_0/2\pi = 6.39$ GHz. Based on this value, as well as on the linear inductance of $L_{\text{lin}} = 8$ nH, the total capacitance of this qubit design was then estimated to be around $C = \omega_0^2/L_{\text{lin}} = 86.0$ fF, and from this value the ratio $E_J/E_C = 119$ was deduced.

Note the extension of the bottom capacitor plate at the level of the qubit in the electromagnetic structure (Fig. 5.1a). The reason for this adjustment is that the large cut in the upper ground plate, made to accommodate the qubit, creates an impedance mismatch leading to non-negligible reflection, even for signals far detuned above the qubit resonance, as shown by the purple-dashed line in Fig. 5.2b. The idea is then that by empirically adjusting the width of the gap opposite to the qubit, one can find a narrower gap width that reduces the impedance mismatch. As demonstrated by the solid orange curve in Fig. 5.2b, this adjustment allows us to bring down the off-resonant reflection above the qubit resonance by about 10 dB.

The whole device was fabricated on a high resistivity intrinsic silicon chip in two electron-beam lithography steps, with a strong dose for the rectangular plates and a weaker dose for the junctions. After depositing the aluminum using a double-angle evaporation, the sample was glued to a PCB[1] chip using silver epoxy which was designed and milled specifically for this sample. After wire-bonding of the sample (Fig. 5.1b), the PCB with the sample was clamped between two SMA connectors (Fig. 5.1c). Fig. 5.1d shows two of these devices tightly screwed to an OFHC copper plate, which itself is connected to the base plate of the dilution fridge that reaches 30 mK after cool down. On the opposite side of the copper bar is a superconducting coil, which is used to tune the resonance frequencies of the qubits by varying the magnetic flux

[1]Printed Circuit Board: 762 μm-thick layer of TMM6 dielectric between two layers of copper.

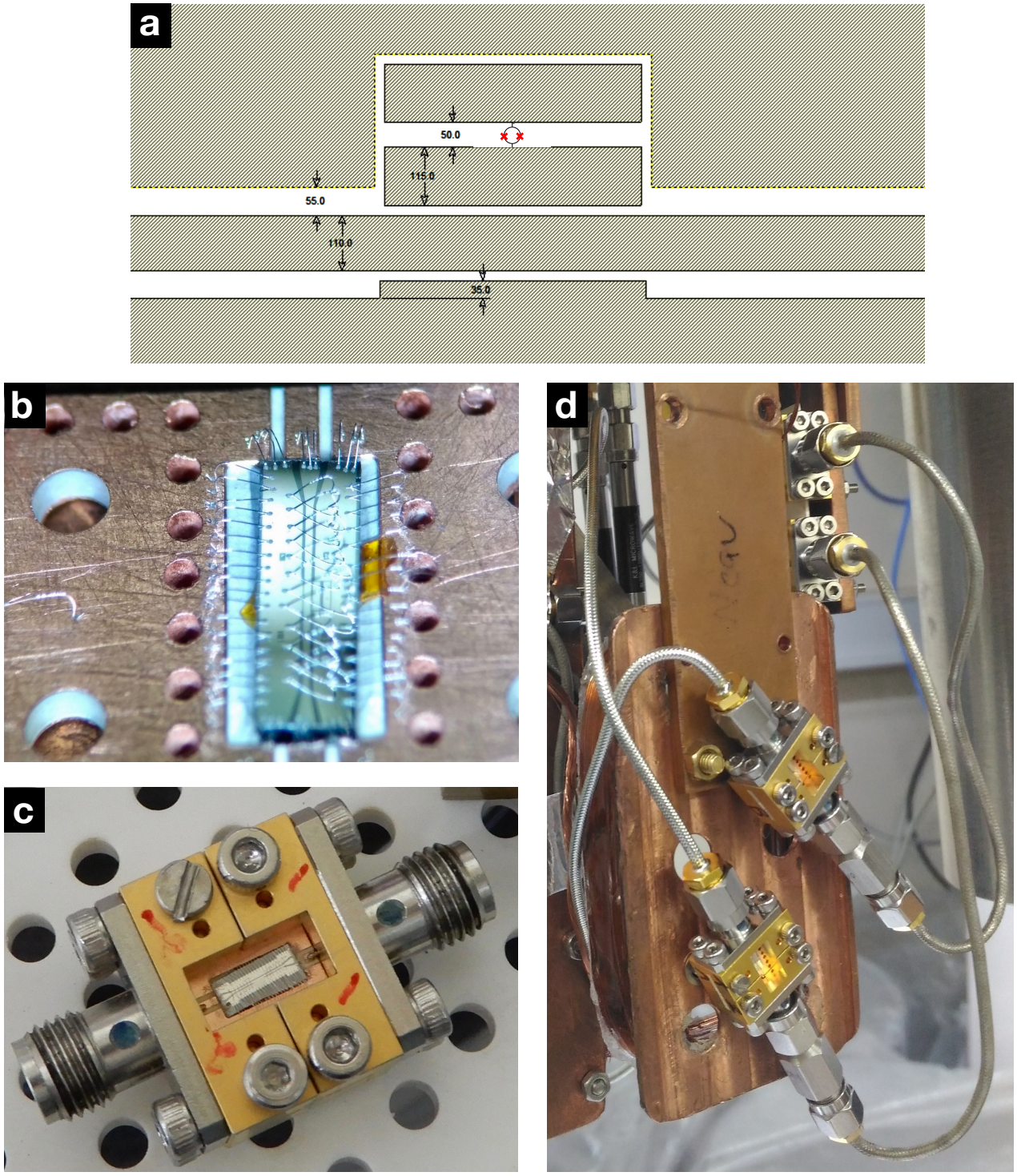

Figure 5.1: CPW sample fabrication and mounting: **(a)** AWR (microwave office) EM structure used to simulate the response of the qubit that is coupled via its large capacitance to the CPW transmission line. In these classical simulations, the SQUID is assigned via the AWR the non-linear inductance derived from the Josephson relation. **(b)** Picture of the sample after wire-bonding on the silicon chip. **(c)** Picture of the chip clamped between SMA connectors. **(d)** Two samples mounted on the 20 mK stage of the dilution fridge. Opposite to the samples is a superconducting coil used to tune the resonance frequency of the qubits.

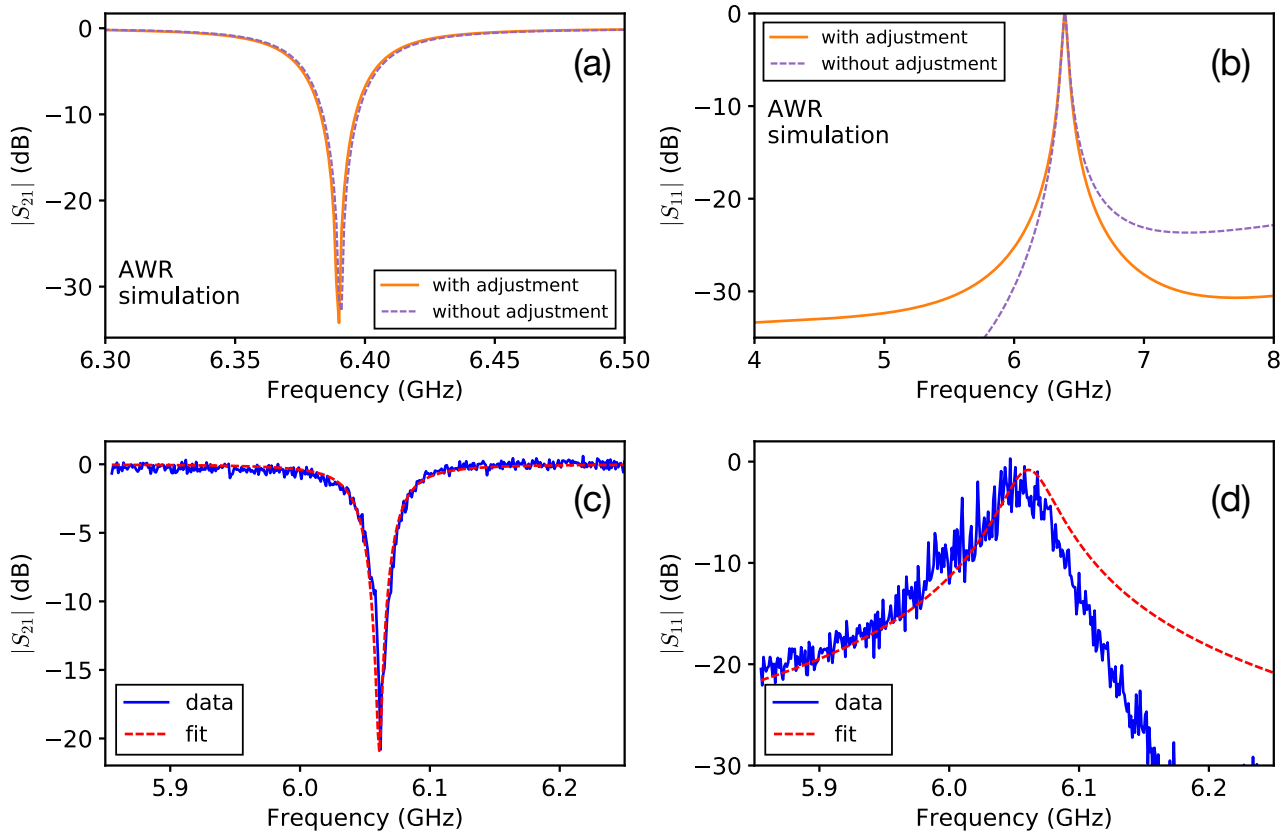

Figure 5.2: **Top panels:** AWR simulation of the qubit response before fabrication. The curves labelled "without adjustment" correspond to the predicted response of the qubit without the expansion of the bottom ground plate in Fig. 5.1a. **Lower panels:** CPW sample response. Fitted parameters using Eq. (5.1): $\Gamma/2\pi = 34$ MHz, $\Gamma_\phi/2\pi = 1.6$ MHz, $f_0 = 6.061$ GHz. Note also that it does not matter that the measured resonance frequencies differ from the ones initially designed by a few hundreds of MHz, as this will only slightly change the resonance frequency and the E_J/E_C ratio.

threading their SQUID loops.

The response of the qubits after cool down is shown in the lower panels of Fig. 5.2, which indicate that the resonance frequency is $\omega_0/2\pi = 6.06$ GHz. By probing the room-temperature resistance of the sample, we found the linear SQUID inductance to be $L_J = 6.10$ nH, from which we deduced the qubit capacitance C_J, and the ratio $E_J/E_C \sim 156$. The theoretical result for the reflection as a function of the detuning $\delta\omega = \omega - \omega_0$ is given by [5]:

$$S_{11}(\delta\omega) = \frac{\Gamma}{2\Gamma_\phi} \frac{1 - i\delta\omega/\Gamma_\phi}{1 + (\delta\omega/\Gamma_\phi)^2 + 2(\Omega^2/\Gamma_\phi\Gamma)}, \tag{5.1}$$

where Ω is the Rabi oscillation frequency. Fitting this expression to the data at low power (dashed lines in the bottom panels of Fig. 5.2), revealed the relaxation rate $\Gamma/2\pi = 34$ MHz and the pure dephasing $\Gamma_\phi/2\pi = 1.6$ MHz. Note also the strikingly asymmetric line-shape of the S_{11} in Fig. 5.2d. This is because of a Fano resonance [105], which arises here from the interference between the qubit-reflected signal and a spurious reflection due to an impedance mismatch in the transmission line.

Using the micro-strip sample, we were also able to fit the saturation of the qubit when the incident power is increased, as shown in Fig. 5.3. This demonstrates the strongly anharmonic nature of our sample.

The properties of the two samples mentioned above are summarized in Table 5.1. As

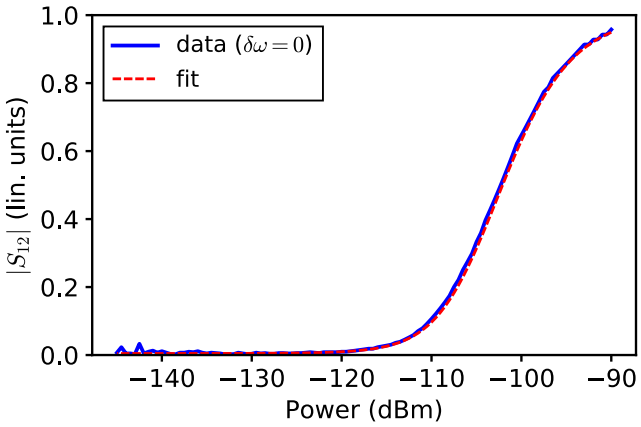

Figure 5.3: Qubit saturation fitted with Eq. (5.1). The qubit measured was fabricated using the micro-strip design, with parameters very similar to those of the CPW sample of Fig. 5.2c-d.

Samples	E_J/E_C	$\omega_0/2\pi$ (GHz)	$\Gamma/2\pi$ (MHz)	$\Gamma_\phi/2\pi$ (MHz)
Micro-strip sample	188	6.061	34	1.6
CPW sample	156.3	5.475	33.9	1.21

Table 5.1: List of samples and their measured/calculated parameters.

expected, both qubits present a relaxation rate much greater than the intrisinc losses, $\Gamma \gg \Gamma_\phi$, indicating that coupling strength is well within the strong coupling regime. In the following sections, all the results presented have been obtained using the CPW sample.

5.2 Signal processing

Having characterized the qubit via the S parameters the electromagnetic response, we will now describe how the quantum electrical signal is processed after it exits the sample. After using a chain of amplifiers (JPA, HEMT and room temperature amplifier), the signal will go through an analog demodulation, followed by a digital demodulation in software. The 5 main steps discussed in this section are illustrated in Fig. 5.4.

5.2.1 Analog signal processing

Classically, the voltage for a generic signal with carrier frequency ω_0 and amplitude $A(t)$ can be written as $A(t)\cos\big(\omega_0 t + \phi(t)\big)$. Since in the following we will only be interested in signals with constant average power and normalized correlation functions, let us set $A(t) = 1$ and work with dimensionless signals. Expanding the sine, we can cast the expression for the voltage into the "IQ" form:

$$\begin{aligned}\cos\big(\omega_0 t + \phi(t)\big) &= \cos(\omega_0 t)\cos(\phi(t)) - \sin(\omega_0 t)\sin(\phi(t)) \\ &= I(t)\cos(\omega_0 t) - Q(t)\sin(\omega_0 t) \\ &= \Re\Big[\big(I(t) + iQ(t)\big)e^{-i\omega_0 t}\Big],\end{aligned} \tag{5.2}$$

where in the second line we have defined the dimensionless field quadratures

$$I(t) = \cos(\phi(t)) \qquad \text{and} \qquad Q(t) = \sin(\phi(t)). \tag{5.3}$$

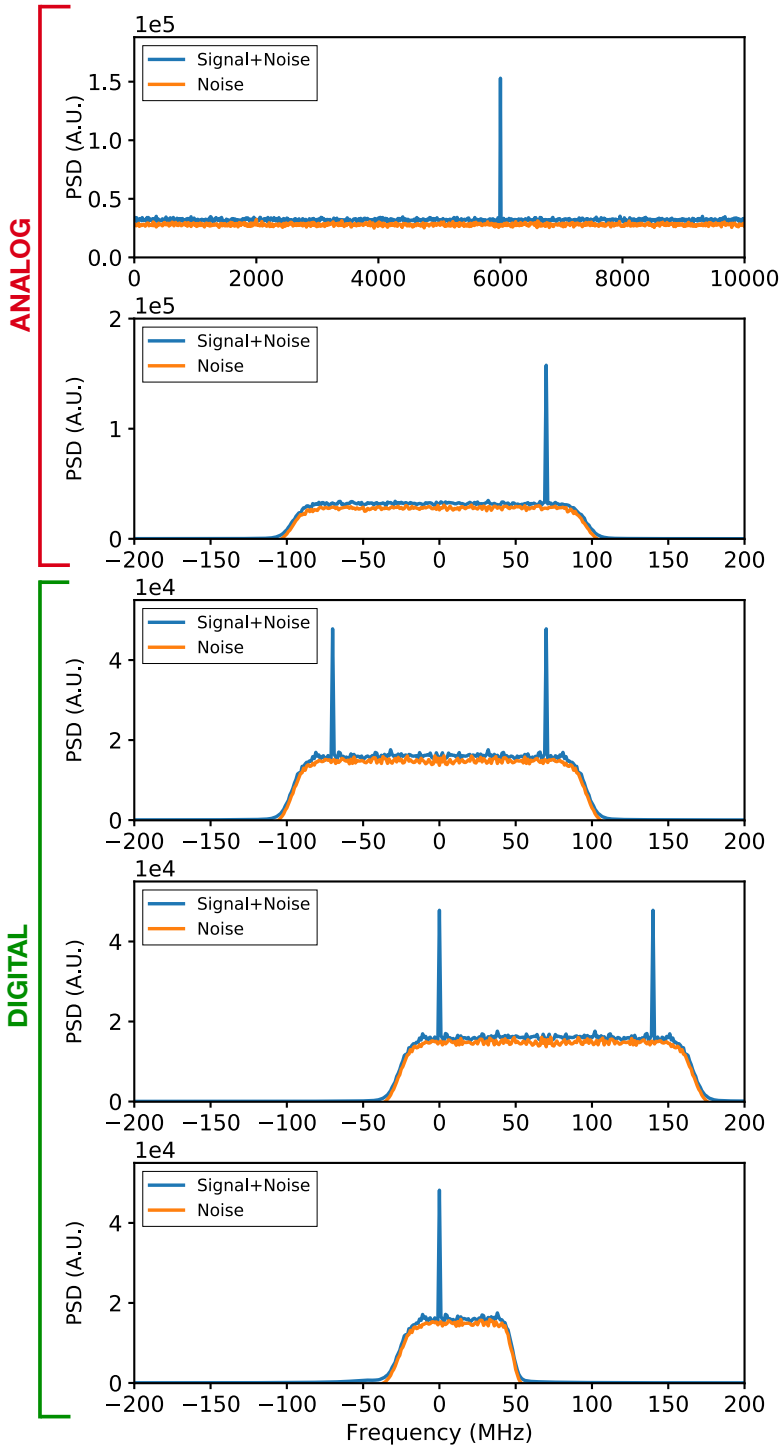

1. Simulated signal coming out of the sample. Gaussian noise, in orange with a small offset, is superposed with a coherent wave at ω/2π=6 GHz (in blue).

2. Analogue demodulation from 6 GHz to $\omega_{if}/2\pi$=70 MHz, followed by filtering of the noise above 100 MHz.

3. Digitisation of the voltage, that is the real part of the signal.

4. Digital demodulation to DC. The PSD shown here was computed on the complex signal $S(t) = I(t) + iQ(t)$, after having re-combined on solftware the quadratures I and Q (see Fig. 5.5).

5. Filtering out frequencies above and below 50MHz to remove the high-frequency replica. This is the PSD of the final complex signal on which the correlations will be computed.

Figure 5.4: Calculation of the power spectral density at the five steps of the simulated demodulation described in section 5.4. A schematic of the corresponding demodulation setup is provided in Fig. 5.5. To make these plots, a 6 GHz signal was initially generated numerically and superposed to Gaussian random noise. Note that during the demodulation stages, both the signal and the finite range of noise are shifted down in frequency. (the signal to noise ratio was not chosen to model the experiment, but only to provide an illustration)

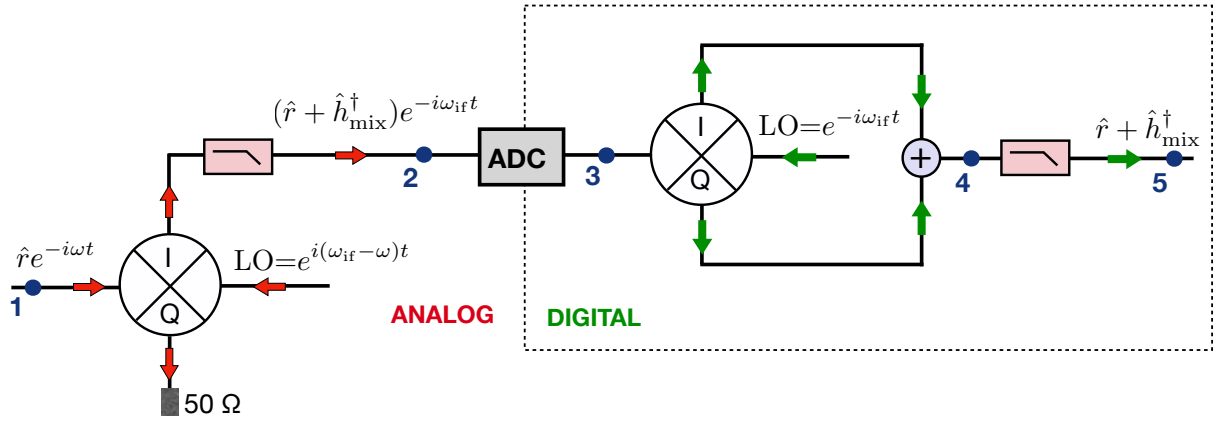

Figure 5.5: Schematic of the analog and digital down-conversion processes (compare with the corresponding power spectral densities of Fig. 5.4 computed to the 5 blue points). First, an analog mixer is used to down-convert a signal $\hat{r}e^{-i\omega t}$ with carrier frequency ω to the intermediate frequency $\omega_{\rm if}$, by multiplying it with a local oscillator (LO) at frequency $\omega_{\rm if}-\omega$. Note that only the I output is needed here as it alone contains the two quadratures of $\hat{r}$. Secondly, after digitization using an analog to digital converter (ADC), the digitized signal is further down-converted to DC, and the I and Q outputs are combined to reconstruct the initial signal $\hat{r}$. In the text, it is the amplified signal $\hat{a}'$ as given by Eq. (5.6) that has the role of $\hat{r}$.

To obtain a quantum mechanical description, we promote I and Q to operators, and define the corresponding creation and annihilation operators:

$$\hat{I}(t)=\frac{\hat{a}(t)+\hat{a}^\dagger(t)}{2}\qquad \hat{Q}(t)=-i\frac{\hat{a}(t)-\hat{a}^\dagger(t)}{2}. \tag{5.4}$$

These are the same operators we had defined in Eq. (2.5) verifying the bosonic commutation relations (2.6), except for the fact that we have switched from the $\hat{X}/\hat{P}$ to the $\hat{I}/\hat{Q}$ notation to conform with the usual notation in quantum microwave optics. Since $\hat{a}=\hat{I}+i\hat{Q}$, $\hat{a}$ is a convenient way of expressing the two quadratures of the signal at once:

$$\hat{a}(t)e^{-i\omega_0 t}=\big(\hat{I}(t)+i\hat{Q}(t)\big)e^{-i\omega_0 t}. \tag{5.5}$$

Let us now assume that (5.5) is the amplitude of the electrical signal leaving the sample, and entering the amplification/demodulation chain of the experiment. If we are considering, for instance, a signal that just got reflected on the qubit, then that signal is a train of anti-bunched photons. After being pre-amplified by a Josephson parametric amplifier at 30 mK, the signal $\hat{a}(t)$ is amplified by two amplifiers which add a background noise $h^\dagger_{\rm amp}$. Mathematically, this process of amplification can be written as [9, 106]:

$$\hat{a}\to\hat{a}'=\sqrt{\lambda}\hat{a}+\sqrt{\lambda-1}\hat{h}^\dagger_{\rm amp}, \tag{5.6}$$

where λ is total gain of the amplification chain. Note that this form of the amplified signal conserves the bosonic commutation relations.

Since the sampling frequency of our digitizer is 1 GHz, much lower than the signal frequency, we must down-convert our signal to an intermediate frequency $\omega_{\rm if}$. This is done by mixing the qubit signal with a local oscillator (LO) at frequency $\omega_{\rm q}-\omega_{\rm if}$, as illustrated in Fig. 5.5. Since both quadratures are present in each of the two outputs of the mixer, we can collect only the signal coming from the I output, and not loose any information. Note that

in addition to down-converting the signal, the mixer will also contribute a certain amount of noise $h^\dagger_{\text{mix}}$, leading to the following signal transformation [9]:

$$\hat{a} \to \hat{a}' = \hat{a} + \hat{h}^\dagger_{\text{mix}}, \tag{5.7}$$

Applying amplification (5.6) and mixing (5.7) to the signal (5.5), we obtain:

$$\hat{S}(t)e^{-i\omega_{\text{if}}t} = (\hat{I} + i\hat{Q})e^{-i\omega_{\text{if}}t}, \tag{5.8}$$

with the signal envelope given by

$$\hat{S} = \sqrt{\lambda}(\hat{a} + \hat{h}^\dagger), \tag{5.9}$$

Here we have denoted $\hat{h}^\dagger$ the combined noise contribution from amplification and mixing, as is standard practice [9, 107]:

$$\hat{h}^\dagger = \sqrt{\frac{\lambda - 1}{\lambda}}\hat{h}^\dagger_{\text{amp}} + \sqrt{\frac{1}{\lambda}}\hat{h}^\dagger_{\text{mix}}. \tag{5.10}$$

Note that because of the added noise $\hat{h}^\dagger_{\text{mix}}$ from the mixer, $\hat{S}$ and $\hat{S}^\dagger$ now commute:

$$\left[\hat{S}, \hat{S}^\dagger\right] = 0 \tag{5.11}$$

To provide an illustration of the successive transformations undergone by the signal, a 6 GHz coherent pulse superposed to Gaussian random noise was generated numerically to represent the amplified signal (5.6), and the corresponding power spectral density (PSD) was plotted in the top panel of Fig. 5.4. The PSD following down-conversion to an intermediate frequency $\omega_{\text{if}}/2\pi = 70$ MHz, and after filtering of frequencies below 100 MHz, is shown on the second panel of Fig. 5.4. The next steps of demodulation are digital, which we now discuss.

5.2.2 Digital signal processing

The voltage from the I output of the mixer is acquired on the memory card of the digitizer at the rate of 1 sample every nanosecond, with 1600 points per buffer, that is a total time of 1.6 μs. The digitized voltage is the real part of the signal (5.8):

$$\begin{aligned}\hat{V}(t) &= \Re(\hat{S}(t)e^{-i\omega_{\text{if}}t}) \\ &= \frac{1}{2}\left(\hat{S}(t)e^{i\omega_{\text{if}}t} + \hat{S}^\dagger(t)e^{-i\omega_{\text{if}}t}\right).\end{aligned} \tag{5.12}$$

As shown by the second line of Eq. (5.12), the digitization does not distinguish between positive and negative frequencies, meaning that the measured signal at frequency $f_{\text{if}} = \omega_{\text{if}}/2\pi$ includes part of the noise at $-f_{\text{if}}$, effectively reducing the signal to noise ratio by 50%. For this reason, the PSD right after digitizing the signal (shown in the third panel of Fig. 5.4) is symmetrical and contains both a positive peak and a negative peak.

The digitized signal is then brought down to DC by digitally mixing it with an LO at $\omega_{\text{if}}/2\pi = 70$ MHz. The resulting quadratures are then recombined on software into the complex signal $S = I + iQ$, which leads to the PSD in the fourth panel. Note that aside from the DC signal, we also have a 140 MHz replica, since mixing generates a signal at the difference and at the sum of the frequencies of the input signals. Finally, the high-frequency replica and the unwanted high-frequency noise are filtered out by applying a low-pass digital filter with cutoff frequency 50 MHz. The resulting PSD is shown in the bottom panel of Fig. 5.4.

This completes the demodulation of the signal. In the next section, we will describe how to compute the g_1 and g_2 correlation functions on this demodulated signal.

5.3 Two-time correlation functions

5.3.1 General formalism

Let us first define a generic two-time correlation function:

$$(S_1 \star S_2)[\tau] = \sum_{t=0}^{T-t_s} S_1^*(t) S_2(t+\tau), \tag{5.13}$$

where $\star$ denotes correlation and T is the total integration time (in our case $T = 1.6$ μs, the length of a buffer). The time delay τ takes the values $\tau = 0, t_s, ..., T - t_s$, and $t_s = 1/f_s$, where f_s is the acquisition frequency of the digitizer. Note that in (5.13) we take $S_2(t) = 0$ for $t > T - t_s$. Moreover, to give the correlation function the same weight for all τ (since the sum involves different numbers of elements for different τ values), it would also be necessary to apply an unbiased normalization [108] to the sum in (5.13). It turns out however that this is not necessary, as this correlation function is more efficiently computed via Fourier space. To do so, one first calculates the product of the Fourier transforms of the signals S_1 and S_2, and then applies an inverse transform to get back to the time domain:

$$(S_1 \star S_2)[\tau] = F^{-1}\Big(F^*(S_1)F(S_2)\Big)[\tau], \tag{5.14}$$

where the discrete Fourier transform (and inverse transform) for a signal $y(t)$ is given by:

$$F(y)[\nu] = \sum_{t=0}^{T-t_s} y(t) \mathrm{e}^{-i2\pi t\nu/N}, \qquad F^{-1}(y)[\tau] = \frac{1}{N} \sum_{\nu=0}^{f_s-\Delta\nu} y(\nu) \mathrm{e}^{i2\pi\tau\nu/N}, \tag{5.15}$$

with $N = T/f_s$ and $\Delta\nu = 1/T$. Here ν takes the values $\nu = f_s/2, ..., -\Delta\nu, 0, \Delta\nu, ..., f_s/2 - \Delta\nu$.

Using this correlation function, we can define the quantum mechanical second-order correlation functions of the amplitude and power of the signal [38]:

$$\begin{aligned} G_1[\tau] &= \langle \hat{a} \star \hat{a} \rangle [\tau], \\ G_2[\tau] &= \langle :\hat{a}^\dagger \hat{a} \star \hat{a}^\dagger \hat{a}: \rangle [\tau], \end{aligned} \tag{5.16}$$

where the normal ordering[2] :: is introduced here for the convenience of writing the G_2 function as a correlation of intensities $\hat{I} = \hat{a}^\dagger \hat{a}$. One can easily check that by writing down the full expression for G_2 in Eq. (5.16), and implementing the normal-ordering, one recovers the form of Eq. (4.1). Note that for correlations on operators, complex conjugation in Eq. (5.13) is replaced by Hermitian conjugation. The normalized forms of the functions are given by:

$$g_1[\tau] = \frac{G_1[\tau]}{G_1[0]}, \qquad g_2[\tau] = \frac{G_2[\tau]}{G_1[0]^2}. \tag{5.17}$$

Let us point out that $g_1[\tau]$ can be a complex quantity, while $g_2[\tau]$ is real by construction.

There are two main strategies for measuring correlation functions [109]. One is a Hanbury-Brown-Twiss (HBT) type of setup as shown on the left panel of Fig. 5.6, where the signal is split into two branches and amplified by two distinct amplification chains. In this case, cross-correlations are calculated between the signals digitized by the two distinct digitizers. Another possibility is to use only one detection chain and to calculate the *auto*-correlation of the signal,

[2] For any two operators A and B normal-ordering is defined as: $:A^\dagger B: = A^\dagger B$, $:BA^\dagger: = A^\dagger B$

as shown on the right panel of Fig. 5.6. In this case, noise correlations mix with the signal correlations of interest, and it is then necessary to subtract the noise contributions digitally, as we will explain in the next paragraph.

Both setups were implemented experimentally, but all the results presented in the following were obtained using the single-channel setup. The main reason for using this setup is that it involves less components. In particular, a technical difficulty is that a double-channel setup requires to have two broadband amplifiers at the beginning of the two measurement chains, each powered by a different pump line, and each operating with enough bandwidth around the frequency of the qubit. The single-channel setup on the other hand is lighter to implement, and therefore appears as a more convenient option. Because it requires noise cancellation however, the single-channel setup has the disadvantage of being very sensitive to any saturation in the amplification chain, as we will see in the following.

5.3.2 The HBT-type two-channel setup

In the two-channel setup, a hybrid coupler (symbolized in blue on Fig. 5.6) splits the signal $a(t)$ into two equal signals $b(t)$ and $c(t)$, which implies that $b(t) = c(t) = a(t)/\sqrt{2}$ (here we have dropped the carrier frequencies for the sake of clarity). It follows that we can derive the second-order correlation function of the amplitude of the signal $a(t)$ from the cross-correlation between the amplitudes $S_b(t)$ and $S_c(t)$:

$$\begin{aligned}
\Gamma_1^{\mathrm{bc}}[\tau] &= \langle S_b \star S_c \rangle [\tau] \\
&= \sqrt{\lambda_b \lambda_c} \langle (b + h_b^\dagger) \star (c + h_c^\dagger) \rangle [\tau] \\
&= \sqrt{\lambda_b \lambda_c} \langle b \star c \rangle [\tau] \\
&= \frac{\sqrt{\lambda_b \lambda_c}}{2} \langle a \star a \rangle [\tau] \\
&\equiv \frac{\sqrt{\lambda_b \lambda_c}}{2} G_1[\tau].
\end{aligned} \tag{5.18}$$

$G_1[\tau]$ is therefore directly proportional to $\Gamma_1^{\mathrm{bc}}[\tau]$. Similarly, we can directly obtain the $G_2[\tau]$ correlation function from the cross-correlation of the powers:

$$\begin{aligned}
\Gamma_2^{\mathrm{bc}}[\tau] &= \langle S_b^* S_b \star S_c^* S_c \rangle [\tau] \\
&= \lambda_b \lambda_c \langle (b^\dagger + h_b)(b + h_b^\dagger) \star (c^\dagger + h_c)(c + h_c^\dagger) \rangle [\tau] \\
&= \lambda_b \lambda_c \langle b^\dagger b \star c^\dagger c \rangle [\tau] \\
&= \frac{\lambda_b \lambda_c}{4} \langle : a^\dagger a \star a^\dagger a : \rangle [\tau] \\
&\equiv \frac{\lambda_b \lambda_c}{4} G_2[\tau].
\end{aligned} \tag{5.19}$$

Note that in deriving G_2 and G_1, all noise correlations conveniently cancel out, as the noise generated by the two individual amplification chains is uncorrelated.

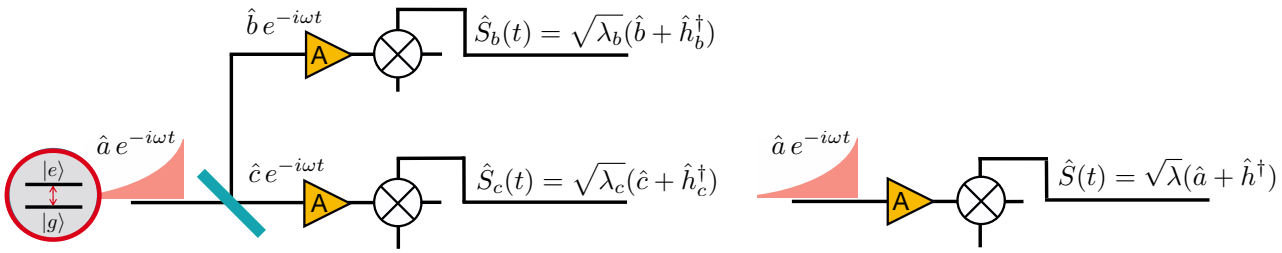

Figure 5.6: The one-channel versus the two channel measurement setups. The one channel setup has the advantage of using less components, but it requires performing noise subtraction, which is very sensitive to saturation. The two-channel setup has the advantage of being insensitive to the noise correlations between the two channels, but it uses more components.

5.3.3 The one-channel setup

With a single-line setup, the auto-correlation function of the amplitude $S(t)$ is given by:

$$\begin{aligned}\Gamma_1[\tau] &= \langle S \star S \rangle [\tau] \\ &= \lambda \langle (a + h^\dagger) \star (a + h^\dagger) \rangle [\tau] \\ &= \lambda \big(\langle a \star a \rangle [\tau] + \langle h^\dagger \star h^\dagger \rangle [\tau] \big),\end{aligned} \tag{5.20}$$

from which we deduce:

$$\lambda G_1[\tau] = \Gamma_1[\tau] - H_1[\tau], \tag{5.21}$$

where we have defined $H_1[\tau] = \lambda \langle h^\dagger \star h^\dagger \rangle [\tau]$. In contrast to the two-channel setup, here the auto-correlation of the signal includes the auto-correlation function of the noise amplitude $H_1[\tau]$. This quantity is obtained by calculating the auto-correlation function of the data acquired when the qubit drive is *'off'*.

Similarly, in the one-channel setup, the second-order correlation function of the power is given by:

$$\Gamma_2[\tau] = \langle |S|^2 \star |S|^2 \rangle [\tau]. \tag{5.22}$$

Unlike the previous correlation functions we have derived, it is not obvious how to relate this average product of four complex numbers (that is our digital waveform), to the expectation value of the normal-ordered product of signal operators a and $a^\dagger$ that define the G_2 function. Indeed, although $S^\dagger$ and S commute, as we pointed out in Eq. (5.11), $a^\dagger$ and a do not, which seems to suggest the odd consequence that different choices of ordering of the S and S^* complex numbers could result in different expressions for $G_2(\tau)$. It turns out however, that regarding the process of field measurement by annihilation of a photon, the optical equivalence theorem [42, 43, 38] states that it is only the expectation value of normally-ordered operators that is equivalent to the corresponding average of complex numbers. As an annihilation operator, this applies to $\hat{a}$, but for the noise on the other hand, ascribed to the creation operator $h^\dagger$, we have to use the opposite prescription and instead apply *anti-normal* ordering[3]. Thus, expanding

[3]For any two operators A and B anti-normal-ordering is defined in the following way: " $A^\dagger B$ " $= BA^\dagger$, " $BA^\dagger$ " $= BA^\dagger$

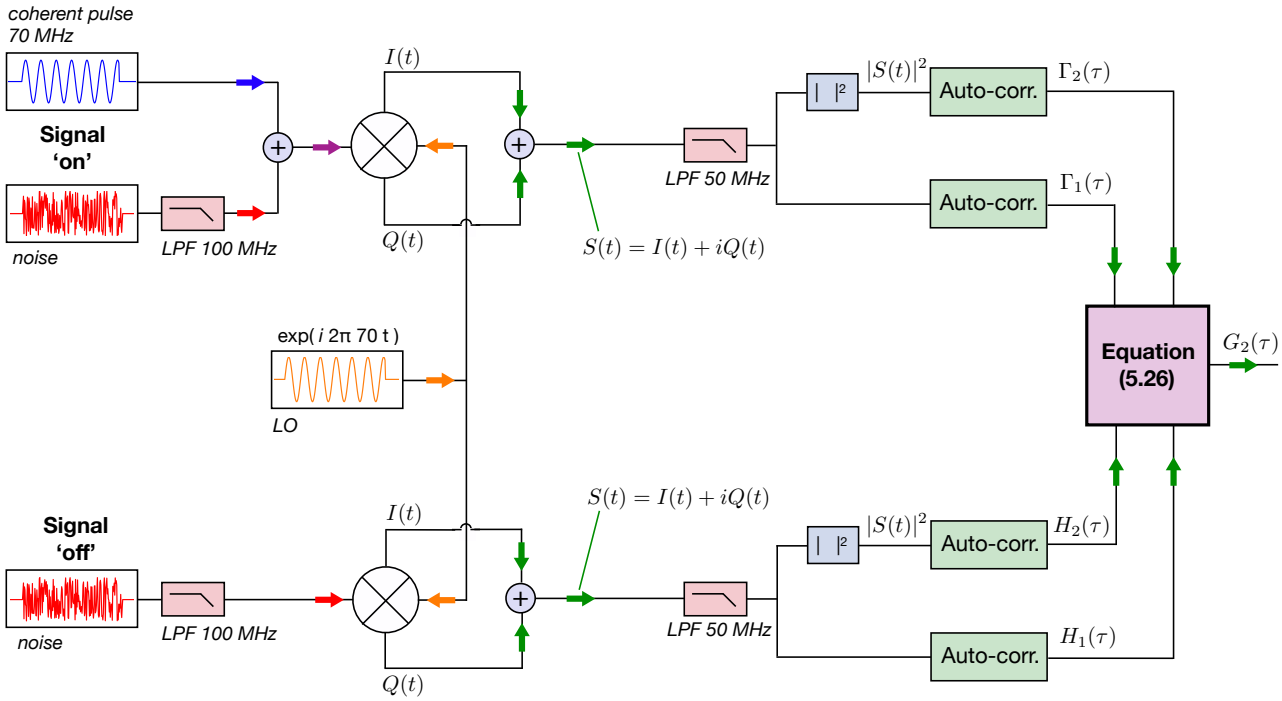

Figure 5.7: Block-diagram of the code used to calculate the G_2 function on a numerically generated noisy coherent signal in the case of a single-channel setup. Because correlations of the signal mix with the noise correlations, it is necessary to subtract the noise contribution using Eq. (5.26).

Eq. (5.22) while applying ordering to $a, a^\dagger$ and anti-normal ordering to $h, h^\dagger$, we obtain:

$$\begin{aligned}
\Gamma_2[\tau] &= \lambda^2 \left\langle |a + h^\dagger|^2 \star |a + h^\dagger|^2 \right\rangle [\tau] \\
&= \lambda^2 \left\langle (a^\dagger a + a^\dagger h^\dagger + ha + hh^\dagger) \star (a^\dagger a + a^\dagger h^\dagger + ha + hh^\dagger) \right\rangle [\tau] \\
&= \lambda^2 \Big[\left\langle :a^\dagger a \star a^\dagger a: \right\rangle + 2 \left\langle a^\dagger a \star hh^\dagger \right\rangle + \left\langle a^\dagger h^\dagger \star a^\dagger h^\dagger \right\rangle + \left\langle a^\dagger h^\dagger \star ha \right\rangle \\
&\qquad + \left\langle ha \star a^\dagger h^\dagger \right\rangle + \left\langle ha \star ha \right\rangle + \left\langle \text{“ } hh^\dagger \star hh^\dagger \text{ ”} \right\rangle \Big] \\
&= \lambda^2 \Big[\left\langle :a^\dagger a \star a^\dagger a: \right\rangle + 2 \left\langle a^\dagger a \right\rangle \left\langle hh^\dagger \right\rangle + \left\langle :a^\dagger \star a^\dagger: \right\rangle \left\langle h^\dagger \star h^\dagger \right\rangle + \left\langle a^\dagger \star a \right\rangle \left\langle h^\dagger \star h \right\rangle \\
&\qquad + \left\langle a \star a^\dagger \right\rangle \left\langle h \star h^\dagger \right\rangle + \left\langle a \star a \right\rangle \left\langle \text{“ } h \star h \text{ ”} \right\rangle + \left\langle \text{“ } hh^\dagger \star hh^\dagger \text{ ”} \right\rangle \Big], \qquad (5.23)
\end{aligned}$$

where we have introduced the second-order correlation function of the noise power:

$$H_2[\tau] = \lambda^2 \left\langle \text{“ } hh^\dagger \star hh^\dagger \text{ ”} \right\rangle [\tau]. \qquad (5.24)$$

For $\tau = 0$, note that $G_1[0] = \frac{1}{N} \sum_{t=0}^{T-t_s} \langle a^\dagger(t) a(t) \rangle = \langle a^\dagger a \rangle$, and similarly that $H_1[0] = \lambda \langle hh^\dagger \rangle$. Moreover, it is easy to show that:

$$\begin{aligned}
\left\langle a^\dagger \star a^\dagger \right\rangle [\tau] &= G_1[-\tau], \\
\lambda \left\langle h \star h \right\rangle [\tau] &= H_1[-\tau]. \qquad (5.25)
\end{aligned}$$

Combining everything, and noting that $\langle h \star h^\dagger \rangle = \langle h^\dagger \star h \rangle = 0$, Eq. (5.23) becomes:

$$\begin{aligned}
\lambda^2 G_2[\tau] = \Gamma_2[\tau] &- H_2[\tau] - 2\lambda G_1[0] H_1[0] \\
&- \lambda G_1[-\tau] H_1[\tau] - \lambda G_1[\tau] H_1[-\tau]. \qquad (5.26)
\end{aligned}$$

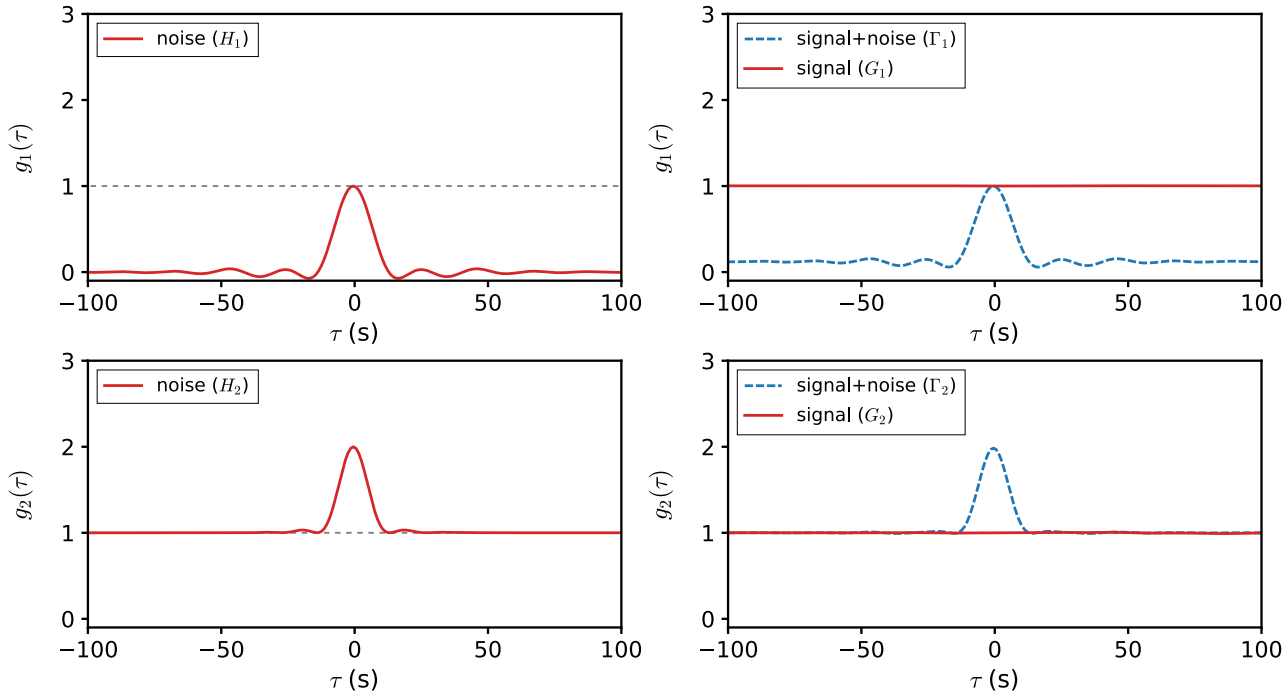

Figure 5.8: Normalized correlation functions g_1 and g_2 obtained from the code described by the block-diagram in Fig. 5.7.

Thus, to find the second-order correlation function $G_2[\tau]$, we will need to evaluate the noise correlations $H_1[\tau]$ and $H_2[\tau]$. In order to illustrate how this is done, we provide in the next subsection a demonstration of the calculation of the $G_2[\tau]$ function using a Python simulation.

5.3.4 Example of noise subtraction: g_1 and g_2 for a coherent state.

Here we present the calculation of the G_2 function, in the case of a single-channel setup, on a numerically generated noisy coherent state. As explained in the previous paragraph, the strategy will be to use Eq. (5.26) to extract the correlations of interest from the full signal. A block-diagram representation of the code is given in Fig. 5.7. Note that only the numerical generation of the signal (left-most blocks) differs from the data processing performed in the actual experiment, in which the signal is directly provided by the digitizer.

As shown in the top-left part of the diagram, the 70 MHz sinusoidal pulse with unit amplitude (in blue) is first added to Gaussian noise (in red) with a standard deviation of 3.5. This noisy signal is then demodulated to DC by mixing (i.e. multiplying) it with another coherent pulse $e^{i\omega_{\text{if}}t}$ (in orange, with $\omega_{\text{if}}/2\pi = 70$ MHz), with identical frequency. The resulting quadratures $I(t)$ and $Q(t)$ are then combined together and filtered with a 50 MHz low-pass filter, to obtain $S(t)$. The calculation of the auto-correlations of $S(t)$ and $|S(t)|^2$ then yields $\Gamma_1[\tau]$ and $\Gamma_2[\tau]$, which are combinations of signal-only correlations, $G_1[\tau]$ and $G_2[\tau]$, and of noise-only correlations, $H_1[\tau]$ and $H_2[\tau]$. In order to remove the noise contributions, we need to generate noise-only signal, which is done in the lower-left of the block-diagram. This noise-only signal is then demodulated, recombined, and filtered in exactly the same way as the noisy signal above. With $\Gamma_2[\tau]$, $\Gamma_1[\tau]$, $H_1[\tau]$ and $H_2[\tau]$ thus obtained, and Eq. (5.26), we can find $G_2[\tau]$. Finally, using Eq. (5.17), we obtain the normalized second-order correlation function $g_2[\tau]$.

The resulting correlation functions are shown in Fig. 5.8. As expected from standard

literature [33], we have that for pure Gaussian noise $g_1[0] = 1$, and $g_2[0] = 2$, as shown in the left panels. For $\tau \neq 0$, although one could have expected $g_1[\tau] = 0$ and $g_2[\tau] = 1$, the 50 MHz filter we applied induces a broadening of the central peak. The correlations of the noisy signal, plotted in dashed blue lines in the right panels, are very similar to those of the noise only correlations. This is consistent with the fact the noise generated in this simulation is about 12 times greater than the signal power. After performing noise subtraction with 10^6 averages, we obtain the second order correlation of the signal, given by the solid red line. As expected for a coherent signal, the result is $g_1[\tau] = 1$ and $g_2[\tau] = 1$, for all τ.

Ultimately, the goal of the experiment is to measure the second-order correlations of the signal reflected by a qubit. Since that signal is expected to be anti-bunched, meaning that at every point in the reflected signal there is at most one photon, the correlation function is expected to be $g_2[0] = 0$, as shown on Fig. 4.4a (discussed in Chapter 5).

An important requisite for this extraction of the G_2 function to work, is that the amplitude of the noise in the 'off' and 'on' pulses be strictly identical. In our simulations, of course, this is given, as the noise was intentionally generated identical in both pulses.

Finally, note that the number of averages required to converge the g_1 scales as $1 + P_N$, where P_N is the noise power, much less than the number of averages required to converge the g_2, which scales as $(1 + P_N^2)$ [9].

5.4 Measurements

5.4.1 The broadband parametric amplifier

A key element of this experiment is the broadband parametric amplifier [103]. A picture of the device is given in the left panel of Fig. 5.9. Using bandwidth engineering, the bandwidth of the amplifier was broadened to as much as 650 MHz, as shown by the gain profile in the right panel of Fig. 5.9. Because the pump operates at the central frequency of this band, only 300 MHz of this range are in practice available for signal amplification. Since the correlations we are looking for are of the order of 30 MHz, this provides more than enough bandwidth for performing this experiment.

It should be noted that these parametric amplifiers have to be biased at specific frequencies in order to generate the maximum bandwidth. This puts a constraint on the qubit frequency which should fall around the centre of the upper or lower half of the parametric amplifier bandwidth. As long as the qubit frequency is not below that frequency, the resonance can always be tuned down using the SQUID loop, and positioned in the middle of the upper or lower band of the gain profile.

5.4.2 Measurement of the g_1 and g_2 functions

The schematic of the full experimental setup is shown in Fig. 5.10. The protocol for generating an anti-bunched signal consists in sending a coherent signal through line 2: after the signal reaches the sample, the qubit reflects single photons while the rest of the signal is transmitted. The three circulators direct this train of single photons to the parametric amplifier, shown in red. The last circulator then reroutes the signal up towards the amplification and demodulation chain. Note that in this chapter, we will not present any results regarding the measurement of the g_2 function on anti-bunched signal, due to technical difficulties encountered in the experiment. Instead, we will present the measurement of the g_2 function for a coherent signal, which is a test that should be performed before any more complex measurement is attempted.

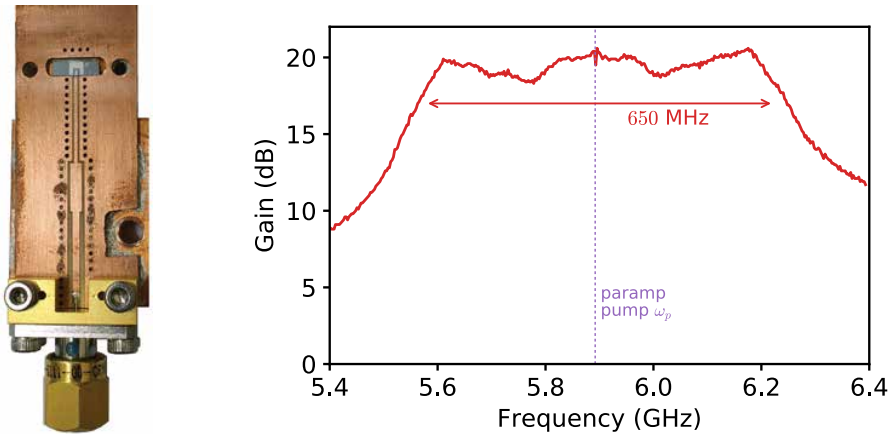

Figure 5.9: Broadband parametric amplifier gain profile. To obtain this profile the pump was set to 5.893 GHz. The signal cannot be amplified at precisely the frequency of the pump, since otherwise the signal and pump would interfere. Therefore, only the 300 MHz to the right or the left of the pump are available for amplification. Ideally, the qubit frequency should be in the middle of this band to benefit from the maximum bandwidth.

As was shown in the simulation of paragraph 5.3.4, the $g_1[\tau]$ and $g_2[\tau]$ functions for such a coherent state should give 1 for all τ.

To perform the measurement of the g_2 function on a coherent state, we set the frequency generated by the BNC to be off resonance from the qubit, and we connected the switch to line 1. This way, the signal reaches the qubit from the right and is completely transmitted through the sample. After exiting from the left, the signal is then amplified by the parametric amplifier and redirected to the demodulation chain the way it was described above for an anti-bunched signal. After being digitized, the signal is processed numerically as described by the block diagram in Fig. 5.7. The reader may refer back to Fig. 5.4, for an illustration of these 5 steps of analog and digital demodulation.

In the left panels of Fig. 5.11, we show in solid red the g_1 and g_2 thus obtained for a signal amplitude of 0.32 Vpp (Volt peak to peak). In the upper right panel is plotted the power spectral density (PSD) of the {signal+noise} and of the noise-alone, *right* after being digitized. The same are plotted in the bottom right panel, after having been demodulated to DC. Surprisingly, $g_1[\tau] > 1$ for $\tau \neq 0$ and $g_2[0] < 0$, when we were expecting to get $g_1[\tau] = 1$, and $g_2[0] = 0$. This result can be easily explained by noting from the power spectral density plots that the digitized noise power is higher when the noise is alone than when it is combined with the signal. This clearly indicates saturation of one of the electrical components of the setup. Moreover, coming back to the simulation of the previous section, one can tell from the bottom panels of Fig. 5.8 that the noise subtraction consists in subtracting from the {signal+noise} g_2 the central peak of the noise g_2. Clearly, therefore, if the power of the noise when the drive is 'off' is more than when it is 'on', the peak in the {signal+noise} g_2 will be over-subtracted, which will lead to the dip that we obtain.

To correct for this saturation, we considered decreasing numerically the noise digitized alone by multiplying it by a "noise factor", right before the calculation of the auto-correlation functions. If that noise factor is taken to be 0.925, the resulting g_1 is adequately corrected as shown by the dashed line in the top left panel of Fig. 5.11. The spurious dip in the g_2 is however only partially corrected, going from about -3 to about -1. The fact that this quick fix does not correct the g_2 by making it 1 indicates that the saturation is due to a complex non-linearity that cannot be modeled by simply including a noise factor.

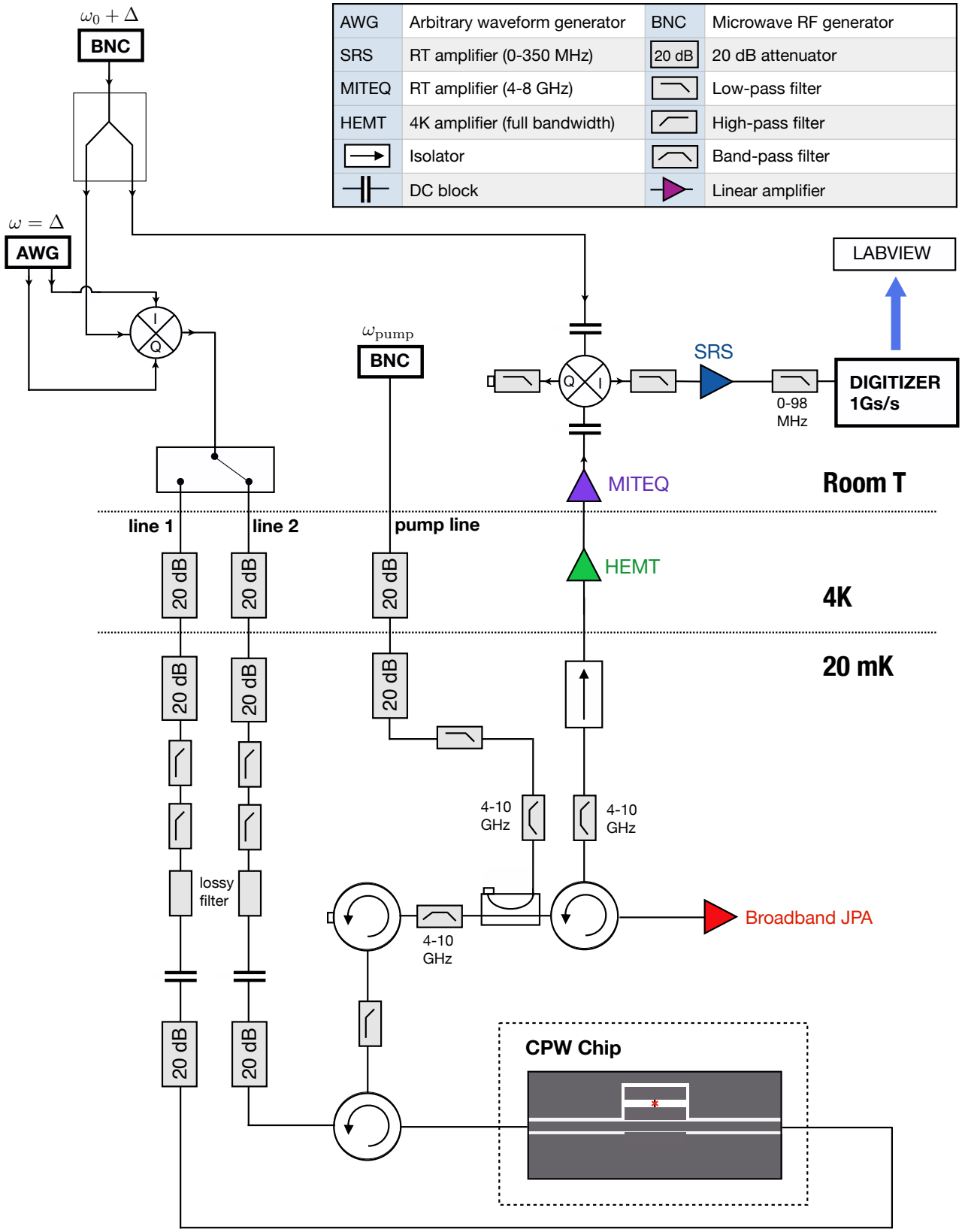

Figure 5.10: The complete experimental setup. As explained in the text, the switch set on line 2 corresponds to the configuration leading to the digitization of an anti-bunched signal, while the switch set on line 1, together with ω_0 detuned from the qubit resonance, corresponds to the digitization of a coherent signal. The latter configuration is the one studied in this chapter.

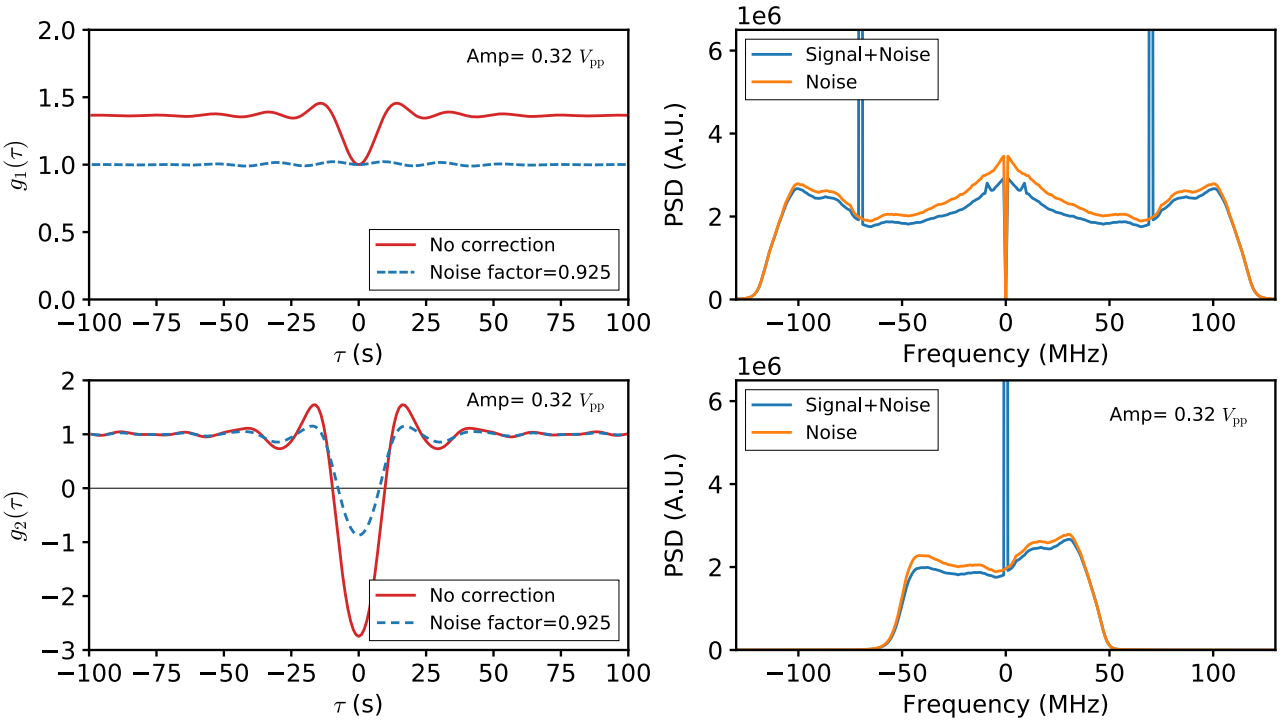

Figure 5.11: Left panels: g_1 and g_2 correlation functions of an off-resonant coherent signal with amplitude 0.32 Vpp sent through line 2 of the setup shown in Fig. 5.10. Top right panel: PSD of the signal right before digitization. Lower right panel: PSD of the demodulated signal on which the correlation functions were calculated.

To reduce this non-linearity causing the saturation, we attempted to decrease the signal power. In Fig. 5.12, we show the same results but with a signal of amplitude of 0.16 Vpp and 0.08 Vpp. From the PSD plots, in the bottom panels, it is clear that the saturation reduces with the signal power. On the other hand, instead of becoming smaller, the dip in the g_2 functions becomes deeper. This can be explained by the fact the amplitude of G_2 scales as the square of the signal power, while H_2 is independent of power (remember that G_2 and H_2 are the *un-normalized* second-order correlation functions of the power). Therefore, provided the imbalance between the 'on' and 'off' noises ($H_2^{\text{on}} - H_2^{\text{off}}$) scales as less than the square of the power, reducing the signal power will make the noise imbalance more dominant over the G_2. In other words, $G_2[0]$ reduces faster than $H_2^{\text{on}}[0] - H_2^{\text{off}}[0]$. This explains that for a signal amplitude of 0.08 Vpp, the dip of the g_2 function reaches all the way down to $g_2[0] = -40$.

The component most prone to saturation is the parametric amplifier, which has low saturation power. However, when performing the experiment without it, that is by using the HEMT and the room temperature amplifiers only for amplification, we still obtain a negative dip in the g_2 function. This suggests that another component must be saturating as well, which could be the mixer used in the demodulation chain. The next step is therefore to solve this issue of saturation, after which it will be checked that the g_2 function for a coherent state is indeed 1. We will then move on to measure the g_2 function for an anti-bunched signal, and attempt to obtain the expected dip at $\tau = 0$, signature of photon anti-bunching. Note that the experiment is still on-going at the time of the writing of this thesis.

Thus, in this experimental chapter, we have described an on-going attempt to measure second-order correlations in the signal reflected by a qubit strongly coupled to a transmission

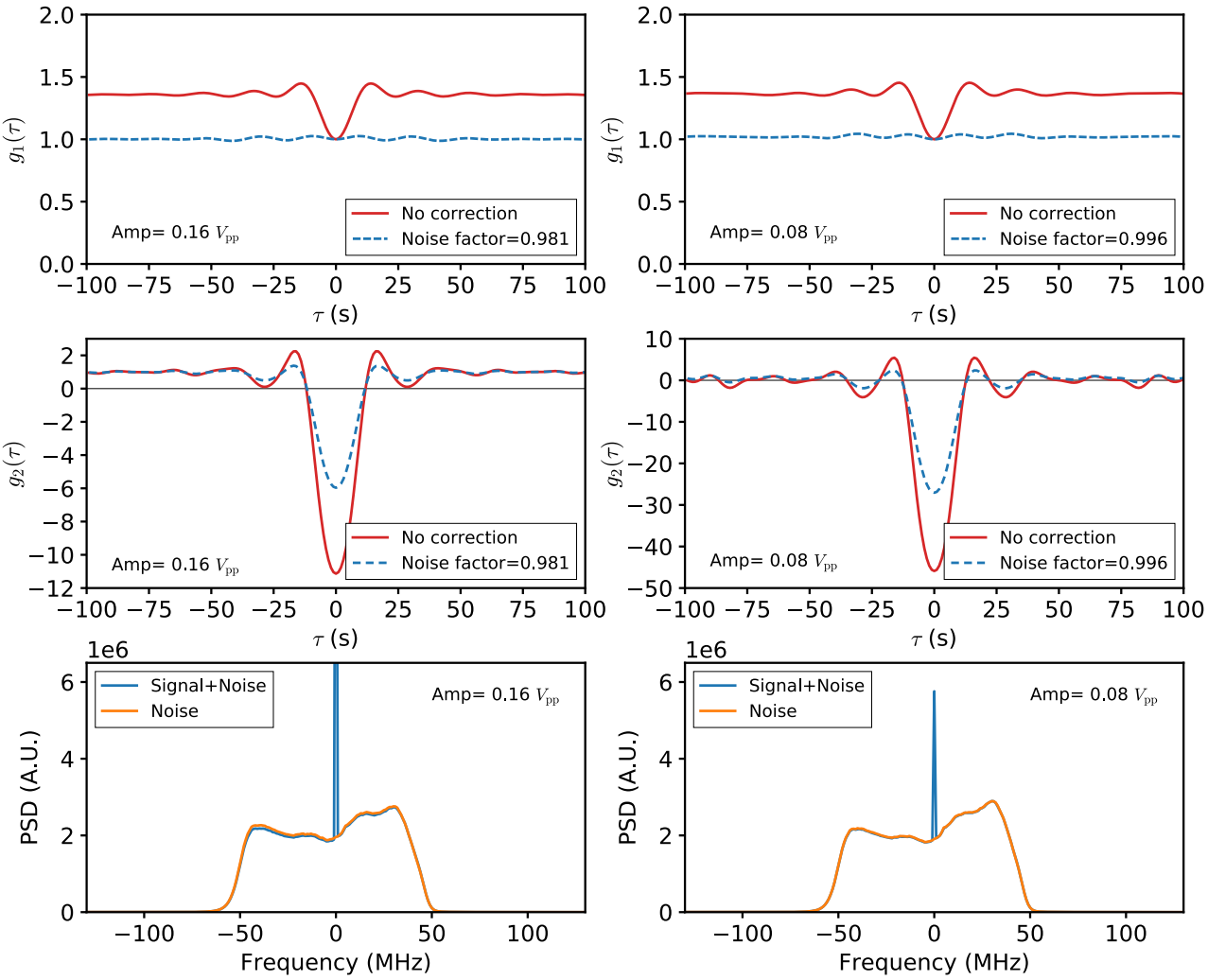

Figure 5.12: Middle and top panels: g_1 and g_2 correlation functions of an off-resonant coherent state of with amplitude 0.08 Vpp sent through line 2 of the setup shown in Fig. 5.10. Bottom panels: PSD of the demodulated signal on which the correlation functions were calculated.

line. After presenting the sample design and fabrication, we gave a detailed account of how the qubit parameters were extracted. Following this, we introduced the single- and double-channel setups which were used to attempt the experiment, and the corresponding procedures for extracting the correlations of interest. The code used to perform this extraction in the case of the single-channel setup was then presented, and was shown to successfully carry out the task it was designed for when applied to a numerically generated noisy coherent state. Finally, we discussed the measurement of the g_1 and g_2 correlation functions applied to an analog sinusoidal signal. Saturation in the amplification chain however hampered the noise correlation subtraction process, leading to distorted correlation functions. Although the second-order correlation function of the amplitude was successfully corrected by restoring the noise balance between the 'on' and 'off' signals, the second-order correlation of the power could not be corrected in this way.

Clearly, the measurement of quantum correlations in microwave signals is still in its infancy. We hope that the experimental developments and the simulation tools presented in this chapter will provide in the near future useful diagnostic tools for quantum signals traveling in superconducting waveguides, that could be used to investigate both the strong and ultra-strong coupling regimes of light-matter interaction.

Chapter 6

Conclusion and Perspectives

To summarize, the core result of the theoretical work presented in this thesis is a new variational technique based on a coherent state expansion for solving the spin-boson model. Similar in spirit to the frozen Gaussian technique introduced by E. J. Heller in the 1970s, it allows to harness the classical-like nature of the coherent state trajectories to describe the macroscopic dynamics arising in the ultra-strong coupling regime, while at the same time preserving the complete quantum behavior. Besides giving an intuitive description of the underlying physical machinery in terms of superpositions of classical-like trajectories, as we saw in the case of the Rabi model, the MCS technique also offers a dramatic computational speed-up for solving the dynamics of spin-bosonic systems involving a near continuum of modes. This numerical gain allowed us in section 3.3 to reach deep-ultra strong levels of coupling ($\alpha \simeq 1$) between a qubit and the thousands of modes present in the bosonic bath, and to demonstrate the surprising result that in this regime spontaneous emission of the qubit involves the emission of a Schrödinger cat state of light. Interestingly, this drastic speed-up seems to be very specific to the choice of the coherent states basis we have made, as such a speed-up was never reported in the context of the previously developed Gaussian-based methods (such as the recent variational multi-configuration Gaussian technique (vMCG)).

The success of the MCS technique with spontaneous emission then prompted us to move on to a more challenging simulation involving the scattering of a coherent state on a qubit. For the first time, we obtained the frequency resolved scattered spectra of the radiated field at the onset of the ultra-strong coupling regime ($\alpha = 0.1 - 0.3$). The most striking feature of those spectra is a low-energy continuum that arises from a non-RWA process involving the splitting of a single photon into 3 lower energy photons. This process had been first discovered perturbatively by Goldstein *et al.* for $\alpha \to 0$ (and for the value of $\alpha = 0.5$) [29], and in this work we have generalized this result numerically up to $\alpha = 0.3$. Moreover, the high accuracy we achieved with our technique allowed us to go beyond the study of scattered spectra, and to investigate the second-order correlations in the radiation scattered by the qubit. Most notably, the $g_2(\tau)$ function revealed striking features that are not present in the RWA treatment of the same problem. We have argued for example that the partial anti-bunching occurring at $t = 0$ ($0 < g_2(0) < 1$) is a signature of the particle production that was observed in the power spectra.

This study of the second-order correlations at ultra-strong coupling was in fact inspired by the theoretical considerations related to the experimental work presented in chapter 5. The aim of this experiment was to measure the photon anti-bunching in the field radiated by a strongly coupled qubit. Although final results are not yet available, we have presented the scattering measurements on the qubit that allowed us to characterize its properties and gave

an account of the different steps involved in processing of the signal emitted by the qbit. Following this, we defined the G_2 correlation function and described mathematically how it can be retrieved from the bare correlations of the signal that include noise contributions (Γ_1 and Γ_2). A python simulation was then presented that gave an example of the calculation of the g_2 function for a coherent state in the case of a two-channel setup, and that demonstrated our algorithm for subtracting the unwanted noise correlations. Finally, we showed preliminary results for the measurement of the second-order correlation function on a coherent state which was being used as a test. It turned out saturation in the amplification and/or demodulation chain did not allow us to perform an accurate subtraction of the noise correlations.

To conclude this thesis, we will present some perspectives on future research directions, and some ideas that are currently being investigated in the lab.

6.1 From the Cooper-pair box to the transmon qubit

The MCS technique we presented in this thesis focuses on the case of an ideal qubit with only two discrete levels, such as a Copper pair box ultra-strongly coupled to a waveguide. The Cooper pair box however generally suffers for significant charge noise that leads to very small coherence times, making it very impractical for most applications. For this reason, the transmon qubit is more commonly used, which is similar to a Cooper-pair box but with less anharmonicity, as discussed in section 2.2.4. It is therefore important that we generalize our model to this more practical implementation. We will discuss two possible strategies to achieve this.

One is to simply extend the 2-dimensional Hilbert space of the qubit to include higher energy levels of the transmon. Supposing that we want to include the first three energy levels of the qubit, we could rewrite our MCS ansatz as:

$$|\Psi(t)\rangle = \sum_{m=1}^{N_{\text{cs}}} \Big[a_m(t) \, |\alpha_m(t)\rangle \, |g\rangle + b_m(t) \, |\beta_m(t)\rangle \, |e\rangle + c_m(t) \, |\gamma_m(t)\rangle \, |f\rangle \Big]. \tag{6.1}$$

We have here used $\{|g\rangle, |e\rangle, |f\rangle\}$ to describe the qubit eigenbasis, as the $\{|\uparrow\rangle, |\downarrow\rangle\}$ notation used throughout this thesis was only useful as long as we could identify the two spin states with the two charge states of a Cooper pair box. We have also switched to Greek letters to designate the fields displacements. The present algorithm presented in this thesis could be easily generalized to this situation of a multilevel qubit (or to describe several coupled two-level system) provided the Hilbert space spanned by the discrete levels remains small.

Another possibility for extending our technique consists in describing the qubit quantum states using coherent states, in the same way the degrees of freedom of the bath are described. The idea here is that the transmon is basically an harmonic oscillator with a certain degree of anharmonicity, and that therefore it is likely that the representation used to describe the state of the harmonic modes of the chain will also be an effective way of describing the state of an oscillator with weak to moderate anharmonicity. Moreover, as we saw in Eq. (3.42), we already know that the first excited state of an oscillator can be described by using only two coherent states:

$$\lim_{\alpha \to 0} \frac{1}{2\alpha} \left(|\alpha\rangle - |-\alpha\rangle \right) = a^\dagger |0\rangle ,$$

and higher energy levels can be described in a similar fashion. Another advantage of this approach is that all the degrees of freedom are treated in the same way, as opposed to the

approach chosen in this thesis, where the qubit has its own discrete Hilbert space while the bosons are described by multi-mode coherent states. While we can be confident that the transmon regime can be captured with this new method, it is an open question wether generic quantum circuits can be tackled using coherent state superpositions.

6.2 Improvements to the numerical integrator

One of the main limitations of the MCS technique is that the iterative algorithm requires huge computation times as soon as the number of coherent states in the MCS ansatz (3.1) becomes large. The inversion of the linear system of equations (3.21) is the main cause of the high numerical cost.

An alternative that would avoid having to recalculate the solution at every time-step would be to use an iterative method, and more specifically the Krylov subspace method [110]. The idea is that the solution at time $t + dt$ can be found iteratively by starting from the nearly identical solution at t. One restriction for using the most optimized version of this technique, the Conjugate Gradient (CG), is that the matrix representing the system of equations be symmetric-positive-definite, which is not the case of our system of equations. Alternative Krylov-based methods, including optimal pre-conditioning strategies, are currently explored.

6.3 Production of many-body Bell states

As we have seen in this thesis, the ultra-strong interaction between a single qubit and a waveguide provides vast possibilities for doing many-body quantum optics. We present here an idea to build on the prediction of the down-conversion of a single photon described in chapter 4 to create a source of on-demand many-body Bell states built from photonic pairs.

As we have shown in chapter 4, in the ultra-strong coupling regime non-linear effects become prominent, allowing the down-conversion of an input single photon state into three photons with lower frequencies. According to quantum mechanics, these three photons are emitted in a quantum superposition of all the possible combinations of the available low-energy modes. If the number of available low-frequency modes is large enough therefore, the incoming single photon will be transformed into a quantum many-body entangled state.

The main difficulty is that the inelastic cross-sections are associated to a very low probability, because down-conversion from a qubit is a high order process. To enhance the splitting to the low-frequency many-mode entangled state, one could ultra-strongly couple the qubit to an auxiliary resonator with resonance frequency identical to that of the qubit. This original development would lead to a considerable increase of the re-emission by the qubit of a single photon at frequency Δ in the resonator, thus forcing the qubit to release the excess energy in the form of two entangled photons into the low frequency modes of the waveguide. Note that implementing this development implies that the resulting many-body entangled state now involves only two photons, as the third is emitted with high probability to the resonator.

The protocol of the proposed experiment, illustrated in Fig. 6.1, is the following: a photon with energy k_0 is sent through the waveguide towards a single qubit (with resonance frequency Δ), in a non-resonant condition such that $k_0 > \Delta$. Because of the dominant coupling to the auxiliary resonator (shown above the qubit), the qubit is compelled to give away a part of its energy by emitting one photon with frequency k_1 in that resonator, which implies that $k_1 = \Delta$. Since the incoming photon had energy k_0, $k_0 - \Delta$ of extra energy still remains, which can now only be released in the form of two photons with momenta k_2 and k_3 restricted as follows by

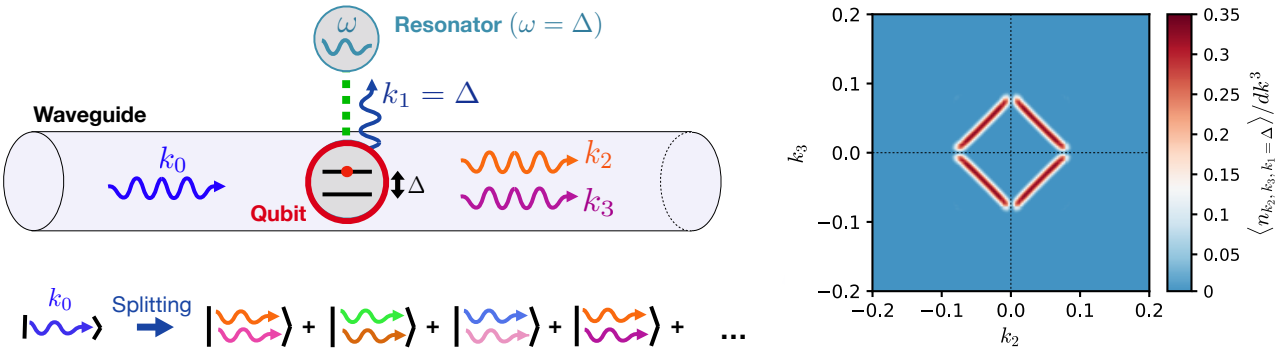

Figure 6.1: Left: illustration of the ultra-strongly coupled waveguide-qubit system. The experimental protocol taking place is the following: a photon with energy k_0 gets absorbed by the qubit, which ends up in the excited state. To relax back to the ground state, the qubit emits simultaneously one photon at $k_1 = \Delta$ to the ultra-strongly coupled auxiliary resonator and two photons at (k_2, k_3), such that $\Delta + k_2 + k_3 = k_0$. Because of the multitude of possible (k_2, k_3) states, these photonic pairs end up in an entangled state of all the possible combinations. The process involved is illustrated below the waveguide, where the various colors indicate the various frequencies of the two photons included in the many-body entangled superposition. Right panel: probability of measuring photonic pairs with energy (k_2, k_3) in the waveguide, discussed in paragraph 4.3.2.

conservation of energy:

$$k_2 + k_3 = k_0 - \Delta. \tag{6.2}$$

This is the origin of the entanglement: the photonic pair is emitted in all the states that verify this restriction at the same time. In the right panel of Fig. 6.1 is displayed the result from paragraph 4.3.2 (that did not consider any auxiliary cavity) which shows the probability of emitting photon pairs at the pair frequencies (k_2, k_3) for a fixed energy k_1 of the third photon. In such a scheme that does not involve a cavity, the resonant photon is dominantly emitted in the reflection channel.

The measurement of this entanglement would be performed using standard correlation measurement as demonstrated for example in a recent work [111]. This would involve measuring correlations between pairs of modes (k_2, k_3), for all the possible photon energies k_2, k_3. By measuring all the possible combinations, one obtains a global measure of the entanglement of the many-body wave-function, proving the realization of a massively-complex Bell state.

Previous experiments have demonstrated entanglement between a maximum of three modes [111], which makes this idea of generating many-mode entanglement an exciting experimental project.

6.4 Measurement of anti-bunching and high saturation power SPAs

We saw in chapter 5, that saturation in the setup prevented us from performing the noise subtraction required to recover the g_2 correlation function of the signal. This origin of this issue is most likely to be the low saturation power of the JPAs that was used in this experiment. Since the G_2 correlation is small compared to the correlation of the noise (H_2), any small noise imbalance between the noise when the signal is 'on' and the noise when the signal is 'off' will make it almost impossible to retrieve the correlation G_2.

To avoid this saturation problem, we will attempt again the experiment with the two channel setup. In this setup the signal is split in two right after being emitted by the qubit, and

two different amplification and demodulation chains process the two copies of signal independently. This way the noise arising in the two amplification chains is uncorrelated, which will avoid the saturation issues we have encountered. As mentioned in paragraph 5.3.1, this is a more challenging setup to implement.

Another idea that is currently being investigated is to use parametric amplifiers with a better dynamic range. In particular, a promising device is the SNAIL parametric amplifier (SPA) [112] developed by the Yale group, which consists of an array of Superconducting Nonlinear Asymmetric Inductive eLements (SNAILs). The SNAIL [113] is a device made of four SQUIDs designed to optimize the 3-wave mixing process used for amplification, and to reduce the 4-wave mixing Kerr nonlinearity which is suspected to lead to the saturation effects in JPAs [114, 112]. This amplifier will therefore provide us with a higher saturation power, which will hopefully allow the experiment to succeed. Because the bare SPA has narrow operational bandwidth, it will also be necessary to engineer the impedance of this SPA to make it broadband before is can be used to amplify the signal emitted by the strongly coupled qubit. This impedance matching can be done in a way similar to how the JPA was impedance matched for this experiment [103].

Appendices

Appendix A

Derivation of the spin-boson model from a superconducting circuit

This appendix follows the derivation by Snyman and Florens [27]. We start with the Hamiltonian

$$\hat{H} = \hat{H}_0 + \hat{H}_1 \tag{A.1}$$

of the circuit illustrated in Fig. 2.9, where the quadratic part $\hat{H}_0$ describes the linearized semi-infinite Josephson junction chain:

$$\hat{H}_0 = \frac{1}{2}\sum_{m,n=0}^{+\infty} \hat{N}_m \left(M^{-1}\right)_{mn} \hat{N}_n + \frac{1}{2}\sum_{m,n=0}^{+\infty} \hat{\varphi}_m V_{mn} \hat{\varphi}_n, \tag{A.2}$$

The impurity located at the end of the chain contains the only source of non-linearity of the problem, encoded in the Josephson energy:

$$\hat{H}_1 = -E_{Jd}\cos(\hat{\varphi}_0 - \hat{\varphi}_1). \tag{A.3}$$

The matrices M and V are defined in the main text. One would like to express $\hat{H}_0$ as a bath of independent oscillators that are linearly coupled to the impurity at site 0. This is achieved by expressing the set of harmonic variables in terms of bosonic operators:

$$\hat{N}_m = \frac{1}{\sqrt{2}}\int_0^{+\infty} dk\ \theta_{mk}(\hat{b}_k + \hat{b}_k^\dagger) \qquad m = 1, 2, \ldots, +\infty \tag{A.4}$$

$$\hat{\varphi}_m = \frac{i}{\sqrt{2}}\int_0^{+\infty} dk\ \xi_{mk}(\hat{b}_k - \hat{b}_k^\dagger) \qquad m = 1, 2, \ldots, +\infty \tag{A.5}$$

where ξ_{mk} and θ_{mk} are real numbers. We stress that the coordinates $(\hat{\varphi}_0, \hat{N}_0)$ at the end of the chain are not part of this decomposition, which will facilitate the later projection onto the two-level system. A first important relation follows from (A.4-A.5) by imposing the commutation relation $[\hat{\varphi}_m, \hat{N}_n] = i\delta_{m,n}$ and assuming standard algebra of the bosonic operators, namely $[\hat{b}_k, \hat{b}_k] = 0$, $[\hat{b}_k, \hat{b}_k^\dagger] = \delta(k - k')$:

$$\int_0^{+\infty} dk\ \xi_{mk}\theta_{nk} = \delta_{m,n}. \tag{A.6}$$

Let's focus first on the chain part of H_0 which contains the sites $m = 1, 2, \ldots, +\infty$ only, and impose that it is diagonalized by the bosonic operators:

$$H_0^{\text{chain}} = \frac{1}{2}\sum_{m,n\neq 0} \hat{N}_m \left(M^{-1}\right)_{mn} \hat{N}_n + \frac{1}{2}\sum_{m,n\neq 0} \hat{\varphi}_m V_{mn} \hat{\varphi}_n \equiv \int_0^{+\infty} dk\ \omega_k b_k^\dagger b_k, \tag{A.7}$$

with ω_k the positive frequencies of the normal modes. Using the decomposition (A.4-A.5), this provides several constraints on the set of unknown parameters:

$$0 = \sum_{m,n\neq 0} \left[\theta_{mk}\left(M^{-1}\right)_{mn}\theta_{nk'} - \xi_{mk}V_{mn}\xi_{nl'}\right] \tag{A.8}$$

$$2\omega_k\delta(k-k') = \sum_{m,n\neq 0} \left[\theta_{mk}\left(M^{-1}\right)_{mn}\theta_{nk'} + \xi_{mk}V_{mn}\xi_{nl'}\right]. \tag{A.9}$$

One can then take the sum and differences of Eq. (A.8-A.9), and integrate them respectively with $\int_0^{+\infty} dk\ \xi_{pk'}$ and with $\int_0^{+\infty} dk\ \theta_{pk'}$. Using the orthogonality condition (A.6), one readily gets:

$$\sum_{m\neq 0} \theta_{mk}\left(M^{-1}\right)_{mp} = \omega_k \xi_{pk} \tag{A.10}$$

$$\sum_{m\neq 0} \xi_{mk} V_{mp} = \omega_k \theta_{pk}. \tag{A.11}$$

In order to write the above equations as full matrix products, we extend the variables to the range $m = 0, 1, \ldots, +\infty$, and define the vectors $\vec{\xi}_k = (\xi_{0k}, \xi_{1k}, \xi_{2k}, \ldots)$ and $\vec{\theta}_k = (\theta_{0k}, \theta_{1k}, \theta_{2k}, \ldots)$. Noting that $V_{0p} = 0$ and with the condition $\theta_{0k} = 0$, we can write:

$$M^{-1}\vec{\theta}_k = \omega_k \vec{\xi}_k \tag{A.12}$$

$$V\vec{\xi}_k = \omega_k \vec{\theta}_k. \tag{A.13}$$

This results in an eigenvalue equation $M^{-1}V\xi_k = \omega_k^2 \xi_k$, which can be rewritten in the explicit form (that avoids inverting explicitly the matrix $\hat{M}$):

$$V\vec{\xi}_k = \omega_k^2 M \vec{\xi}_k. \tag{A.14}$$

This gives a set of conditions, for the different cases $m = 0$, $m = 1$, and $m \geq 2$:

$$\xi_{0k} = \frac{C_d}{C_{gd} + C_d}\xi_{1k} \tag{A.15}$$

$$\xi_{2k} = \left[1 - \frac{C_{\text{eff}}\omega_k}{(2e)^2 E_J - C\omega_k^2}\right]\xi_{1k} \tag{A.16}$$

$$\xi_{m+1,k} = 2\frac{(2e)^2 E_J - (C + C_g/2)\omega_k^2}{(2e)^2 E_J - C\omega_k^2}\xi_{mk} - \xi_{m-1,k} \tag{A.17}$$

with $C_{\text{eff}} = C_g + C_{gd}C_d/(C_{gd} + C_d)$. Now we exploit the fact that the Josephson chain is uniform except at the first two sites. We thus introduce scattering states that we parametrize as follows:

$$\xi_{mk} = N_k \cos\left[k(m - 1/2) - \delta_k\right] \quad m = 1,\ 2,\ \ldots, +\infty \tag{A.18}$$

with amplitude N_k and phase shift δ_k to be determined. Inserting the above expression into Eq. (A.17), we readily find the eigenfrequency:

$$\omega_k^2 = \frac{4(2e)^2 E_J \sin^2(k/2)}{C_g + 4C\sin^2(k/2)}. \tag{A.19}$$

The phase shift is then determined from condition (A.16), which reads:

$$\cos\left(\frac{3k}{2} - \delta_k\right) = \left[1 - \frac{C_{\text{eff}}\omega_k^2}{(2e)^2 E_J - C\omega_k^2}\right]\cos\left(\frac{k}{2} - \delta_k\right). \tag{A.20}$$

After some trigonometric manipulation and using Eq. (A.19), one finds the simple condition:

$$\sin(\delta_k) = \left[1 - \frac{C_g}{C_{\text{eff}}}\right]\sin(\delta_k - k), \tag{A.21}$$

which is solved explicitly as:

$$\delta_k = \arctan\left[\frac{\left(1 - \frac{C_g}{C_{\text{eff}}}\right)\sin(k)}{\left(1 - \frac{C_g}{C_{\text{eff}}}\right)\cos(k) - 1}\right]. \tag{A.22}$$

It is useful to establish an inverse relation between the harmonic variables and bosonic operators. Using (A.6), it is straightforward to check that the relations (A.4-A.5) can be inverted by:

$$\hat{b}_k = \frac{1}{\sqrt{2}}\sum_{m=1}^{\infty}\left[\xi_{mk}\hat{N}_m - i\theta_{mk}\hat{\varphi}_m\right] \tag{A.23}$$

$$\hat{b}_k^\dagger = \frac{1}{\sqrt{2}}\sum_{m=1}^{\infty}\left[\xi_{mk}\hat{N}_m + i\theta_{mk}\hat{\varphi}_m\right]. \tag{A.24}$$

One is equipped now to determine the normalization factor N_k, which follows from the commutation relation $[b_k, b_k^\dagger] = \delta(k-k')$. This relation is equivalent to the condition $\vec{\theta}_k \cdot \vec{\xi}_{k'} = \delta(k-k')$, which can be rewritten as:

$$\sum_{m,n\neq 0} \xi_{mk} V_{mn} \xi_{nk'} = \delta(k - k'). \tag{A.25}$$

From the explicit expression of V and the recursion relations (A.16-A.17), one gets:

$$\delta(k-k') = 4\frac{E_J}{\omega_k}\sin^2(k/2)\left[\frac{C_{\text{eff}} - C_g}{C_g}\xi_{1k}\xi_{1k'} + \sum_{m=1}^{+\infty}\xi_{mk}\xi_{mk'}\right]. \tag{A.26}$$

Finally, using expression (A.18) and the following standard algebraic identities $\sum_{m=1}^{\infty}\cos(mk) = \pi\delta(k) - 1/2$ and $\sum_{m=1}^{\infty}\sin(mk) = 1/[2\tan(k/2)]$, one finds:

$$\delta(k-k') = 2\pi\frac{E_J}{\omega_k}\sin^2(k/2)N_k^2\delta(k-k') + \text{Finite Terms}, \tag{A.27}$$

where we have singled out the delta-function contribution. Let us prove that the finite terms are actually zero, which implies the choice of normalization:

$$N_k = \frac{1}{\sin(k/2)}\sqrt{\frac{\omega_k}{2\pi E_J}}. \tag{A.28}$$

For this purpose, let us show that $\vec{\theta}_k \cdot \vec{\xi}_{k'} = 0$ for all $k \neq k'$. The proof relies on equations (A.12-A.13):

$$\omega_{k'}^2 \vec{\theta}_k \cdot \vec{\xi}_{k'} = \vec{\theta}_k \cdot M^{-1} V \vec{\xi}_{k'} = \left(V M^{-1} \vec{\theta}_k\right)^{\mathrm{T}} \xi_{k'} = \omega_k^2 \vec{\theta}_k \cdot \vec{\xi}_{k'}. \tag{A.29}$$

Since ω_k^2 is a monotonous function of k, the scalar product $\vec{\theta}_k \cdot \vec{\xi}_{k'}$ indeed vanishes for $k \neq k'$.

The impurity part of the quadratic Hamiltonian (A.2) related to the site $m = 0$ reads:

$$\hat{H}_0^{\mathrm{imp}} = \frac{1}{2} \left(M^{-1}\right)_{00} \hat{N}_0^2 + \hat{N}_0 \sum_{m=1}^{+\infty} \left(M^{-1}\right)_{0m} \hat{N}_m. \tag{A.30}$$

Using Eq. (2.103) and Eq. (A.10), we finally obtain an exact and remarkably compact expression for the full Hamiltonian in terms of the normal modes and of the variables at the first two sites of the Josephson chain:

$$\hat{H} = \frac{1}{2} \left(M^{-1}\right)_{00} \hat{N}_0^2 + \int_0^\pi dk \; \omega_k \hat{b}_k^\dagger \hat{b}_k + \hat{N}_0 \int_0^\pi dk \; g_k (\hat{b}_k + \hat{b}_k^\dagger) - E_{Jd} \cos(\hat{\varphi}_0 - \hat{\varphi}_1), \tag{A.31}$$

where we have introduced the mode-dependent coupling constant

$$g_k = \frac{1}{2} \frac{C_d}{C_{gd} + C_d} \frac{1}{\sin(k/2)} \sqrt{\frac{\omega_k^3}{2\pi E_J}} \cos\left[\frac{k}{2} - \arctan\left(\frac{(1 - C_g/C_{\mathrm{eff}}) \sin(k)}{(1 - C_g/C_{\mathrm{eff}}) \cos(k) - 1}\right)\right]. \tag{A.32}$$

Appendix B

Expression for the dynamical error

To check the accuracy of our wave-function, we monitor the norm of the following vector:

$$|\Phi\rangle = \left(i\frac{\overrightarrow{\partial_t}}{2} - i\frac{\overleftarrow{\partial_t}}{2} - H\right)|\Psi\rangle \tag{B.1}$$

$$\boxed{\langle\Phi|\Phi\rangle = -\frac{1}{2}\Re\big(\langle\Psi|\ \overrightarrow{\partial_t}\ \overrightarrow{\partial_t}\ |\Psi\rangle\big) + \frac{1}{2}\langle\Psi|\ \overleftarrow{\partial_t}\ \overrightarrow{\partial_t}\ |\Psi\rangle + 2\ i\ \Re\big(\langle\Psi|\ \overleftarrow{\partial_t}\ H\ |\Psi\rangle\big) + \langle\Psi|H^2|\Psi\rangle} \tag{B.2}$$

- $\langle\Psi|\ \overleftarrow{\partial_t}\ \overrightarrow{\partial_t}\ |\Psi\rangle = \sum_{i,j}\langle f_i|f_j\rangle\Big[\dot{p}_i^*\dot{p}_j - \frac{\dot{p}_i^*p_j}{2}\sum_k(\dot{f}_j^k f_j^{k*} + \dot{f}_j^{k*}f_j^k - 2\dot{f}_j^k f_i^{k*})$
$- \frac{p_i^*\dot{p}_j}{2}\sum_k(\dot{f}_i^k f_i^{k*} + \dot{f}_i^{k*}f_i^k - 2\dot{f}_i^{k*}f_j^k) + \frac{p_i^*p_j}{4}\Big(\Big(\sum_k \dot{f}_i^k f_i^{k*} + \dot{f}_i^{k*}f_i^k\Big)\Big(\sum_k \dot{f}_j^k f_j^{k*} + \dot{f}_j^{k*}f_j^k - 2\dot{f}_j^k f_i^{k*}\Big)$
$- 2\Big(\sum_k \dot{f}_i^{k*}f_j^k\Big)\Big(\sum_k \dot{f}_j^k f_j^{k*} + \dot{f}_j^{k*}f_j^k\Big) + 4\Big(\sum_k \dot{f}_i^{k*}f_j^k\Big)\Big(\sum_k \dot{f}_j^k f_i^{k*}\Big) + 4\Big(\sum_k \dot{f}_i^{k*}\dot{f}_j^k\Big)\Big)\Big]$
$+ (p\to q,\ f\to h)$
- $\langle\Psi|\ \overrightarrow{\partial_t}\ \overrightarrow{\partial_t}\ |\Psi\rangle = \sum_{i,j} p_j^*\langle f_j|f_i\rangle\Big[\ddot{p}_i - \dot{p}_i\Big(\sum_k \dot{f}_i^{k*}f_i^k + \dot{f}_i^k f_i^{k*} - 2\dot{f}_i^k f_j^{k*}\Big)$
$+ \frac{p_i}{4}\Big(\sum_k \dot{f}_i^{k*}f_i^k + \dot{f}_i^k f_i^{k*} - 2\dot{f}_i^k f_j^{k*}\Big)^2 - \frac{p_i}{2}\Big(\sum_k 2\Re(\ddot{f}_i^{k*}f_i^k) + 2\dot{f}_i^{k*}\dot{f}_i^k - 2\ddot{f}_i^k f_j^{k*}\Big)\Big]$
$+ (p\to q,\ f\to h)$
- $\langle\Psi|H^2|\Psi\rangle = \frac{\Delta^2}{4} + \frac{1}{4}\sum_k g_k^2 + \Delta\sum_{i,j} p_i^*q_j\langle f_i|h_j\rangle\Big(\sum_k \omega_k f_i^{k*}h_j^k\Big) + \sum_{i,j} p_i^*p_j\langle f_i|f_j\rangle\Big[\Big(\sum_k \omega_k^2 f_i^{k*}f_j^k\Big)$
$+ (\Omega_{ij}^f)^2 + \frac{1}{4}(G_{ij}^f)^2 - \frac{1}{2}\Big(\sum_k g_k\omega_k(f_i^{k*} + f_j^k) - G_{ij}^f\Omega_{ij}^f\Big)\Big] + (p\to q,\ f\to h,\ g\to -g)$
- $\langle\Psi|\ \overleftarrow{\partial_t}\ H\ |\Psi\rangle = \sum_{i,j} p_j\langle f_i|f_j\rangle\Big[\Big(\dot{p}_i^* - \frac{1}{2}p_i^*\Big(\sum_k \dot{f}_i^k f_i^{k*} + \dot{f}_i^{k*}f_i^k\Big)\Big)\Big(\Omega_{ij}^f - \frac{1}{2}G_{ij}^f\Big)$
$+ p_i^*\Big(\sum_k \dot{f}_i^{k*}f_j^k\Big)\Big(\Omega_{ij}^f - \frac{1}{2}G_{ij}^f\Big) + p_i^*\Big(\sum_k \omega_k f_i^{k*}f_j^k - \frac{g_k}{2}\dot{f}_i^{k*}\Big)\Big] + \frac{\Delta}{2}\sum_{i,j} q_j\langle f_i|h_j\rangle\Big[\dot{p}_i^*$
$- \frac{1}{2}p_i^*\Big(\sum_k \dot{f}_i^k f_i^{k*} + \dot{f}_i^{k*}f_i^k - 2\dot{f}_i^{k*}h_j^k\Big)\Big] + (p\to q,\ f\to h,\ g\to -g)$

Appendix C

The Wigner distribution of a superposition of coherent states

C.1 For single-mode coherent states

The Wigner function $W^{[\rho]}(\alpha)$ of a density matrix $\rho = |\Psi\rangle\langle\Psi|$ function is defined as the two-dimensional Fourier transform of the symmetric order characteristic function [18]:

$$W^{[\rho]}(\alpha) = \frac{1}{\pi^2}\int d^2\ \lambda C_s^{[\rho]}(\lambda)e^{\alpha\lambda^* - \alpha^*\lambda} \tag{C.1}$$

where

$$C_s^{[\rho]}(\lambda) = \langle\Psi|D(\lambda)|\Psi\rangle = \langle\Psi|e^{\lambda a^\dagger - \lambda^* a}|\Psi\rangle \tag{C.2}$$

For a superposition of coherent states

$$|\Psi\rangle = \sum_n p_n\,|f_n\rangle\,, \tag{C.3}$$

corresponding for example to one of the sectors of the MCS state vector, the characteristic function becomes:

$$C_s^{[\rho]}(\lambda) = \sum_{m,n} p_m^* p_n\,\langle f_m|f_n\rangle\,e^{\frac{1}{2}(|\lambda|^2 + 2(\lambda^* f_n - \lambda f_m^*))} \tag{C.4}$$

Obtaining the Wigner function is then a matter of evaluating the following 2-dimensional Gaussian integral:

$$\begin{aligned} I_{mn} &= \int d^2\lambda\ e^{|\lambda|^2/2 + 2(\lambda^* f_n - \lambda f_m^*)}e^{\alpha\lambda^* - \alpha^*\lambda} \\ &= 2\pi e^{2(f_m^* - \alpha^*)(f_n - \alpha)} \end{aligned} \tag{C.5}$$

Substituting eq. (C.10) and this result into eq. (C.1), we deduce that

$$W^{[\rho]}(\alpha) = \frac{2}{\pi}\sum_{m,n} p_m^* p_n e^{-2(f_m^* - \alpha^*)(f_n - \alpha)}\,\langle f_m|f_n\rangle \tag{C.6}$$

C.2 For a many-mode wave-packet

For calculating the Wigner function of the propagating multi-mode wave-packets in paragraph 3.3.3, we define an effective mode b on which to evaluate the characteristic function $C_s^{[\rho]}(\lambda)$:

$$b^\dagger = \sum_x w(x) a^\dagger(x) \Theta(x - L_K) \tag{C.7}$$

where we have used a normalized complex optimized temporal filter $w(x)$ given by:

$$w(x) = \frac{z(x)}{\sqrt{\sum_x |z(x)|^2}} \tag{C.8}$$

with

$$z(x) = \sum_n p_n f_{n,x}. \tag{C.9}$$

We can then evaluate the characteristic function, which now reads

$$C_s^{[\rho]}(\lambda) = \sum_{m,n} p_m^* p_n \langle f_m | f_n \rangle \, e^{\frac{1}{2}(|\lambda|^2 + 2(\lambda^* w^*(x) f_n - \lambda w(x) f_m^*))} \tag{C.10}$$

In the same way as for the single-mode coherent states above, we obtain the Wigner distribution:

$$W^{[\rho]}(\alpha) = \frac{2}{\pi} \sum_{m,n} p_m^* p_n \langle f_m | f_n \rangle \, e^{-2(\sum_x w(x) f_{m,x}^* - \alpha^*)(\sum_x w^*(x) f_{n,x} - \alpha)} \tag{C.11}$$

Appendix D

RWA input-output theory for coherent state scattering

Transport under the RWA is obtained in the framework of input-output theory. Within the RWA, it is convenient to work in the basis that diagonalizes the qubit. After applying the rotating wave approximation to the Hamiltonian (4.2) and assuming a frequency-independent coupling constant $g_k = \sqrt{\alpha \Delta_R}$, one finds that the system is described by the Hamiltonian

$$H = \frac{\Delta}{2}\sigma^z + \int d\omega \, \frac{g}{2}\left[\sigma^+(r_\omega + l_\omega) + h.c.\right] + \int d\omega \, \omega\left(r_\omega^\dagger r_\omega - l_\omega^\dagger l_\omega\right), \tag{D.1}$$

where σ^+ is the raising operator of the qubit and $r_\omega(l_\omega)$ is the annihilation operator for the right(left)-going mode of frequency ω. We adapt standard input-output theory for a monochromatic input [33, 115, 116, 117] to our case of an incoming wavepacket with finite energy resolution. The input-output relations remains the usual ones,

$$\begin{aligned} r_{\text{out}}(t) &= r_{\text{in}}(t) - i\sqrt{\frac{\pi}{2}}\, g\, \sigma^-(t) \\ l_{\text{out}}(t) &= -i\sqrt{\frac{\pi}{2}}\, g\, \sigma^-(t), \end{aligned} \tag{D.2}$$

where we have taken into account that the wavepacket is incoming from the left. This allows one to find the properties of the outgoing field from a master equation for the qubit. In this way the power spectrum is calculated through the first-order correlation function $G^{(1)}(t_1, t_2) = \langle a_{\text{out}}^\dagger(t_1) a_{\text{out}}(t_2)\rangle$ (a_{out} being either r_{out} or l_{out}) by a Fourier transform

$$S[\omega] = \frac{1}{2\pi}\int_0^T dt_1 \int_0^T dt_2 \, G^{(1)}(t_1, t_2) e^{i\omega(t_2 - t_1)}. \tag{D.3}$$

We assume that the qubit is located at $x = 0$ while the input and output ends are located at $x = -T/2$ and $T/2$ respectively ($c = 1$). From the definition (4.9), we can write the wavepacket in frequency as

$$z(\omega) = \sqrt{\bar{n}}\left(\frac{1}{2\pi\sigma^2}\right)^{\frac{1}{4}} e^{-\frac{(\omega - k_0)^2}{4\sigma^2}} e^{i(\omega - k_0)T/2}, \tag{D.4}$$

through which the input coherent state is defined as

$$|z^+\rangle = \exp\left[\int dk \, z(\omega)\, r_{\text{in}}^\dagger(\omega) - h.c.\right]|0\rangle\,, \tag{D.5}$$

where $r_{\text{in}}^{\dagger}(\omega)$ is the standard monochromatic input operator [33, 115, 116, 117] of input-output theory. The input operator describing our wavepacket then satisfies

$$r_{\text{in}}(t)\,|z^{+}\rangle = \frac{1}{\sqrt{2\pi}} A(t) e^{-ik_0 t}\,|z^{+}\rangle \qquad \text{and} \qquad l_{\text{in}}(t)\,|z^{+}\rangle = 0, \tag{D.6}$$

where $A(t) = \tilde{A} e^{-\sigma^2 (t-T/2)^2}$ with $\tilde{A} = \sqrt{2\bar{n}\sigma}(2\pi)^{1/4}$ is the change of driving amplitude on the qubit with time as the Gaussian wavepacket passes by.

A master question for the qubit density matrix ρ_s is then obtained by transforming to the Schrödinger picture using a rotating frame given by $k_0\sigma^z/2$

$$\begin{aligned} \frac{\partial}{\partial t}\rho_{\text{s}} &= -i\big[\frac{\delta}{2}\sigma^z + gA(t)\sigma_+ + h.c.\,, \rho_{\text{s}}\big] + \pi g^2\big(\sigma_-\rho_{\text{s}}\sigma_+ - \frac{1}{2}\{\rho_{\text{s}}, \sigma_+\sigma_-\}\big) \\ &\equiv \mathcal{L}\rho_{\text{s}}, \end{aligned} \tag{D.7}$$

where in the last line we have defined the system's Liouvillian $\mathcal{L}$. Note that decay rate is $\Gamma = \pi g^2 = \pi\alpha\Delta_{\text{R}}$. For the reflected light, the power spectrum can be shown to be

$$S_{\text{L}}[\omega] = g^2 \int_0^T dt \int_{-t}^{T-t} d\tau\, \langle \sigma_+(t)\sigma_-(t+\tau)\rangle\, e^{i(\omega-k_0)\tau}; \tag{D.8}$$

two additional interference terms appear in the power spectrum for the transmitted light and are not given here. The desired correlation function $\langle\sigma_+(t)\sigma_-(t+\tau)\rangle$ can be calculated through the master equation (D.7) and the quantum regression theorem [99]:

$$\langle \sigma_+(t)\sigma_-(t+\tau)\rangle = \text{Tr}\Big\{\sigma_+(0)e^{-\mathcal{L}\tau}\big[\sigma_-(0)\rho_{\text{s}}(t)\big]\Big\}. \tag{D.9}$$

In the main text, we also require the RWA 2$^{\text{nd}}$ order correlation function of the radiation emitted towards the left $\langle l_{\text{out}}^{\dagger}(t) l_{\text{out}}^{\dagger}(t+\tau) l_{\text{out}}(t+\tau) l_{\text{out}}(t)\rangle$. To calculate this field correlator, we first express it in terms of a spin correlator by using Eq. (D.2):

$$\langle l_{\text{out}}^{\dagger}(t) l_{\text{out}}^{\dagger}(t+\tau) l_{\text{out}}(t+\tau) l_{\text{out}}(t)\rangle = \frac{\pi^2}{4} g^4 \langle \sigma_+(t)\sigma_+(t+\tau)\sigma_-(t+\tau)\sigma_-(t)\rangle \tag{D.10}$$

Using again the quantum regression theorem, we then obtain an expression for the spin correlator:

$$\langle \sigma_+(t)\sigma_+(t+\tau)\sigma_-(t+\tau)\sigma_-(t)\rangle = \text{Tr}\Big\{\sigma_+(0)\sigma_-(0)e^{\mathcal{L}\tau}\big[\sigma_-(0)\rho_{\text{s}}(t)\sigma_+(0)\big]\Big\} \tag{D.11}$$

Appendix E

Perturbative calculation of the $1 \to 3$ photon process

We proceed here with a systematic study of particle production spectra in the off-resonant case, as a function of incoming momentum k_0 (see right panel of Fig. 4.8). A weak coupling calculation of the one photon to three photon conversion process (see Fig. 4.9) was given in the $\alpha \to 0$ limit in Ref. [29]. We have found that this theory can quantitatively account for our data at small α upon two important modifications.

First, as we already saw from the frequency shift in the reflection spectrum in Fig. 4.5, one must replace the bare qubit frequency Δ by the renormalized quantity Δ_R within the analytical results given by the perturbative approach. Second, the golden rule value for the qubit linewidth appearing in the transmission line-shape, given by $\Gamma = \pi\alpha\Delta$ at small α, cannot be used. For the elastic response, one can use reliably $\Gamma_R = \pi\alpha\Delta_R$ up to moderate values of α. However, we find that the renormalized broadening parameter $\gamma_R^{\rm inel}$ entering the inelastic response function for fixed value of the incoming momentum k_0 is not given by Γ_R, but rather displays a strong momentum dependence, $\gamma_R^{\rm inel} = \gamma_R(k_0)$. This is not completely unexpected, since a consistent calculation should include the full momentum variation of the self-energy, and we found that the theory of Ref. [29] is very sensitive to the way the inelastic regularization is implemented. For the present purpose, we will only use a phenomenological model that uses (as fitting parameters) only two renormalized quantities Δ_R and $\gamma_R(k_0)$ within the perturbative formula:

$$\langle n_k \rangle_{\rm 3photon} = \frac{\alpha^4}{8}\Delta_R^2 \int_0^{k_0-k} {\rm d}k_1 \; k k_0 k_1 k_2 \left| \frac{k_0 k k_1 k_2 - k_\Delta^2(k^2+k_1^2+k_2^2+kk_1+kk_2+k_1k_2)+3k_\Delta^4}{(k^2-k_\Delta^2)(k_0^2-k_\Delta^2)(k_1^2-k_\Delta^2)(k_2^2-k_\Delta^2)} \right|^2, \tag{E.1}$$

with $k_2 = k_0 - k_1 - k$ and $k_\Delta = \Delta_R + i\gamma_R(k_0)$, with Δ_R the renormalized qubit frequency and $\gamma_R(k_0)$ the linewidth describing the inelastic spectrum, which is fitted from our numerical data. The resulting comparison is shown in the right panel of Fig. 4.8 for $\alpha = 0.1$, with excellent quantitative agreement.

Bibliography

[1] A. O. Caldeira and A. J. Leggett, *Quantum tunnelling in a dissipative system*, Annals of Physics, 149 (1983), pp. 374–456.

[2] Y. Nakamura, Y. A. Pashkin, and J. S. Tsai, *Coherent control of macroscopic quantum states in a single-Cooper-pair box*, Nature, 398 (1999), pp. 786–788.

[3] I. Chiorescu, Y. Nakamura, C. J. P. M. Harmans, and J. E. Mooij, *Coherent Quantum Dynamics of a Superconducting Flux Qubit*, Science, 299 (2003), pp. 1869–1871.

[4] V. Bouchiat, D. Vion, P. Joyez, D. Esteve, and M. H. Devoret, *Quantum coherence with a single Cooper pair*, Phys. Scr., 1998 (1998), p. 165.

[5] O. Astafiev, A. M. Zagoskin, A. A. Abdumalikov, Y. A. Pashkin, T. Yamamoto, K. Inomata, Y. Nakamura, and J. S. Tsai, *Resonance Fluorescence of a Single Artificial Atom*, Science, 327 (2010), pp. 840–843.

[6] A. N. Vamivakas, M. Atatüre, J. Dreiser, S. T. Yilmaz, A. Badolato, A. K. Swan, B. B. Goldberg, A. Imamoğlu, and M. S. Ünlü, *Strong Extinction of a Far-Field Laser Beam by a Single Quantum Dot*, Nano Lett., 7 (2007), pp. 2892–2896.

[7] G. Wrigge, I. Gerhardt, J. Hwang, G. Zumofen, and V. Sandoghdar, *Efficient coupling of photons to a single molecule and the observation of its resonance fluorescence*, Nature Physics, 4 (2008), pp. 60–66.

[8] I.-C. Hoi, T. Palomaki, J. Lindkvist, G. Johansson, P. Delsing, and C. M. Wilson, *Generation of Nonclassical Microwave States Using an Artificial Atom in 1d Open Space*, Phys. Rev. Lett., 108 (2012), p. 263601.

[9] C. Eichler, D. Bozyigit, and A. Wallraff, *Characterizing quantum microwave radiation and its entanglement with superconducting qubits using linear detectors*, Phys. Rev. A, 86 (2012), p. 032106.

[10] C. Eichler, D. Bozyigit, C. Lang, L. Steffen, J. Fink, and A. Wallraff, *Experimental State Tomography of Itinerant Single Microwave Photons*, Phys. Rev. Lett., 106 (2011), p. 220503.

[11] B. Yurke, P. G. Kaminsky, R. E. Miller, E. A. Whittaker, A. D. Smith, A. H. Silver, and R. W. Simon, *Observation of 4.2-K equilibrium-noise squeezing via a Josephson-parametric amplifier*, Phys. Rev. Lett., 60 (1988), pp. 764–767.

[12] B. Yurke, L. R. Corruccini, P. G. Kaminsky, L. W. Rupp, A. D. Smith, A. H. Silver, R. W. Simon, and E. A. Whittaker, *Observation of parametric amplification and deamplification in a Josephson parametric amplifier*, Phys. Rev. A, 39 (1989), pp. 2519–2533.

[13] R. Vijay, D. H. Slichter, and I. Siddiqi, *Observation of Quantum Jumps in a Superconducting Artificial Atom*, Phys. Rev. Lett., 106 (2011), p. 110502.

[14] S. Gasparinetti, M. Pechal, J.-C. Besse, M. Mondal, C. Eichler, and A. Wallraff, *Correlations and Entanglement of Microwave Photons Emitted in a Cascade Decay*, Phys. Rev. Lett., 119 (2017), p. 140504.

[15] H. Zheng and H. U. Baranger, *Persistent Quantum Beats and Long-Distance Entanglement from Waveguide-Mediated Interactions*, Phys. Rev. Lett., 110 (2013), p. 113601.

[16] J. P. Martinez, S. Leger, N. Gheeraert, R. Dassonneville, L. Planat, F. Foroughi, Y. Krupko, O. Buisson, C. Naud, W. Guichard, S. Florens, I. Snyman, and N. Roch, *Probing a transmon qubit via the ultra-strong coupling to a Josephson waveguide*, arXiv:1802.00633 [cond-mat, physics:quant-ph], (2018). arXiv: 1802.00633.

[17] P. Forn-Díaz, J. J. García-Ripoll, B. Peropadre, J.-L. Orgiazzi, M. A. Yurtalan, R. Belyansky, C. M. Wilson, and A. Lupascu, *Ultrastrong coupling of a single artificial atom to an electromagnetic continuum in the nonperturbative regime*, Nat Phys, 13 (2017), pp. 39–43.

[18] J. M. Raimond and S. Haroche, *Exploring the Quantum*, Oxford Graduate Series, 2006.

[19] H. Mabuchi and A. C. Doherty, *Cavity Quantum Electrodynamics: Coherence in Context*, Science, 298 (2002), pp. 1372–1377.

[20] S. Haroche, *Nobel Lecture: Controlling photons in a box and exploring the quantum to classical boundary*, Rev. Mod. Phys., 85 (2013), pp. 1083–1102.

[21] T. Peyronel, O. Firstenberg, Q.-Y. Liang, S. Hofferberth, A. V. Gorshkov, T. Pohl, M. D. Lukin, and V. Vuletić, *Quantum nonlinear optics with single photons enabled by strongly interacting atoms*, Nature, 488 (2012), pp. 57–60.

[22] O. Firstenberg, T. Peyronel, Q.-Y. Liang, A. V. Gorshkov, M. D. Lukin, and V. Vuletić, *Attractive photons in a quantum nonlinear medium*, Nature, 502 (2013), pp. 71–75.

[23] J. Kondo, *Resistance Minimum in Dilute Magnetic Alloys*, Progress of Theoretical Physics, 32 (1964), pp. 37–49.

[24] D. Goldhaber-Gordon, H. Shtrikman, D. Mahalu, D. Abusch-Magder, U. Meirav, and M. A. Kastner, *Kondo effect in a single-electron transistor*, Nature, 391 (1998), pp. 156–159.

[25] S. M. Cronenwett, *A Tunable Kondo Effect in Quantum Dots*, Science, 281 (1998), pp. 540–544.

[26] A. J. Leggett, S. Chakravarty, A. T. Dorsey, M. P. A. Fisher, A. Garg, and W. Zwerger, *Dynamics of the dissipative two-state system*, Rev. Mod. Phys., 59 (1987), pp. 1–85.

[27] I. Snyman and S. Florens, *Robust Josephson-Kondo screening cloud in circuit quantum electrodynamics*, Physical Review B, 92 (2015).

[28] H. T. M. Nghiem, D. M. Kennes, C. Klöckner, V. Meden, and T. A. Costi, *Ohmic two-state system from the perspective of the interacting resonant level model: Thermodynamics and transient dynamics*, Phys. Rev. B, 93 (2016), p. 165130.

[29] M. Goldstein, M. H. Devoret, M. Houzet, and L. I. Glazman, *Inelastic Microwave Photon Scattering off a Quantum Impurity in a Josephson-Junction Array*, Physical Review Letters, 110 (2013).

[30] P. Orth, A. Imambekov, and K. Le Hur, *Nonperturbative stochastic method for driven spin-boson model*, Phys. Rev. B, 87 (2013), p. 014305.

[31] H. Wang and M. Thoss, *From coherent motion to localization: dynamics of the spin-boson model at zero temperature*, New J. Phys., 10 (2008), p. 115005.

[32] F. A. Y. N. Schröder and A. W. Chin, *Simulating open quantum dynamics with time-dependent variational matrix product states: Towards microscopic correlation of environment dynamics and reduced system evolution*, Phys. Rev. B, 93 (2016), p. 075105.

[33] D. F. Walls and G. J. Milburn, *Quantum Optics*, Springer, 2nd ed., 2007.

[34] P. Meystre and M. Sargent, *Elements of quantum optics*, Springer-Verlag Berlin, Heidelberg, 2010.

[35] U. Vool and M. Devoret, *Introduction to quantum electromagnetic circuits*, International Journal of Circuit Theory and Applications, 45 (2017), pp. 897–934.

[36] J. Sakurai, *Modern Quantum Mechanics*, 1994.

[37] E. Schrödinger, *Der stetige übergang von der Mikro- zur Makromechanik*, Die Naturwissenschaften, (1926), pp. 664–666.

[38] L. Mandel and E. Wolf, *Optical Coherence*, Cambridge University Press, 1995.

[39] R. J. Glauber, *Coherent and Incoherent States of the Radiation Field*, Phys. Rev., 131 (1963), pp. 2766–2788.

[40] R. J. Glauber, *The Quantum Theory of Optical Coherence*, Phys. Rev., 130 (1963), pp. 2529–2539.

[41] R. J. Glauber, *Photon Correlations*, Phys. Rev. Lett., 10 (1963), pp. 84–86.

[42] E. C. G. Sudarshan, *Equivalence of Semiclassical and Quantum Mechanical Descriptions of Statistical Light Beams*, Phys. Rev. Lett., 10 (1963), pp. 277–279.

[43] J. R. Klauder, *Improved Version of Optical Equivalence Theorem*, Phys. Rev. Lett., 16 (1966), pp. 534–536.

[44] C. Cohen-Tannoudji, J. Dupont-Roc, and G. Grynberg, *Photons and Atoms: Introduction to Quantum Electrodynamics*, Wiley, 1997.

[45] A. P. Reed, K. H. Mayer, J. D. Teufel, L. D. Burkhart, W. Pfaff, M. Reagor, L. Sletten, X. Ma, R. J. Schoelkopf, E. Knill, and K. W. Lehnert, *Faithful conversion of propagating quantum information to mechanical motion*, Nature Physics, 13 (2017), pp. 1163–1167.

[46] M. Tinkham, *Introduction to Superconductivity*, McGraw-Hill, Inc., 2nd ed., 1996.

[47] M. H. Devoret, A. Wallraff, and J. M. Martinis, *Superconducting Qubits: A Short Review*, arXiv:cond-mat/0411174, (2004). arXiv: cond-mat/0411174.

[48] P. de Gennes, *Superconductivity of Metals and Alloys*, Westview Press, 1999.

[49] V. Ambegaokar and A. Baratoff, *Tunneling Between Superconductors*, Phys. Rev. Lett., 10 (1963), pp. 486–489.

[50] R. Lutchyn, L. Glazman, and A. Larkin, *Quasiparticle decay rate of Josephson charge qubit oscillations*, Phys. Rev. B, 72 (2005), p. 014517.

[51] J. M. Martinis, M. Ansmann, and J. Aumentado, *Energy Decay in Superconducting Josephson-Junction Qubits from Nonequilibrium Quasiparticle Excitations*, Phys. Rev. Lett., 103 (2009), p. 097002.

[52] J. Koch, T. M. Yu, J. Gambetta, A. A. Houck, D. I. Schuster, J. Majer, A. Blais, M. H. Devoret, S. M. Girvin, and R. J. Schoelkopf, *Charge-insensitive qubit design derived from the Cooper pair box*, Physical Review A, 76 (2007).

[53] J. A. Schreier, A. A. Houck, J. Koch, D. I. Schuster, B. R. Johnson, J. M. Chow, J. M. Gambetta, J. Majer, L. Frunzio, M. H. Devoret, S. M. Girvin, and R. J. Schoelkopf, *Suppressing charge noise decoherence in superconducting charge qubits*, Phys. Rev. B, 77 (2008), p. 180502.

[54] A. Cottet, *Implementation of a quantum bit in a superconducting circuit*, PhD thesis, 2002.

[55] T. Weissl, *Dynamique quantique de la phase et de la charge dans les chaînes des jonctions Josephson*, PhD thesis, 2016.

[56] T. Heinzel, *Mesoscopic Electronics in Solid State Nanostructures*, Wiley-VCH, 2007.

[57] D. Braak, *Integrability of the Rabi Model*, Phys. Rev. Lett., 107 (2011), p. 100401.

[58] J. Braumüller, M. Marthaler, A. Schneider, A. Stehli, H. Rotzinger, M. Weides, and A. V. Ustinov, *Analog quantum simulation of the Rabi model in the ultra-strong coupling regime*, Nature Communications, 8 (2017), p. 779.

[59] D. Z. Rossatto, C. J. Villas-Bôas, M. Sanz, and E. Solano, *Spectral classification of coupling regimes in the quantum Rabi model*, Phys. Rev. A, 96 (2017), p. 013849.

[60] C. Leroux, L. C. G. Govia, and A. A. Clerk, *Simple variational ground state and pure-cat-state generation in the quantum Rabi model*, Phys. Rev. A, 96 (2017), p. 043834.

[61] L. Yu, S. Zhu, Q. Liang, G. Chen, and S. Jia, *Analytical solutions for the Rabi model*, Phys. Rev. A, 86 (2012), p. 015803.

[62] F. A. Wolf, F. Vallone, G. Romero, M. Kollar, E. Solano, and D. Braak, *Dynamical correlation functions and the quantum Rabi model*, Phys. Rev. A, 87 (2013), p. 023835.

[63] M.-J. Hwang, R. Puebla, and M. B. Plenio, *Quantum Phase Transition and Universal Dynamics in the Rabi Model*, Phys. Rev. Lett., 115 (2015), p. 180404.

[64] K. Le Hur, *Kondo resonance of a microwave photon*, Physical Review B, 85 (2012).

[65] A. A. Abdumalikov, O. Astafiev, A. M. Zagoskin, Y. A. Pashkin, Y. Nakamura, and J. S. Tsai, *Electromagnetically Induced Transparency on a Single Artificial Atom*, Phys. Rev. Lett., 104 (2010), p. 193601.

[66] L. Magazzù, P. Forn-Díaz, R. Belyansky, J.-L. Orgiazzi, M. A. Yurtalan, M. R. Otto, A. Lupascu, C. M. Wilson, and M. Grifoni, *Probing the strongly driven spin-boson model in a superconducting quantum circuit*, Nature Communications, 9 (2018), p. 1403.

[67] N. Gheeraert, S. Bera, and S. Florens, *Spontaneous emission of Schrödinger cats in a waveguide at ultrastrong coupling*, New J. Phys., 19 (2017), p. 023036.

[68] N. Gheeraert, X. H. H. Zhang, S. Bera, N. Roch, H. U. Baranger, and S. Florens, *Particle Production in Ultra-Strong Coupling Waveguide QED*, arXiv:1802.01665 [cond-mat, physics:quant-ph], (2018). arXiv: 1802.01665.

[69] S. Bera, S. Florens, H. U. Baranger, N. Roch, A. Nazir, and A. W. Chin, *Stabilizing Spin Coherence Through Environmental Entanglement in Strongly Dissipative Quantum Systems*, Physical Review B, 89 (2014).

[70] S. Bera, A. Nazir, A. W. Chin, H. U. Baranger, and S. Florens, *Generalized multipolaron expansion for the spin-boson model: Environmental entanglement and the biased two-state system*, Physical Review B, 90 (2014), p. 075110.

[71] E. J. Heller, *Time-dependent approach to semiclassical dynamics*, The Journal of Chemical Physics, 62 (1975), pp. 1544–1555.

[72] S. Florens and I. Snyman, *Universal spatial correlations in the anisotropic Kondo screening cloud: Analytical insights and numerically exact results from a coherent state expansion*, Phys. Rev. B, 92 (2015), p. 195106.

[73] P. Kramer and M. Saraceno, *Geometry of the Time-Dependent Variational Principle in Quantum Mechanics*, Springer, 1981.

[74] Y. Yao, L. Duan, Z. Lü, C.-Q. Wu, and Y. Zhao, *Dynamics of the sub-Ohmic spin-boson model: A comparison of three numerical approaches*, Phys. Rev. E, 88 (2013), p. 023303.

[75] S. Bera, H. U. Baranger, and S. Florens, *Dynamics of a qubit in a high-impedance transmission line from a bath perspective*, Phys. Rev. A, 93 (2016), p. 033847.

[76] I. Burghardt, M. Nest, and G. A. Worth, *Multiconfigurational system-bath dynamics using Gaussian wave packets: Energy relaxation and decoherence induced by a finite-dimensional bath*, The Journal of Chemical Physics, 119 (2003), pp. 5364–5378.

[77] E. J. Heller, *Frozen Gaussians: A very simple semiclassical approximation*, The Journal of Chemical Physics, 75 (1981), pp. 2923–2931.

[78] K. G. Kay, *Integral expressions for the semiclassical time-dependent propagator*, The Journal of Chemical Physics, 100 (1994), pp. 4377–4392.

[79] M. A. Sepulveda, S. Tomsovic, and E. J. Heller, *Semiclassical propagation: How long can it last?*, Physical Review Letters, 69 (1992), p. 5.

[80] S. Tomsovic and E. J. Heller, *Semiclassical dynamics of chaotic motion: Unexpected long-time accuracy*, Phys. Rev. Lett., 67 (1991), pp. 664–667.

[81] H. D. Meyer, U. Manthe, and L. S. Cederbaum, *The multi-configurational time-dependent Hartree approach*, Chemical Physics Letters, 165 (1990), pp. 73–78.

[82] H. Wang and M. Thoss, *Multilayer formulation of the multiconfiguration time-dependent Hartree theory*, The Journal of Chemical Physics, 119 (2003), pp. 1289–1299.

[83] I. Kondov, M. Čížek, C. Benesch, H. Wang, and M. Thoss, *Quantum Dynamics of Photoinduced Electron-Transfer Reactions in Dye-Semiconductor Systems: First-Principles Description and Application to Coumarin 343-TiO2*, J. Phys. Chem. C, 111 (2007), pp. 11970–11981.

[84] I. R. Craig, M. Thoss, and H. Wang, *Proton transfer reactions in model condensed-phase environments: Accurate quantum dynamics using the multilayer multiconfiguration time-dependent Hartree approach*, The Journal of Chemical Physics, 127 (2007), p. 144503.

[85] I. Burghardt, H.-D. Meyer, and L. S. Cederbaum, *Approaches to the approximate treatment of complex molecular systems by the multiconfiguration time-dependent Hartree method*, The Journal of Chemical Physics, 111 (1999), pp. 2927–2939.

[86] G. Richings, I. Polyak, K. Spinlove, G. Worth, I. Burghardt, and B. Lasorne, *Quantum dynamics simulations using Gaussian wavepackets: the vMCG method*, International Reviews in Physical Chemistry, 34 (2015), pp. 269–308.

[87] F. A. Wolf, M. Kollar, and D. Braak, *Exact real-time dynamics of the quantum Rabi model*, Phys. Rev. A, 85 (2012), p. 053817.

[88] T. J. Martínez, M. Ben-Nun, and R. D. Levine, *Multi-Electronic-State Molecular Dynamics: A Wave Function Approach with Applications*, J. Phys. Chem., 100 (1996), pp. 7884–7895.

[89] T. J. Martínez, M. Ben-Nun, and R. D. Levine, *Molecular Collision Dynamics on Several Electronic States*, J. Phys. Chem. A, 101 (1997), pp. 6389–6402.

[90] M. Ben-Nun and T. J. Martínez, *Nonadiabatic molecular dynamics: Validation of the multiple spawning method for a multidimensional problem*, The Journal of Chemical Physics, 108 (1998), pp. 7244–7257.

[91] S. Deléglise, I. Dotsenko, C. Sayrin, J. Bernu, M. Brune, J.-M. Raimond, and S. Haroche, *Reconstruction of non-classical cavity field states with snapshots of their decoherence*, Nature, 455 (2008), pp. 510–514.

[92] B. Peropadre, D. Zueco, D. Porras, and J. J. García-Ripoll, *Nonequilibrium and Nonperturbative Dynamics of Ultrastrong Coupling in Open Lines*, Phys. Rev. Lett., 111 (2013), p. 243602.

[93] G. Díaz-Camacho, A. Bermudez, and J. J. García-Ripoll, *Dynamical polaron Ansatz: A theoretical tool for the ultrastrong-coupling regime of circuit QED*, Phys. Rev. A, 93 (2016), p. 043843.

[94] E. Sanchez-Burillo, D. Zueco, J. J. Garcia-Ripoll, and L. Martin-Moreno, *Scattering in the Ultrastrong Regime: Nonlinear Optics with One Photon*, Physical Review Letters, 113 (2014).

[95] T. Shi, Y. Chang, and J. J. García-Ripoll, *Ultrastrong Coupling Few-Photon Scattering Theory*, Phys. Rev. Lett., 120 (2018), p. 153602.

[96] T. Shi, E. Demler, and J. I. Cirac, *Variational Study of Fermionic and Bosonic Systems with Non-Gaussian States: Theory and Applications*, Annals of Physics, 390 (2018), pp. 245–302.

[97] T. Shi, D. E. Chang, and J. I. Cirac, *Multiphoton-scattering theory and generalized master equations*, Physical Review A, 92 (2015).

[98] H. Zheng, D. J. Gauthier, and H. U. Baranger, *Waveguide QED: Many-body bound-state effects in coherent and Fock-state scattering from a two-level system*, Phys. Rev. A, 82 (2010), p. 063816.

[99] H. Carmichael, *An Open Systems Approach to Quantum Optics*, Springer-Verlag, Berlin, 1993.

[100] E. Sánchez-Burillo, L. Martín-Moreno, J. J. García-Ripoll, and D. Zueco, *Full two-photon down-conversion of a single photon*, Phys. Rev. A, 94 (2016), p. 053814.

[101] M. Laakso and M. Pletyukhov, *Scattering of Two Photons from Two Distant Qubits: Exact Solution*, Phys. Rev. Lett., 113 (2014), p. 183601.

[102] Y.-L. L. Fang and H. U. Baranger, *Waveguide QED: Power spectra and correlations of two photons scattered off multiple distant qubits and a mirror*, Phys. Rev. A, 91 (2015), p. 053845.

[103] T. Roy, S. Kundu, M. Chand, A. M. Vadiraj, A. Ranadive, N. Nehra, M. P. Patankar, J. Aumentado, A. A. Clerk, and R. Vijay, *Broadband parametric amplification with impedance engineering: Beyond the gain-bandwidth product*, Appl. Phys. Lett., 107 (2015), p. 262601.

[104] D. M. Pozar, *Microwave Engineering*, Wiley, fourth ed., 1998.

[105] U. Fano, *Effects of Configuration Interaction on Intensities and Phase Shifts*, Phys. Rev., 124 (1961), pp. 1866–1878.

[106] M. P. da Silva, D. Bozyigit, A. Wallraff, and A. Blais, *Schemes for the observation of photon correlation functions in circuit QED with linear detectors*, Phys. Rev. A, 82 (2010), p. 043804.

[107] C. Lang, *Quantum Microwave Radiation and its Interference Characterized by Correlation Function Measurements in Circuit Quantum Electrodynamics*, PhD thesis, 2014.

[108] *AutoCorrelation VI - LabVIEW 2012 Help - National Instruments*.

[109] D. Bozyigit, C. Lang, L. Steffen, J. M. Fink, C. Eichler, M. Baur, R. Bianchetti, P. J. Leek, S. Filipp, M. P. da Silva, A. Blais, and A. Wallraff, *Antibunching of microwave-frequency photons observed in correlation measurements using linear detectors*, Nat Phys, 7 (2011), pp. 154–158.

[110] H. A. van der Vorst, *Iterative Krylov Methods for Large Linear Systems*, no. 13 in Cambridge Monographs on Applied and Computational Mathematics, Cambridge University Press, 1st ed., Nov. 2009.

[111] C. W. S. Chang, M. Simoen, J. Aumentado, C. Sabín, P. Forn-Díaz, A. M. Vadiraj, F. Quijandría, G. Johansson, I. Fuentes, and C. M. Wilson, *Generating Multimode Entangled Microwaves with a Superconducting Parametric Cavity*, arXiv:1709.00083 [quant-ph], (2017). arXiv: 1709.00083.

[112] N. E. Frattini, V. V. Sivak, A. Lingenfelter, S. Shankar, and M. H. Devoret, *Optimizing the nonlinearity and dissipation of a SNAIL Parametric Amplifier for dynamic range*, arXiv:1806.06093 [cond-mat, physics:quant-ph], (2018). arXiv: 1806.06093.

[113] N. E. Frattini, U. Vool, S. Shankar, A. Narla, K. M. Sliwa, and M. H. Devoret, *3-wave mixing Josephson dipole element*, Appl. Phys. Lett., 110 (2017), p. 222603.

[114] G. Liu, T.-C. Chien, X. Cao, O. Lanes, E. Alpern, D. Pekker, and M. Hatridge, *Josephson parametric converter saturation and higher order effects*, Appl. Phys. Lett., 111 (2017), p. 202603.

[115] S. Fan, Ş. E. Kocabaş, and J.-T. Shen, *Input-output formalism for few-photon transport in one-dimensional nanophotonic waveguides coupled to a qubit*, Phys. Rev. A, 82 (2010), p. 063821.

[116] Ş. E. Kocabaş, E. Rephaeli, and S. Fan, *Resonance fluorescence in a waveguide geometry*, Phys. Rev. A, 85 (2012), p. 023817.

[117] K. Lalumière, B. C. Sanders, A. F. van Loo, A. Fedorov, A. Wallraff, and A. Blais, *Input-output theory for waveguide QED with an ensemble of inhomogeneous atoms*, Phys. Rev. A, 88 (2013), p. 043806.